

Thomas Hornung

---

**Optimal control  
with ultrashort laser pulses:  
Theory and experiment**



# **Optimal control with ultrashort laser pulses: Theory and experiment**

Dissertation an der Fakultät für Physik  
der Ludwig-Maximilians-Universität München

Thomas Hornung

München, den 10. April 2002

1. Gutachten: PD Dr. Regina de Vivie-Riedle
2. Gutachten: Prof. Dr. Hänsch

Tag der mündlichen Prüfung:

## Zusammenfassung

Die **kohärente Kontrolle** ist ein neues faszinierendes Feld, welches theoretische und experimentelle Bemühungen zur Kontrolle von Quantenphänomenen mittels geformter Laserimpulse umfasst. Unter Ausnutzung der Kohärenz wird das Quantensystem so angeregt, dass ein bestimmter quantenmechanischer Zustand oder ein Reaktionsprodukt erreicht wird. Die nötige Impulsform für ein gewünschtes Kontrollziel kann nur in wenigen, einfachen Fällen durch eine analytische Rechnung gewonnen werden. Stattdessen werden iterative Verfahren angewendet, die keinerlei Kenntnis über den Kontrollmechanismus voraussetzen. In Experimenten wird eine **Lernschleife** eingesetzt, bestehend aus einem Impulsformer, der durch einen evolutionären Computercode gesteuert wird. Dieser evolutionäre Algorithmus selektiert und erzeugt mittels Rekombination und Mutation jene geformten Impulse, die ein direkt mit dem Kontrollziel korreliertes experimentelles Signal maximieren. In der optimalen Kontrolltheorie (**OCT**) wird die adäquateste Impulsform dagegen durch die numerische iterative Lösung eines gekoppelten Satzes von drei Gleichungen bestimmt, die zuvor durch Variation eines Funktionals gewonnen wurden.

Diese Arbeit befasst sich mit dem Gebiet der kohärenten Kontrolle und verfolgt zunächst einen experimentellen Ansatz, schafft dann die Brücke zur Theorie, und entwickelt schließlich die Theorie weiter, so dass neue Systeme und Anwendungskonzepte untersucht werden konnten.

**Teil I.** In diesem experimentellen Teil wird die Lernschleife angewendet und durch gezielte Parametrisierungen die Suchmethodik verbessert. Das Natrium Atom und das Kalium Dimer dienen dabei als Testsysteme, da hier entweder theoretische Modelle zur Beschreibung der Feldwechselwirkung bereits vorlagen oder im Rahmen dieser Arbeit neu entwickelt wurden. Dabei konnte auch die entscheidende Frage studiert werden, ob das komplexe Laserfeld im Wechselwirkungsbereich noch die anfänglich aufgeprägte Form besitzt. Die Kontrolle eines 1-Photonenüberganges im Na basiert auf der einzigartigen Möglichkeit mit Impulsformung einen beliebig phasenkorrelierten Doppelimpuls zu erzeugen. Zusätzlich konnte der Besetzungstransfer über einen 2-Photonenübergang unter Verwendung einer Lernschleife maximiert oder minimiert werden. Die sich dabei ergebenden einfacheren Impulsformen sind in hervorragender Übereinstimmung mit dem theoretischen Modell. Nachdem die Kontrolle in einem Atom gezeigt werden konnte, wurde die Lernschleife verwendet, um das Vierwellenmisch (FWM) Antwortsignal des  $K_2$  in der Gasphase zu manipulieren. Das FWM Signal erlaubt es die Dynamik auf der Grundzustands- und einer angeregten Potentialfläche gleichzeitig zu erfassen. Es konnte nun gezeigt werden, dass eine korrekte Modulation der wechselwirkenden Laserfelder das FWM Signalfeld auf die Messung einer gewünschten Dynamik beschränkt. Theoretische Modelle wurden hergeleitet und erklären diesen Effekt. Zudem konnte eine Impulscharakterisierung di-

rekt im Interaktionsbereich vorgenommen werden, indem das FWM Signal spektral aufgelöst wurde.

**Teil II.** Die Lösungen der OCT können sehr komplexe optimale Laserfelder sein, die schwer experimentell zu realisieren sind und zudem den Kontrollmechanismus verbergen. Die theoretischen Ansätze zu neuen Funktionalen und Optimierungsstrategien in diesem Teil der Dissertation versuchen, diese Lücke zwischen OCT und Experiment zu schließen. Mit ihrer Hilfe ist es möglich, die Komplexität der optimalen Impulse auf ein Minimum zu reduzieren. Das Ergebnis sind robuste Felder, deren Spektren die Handschrift des Kontrollmechanismus tragen. Ferner ist es möglich, neben diesem robusten auch weitere optimale Wege zum Kontrollziel aufzudecken. Diese Techniken erlauben ein detailliertes Studium selektiven Zustandstransfers und molekularer Besetzungsinversion mit geformten Femtosekunden-Impulsen. Auch die Einflüsse typischer experimenteller Gegebenheiten, wie molekulare Rotation oder das Vorliegen eines thermischen Ensembles, wurden auf ihre Kontrollierbarkeit hin erforscht. Schließlich wurde ein einfacher Weg für die experimentelle Realisierung eines mit OCT optimierten Laserfeldes vorgeschlagen, indem das nötige Transmission- und Phasemuster für den Impulsformer berechnet wird.

**Teil III.** Dieser abschließende theoretische Teil erweitert den Anwendungsbereich von OCT auf die Kontrolle dissipativer Systeme und solcher, deren Zeitentwicklung durch eine nichtlineare Gleichung gegeben ist. In bezug auf Dissipation werden in atomaren Systemen STIRAP<sup>1)</sup>-ähnliche optimale Lösungen erreicht. Komplexere Laserfelder ermöglichen es, interne Freiheitsgrade von Molekülen zu kühlen. In bezug auf die nichtlineare Zeitentwicklung wurde OCT angewendet, um die partielle Umwandlung eines atomaren in ein molekulares Kondensat mittels Ramantransfer, verstärkt durch eine zeitabhängige magnetische Feldänderung über eine Feshbach Resonanz zu optimieren. Dieser Prozess wird durch eine erweiterte Gross-Pitaevskii Gleichung beschrieben. Somit ist es das erste Mal, dass die optimalen Kontrollgleichungen für eine nichtlineare Schrödingergleichung hergeleitet und numerisch gelöst wurden. Optimale Nanosekunden-STIRAP- und Femtosekunden-Ramanimpulse werden vorgestellt, die eine signifikant höhere Konversionsrate aufweisen als bisherige Rechnungen.

---

<sup>1)</sup>stimulated Raman scattering involving rapid adiabatic passage

## Abstract

**Coherent control** is a new fascinating field subsuming theoretical and experimental efforts aiming at controlling quantum phenomena using the interaction with tailored laser fields. Building on the coherence property a quantum mechanical system is laser-driven into a specific quantum mechanical state or along a reaction pathway to a desired product. The needed pulse shape for a specific aim can be calculated analytically in a straightforward way only in a few simple cases. Instead the problem of finding the correct field is solved by iterative procedures that require no knowledge about the control mechanism. In experiments a **learning-loop** is set up, consisting of a pulse shaper steered by an evolutionary computer code. The evolutionary algorithm selects and produces by mutation and recombination tailored pulses maximizing an experimental signal, directly correlated with the control aim. In optimal control theory (**OCT**) instead, the optimal pulse shape is found by the numerical iterative solution of a coupled set of three equations, previously obtained from the variation of a functional.

The work in the present thesis researches the field of coherent control and investigates at first an experimental approach, bridges than the gap to theory and finally further develops theory in order to study new systems and applications.

**Part I.** This experimental part concentrates on characterizing the usefulness of the learning-loop setup including efforts to improve its search methodology by developing the concept of parameterizations. The sodium atom and the potassium dimer served as test systems, for which an accurate theory of the interaction with the tailored light field already existed before or could be developed in this thesis. Thereby also the important question of the accurate delivery of a complex shaped pulse into the interaction region could be addressed. In the sodium atom the control of the one-photon transition served to characterize the unique possibility of pulse shaping to produce an arbitrary relative carrier phase shift between consecutive pulses. In addition, the population transfer via a two-photon transition could be maximized (“bright” pulses) or cancelled (“dark” pulses) using the learning-loop approach. The simpler optimal tailored pulses could be compared with theory and were in excellent agreement. After the successful control in an atom, the learning-loop was applied to manipulate the four-wave mixing (FWM) response of  $K_2$  in the gas phase. The FWM signal monitors simultaneously the dynamics occurring on ground and excited electronic potentials. It is shown, that suitable modulation of the interacting pulses can restrict the FWM signal field to only monitor one selected of the two dynamics. Theoretical models explaining this effect were deduced. Finally a pulse characterization within the interaction area could be realized by spectrally resolving the FWM signal.

**Part II.** The use of OCT can result in complex optimal pulses difficult to realize in experiment and hiding the control mechanism in their intricate pulse shapes. The theoretical work in this part of the thesis tries to bridge this gap between OCT and experiment by introducing new functionals and optimization strategies. With these efforts it is possible to restrict the optimal pulse complexity to a minimum, thereby obtaining robust pulses, whose spectra are a direct signature of the control mechanism. Moreover it is possible to distill for a single control task besides the most robust also further optimal pathways. These techniques allow the detailed study of state selective transfer and molecular population inversion using tailored femtosecond pulses. The influence of typical conditions in experiment such as molecular rotation or a thermal ensemble on controllability is investigated. Lastly an elegant way is proposed to characterize the possibility of experimental realization of a theoretically optimized pulse by calculating the required transmission and phase pattern for pulse shaping.

**Part III.** This last theoretical part concentrates on extending the applicability range of OCT to the control including dissipation and to the control of systems governed by nonlinear dynamical equations. Concerning dissipation, optimal solutions of STIRAP<sup>2)</sup> character are obtained for simple atomic systems and more complex fields are used to cool internal degrees of freedom of a molecular sample. Concerning nonlinear time evolution, OCT is applied to the partial conversion of an atomic to a diatomic molecular condensate via Raman transition, enhanced by a time-dependent magnetic field sweep over a Feshbach resonance. This process is described by a generalized Gross-Pitaevskii equation. It is the first time that optimal control equations are derived for a nonlinear Schrödinger equation and solved numerically. Optimal nanosecond STIRAP type and femtosecond Raman pulses are presented, that enhance the conversion rate to a molecular Bose-Einstein condensate over previous results.

---

<sup>2)</sup>stimulated Raman scattering involving rapid adiabatic passage

# Contents

<b>Introduction</b>	<b>1</b>
<b>I Coherent control experiments</b>	<b>7</b>
<b>1 Essentials: The learning-loop</b>	<b>11</b>
1.1 Tailored femtosecond pulses . . . . .	13
1.2 Feedback algorithm and parameterization . . . . .	16
1.3 Pulse characterization and interpretation . . . . .	18
1.4 Simple example of a learning loop application: pulse compression . . . . .	20
<b>2 Control of atomic transitions with phase-related pulses</b>	<b>25</b>
2.1 Experimental setup . . . . .	25
2.2 One-photon Na(3s $\rightarrow$ 3p) transition . . . . .	28
2.3 Two-photon Na(3s $\rightarrow\rightarrow$ 5s) transition . . . . .	37
2.4 Summary and Outlook . . . . .	46
<b>3 Control of dimers using shaped DFWM</b>	<b>47</b>
3.1 Theory of nonlinear spectroscopy . . . . .	47
3.2 Control using shaped pulses in the DFWM process: Theory .	49
3.3 Control using shaped pulses in the DFWM process: Experiment	58
3.4 Using DFWM as an in situ-FROG . . . . .	68
3.5 Summary and Outlook . . . . .	69
<b>4 Coherent control experiments: Concluding remarks</b>	<b>71</b>
<b>II Coherent control theory</b>	<b>73</b>
<b>5 Essentials: Optimal Control Theory (OCT)</b>	<b>77</b>
5.1 Global control as a variational problem . . . . .	78
5.2 Propagators for the dynamical equation . . . . .	82

<b>6</b>	<b>The system and the transfers under study</b>	<b>85</b>
<b>7</b>	<b>Experimentally realizable laser pulses</b>	<b>89</b>
7.1	The definition of a realizable laser pulse . . . . .	91
7.2	The role of the penalty factor . . . . .	93
7.3	The additional laser source . . . . .	97
7.4	Projector method . . . . .	101
<b>8</b>	<b>Application</b>	<b>107</b>
8.1	State selective population transfer (SST) . . . . .	107
8.2	Molecular $\pi$ -pulse (PI) . . . . .	114
<b>9</b>	<b>Comparison experiment and theory</b>	<b>117</b>
9.1	Rotation and orientation effects . . . . .	117
<b>III</b>	<b>New directions of coherent control theory</b>	<b>123</b>
<b>10</b>	<b>Cold molecules, a first approach</b>	<b>127</b>
10.1	Simple example: STIRAP an optimal control solution . . . . .	129
10.2	Molecular cooling with shaped laser fields . . . . .	132
<b>11</b>	<b>Cold molecules, a second approach</b>	<b>141</b>
11.1	Bose-Einstein-Condensates and Feshbach resonances . . . . .	141
11.2	Optimal conversion of an atomic to a molecular BEC . . . . .	146
11.2.1	Nonlinearity . . . . .	147
11.2.2	Use of optimal nanosecond pulses . . . . .	154
11.2.3	Use of optimal femtosecond pulses . . . . .	161
<b>12</b>	<b>Coherent control theory: Concluding remarks</b>	<b>167</b>

# Introduction

There has been longstanding interest in optimizing naturally occurring processes or in controlling them to occur in a specific way. To this end mathematician J. Bernoulli developed the formalism of variational calculus, while engineers build a feedback controlled loop, where the control knobs are steered according to some signal obtained from the system under control. This approach was so general that it could be applied to any field of natural science. In chemistry it was however soon realized, that the control knobs at hand, like temperature, pressure or the choice of a catalyst with which to influence the outcome of reactions were limited.

With the advent of coherent light sources, the continuous wave (cw) lasers, a new possibility of control was realized. The coherence property of lasers allowed to speak of phase as a meaningful quantity, since for the first time interference experiments with light were made possible. Then way back in the 1986 Brumer and Shapiro realized that the concept of interference could have potential implications for the control of chemical reactions [1]. As a proof of principle they devised a simple experiment, where initial and final state were lower and upper level of an atom. Then they connected both states with two light induced pathways, a one- and three-photon transition. A relative phase change between the two lasers of different color allows to choose between constructive or destructive interference of the two pathways controlling thereby the amount of excited state population. In the same year Tannor, Kosloff and Rice proposed to use coherent pulse sequences beyond the cw-limit to control the selectivity of reactions [2]. The experimental realization of this proposal was however only in reach with the advent of femtosecond laser sources.

The rapid development of new laser sources towards ever shorter pulse durations spurred the field of coherent control for three main reasons. One is simply related to the pulse duration itself. Control is coherent only if the coherence or phase relationship in the system generated by the interaction with the laser pulse survives the control period. Now a number of dephasing mechanism that destroy coherence, and distribute the initially localized energy all over the system, can occur even on a femtosecond timescale. This means femtosecond laser pulses are really necessary to control these systems. Another argument for short pulse durations is that the controlled

action must match the timescale of the dynamics occurring in the system. The fastest possible motion of nuclei is the vibration of  $\text{H}_2$  and occurs on a few femtosecond timescale. The 1999 nobel prize in chemistry was awarded to the field of femtosecond pump-probe experiments, since these were the first experiments showing snapshots of nuclear motion. Photography of electron motion needs even shorter, attosecond pulses. Another implication of femtosecond pulses is their high intensities and broad spectra hosting a rainbow of colors. Both of these properties greatly enhance the possibilities of control since the number of pathways is increased considerably. The many coherent frequencies make it possible to induce a phase relationship between transitions energetically far apart and the high intensities enable highly non-linear processes.

But control with light deserves control of the light itself. An ultrashort pulse has a shape, a temporal phase and a polarization state and all of them need to be controlled and measured accurately. Various methods have been used to shape femtosecond pulses. Most of these techniques involve devices such as liquid-crystal spatial light modulators, acousto-optic modulators, or deformable mirrors, that are designed to modulate the phase and/or amplitude of the dispersed spectral components of a femtosecond pulse [3–6]. It is routinely possible to generate user-defined waveforms for coherent control with these pulse shapers and characterize them using a variety of ultrafast measuring techniques. Several experiments show control using simple tailored fields [7–13].

Unfortunately it is by far not always possible to figure out, how to control a system. The difficulty is to find the optimal tailored pulse, that leads to the wanted outcome of the experiment by the correct interference of the multiple light-induced pathways. Consequently, the optimal control revolution began, when Judson and Rabitz proposed to use the feedback or learning loop, adapted to the experimental techniques used in ultrafast laser pulse control, to solve this search problem [14]. Starting from some initial randomly tailored pulse a signal, from the system under control, directly correlated to the desired aim is used as feedback to a learning algorithm, that accordingly steers the pulse shaper. After thousands of experiments or hundreds of iterations the optimized pulse is automatically found without the need of theoretical input. This idea has been very successfully applied to many problems in physics, chemistry and biology [15–25].

A similar challenge had to be solved in theory, where the optimal pulse should drive the theoretical model system in a specified way. Of course the model system governed by some dynamical equation is devised by the theorist himself, however this does not imply that the control of the system is always obvious to him. Therefore, Rabitz [26,27] and independently Tannor, Rice and coworkers [2,28,29] derived a numerical framework named optimal control theory (OCT) using variational calculus. OCT is an iterative pro-

cedure that solves the control problem by itself. It converges in a few tens of iterations by making use of the known future information and the possibility of backward in time propagation. The fast convergence is essential, since the numerical propagation of the system is very time consuming. In experiment this is not an issue, since the quantum mechanical system solves its dynamical equation in real time. With OCT numerous control problems could be solved [30–35].

The experimental and theoretical efforts to control quantum systems with tailored ultrashort pulses constitute the field of coherent control [8, 36–40]. The learning-loop in experiment and the OCT in theory are both iterative procedures that provide an optimal field in a fully self-contained way. No knowledge about the mechanism is needed as input, but also no understanding is obtained about the way the field acts to achieve the desired goal. Moreover, no general approach exists to obtain this information. Analytical calculations are in this sense more elegant, since an equation is obtained describing the interaction of the tailored field with the system, manifesting the control possibilities [41–43].

The experimental work in part I of this thesis is part of the first generation coherent control experiments. Simple systems were chosen in order to be able to derive a closed form equation describing exhaustively the tailored laser field interaction with the system. This approach makes the control mechanism evident. This was a good starting point to test the accurate delivery of the pulse shape into the interaction region, the limits of the pulse shaping apparatus and the performance of the feedback approach. The new concept of parameterizations in time and frequency domain was first introduced as a method of implementing knowledge into the iterative search, simplifying considerably the interpretation of the control mechanism. This allows to establish whether the control is due to, i.e. the ordering of frequencies (chirp), some relative phase effect in a pulse train or the number of interacting pulses. The work on these simple systems has provided basic understanding of control mechanisms and later found applications in the control of complex molecular and biological systems.

Part II of this thesis tries to adapt OCT in order to bridge the gap between coherent control theory and experiment allowing finally for interpretation of the optimal result. Modified functionals and strategies are shown that obtain simple, robust and realizable tailored laser pulses. Moreover the mask pattern needed to tailor the calculated pulse is defined as direct interface between theory and experiment. This allows to characterize quantitatively to what extent a laser pulse is reproducible in experiment. Finally it is possible to check very precisely the correctness of the theoretical model, by noting discrepancies from theoretically predicted results when applying the calculated tailored pulse shapes in experiment.

In part III new applications and concepts of OCT are presented. This work was done in collaboration with D. Tannor (Weizmann Institute, Israel) and B. Verhaar (TU Eindhoven, Netherlands). Here OCT is applied to molecular cooling with tailored femtosecond pulses and to the partial conversion of an atomic to a diatomic molecular condensate via Raman transition, enhanced by a time-dependent magnetic field sweep over a Feshbach resonance.

## Publications

- Thomas Hornung, Marcus Motzkus, and Regina de Vivie-Riedle  
*Influence of molecular rotation and thermal ensembles on control*  
Journal of Chemical Physics, in preparation
- Thomas Hornung, Sergei Gordienko, and Regina de Vivie-Riedle and Boudewijn J. Verhaar  
*Optimal conversion of an atomic to a molecular Bose-Einstein-Condensate*  
submitted to Physical Review Letters
- Thomas Hornung, Marcus Motzkus, and Regina de Vivie-Riedle  
*Teaching optimal control theory to distill robust pulses even under experimental constraints*  
Physical Review A **65**, 021403R (2002)
- Thomas Hornung, Marcus Motzkus, and Regina de Vivie-Riedle  
*Adapting optimal control theory and using learning loops to provide experimentally feasible shaping mask patterns*  
Journal of Chemical Physics **115**, 3105 (2001)
- Thomas Hornung, Richard Meier, Regina de Vivie-Riedle, and Marcus Motzkus  
*Coherent control of the molecular four-wave mixing response by phase and amplitude shaped pulses*  
Chemical Physics **267**, 261 (2001)
- Thomas Hornung, Richard Meier, and Marcus Motzkus  
*Optimal Control of molecular states in a learning loop parameterization in frequency and time domain*  
Chemical Physics Letters **326**, 445 (2000)
- Thomas Hornung, Richard Meier, Dirk Zeidler, Karl-Ludwig Kompa, Detlev Proch, and Marcus Motzkus  
*Optimal control of one- and two-photon transitions with shaped femtosecond pulses and feedback*  
Applied Physics B **71**, 277 (2000)
- Dirk Zeidler, Thomas Hornung, Detlev Proch, and Marcus Motzkus  
*Adaptive compression of tunable pulses from a noncollinear-type OPA to below 16 fs by feedback-controlled pulse shaping*  
Applied Physics B **70**, S125 (2000)

- Thomas Hornung, Richard Meier, Dirk Zeidler, Karl-Ludwig Kompa, Detlev Proch, and Marcus Motzkus  
*Optimal control of two-photon transitions: bright and dark femtosecond pulses designed by a self-learning algorithm*  
Ultrafast Phenomena XII, T. Elsaesser, S. Mukamel, M. M. Murnane and N. F. Scherer eds. (Springer series in chemical physics; 66) p. 24 (2000)
- Thomas Hornung, Richard Meier, and Marcus Motzkus  
*Feedback optimization of molecular states using a parameterization in frequency and time domain*  
Ultrafast Phenomena XII, T. Elsaesser, S. Mukamel, M. M. Murnane and N. F. Scherer eds. (Springer series in chemical physics; 66) p. 27 (2000)

Part I

Coherent control  
experiments



Coherent control experiments entered a new era when the ultrafast pulse shaping technology [4,44,45] was developed and Judson and Rabitz proposed the concept of a learning-loop [14]. They realized that the system to be controlled can solve its Hamiltonian in real time and that therefore thousands of experiments can be carried out in just a second. This is the essential advantage that allows the use of a feedback-loop to solve the inverse problem of finding the pulse that corresponds to a specific solution of the Schrödinger equation without having to resort to theory. The wanted outcome (e.g. bond breaking) is measured by an experimental signal correlated to it (e.g. mass peak of fragment). Differently shaped laser pulses are consecutively sent onto the system leading to an experimental signal, that again serves as feedback to measure the performance of each individual laser pulse. This "trial and error" approach will finally end up with the perfect laser pulse. No knowledge of the Hamiltonian is needed, but the feedback signal must be chosen carefully to be really a measure of the desired outcome. When designing a coherent control experiment the following considerations are of central importance:

1. The wanted outcome must be dependent on the characteristics of the laser pulse adjustable through the pulse shaping device at hand. On one hand this implies that the nature of the light used is versatile enough. Especially the hope is that the properties of the laser pulses in the femtosecond regime their selves (polarization, bandwidth, phase, intensity, ultrafast interaction) are sufficient to the problem (see section 1.1). Taking again the example of bond-breaking it is essential that energy redistribution processes in the system are much slower than the local deposition of energy by the laser pulse. On the other hand the pulse shaping device must have sufficient capabilities to independently change the necessary characteristics of the laser field (see section 1.1).
2. The "trial and error" strategy can be improved considerably if an intelligent and fast learning scheme is used to adjust the shaping device. This algorithm moreover has to cope with uncorrelated signal changes due to unavoidable experimental noise (see section 1.2) .



# Chapter 1

## Essentials: The learning-loop

The components of a learning-loop can look very different depending on the specific application. In abstract terms a learning-loop consists of an *action under external control* which acts on a system and produces there a *system response*. Due to the natural correlation between action and response an *algorithm* can be used to learn how to change the action to control the response in a desired fashion. In the coherent control experiments as already pointed out in the introduction to this chapter the controlled action are the tailored femtosecond laser pulses. The external control knobs are all integrated in a single pulse shaping device. The system response is the feedback signal retrieved from experiment. It is feeded into the optimization algorithm that accordingly steers the pulse shaper to improve the laser pulse shape. The time for the learning-loop to provide an optimal pulse is given by the total number of iterations multiplied by the time it takes to perform one iteration. This time is given by the response time of each of the elements that constitute a closed-loop experiment: laser repetition rate, pulse shaper, learning algorithm and feedback signal retrieved from experiment. Hence it is not possible to be specific, so the total optimization time can range between a few minutes and several hours. In the following a more detailed description of a tailored pulse, its characterization and the feedback algorithm is discussed. This chapter concludes with a practical application of the learning-loop approach: the compression of femtosecond laser pulses to their bandwidth limit.

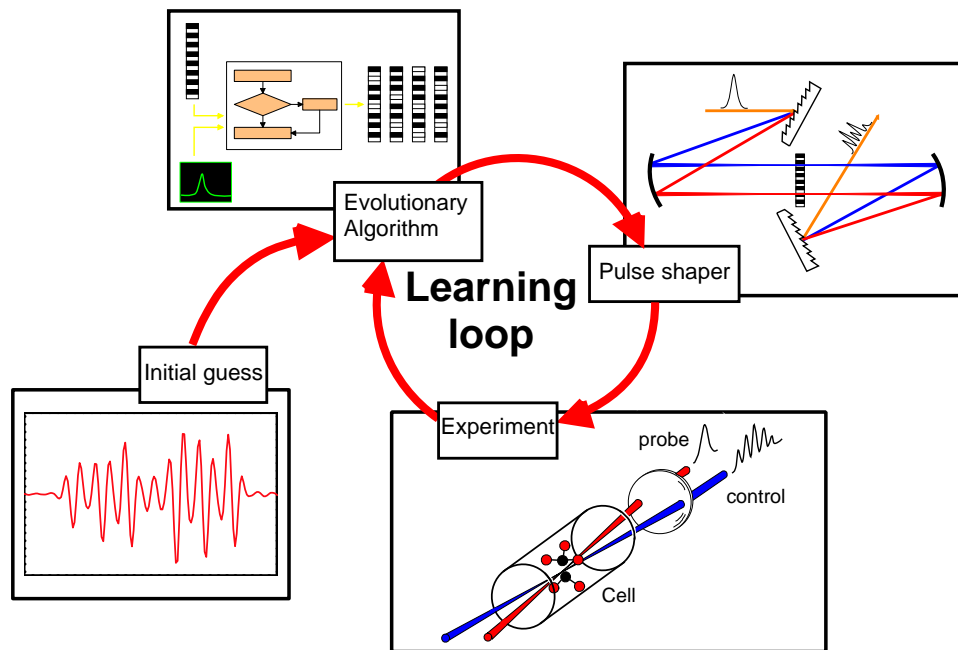


**Figure 1.1:** A closed-loop process for teaching a laser to control quantum systems. The loop is entered with either an initial design estimate or even a random field in some cases. A current laser control field design is created with a pulse shaper and then applied to the sample. The action of the control is assessed, and the results are fed to a learning algorithm to suggest an improved field design for repeated excursions around the loop until the objective is satisfactorily achieved [38].

## 1.1 Tailored femtosecond pulses

The various techniques to tailor a laser field can be divided into two categories. Those operating directly in the time-domain using fast electronic switching devices to structure the time-envelope of the pulse and those in the frequency-domain that shape the spectrum of the pulse. Frequency-domain techniques are the only suitable for shaping femtosecond laser pulses, since these techniques as they operate in parallel on many frequencies of the pulse do not require electronic switches, which are useless in the femtosecond regime due to their comparatively slow switching times (picoseconds). Instead spectral shaping is accomplished by a zero dispersion 4-f setup, that is essentially two spectrometers: the first dispersing the spectral components onto space in its Fourier plane and the second, used in reversed direction to the first, collimates again these frequencies to a single beam of light. The laser pulse passing this setup does not feel any change, but is essentially Fourier transformed and back again. Introducing a device (Spatial Light Modulator = SLM) that can apply a spatial phase and transmission pattern in the Fourier plane of the 4-f setup [see Fig. 1.2] the spectrum of the pulse is modulated [6, 45, 46]. The process of shaping can be described by

$$\epsilon_{out}(\omega) = M(\omega)\epsilon_{in}(\omega). \quad (1.1)$$

Here  $\epsilon_{in}(\omega)$  is the spectrum of the incident pulse and  $\epsilon_{out}(\omega)$  of the outgoing pulse.

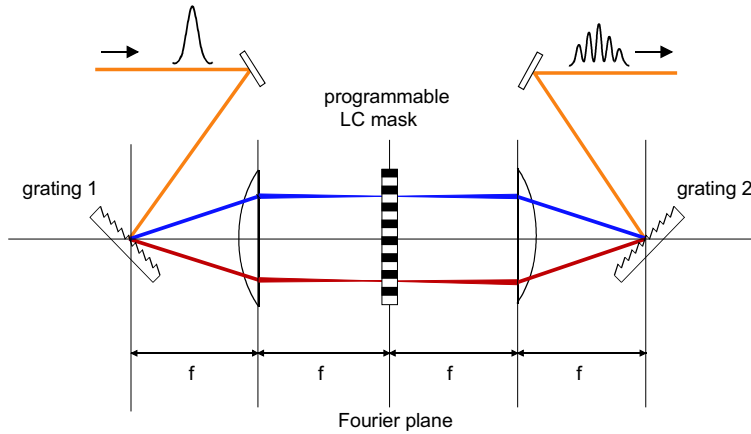


**Figure 1.2:** Typical setup of a femtosecond pulse shaper, consisting of a Spatial Light Modulator located at the Fourier plane of the 4-f geometry. Here  $f$  is the focal length of the lenses.

ing. The outgoing pulse is the same as the incoming pulse if the 4f-setup is accurately calibrated and the SLM is not addressed externally. Consequently, in order for the outgoing pulse to be Fourier limited the pulse must be already bandwidth limited as it enters the shaping device. The SLM is

represented mathematically by a complex function of frequency  $M(\omega)$ , since frequency is mapped onto space according to the dispersion relation of the spectrometer. Eq. (1.1) ignores the effect that the spectral components are also scattered away from their incoming direction, after passing the spatial modulation pattern. This leads irremediably to a shaping of the beam profile in conjunction with the time structure of the pulse, also known as space-time coupling [47].

SLM's can be simple static lithographically edged transmission and phase patterns or more sophisticated programmable devices. Essentially three SLM types are used in coherent control experiments. An acoustic optic modulator AOM [5,46], which is a crystal driven by a piezo loud speaker to produce acoustic waves in it. The ultra fast light pulse sees a snapshot of this traveling acoustic pattern and is Bragg scattered acquiring its phases and amplitudes. Then also adaptive, electrostatically deformable membrane mirrors can be used for phase-only shaping [6]. The third type of SLM, a liquid crystal SLM [4] used in this thesis, consists of an array of 128, 97  $\mu\text{m}$  wide active elements (pixels), that change their transmission and/or retardance properties according to locally applied voltages. Between each two pixels 3  $\mu\text{m}$  inactive transmitting areas exist, called gaps. The desired modulation pattern is available within the orientation time of the liquid crystal molecules, which is about 100 ms.

The pulse modulated by a LC-SLM along the tilted axis due to the linear space-time coupling [47] can be expressed mathematically by the discrete Fourier transform of Eq. (1.1) [45]

$$\epsilon(t) = \sum_{-N/2}^{N/2} a_n \exp(i\phi_n) \epsilon_{in}(t - n\tau). \quad (1.2)$$

The pulse consists therefore of an equidistant comb of subpulses with amplitudes  $a_n$  and phases  $\phi_n$  separated from one another by a finite time  $\tau$  and extending in time from  $[-N/2\tau, N/2\tau]$ . This time interval is called effective shaping window, since the controllable portion of the modulated pulse can only extend in this time interval due to a finite number  $N$  of adjustable pixels. The minimal time step  $\tau$  can be evaluated to be approximately one half of the incident pulse duration, depending on how much spectrum is made to fit on the active mask area. In Fig. 1.3 these and further peculiarities of the LC-SLM due to its pixelation are depicted and are also described in Refs. [47, 48]. The spectrum on the gaps is transmitted without being changed and therefore recollimates to a weak replication of the incident pulse at  $t=0$  [Fig. 1.3(b)]. Also replica of the modulated pulse occur outside the shaping window inside the antinodes of a sinc modulation pattern in time [Fig. 1.3(c)]. This is due to scattering of the frequency components at the rectangularly shaped pixels. The finite focal size of the spectral components however smears out this modulation pattern in space leading to a Gaussian

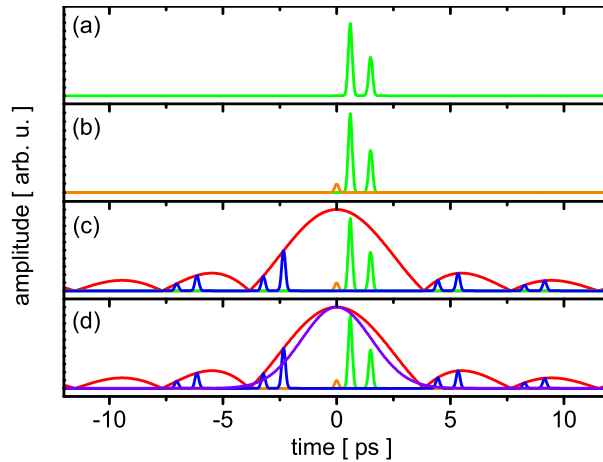


**Figure 1.3:** Peculiarities of a liquid crystal Spatial Light Modulator. (a) Desired pulse shape. (b) Effect of the gaps leading to an unshaped pulse at time zero. (c) Effects due to the discreteness of pixels introducing diffraction of the spectral components and generating pulse replicas. (d) Effect of the finite focal size of each spectral component leading to a Gaussian weighted suppression of the waveform.

centered around  $t=0$  and diminishing considerably the replica [Fig. 1.3(d)]. Due to the space time coupling these replica occur at the outermost parts of the spatial profile and can therefore be taken away spatially using a pinhole. The last effect of discreteness to be pointed out is the sampling criterion. As shaping by an LC-SLM can be at best a discrete sampling of a desired modulation pattern it suffers from the Nyquist theorem. Nyquist's sampling theorem states that a periodic function must be probed at least twice per period, or twice over a phase interval of  $2\pi$ . With reference to a phase function that is to be imposed onto a spectrum, a phase interval of  $2\pi$  hence must be sampled by at least two pixels. Consequently the phase jump over one pixel must be much less than  $\pi$ .

In order to calculate the mask pattern necessary to tailor a desired pulse shape an algorithm is needed. In the case of phase and amplitude shaping a simple Fourier transform connects the coefficients  $128 a_n$  and  $128 \phi_n$  values of Eq. (1.1) with the 128 retardance and 128 transmission values of the pixels [47,48]. Things complicate if a pulse form specified by the set  $(a_n, \phi_n)$  is to be produced by phase-only shaping. It is clear that this problem can only be approximatively solved since 128 phase mask values can not specify 256 time domain values characterizing the shape of the pulse. A fast and practical algorithm to solve this problem is described in Ref. [49].

Recent developments of pulse shaping have been to increase the LC-SLM number of pixels [50], to modify the setup in order to arbitrarily modulate also the polarization of the laser pulse [51] and to obtain spatiotemporal coherent waveforms [52]. Since there exist no liquid crystal materials being

transmissive and producing the necessary retardance values in the ultraviolet and mid IR, shaping at these frequency ranges was essentially obtained by frequency conversion of shaped visible pulses [53,54].

## 1.2 Feedback algorithm and parameterization

**Feedback algorithm.** Finding an extremum of a function depending on many variables is a problem that has been under investigation since the invention of differential calculus. The primary task of any optimization algorithm is to start from an ensemble of suitably chosen initial parameters and then to suggest a revised set which drives the critical observable towards the desired optimum, i.e. to generate new search directions in the multidimensional parameter space. Starting from this new parameter set, the procedure is reiterated until some convergence criterion is fulfilled.

The algorithm of choice for the learning-loop has to fulfill various additional properties: it must be stable against experimental noise, it has to learn as much as possible from the feedback signal in order to rapidly improve the tailored pulse performance, it must avoid local maxima and it has to cope with many adjustable parameters namely the voltages applied to the mask. Therefore deterministic schemes such as steepest descent are not suited since they are prone to get stuck in local minima and are very sensitive to noise. The learning-loop therefore implements the more suited random schemes such as evolutionary strategies [55], genetic algorithms [56] and simulated annealing [57]. Out of these indeterministic schemes evolutionary strategies are known to be robust against experimental noise [58]. However their convergence to a global maximum is not proven mathematically while it is for simulated annealing.

In this thesis an evolutionary strategy which uses 48 individuals (vectors of LC voltages) was applied. These are randomly chosen and represent one generation. For every one of the 48 mask settings of one generation the fitness value is read from the experiment. This serves to quantify the performance of each individual. The most successful ones are taken as parents to the next generation, while the others are discarded. By mutating the parents, i.e. addition of Gaussian white noise with a pre-specified width on each of the vector elements (genes), and by recombining pairs of parents, i.e. interchanging of their genes, the new generation is built. By successive repetition of this scheme, only those vectors corresponding to the highest fitness values will survive and produce offsprings ("survival of the fittest"). Mutation serves as dominant search operator, and therefore the extent of random change of each gene must be intelligently restricted. Excessive mutation will cause the new search points to be widespread in parameter space and no convergence will be achieved. Very small mutational changes, on

the other hand, will allow only very slow convergence. Hence an adaptive control of the mutation rate [55] was implemented, which ties the amount of change to the number of foregoing mutations which had proven to be successful (i.e. produced a better fitness value).

**Parameterizations.** A very important aspect in optimization is the right choice of parameters. A reduction or a specific choice of parameters can lead to an increase in convergence rate, but also to a reduction of the final signal value achieved. Instead of using the completely free optimization, where all the voltages applied to the pixels are taken as *individual* parameters it can be much more efficient to parameterize the mask function or the time envelope of the pulse. A nonlinear frequency chirp of Nth order would then most effectively be parameterized by a polynomial phase function  $\phi(n) = \sum_{i=1}^N a_i n^i$ . Instead of  $2 \cdot 128$  voltage parameters only N parameters  $a_i$  would be necessary. Similarly a direct time domain parameterization is more suited to represent, e.g. a train of N pulses with equal amplitude, variable time separation and phase. Here  $2N-1$  parameters suffice according to Eq. (1.2) to fully characterize such a pulse train. This a much reduced number of parameters compared to a parameterization based on the LC voltage settings.

Parameterization achieves a great improvement beyond the mere reduction of parameters [59,60]. This can best be understood in the abstract notion of phase space. One or several optimum solutions for the specific control process are scattered throughout the phase-space of the system considered, hopefully reachable through arbitrary pulse shaping. The algorithm's task is to converge into the global optimum after a number of consecutive runs. Since feedback pulse shaping means e.g. trying all different voltages for each of the 128 pixels of a Spatial Light Modulator (SLM), the number of parameters can be very high and therefore numerous problems arise, that one has to cope with: convergence slows down, the possibility to start at different phase space locations to cover different solutions is statistical, implementation of theoretical knowledge is difficult and there is no structure in the changes the algorithm performs.

Parameterizations establish order into the statistical approach of evolutionary algorithms and have many important consequences. Each parameterization represents a subset of phase space, meaning phase space is fractioned into tiny regions of parameterizations. This involves the starting locations on phase space to be predetermined and the algorithm to converge much faster since the subset can be chosen to be of a specific size by reducing the number of parameters used in that parameterization. This makes it possible to run the algorithm many times and explore thoroughly this chosen region of phase space for solutions. The importance of incorporating theoretical information into the experiment is obvious, but the pulses calculated

by theory are still not always realizable <sup>1)</sup> and therefore can only approximately be used as an initial guess. Nevertheless, it is possible to implement the process, which has been stated by theory to be responsible for the specific control mechanism, into a learning-loop using adequate parameterizations. The evolutionary algorithm then makes only modifications to few parameters compatible with the mechanism. Due to these very structured changes one is able to monitor effects induced in the studied system by the prognosticated process. The whole pulse shaping phase space is addressed if there is no parameterization used at all (for the LC-SLM case  $2 \cdot 128$  independent pixels times  $\approx 1000$  voltage values). Switching between different parameterizations in time and frequency domain therefore still allows to cover a great extent of the pulse shaping phase space with the advantage of having only few parameters the algorithm has to operate on. When the algorithm is free to switch between parameterizations it will essentially try out different control mechanisms and adapt the most optimal one. This idea is culminated if once a database of control mechanisms is established. With parameterizations it is moreover possible to perform experiments with more sophisticated feedback signals that take a long time to be retrieved (as an example see chapter 3).

### 1.3 Pulse characterization and interpretation

**Pulse characterization.** Measurement of the optimal tailored pulse is an essential first step in determining the control mechanism. In order to fully characterize a femtosecond laser pulse, a measurement technique is needed that can retrieve the phase  $\phi(t)$  and intensity  $I(t)$  of a laser field, that is mathematically described in the slowly-varying envelope approximation as:  $\sqrt{I(t)} \exp(i\omega t + \phi)$  [61]. The most widely used methods that can even be applied down to the single cycle 5 fs regime are:

- Frequency resolved optical gating (FROG) [62]. It involves spectrally resolving the signal beam of an autocorrelation measurement.
- Spectral phase interferometry for direct electric-field reconstruction (SPIDER) [63, 64]. SPIDER is a specific implementation of spectral shearing interferometry. Here an interferometer is used to produce two pulse replicas that are delayed with respect to one another. They are then frequency mixed with a chirped pulse in a nonlinear crystal. Each pulse replica is frequency mixed with a different time slice, of the stretched pulse, and, consequently, the upconverted pulses are spectrally sheared. The interference between this pair of pulses is recorded with a spectrometer followed by an integrating detector.

---

<sup>1)</sup>The realizability of calculated laser pulses could be considerably improved using strategies presented in chapter 7.

- Temporal analysis by dispersing a pair of light electric fields (TADPOLE) [65, 66] is a test-plus-reference spectral interferometer. An unknown test pulse is mixed at a beamsplitter with a time delayed reference pulse, whose electric field shape is known from a FROG or SPIDER measurement. The pulse pair enters a spectrometer and the two spectra combined yield a spectral interferogram. The interferogram yields the complete information of the test pulse by a simple Fourier transformation and an inverse filtered Fourier transformation. With TADPOLE it is possible to measure tailored pulses of a few femtojoule and also extend the range of measurable pulse complexities beyond the possibilities of the available nonlinear crystals.

The advantage of the interferometric approaches is that they require only a one dimensional data set to reconstruct the one dimensional field and can use a direct data inversion to do so in real time. In contrast the FROG technique measures a two-dimensional representation of the one-dimensional field and consequently requires the collection of a relatively large amount of data. The needed algorithm to invert the data and reconstruct the field is thereby more sophisticated. The advantage of FROG is of practical nature as it does not require a new apparatus since mostly an autocorrelator and spectrometer are available.

In this thesis the second-harmonic FROG (SHG FROG) technique was used to characterize the tailored pulses. A more detailed description of this technique follows. The method measures the spectrogram of the pulse, which is sufficient to completely determine  $\epsilon(t)$  [62] (besides the absolute phase)

$$S(\omega, \tau) = \left| \int_{-\infty}^{\infty} dt \epsilon(t)g(t - \tau) \exp(-i\omega t) \right|^2. \quad (1.3)$$

Here  $g(t - \tau)$  is the gate function used to represent the autocorrelator type used. The autocorrelator using second harmonic generation has a gate  $g(t, \tau) = \epsilon(t)\epsilon(t - \tau)$ . Measuring the spectrogram hence means to acquire the spectrum of the autocorrelation signal for each time delay  $\tau$ . The algorithm used to retrieve the complete pulse shape from this spectrogram is based on the method of generalized projections. It is quite sophisticated and will therefore not be explained. The interested reader should refer to Ref. [62]. It should be noted however that in the case the incident laser field to the pulse shaping device is well characterized it is possible to use the pulse shaping equation to make a rough "measurement" of the outgoing tailored pulse. The mask pattern itself then serves to characterize the shaped laser field, of course under the premise that further material in the optical path after the pulse shaper does not have a measurable effect on the pulse shape or can be accounted for.

**Interpretation.** The result of an optimization run is the maximum yield achieved and the respective mask pattern and optimized laser field. The laser field shows usually such a complex shape, that it is completely obscure what essentially the control mechanism is. In order to answer this question several approaches can be pursued. Purely experimental approaches include the following possibilities: The learning-loop iteration can be repeated several times with different initial guess laser pulses generations. The optimal mask patterns attained can be then compared to find similarities. Perhaps groups of similar mask patterns then identify the control pathways. Another approach used is to shoot the laser pulse not only onto the experiment of interest but simultaneously on a second experiment with a well known response. This reference experiment could be for example a non-resonant two-photon transition in an atom. If the experimental signal correlates closely with the reference than the control mechanism is clearly the same, i.e. a non-resonant two-photon transition [67].

A very powerful technique was already discussed earlier and is the concept of parameterization. Here, changes applied to individual pulse parameters can determine whether the control is due to the specific pulse separation, chirp or phase relationship.

Perhaps the best way to obtain the control mechanism is to compare the obtained laser pulse with optimal control theory predictions. However in order to do so there is a gap to surmount between them as will be discussed in detail in part II of this thesis [60, 68].

## 1.4 Simple example of a learning loop application: pulse compression

In this section a simple learning-loop setup is realized with the aim of compressing femtosecond pulses originating from an optical parametric amplifier with noncollinear-type phase-matching [69–73]. This simple, but technically important example shall illustrate the individual elements, that constitute a learning-loop as discussed previously and acts as easy introduction to the automated control experiments of increasing complexity in the next chapters.

Pulse compression is commonly achieved by phase-only shaping. The central task is to apply on the shaper the exact phase function compensating for the intrinsic phase of the pulse, that leads to pulse lengthening and distortion. Especially ultrashort pulses in 20 fs regime as considered here, suffer from group velocity dispersion (GVD) of second and higher orders introduced by dispersive elements installed in the beam path behind the compressor, such as cell windows, wave plates, cuvettes filled with solvents, etc. A major problem is hence the faithful delivery of ultrashort pulses to the location where the actual experiment is performed, especially when the ultrafast dy-

namics of molecules in liquid solvents is to be investigated.

An elegant solution to this problem is presented here, where phase tailoring of 20 fs ultrashort pulses steered by an evolutionary algorithm is used to compress distorted pulses to their bandwidth limit at any chosen point in the experiment [74–76]. The main advantages of the setup are the swiftness of the automated compression procedure (typically less than five minutes) and the capability to compensate phase distortions of arbitrary appearance. The learning-loop setup was optimized to the problem at hand by building a pulse shaper able to support the broad bandwidth of the pulses, by choosing an adequate parameterization and finally by choosing a feedback signal reaching a maximum for a flat phase or shortest pulse duration. A schematic of the learning-loop setup is shown in Fig. 1.4.

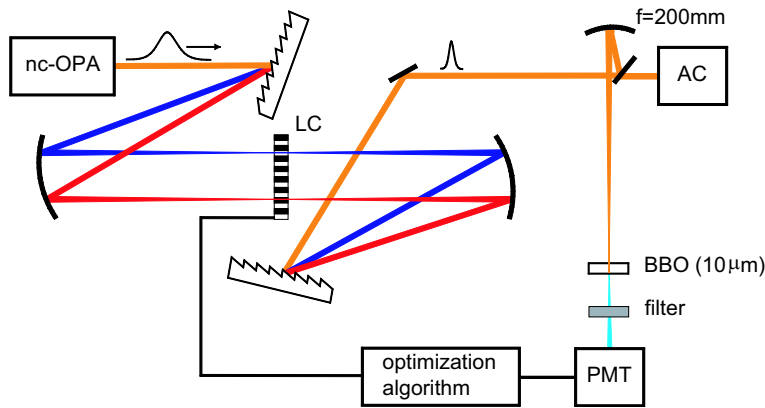


**Figure 1.4:** Learning loop setup for automated compression of pulses from a noncollinear OPA [76].

**Pulse shaper.** An essential requirement for high-quality shaping is an accurate Fourier transformation from the time into the frequency domain and back. The pulses must pass the shaping unit undisturbed as long as no filtering is performed. This is especially restrictive for femtosecond pulses below 30 fs. Great care must thus be taken to avoid clipping of the spectrum (80 nm full width at half maximum) at the aperture of the LC mask. The overall accepted bandwidth of this shaper was designed to be above that of the pulses generated by the noncollinear OPA. Imaging distortion by chromatic aberration becomes important for these very broad spectra and must be avoided. Therefore an all reflective pulse shaping setup is desired, where the lenses are replaced by mirrors [77]. Cylindrical optics are used to reduce the power density impinging on the LC mask and thus prevent damage. The off-axis angles are kept as small as possible to alleviate imaging aberrations introduced by the focusing mirrors. To ensure that the shaper acts as a zero-dispersion compressor as long as the LC mask is inactive, a

pair of prisms before the shaper was installed in a first run to compress the incident pulses close to the Fourier limit ( $< 20$  fs). The shaper was then adjusted until the outgoing pulse was not further broadened.

**Feedback signal.** The frequency doubled light captured by a photomultiplier tube (PMT) after focusing the tailored pulse with a spherical mirror ( $f = 200$  mm) onto a nonlinear crystal (BBO,  $10 \mu\text{m}$ ), serves as feedback signal. A spectral filter (UG-11) in front of the PMT blocks the fundamental wavelengths. This feedback signal is proper since bandwidth limited pulses generate maximum SHG signal [75].

**Parameterization.** Since GVD leads to smooth reshaping of the pulse phase, the most efficient parameterization is of polynomial type

$$\Phi_n = \sum_{k=2}^{K_{max}} c_k \left( \frac{n - N_0}{N} \right)^k, \quad n = 0, \dots, N - 1 = 127, \quad (1.4)$$

with quadratic terms ( $k = 2$ ) as lowest polynomial order  $k$  since constant ( $k = 0$ ) or linear ( $k = 1$ ) phase terms only produce a phase- or time- shift, respectively. In all the following compression experiments the optimization procedure was confined to the search for only second and cubic order phases, i.e.  $K_{max} = 3$  in Eq. (1.4). The parameters  $c_k$  and  $N_0$  are optimized by the algorithm. Because the spectrum of the OPA is widely tunable,  $N_0$  has been included as parameter to ensure that the offset of the phase function coincides with the center of the spectrum after the optimization has been accomplished. Alternative concepts of parameterization such as linear approximation or cubic splines were tested as well but resulted in many more loops of the algorithm while eventually achieving comparable pulse durations.

Having setup the learning-loop its performance is ready to be tested. The chirped output pulses of the noncollinear OPA with a pulse duration of 270 fs [see Fig. 1.5(c)] were sent into the pulse shaper without previous compression using a prism compressor. The algorithm was then applied and a pulse duration below 16 fs was again obtained [see Fig. 1.5(a) and 1.5(c)]. The autocorrelation measurements were performed in a noncollinear arrangement, either with a  $10\text{-}\mu\text{m}$  BBO crystal, or with a 2-photon SiC diode [78]. The mask pattern found by the algorithm to compress the output pulses to their Fourier limit had mainly quadratic chirp [Fig. 1.5(b)]. Since the phases are specified to within modulo  $2\pi$  wrapping of the phase occurs if the  $2\pi$  interval is exceeded. Unwrapping of the phase mask pattern in Fig. 1.5(b) would reveal a strongly curved parabola over all the mask pixel area.

The convergence data of Fig. 1.6 shows the feedback value of the best and worst individual of each generation. In addition the mean feedback value of best and worst is calculated for each generation. At the beginning a random

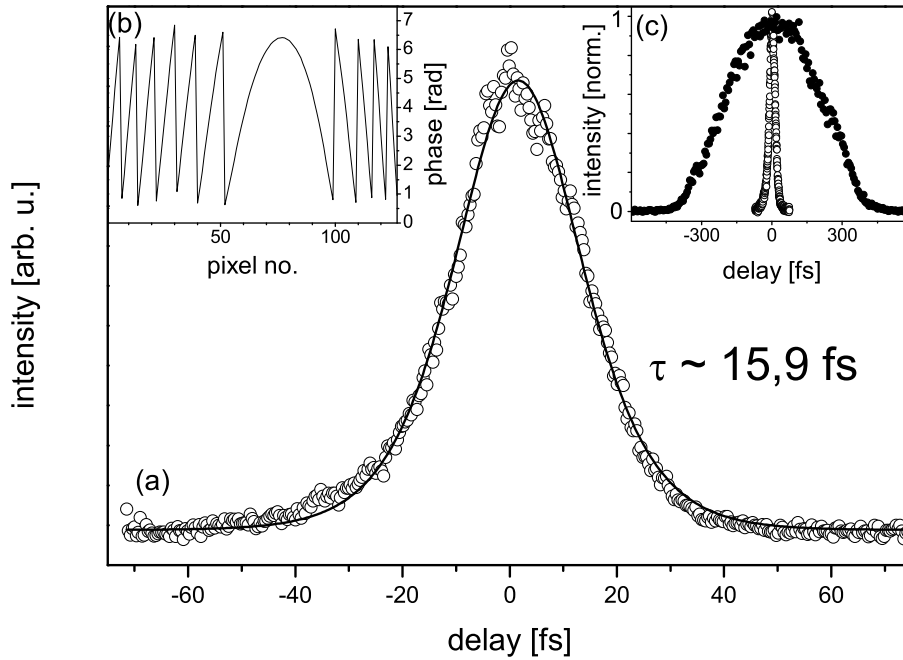


**Figure 1.5:** (a) Autocorrelation of the pulse behind the shaper after polynomial phase optimization. (b) Optimal phase function applied on the mask by the algorithm. (c) Compressed (hollow dots) and uncompressed (filled dots) pulse.

generation is created, whose performance can be already significant depending on the number of individuals and the complexity of the optimization problem. The evolutionary selection then leads to an increase of the best feedback value over the number of iterations until it stagnates at its optimum value. The fluctuation of this value depends on experimental noise and also on the sensitivity of the control parameters - that is large jumps are expected if small changes to the control parameters have a large effect on the feedback signal. This is clearly visible in Fig. 1.6. On the contrary, if the noise level is low and insensitive parameters are used a smooth increase and also an approach of worst and best feedback signal indicating convergence would be expected. The terminal value of the SHG signal was approached after about 25 generations. At a pulse repetition rate of 1 kHz and averaging over 50 pulses the adaptive compressor thus compensates the chirp and produces short output pulses in less than five minutes. This figure should be still reducible with a biased initial population taking advantage of a-priori physical knowledge such as the supposed sign of the chirp to be compensated. With other parameterizations of the phase function, it was found that the convergence speed as well as the final SHG value was dependent on the internal strategy parameters of the algorithms. As a rule of thumb: the more complex the optimization, for example the more parame-

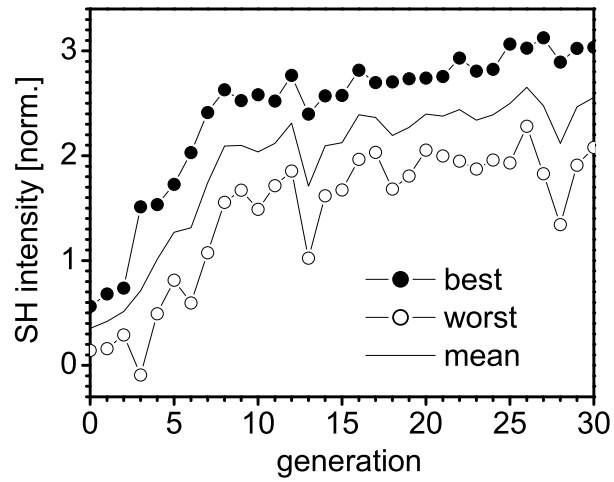


**Figure 1.6:** The convergence curve of pulse compression as measured by the intensity of the SHG signal. Fitness of best (filled dots) and worst (hollow dots) individual of each generation. A mean is also calculated (line).

ters to optimize, the more “careful” the optimum has to be approached by a proper choice of internal strategy parameters mentioned above. This has been investigated in detail in Ref. [58].

## Chapter 2

# Control of atomic transitions with phase-related pulses

The following experiment is part of the first generation of coherent control experiments. At this time it was essential to characterize the effectiveness of the learning-loop and find an answer to the following questions:

- Did the algorithm converge to the global maximum? Is the result dependent on the initial guess?
- How many iterations are necessary? How long does an optimization run take?
- When do the optimal pulses coincide with theory? How can the assumptions of theory be met?
- Is the pulse shape seen by the atoms or molecules in the interaction region really the one applied and measured a distance away? Or is it distorted by pulse propagation, absorption or focusing?
- What is the importance of an accurate initial guess?

The control of the one and two-photon-transition in the sodium atom was chosen due to the existence of an accurate theory predicting already the character of the optimal solutions. This close link between theory and experiment allowed to quantify the above answers and use the atom to "calculate" solutions beyond the analytical limit.

### 2.1 Experimental setup

The femtosecond pulse source for experiments on sodium was a commercial Ti:Sapphire laser system (CPA-1000, Clark MXR Inc.) which supplied 1 mJ

/ 100 fs / 800 nm pulses at a repetition rate of 1 kHz. Frequency conversion to the wavelength interval between 580 nm and 700 nm in an optical parametric amplifier (IR-OPA, Clark) yielded pulse energies around 5 mJ. The programmable pulse shaping apparatus is a symmetric 4-f arrangement [4] composed of one pair each of reflective gratings (1800 lines/mm) and cylindrical lenses ( $f = 150$  mm). Its active element - a liquid crystal (LC) mask - is installed in the common focal plane of both lenses. Meticulous alignment must ensure zero net temporal dispersion. This is achieved once the shapes of input and output pulses match as long as the LC mask is turned off. The technique of frequency resolved optical gating (FROG) [62] served to characterize the generated pulses. Sodium was evaporated in a heat pipe oven [79] pressurized with 10 mbar of Argon as a buffer gas. The temperature was set sufficiently low (520 K) to eliminate pulse propagation effects [80, 81]. The experimental setup is sketched for the one- and two-photon control in Fig. 2.1. Details of the excitation and detection schemes will be supplied in context with the respective experiments.

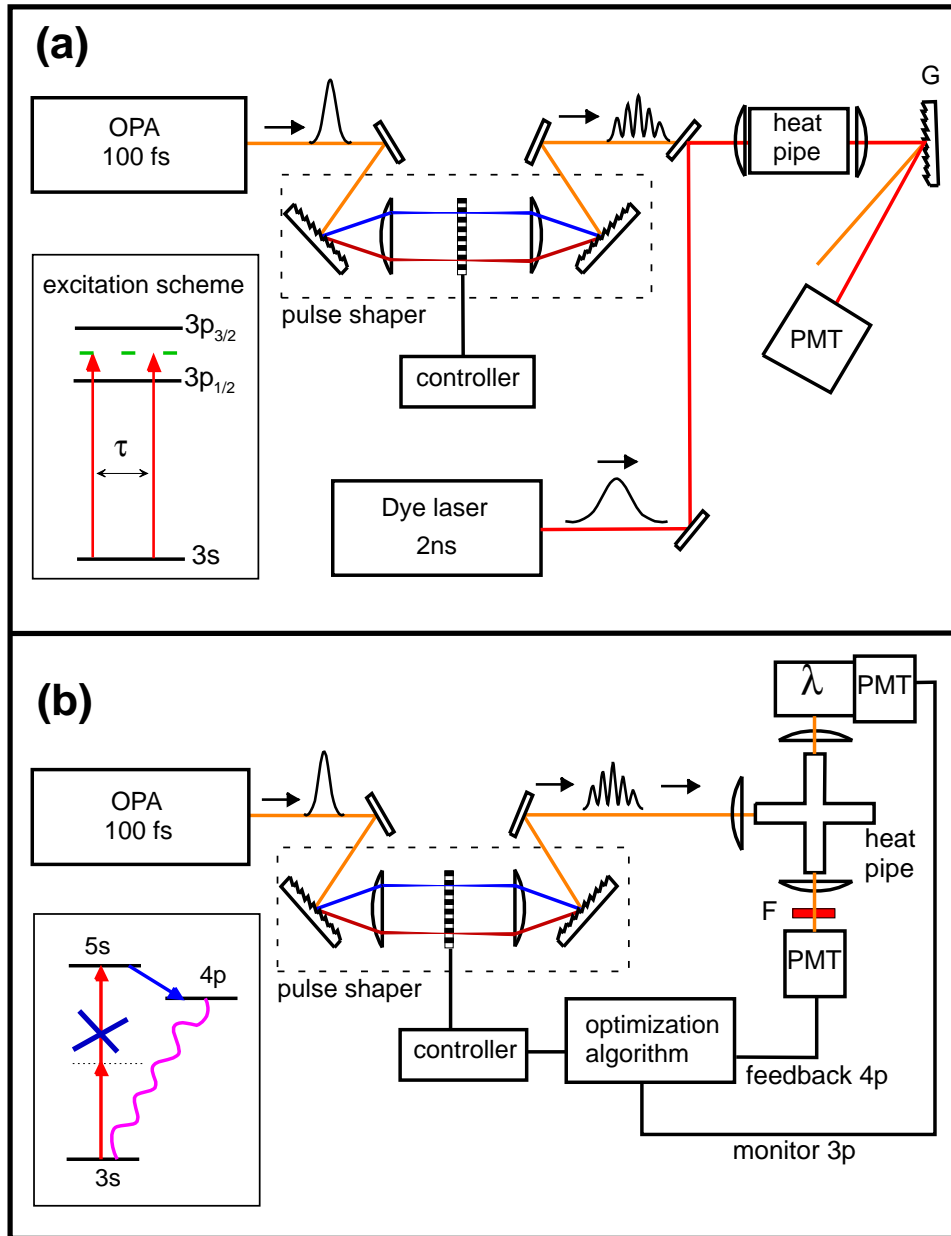


**Figure 2.1:** Experimental setup. (a) Collinear pump-probe arrangement to control the one-photon excitation of Na via a double-pulse sequence. The inset illustrates the pertinent spectroscopic details.  $\tau$  marks the delay between both pulses. (b) Experimental layout and spectroscopic details of the pump- and detection schemes of the two-photon experiment. Fluorescence from 4p serves as feedback to the control algorithm.

## 2.2 One-photon Na(3s $\rightarrow$ 3p) transition

In pursuit of the goal to control the one-photon transition in sodium [see Fig. 2.1(a)] we employed phase- and amplitude shaping of the incident spectrum centered around 589 nm to generate a phase-related double-pulse sequence [see Fig. 2.2]. Moderate focusing ( $f = 300$  mm) into the heat pipe

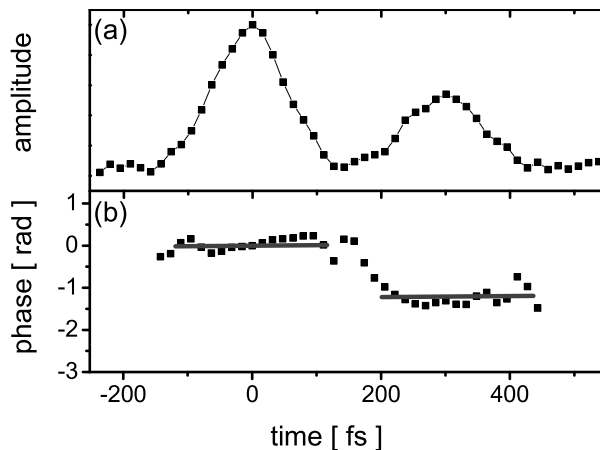


**Figure 2.2:** Typical FROG calculation, in the time domain, of pulse envelope (a) and phase of a generated double pulse (b).

resulted in a power density of  $\approx 10^{11}$  W/cm<sup>2</sup> which was sufficient to saturate the 3s  $\rightarrow$  3p transfer. Only the population induced in the 3p<sub>1/2</sub> state was probed with a narrowband ( $\Delta\omega = 0.2$  cm<sup>-1</sup>) Nd-YAG pumped dye laser (20  $\mu$ J, 3 ns, 50 Hz) which was fired synchronous with the Ti:Sa system and tuned to the 3p<sub>1/2</sub>  $\rightarrow$  5s [see Fig. 2.3]. Pump and probe beams were aligned collinearly and diligent care was taken to ensure that the probed volume was completely overlapped by the pump.

In the following we will give a theoretical description of the response of this two-level system to the sequence of two phase-related pump pulses. The treatment will be restricted to the 3s ( $|1\rangle$ ) and 3p<sub>1/2</sub> ( $|2\rangle$ ) states and the temporal evolution of the excited level as induced by the pulse pair. Coherences between the finesplit 3p levels due to broadband excitation are not detected as only 3p<sub>1/2</sub> is probed. The phase of the initially excited population evolves freely in time as  $\exp(i\omega_{12}t)$  and later interferes with the different phase of the population induced by the follow-up pulse. The description of a one-photon absorption in a first order approximation yields a population of the probed excited state which is given by  $|c_2(t)|^2$ , where

$$c_2(t) = \frac{2\pi}{i\hbar} \int_{-\infty}^t dt H_{12}^s(t') \exp(i\omega_{12}t') \quad (2.1)$$

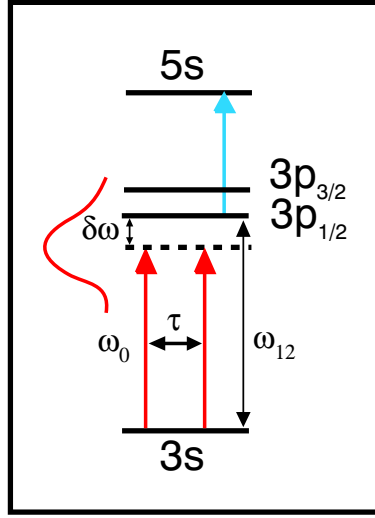


**Figure 2.3:** Level scheme of the sodium atom, showing the one photon transition from  $3s$  to  $3p_{1/2}$  and  $3p_{3/2}$ . Due to the broad bandwidth of the laser pulse both  $3p$  levels are coherently populated. In the experiments only the  $3p_{1/2}$  level population is probed by a nanosecond laser tuned in resonance to  $5s$ . The frequency between  $3s$  and  $3p_{1/2}$  is denoted  $\omega_{12}$  and the femtosecond laser with center frequency  $\omega_0$  is detuned by  $\delta\omega$  from the probed  $3p_{1/2}$  level. The two arrows separated by  $\tau$  indicate, that the excitation is performed with a tailored double pulse having a variable interpulse separation  $\tau$ .

$H_{12}^s(t')$  is the interaction Hamiltonian which, assuming the dipole approximation, is given by  $H_{12}^s(t') = \mu\epsilon(t')$ , where  $\mu$  is the dipole moment and  $\epsilon(t')$  symbolizes the electric field of the laser pulse. In the slowly varying envelope limit a pulse is described as a time dependent envelope function including a carrier wave with the central frequency of the laser field,  $\omega_0$ . This approximation is valid for pulse durations down to a few femtoseconds.

A phase-related double pulse can be created in two ways, simply by an interferometer or alternately using arbitrary pulse shaping and will be used in the following to control the population in the excited state of the one-photon transition. To later understand the two control limits a clear definition of the phase of a femtosecond pulse will be given here. A femtosecond pulse has a constant zero phase if the maxima of electric field and envelope coincide. When the electric field is displaced with respect to the envelope the pulse has a constant nonzero phase in time. The delay between two pulses is defined as the difference in time between the maxima of the pulse envelopes irrespective of the phase, that each individual pulse has. This definition applies to what happens in the time domain.

However as is clear from section 1.1 pulse shaping is best expressed in the frequency domain, since this naturally takes into account that the spectrum

of the pulse can not be increased by additional frequencies. Therefore the best comparison between an optical delay line and the pulse shaper capabilities can be seen in the frequency domain [82].

In this domain, as can be seen easily by calculating the Fourier transform, the phase of a pulse is given by the intercept of the  $\phi(\omega)$  at  $\omega = 0$  and the delay between the pulses is simply given by the slope of the phase function at  $\omega_0$ <sup>1)</sup>. An interferometer with an ideal delay line in one of its arms is only able to create a pulse pair with the same phase as shown in Fig. 2.4. This can be calculated by using the Maxwell equations and the field is given mathematically by the following equation [see also Fig. 2.4(a)].

$$\epsilon(t) = \sum_{n=1}^2 \exp \left[ - \left( \frac{t - n\tau}{\Delta} \right)^2 \right] \cos[\omega_0(t - n\tau)] \quad (2.2)$$

Note that both pulses do not share a common carrier wave<sup>2)</sup>, but instead both have a constant temporal zero phase irrespective of their pulse separation. In the frequency domain this translates to the spectral phase shown for different delays in Fig. 2.4(b). As the delay is increased the slope of the phase function of the second pulse increases, while the intercept is always zero showing that both pulses are phase locked.

The possibilities to create a phase-related double pulse are maximal when using a pulse shaper. The phase and delay can be changed *independently* from one another. Exemplarily in Fig. 2.5 a double-pulse is shown that shares a common carrier wave. That is the envelope slides over this common carrier as the delay is changed. The carrier is shown as dotted line. Hence the phase of the second pulse must change as  $-\omega_0\tau$  if  $\tau$  is the delay. This can be most intuitively seen again in the frequency domain [see Fig. 2.5(b)]. The intercept at  $\omega = 0$  changes exactly according to  $\phi(\omega) = -\omega_0\tau$  as the delay is changed, while the phase at  $\omega_0$  stays always zero showing that both pulses share a common carrier wave. This is mathematically expressed by the following equation [see also Fig. 2.5]

$$\epsilon(t) = \sum_{n=1}^2 \exp \left[ - \left( \frac{t - n\tau}{\Delta} \right)^2 \right] \cos(\omega_0 t) \quad (2.3)$$

Of course a pulse shaper can be used to generate double pulses which are any intermediate configuration between the case discussed here and the ideal interferometer case of Fig. 2.4. Since the one-photon transition is sensitive to the relative phase of the double pulse, the control parameter, the two methods can be distinguished. In order to see this the equations for the interferometer case are derived and thereafter the pulse shaping case is studied.

---

<sup>1)</sup>Not considered here are orders of the phase function higher than one, since these are not needed to create phase-related double pulses.

<sup>2)</sup>A carrier wave is defined by its frequency and the phase

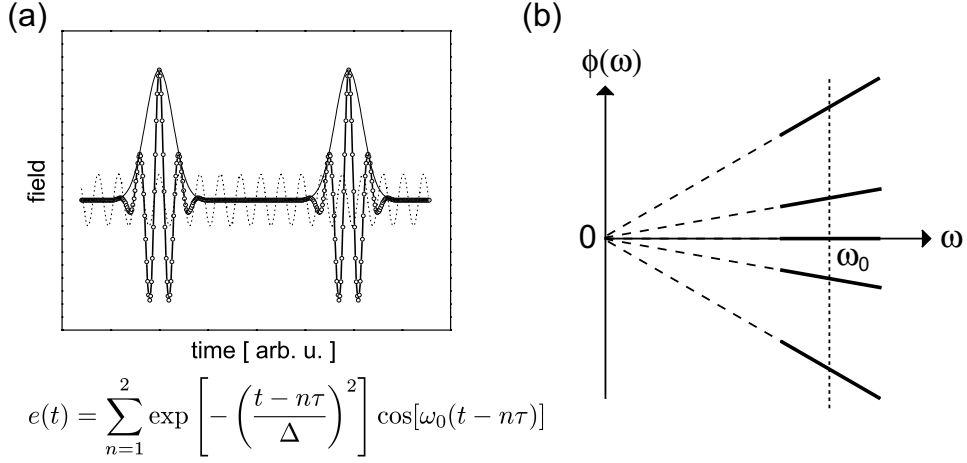


**Figure 2.4:** Double pulse created by a Mach-Zehnder interferometer (ideal delay line). (a) Electric field of both pulses have the same phase, i.e. they are phase locked. They have no common carrier wave and are given by the equation in (a). (b) Spectral phase of the second pulse in (a). Note that the intercept at  $\omega = 0$  is 0, showing that both pulses are phase locked. Increasing phase slopes correspond to increasing pulse separations.

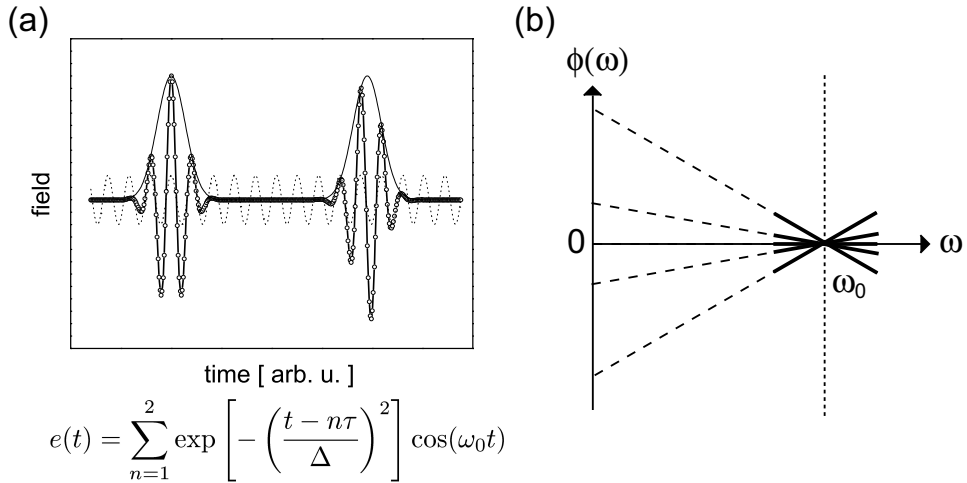


**Figure 2.5:** Double pulse as can be created using a pulse shaper. (a) Envelope of both pulses slide over a common carrier wave, i.e. the two electric fields have different phases. Mathematically they are expressed by equation in (a). (b) Spectral phase of the second pulse in (a). Note that the intercept at  $\omega = 0$  is given by  $-\omega_0\tau$ , while the phase is zero at  $\omega_0$  showing that both pulses have common carrier wave. Increasing phase slopes correspond to increasing pulse separations.

**Interferometer.** Splitting a pulse creates two pulses with the same phase. The time separations between the pulses can be adjusted with a delay stage [see Fig. 2.4]. The electric field is then

$$\begin{aligned} \epsilon(t) &= \exp(-i\omega_0(t-t_1)) \exp(i\phi_1) a_1(t-t_1) \\ &+ \exp(-i\omega_0(t-t_2)) a_2(t-t_2) \exp(i\phi_2) \end{aligned} \quad (2.4)$$

Setting  $t_1 = 0$  and  $\phi_1 = 0$  and introducing the time separation  $t_2 = \tau$  and phase relationship  $\phi_2 = \delta\phi$  the equations simplifies to

$$\epsilon(t) = \exp(-i\omega_0 t) a_1(t) + \exp(-i\omega_0(t-\tau)) a_2(t-\tau) \exp(i\delta\phi). \quad (2.5)$$

Inserting this expression into Eq. (2.1) one obtains

$$\begin{aligned} c_2(t) &\propto \int_{-\infty}^t dt' \exp(i\delta\omega t') a_1(t') + \left[ \int_{-\infty}^t dt' \exp(i\omega_{12}(t'-\tau)) \exp(i\omega_{12}\tau) \right. \\ &\quad \left. \exp(-i\omega_0(t'-\tau)) a_2(t'-\tau) \exp(i\delta\phi) \right] \\ c_2(t) &\propto f_1 + f_2 \exp(i\omega_{12}\tau) \exp(i\delta\phi) \\ |c_2|^2 &\propto \cos(\omega_{12}\tau + \delta\phi) \end{aligned} \quad (2.6)$$

In ideal interferometers  $\delta\phi = 0$ <sup>3)</sup>, hence the phase can not be influenced and changing  $\tau$  will lead to a signal from the excited state that is periodic with a frequency of the one-photon transition frequency  $\omega_{12}$ . For the sodium atom this frequency is  $\omega_{12} = 2\pi/1.97$  fs and will induce very fast oscillations of the probed signal. This signal is not resolvable using the LC based pulse shaper to adjust the interpulse separation, since the minimal time step is restricted due to pixelation to about 40 fs (see section 1.1). Such atomic oscillations were investigated earlier in Cs by Blanchet et al. using a stabilized interferometer [12].

**Pulse shaping.** In frequency domain pulse shaping the phase difference  $\delta\phi$  of the double pulse pair can be chosen arbitrarily and independent of its separation in time,  $\tau$ . Contrary to the interferometer case if only the pulse separation  $\tau$  in a shaped double pulse is changed the phase will change according to  $\delta\phi = -\omega_0\tau$ , since the pulses slide over a *common* carrier wave [see Fig. 2.5]. Pulse shaping however allows to apply an additional phase  $\alpha$ , so that  $\delta\phi = -\omega_0\tau + \alpha$  and complete control over the pulse phase is recovered irrespective of  $\tau$ . Inserting this relation for  $\delta\phi$  into Eq. (2.6) results in [83,84]

$$\begin{aligned} |c_2|^2 &\propto \cos(\omega_{12}\tau - \omega_0\tau + \alpha) \\ |c_2|^2 &\propto \cos(\delta\omega\tau + \alpha), \end{aligned} \quad (2.7)$$

<sup>3)</sup>In reality the mirrors in the delay stage if not interferometrically stabilized will make the phase relation fluctuate around this mean value of zero.

where  $\delta\omega = \omega_{12} - \omega_0$  stands for the detuning of the laser frequency from the one-photon transition, here  $3s \rightarrow 3p_{1/2}$ . This equation predicts, that a change of the temporal pulse pair spacing while  $\alpha = \text{const.}$  induces a slow oscillation characterized by the detuning. Note that the physical phase of the second pulse, that is the position with relation to the carrier is given by  $\phi_2 = -\omega_0\tau + \alpha$  in Eq. (2.7). Again we note here the important difference to the interferometer case: applying mask patterns that change  $\tau$  at constant  $\alpha$ , will in reality change the phase of the second pulse, since the envelope is displaced over the carrier wave. This can be seen in the following sequence of plots [see Fig. 2.6], resembling a set of tailored double pulses with differing time separations, but constant  $\alpha = \pi$ . The column (a) shows the electric

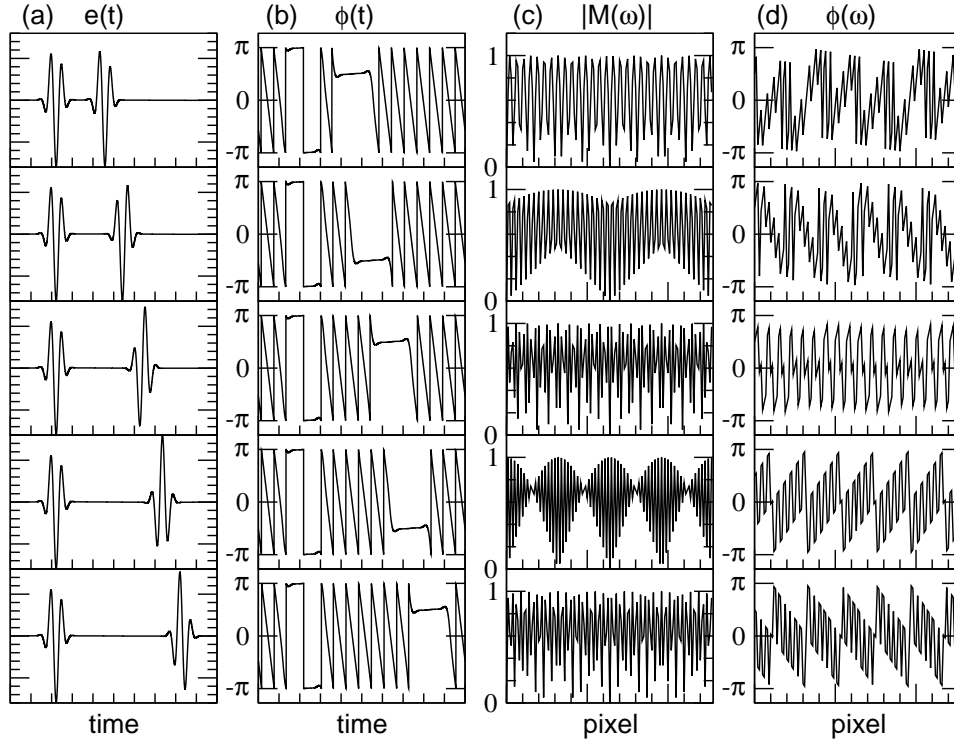


**Figure 2.6:** Shaping a sequence of double pulses with  $\alpha = 0$  differing only in their time separation  $\tau$ . Since both pulses have a common carrier wave, their relative phase changes as  $\omega_0\tau$ , where  $\omega_0$  is the center frequency of the laser. (a) column: Electric fields. (b) column: Phase in time. (c) column: Transmission mask patterns. (d) column: Phase mask patterns.

fields, (b) the flat phase of the pulses in time, (c) and (d) the corresponding transmission and phase pattern on the SLM. The wiggling (or better the slope if unfolded) of the mask patterns increases as the pulse separation becomes bigger. The intercept (not shown) as known from the previous discussion changes here as  $-\omega_0\tau$ .

In essence this Fig. 2.6 is equivalent to Fig. 2.5. In order to clearly distinguish the phase of the two pulses, their temporal width was chosen to be only a few optical cycles. Equation (2.7) predicts on the other hand, that tuning the relative phase  $\alpha$  of the pulse doublet at fixed  $\tau$  gives rise to a periodical ( $1 \text{ s}^{-1}$ ) oscillation shifted by  $\delta\omega\tau$ . In Fig. 2.7 five tailored double pulse pairs at constant separation  $\tau$  are shown, where merely the phase parameter  $\alpha$  was changed. The (c) and (d) column show the mask

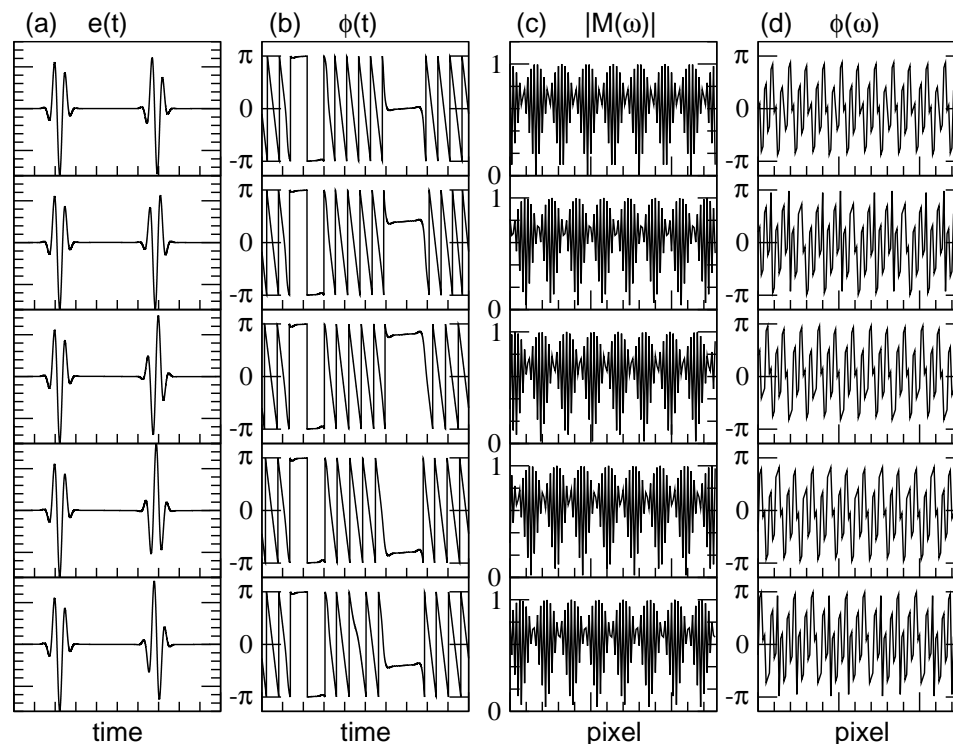


**Figure 2.7:** Shaping a sequence of double pulses with constant time delay differing only in their phase relationship. (a) column: Electric fields. (b) column: Phase in time. (c) column: Transmission mask patterns. (d) column: Phase mask patterns.

patterns, that have to be applied in order to change the relative phase. The mask patterns in all four rows are the same, but shifted sidwise. This is a very general relationship as a sidwise shift of a mask pattern changes the intercept at  $\omega = 0$  and as shown before this is equivalent to influencing the relative phase in a tailored pulse. Note that the slopes in all mask patterns of Fig. 2.7 are exactly the same. This again shows the relationship between slope and delay. The first two columns (a) and (b) depict the electric field and phase of the double pulse as a function of time.

The experimental data presented in Fig. 2.8 show the population of the  $3p_{1/2}$  state in dependence of an exclusive variation of either  $\alpha$  [Fig. 2.8(a)] or  $\tau$  [Fig. 2.8(b) and (c)], respectively.

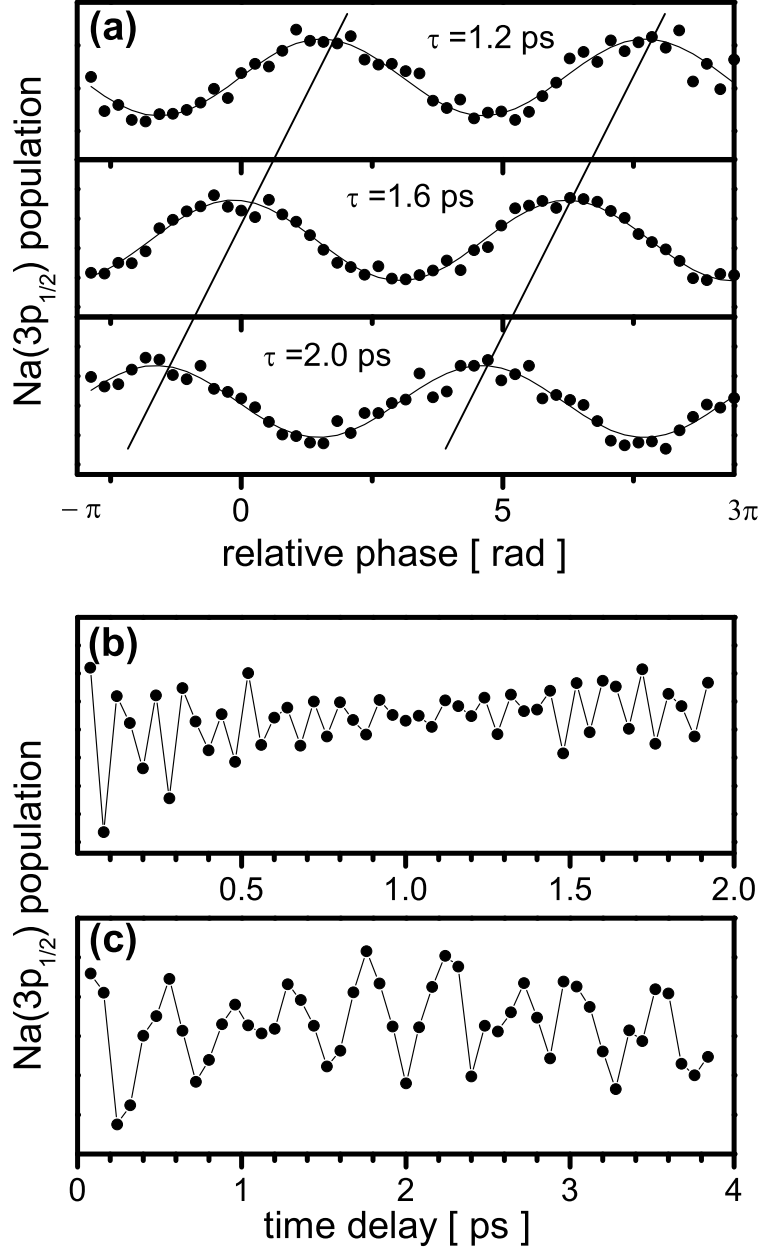


**Figure 2.8:** Population of Na ( $3p_{1/2}$ ) vs. characteristics of double pulse. (a)  $\alpha$ -transient. The relative phase  $\alpha$  is varied and plotted for three different pulse separations  $\tau$  (1.2, 1.6, and 2.0 ps). Cosine functions are fitted to the data. The slope of the lines connecting the maxima allows to deduce the detuning  $\delta\omega$ . (b) and (c)  $\tau$ -transient. The pulses are set to equal phase  $\alpha$  while the time separation  $\tau$  is changed. The time step resolution is  $1 \times 40$  fs for (b) and  $2 \times 40$  fs for (c).

This kind of shaping was obtained by applying the mask patterns of Fig. 2.7 or Fig. 2.6, respectively. The detuning  $\delta\omega$  can be calculated from the slope of the lines connecting the maxima of the cosine modulation. It is  $\delta\omega \approx \frac{\pi}{c \cdot 800 fs} = 131 \text{cm}^{-1}$ . While Fig. 2.8 (a) agrees perfectly with the pulse shaping model [see Eq. (2.7) and Ref. [4]], a change of the pulse spacing seems to cause an ambiguous picture. An oscillatory behavior of the population which exceeds the capability of time resolution of the pulse shaping setup is superimposed by a slow modulation approximately proportional to the detuning [see Fig. 2.8(b) and (c)]. This is in distinct contrast to the expected slow oscillation. If the phase of the second pulse would obey  $\omega_0\tau$  as a function of the time difference  $\tau$ , as is presumed when pulse shaping is performed, only a slow oscillation should show up. This can be explained also in a simple physical picture. The phase of the population excited by the first pulse into the  $3p_{1/2}$  state begins to evolve in time as  $-\omega_{12}t$ . The phase of the follow-up pulse as it slides over the carrier evolves with the carrier frequency and is  $-\omega_0t$ . In the case the laser center frequency would be in perfect resonance with the one-photon transition a phase locking between the laser field and the atom would be achieved, since both phases would be the same at all times evolving in absolute harmony with each other. In this case the follow-up pulse excites a second population that will always constructively interfere with the population already in the  $3p_{1/2}$  state and no modulation would be visible;  $\delta\omega = 0$  and Eq. 2.7 reduces simply to  $|c_2|^2 \propto \cos(\alpha)$ . For any slightly off-resonant excitation one then simply expects a slow modulation, since the phase evolution of the first excited  $3p_{1/2}$  state population is only partly compensated for by the carrier phase evolution. The worst case being the interferometer case, where the phase of the second pulse does not change as a function of the pulse separation and the maximum phase dynamics of the probed  $3p_{1/2}$  state is then visible in the  $\tau$ -transient. Stated in other words, the  $\tau$ -transient is simply the phase evolution of the excited state population that an observer sees when he is locked to the phase of the follow-up pulse. In the case of pulse shaping the phase of the second pulse is locked to the carrier frequency and therefore the observer sees effectively a rotating wave approximation of the excited state phase dynamics.

Referring again to the experimental data, where a very fast not resolvable oscillation is observed, the conclusion is that the shaper cannot create double pulses sharing a common carrier wave, as would be expected for constant  $\alpha$ . As it seems, the phase of the second pulse does not accurately obey  $\phi_2 = -\omega_0\tau$  as a function of the delay with respect to the first. The experimental transient reveals a beating pattern which is seemingly expressible as the sum of cosines with frequencies  $\delta\omega$ ,  $\omega_{12}$ ,  $\omega_0$ . Such a transient would indeed appear if, next to the two pulses with variable time separation  $\tau$  sharing a common carrier wave [ideal pulse shaper, Eq. (2.7)], a third pulse with a fixed phase would act on the system. This third pulse could be created

by reflection on beam optics or as in a detailed discussion by Wefers and Nelson [47] have shown that the passively transmitting gaps of the liquid crystal array give rise to such an additional pulse. Notwithstanding its low intensity it must be considered in the regime of saturation where this experiment was performed. Both possibilities would describe this third pulse with Eq. (2.6). Another tentative explanation of the  $\tau$ -transient rests on the assumption of a general nonlinear  $\tau$ -dependence of the phase of the second pulse. This would ascribe the displacement of the phase from its ideal linear  $\omega_0\tau$  behavior of the second pulse to inhomogeneities in the shaper.

In conclusion, measurements which show the feedback of the controlled one-photon excitation to a variation of  $\tau$  represent an extremely sensitive criterion of the quality of a pulse shaper incorporating a discrete mask and could serve to quantify the deviation from ideality, since an “ideal” shaper satisfies the condition formulated in Eq. (2.7). A possibility is to record the  $\tau$ -transient with enhanced temporal resolution by using shorter pulses, by increasing the number of pixels, and by performing an analogous experiment addressing an atomic transition in the IR (smaller  $\omega_{12}$ ). This should provide deeper understanding of the physical reasons which are behind these surprising results.

### 2.3 Two-photon Na(3s $\rightarrow\rightarrow$ 5s) transition

The objective of the study that will be presented in the forthcoming chapter is the coherent control through spectral phase manipulation of a non resonant two-photon process via feedback optimization steered by an evolutionary algorithm. The aim is to find tailored pulses that maximize or minimize the two-photon transfer of population 3s  $\rightarrow\rightarrow$  5s in sodium. Due to the broad bandwidth of the laser pulse multiple pathways connect initial 3s and final 5s state. Therefore controlling the relative phase of each transition will lead either to constructive or destructive interference, “bright” or “dark” tailored pulses. A schematic diagram of the experimental layout as well as the relevant spectroscopic details of the employed pump and detection scheme are displayed in Fig. 2.1(b). The exciting laser was tuned to  $\lambda = 598$  nm which is close to the 3s  $\rightarrow\rightarrow$  5s resonance, and focused to provide a maximum power density of  $\approx 10^{11}$  W/cm<sup>2</sup> inside the heat pipe. The population of the 5s target level optically decays to 3p or undergoes collisional relaxation to the 4p state [see Fig. 2.9]. Both levels are monitored separately via their fluorescence to the 3s ground state at 589 nm and 330 nm, respectively. Due to the spectral width of the ultrashort 598 nm pulses a competitive (1+1)-photon excitation of 5s via 3p (at 589 nm) can not be excluded right away. The low frequency wing of the spectrum is in resonance with this strong one-photon 3s  $\rightarrow$  3p transition. It must be thus offered evidence that the 5s level is indeed populated as the result of only non resonant

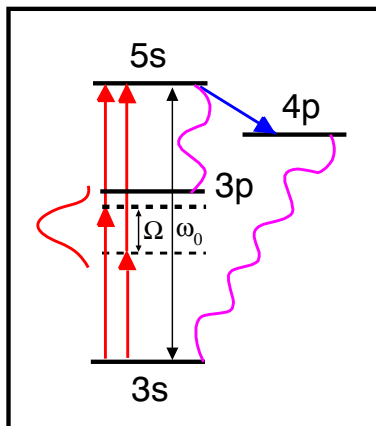


**Figure 2.9:** Level scheme of the sodium atom, showing the two photon transition between 3s and 5s. Due to the broad bandwidth of the laser pulse several two-photon transition pathways exist. The 3p levels are excited by the wings of the spectrum and leads to 1+1 resonant enhancement. The frequency between 3s and 5s is denoted by  $\omega_0$ . The detuning from half of this frequency ( $\omega_0/2$ ) is given by  $\Omega$ . The 5s population decays to the 3p levels and also via 4p back to 3s.

two-photon pathways; only then experiment can be directly compared with the theory of Ref. [11] that will be presented later. To show that indeed spectral blocking of the low frequency wing of the spectrum suppresses the 1+1 photon transition via 3p a prediction from a theoretical treatment of the quantum control of multiphoton transitions by shaped ultrashort pulses which excludes strong field effects by Meshulach et al. [41] will be exploited. In this paper they calculated the effect of a mask pattern consisting of  $\pi$  phase step on the probability of N-photon absorption in a two-level system. The plots of this quantity vs. the normalized step position peak at the frequency of the N-photon absorption. They are symmetric with respect to this maximum and vanish for N values of the phase step position. The number of minima is thus indicative of the order of the absorption process. Fig. 2.10 shows the experimental result for the 3s  $\rightarrow\rightarrow$  5s transition as a function of the  $\pi$  step position induced by the SLM. The position of the maximum and the occurrence of two symmetrically arranged minima suggest a two-photon process induced by a wavelength of  $\approx 602$  nm. This number is directly read from a spectrum of the laser pulse which was taken while pixel #43 (maximum) was blocked (see Fig. 2.10). The implementation of a feedback controlled optimization routine requires to identify an observable which is uniquely tied to the quantity to be controlled. Population of 5s gives rise to fluorescence from the 3p and 4p levels. 3p may, however, also be pumped in a 589 nm one-photon step from 3s. The text to follow describes two experiments which address and settle this tentativeness. The data of the first test are illustrated in Fig. 2.11 and show the fluorescence from the 3p

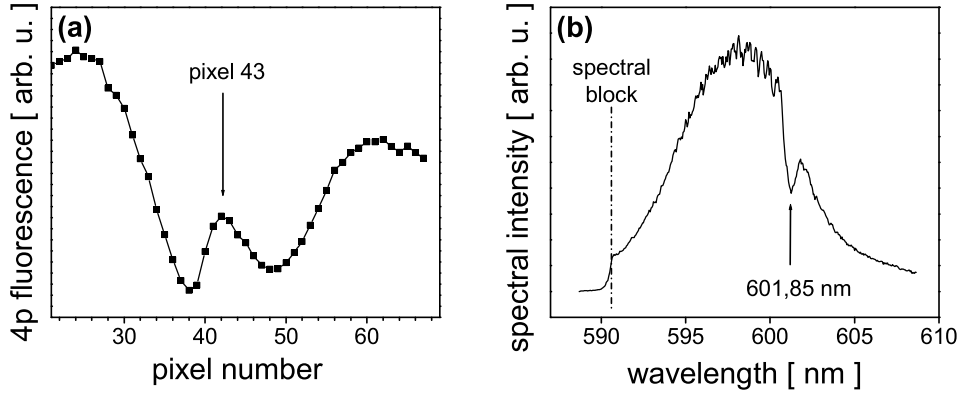


**Figure 2.10:** (a)  $\pi$  phase step shifted across the mask. Fluorescence from collisionally populated 4p shows symmetry around pixel #43. (b) OPA spectrum behind SLM observed with pixel #43 set to minimum transmission and left spectral wing blocked by a razor blade.

and 4p levels, following excitation of 5s by 1 mW of unchanged or modified pump pulses. The latter were obtained by clipping, in the Fourier plane, the blue wings ( $<591$  nm) of the frequency spectrum. The ensuing pulse spectrum is shown in the right panel of Fig. 2.10. Fluorescence from 4p appears with equal intensity for either excitation condition. The 3p analog, however, is drastically diminished in the absence of the wavelength matching the one-photon resonance. The previous measurement strongly indicates that 5s, which is the precursor to 4p, is accessed nonresonantly, rather than by a (1+1)-sequence. Supporting evidence comes from an examination of the fluorescence intensities vs. laser power, which is displayed in Fig. 2.12. Again, the 4p signal appears unimpressed by the particularities of the pump laser's frequency profile and exhibits a quadratic slope, indicative of a two-photon process. The 3p data are more complex. In the presence of 589 nm the signal behaves linearly for low laser intensity and scales  $\propto I^{1.5}$  above approximately 0.2 mW, pointing to saturation [85]. Blocking the resonant wavelength produces the same low-intensity behavior, but a quadratic slope beyond 0.2 mW. The bottom line of the conclusions which may be drawn from both checks is as follows: Given the conditions of our experiment (pump  $\approx 1$  mW) 4p is exclusively fed from 5s which owes its population to a nonresonant 2-photon excitation. The 3p state draws to some extent from 5s, but is predominantly pumped in a resonant single step when the pulse is left unmodified. We may thus apply Meshulach's model [11] to describe the coherently controlled population of Na(5s) and we have identified 4p fluorescence as a directly linked criterion which is suited to serve as input to the steering algorithm which updates the modulator. The nonresonant two-photon interaction of an ultrashort pulse with a two-level system induces a

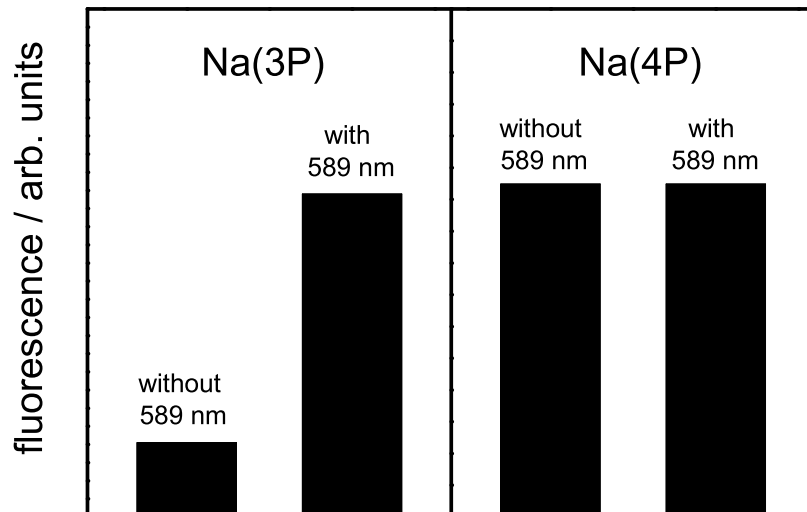


**Figure 2.11:** Response of 3p and 4p fluorescence to the presence or absence of 589 nm light (one-photon resonance)

transition with a probability  $S_2$  [11]:

$$S_2 = \left| \int d\Omega A\left(\frac{\omega_0}{2} + \Omega\right) A\left(\frac{\omega_0}{2} - \Omega\right) \exp\left\{i \left[ \underbrace{\phi\left(\frac{\omega_0}{2} + \Omega\right) + \phi\left(\frac{\omega_0}{2} - \Omega\right)}_{\text{interference term}} \right] \right\} \right|^2 \quad (2.8)$$

where  $\omega_0$  is the energy of the  $3s \rightarrow 5s$  transition which corresponds to 301 nm. Two-photon transitions occur for all pairs of photons which satisfy the condition  $\omega_1 + \omega_2 = \omega_0$ . The detuning of frequencies  $\omega_1, \omega_2$  from  $\omega_0/2$  is denoted by  $\Omega$ . Control of the excitation process is exercised via the interference term and can either maximize or minimize the probability  $S_2$ , as Meshulach et al. [11] have recently demonstrated for the nonresonant two-photon transition of Caesium. Maximization is obviously achieved if the interference term vanishes, which describes the minimum duration transform limited pulse. This solution is not singular, however, since any shaped pulse with the same power spectrum  $A(\omega)$  but with an antisymmetric phase function,  $\phi\left(\frac{\omega_0}{2} + \Omega\right) = -\phi\left(\frac{\omega_0}{2} - \Omega\right)$ , will yield the same result, irrespective of the particular appearance of the phase distribution. This result is counterintuitive since longer, i.e. less intense, pulses should be less effective in transferring population. In their paper, Meshulach et al. [11] have also

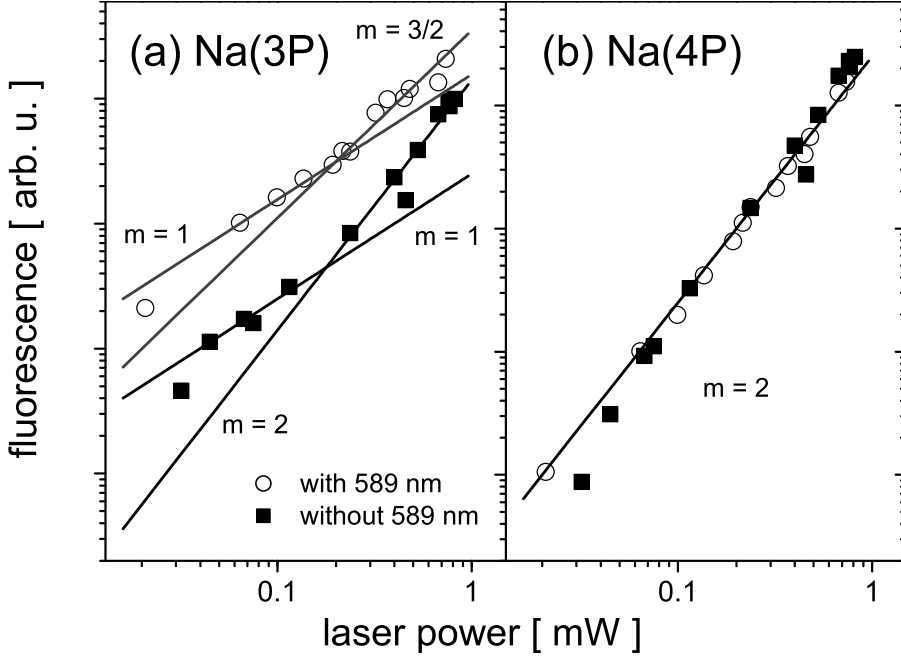


**Figure 2.12:** Power dependence of (a) 3p and (b) 4p fluorescence with or without 589 nm light.

formulated phase requirements to produce so-called *dark pulses* which altogether cancel the two-photon pumping probability. No net transitions are induced as long as  $\phi(\Omega) = \cos(\beta\Omega)$ . The total of solutions, discriminated by virtue of the parameter  $\beta$ , is symmetric with respect to the center frequency  $\omega_0/2$ .

In the present experiment the designed pulses were created by phase-only modulation. The task to pinpoint the conditions which either maximize or cancel  $S_2$  was left to an evolutionary strategy which was integrated in a feedback loop. Unbiased by any a-priori modeling the algorithm set out from a phase filter  $\phi(n) = a \cos(b \cdot n + c)$  with  $n$  as the variable which numbers the LC pixels, and  $a$ ,  $b$ , and  $c$  as free parameters to be optimized. This approach is still tractable but sufficiently general to comprise Meshulach's solution [11]. The experiment was run repeatedly for either objective and achieved convergence within five generations. The phase filters which were retrieved as a result of the optimization procedure are symmetric (cosine) in the case of extinction, and antisymmetric (sine) in the case of enhancement of fluorescence. Symmetry persists with reference to the center frequency  $\omega_0/2$  which impinges on strip #43 (see Fig. 2.13). This good agreement with theory which this three parameter optimization produces requires to put upper and lower restrictions on the parameter  $b$ . In the bright pulse case  $b$  must be sufficiently large to allow at least four oscillations of the phase

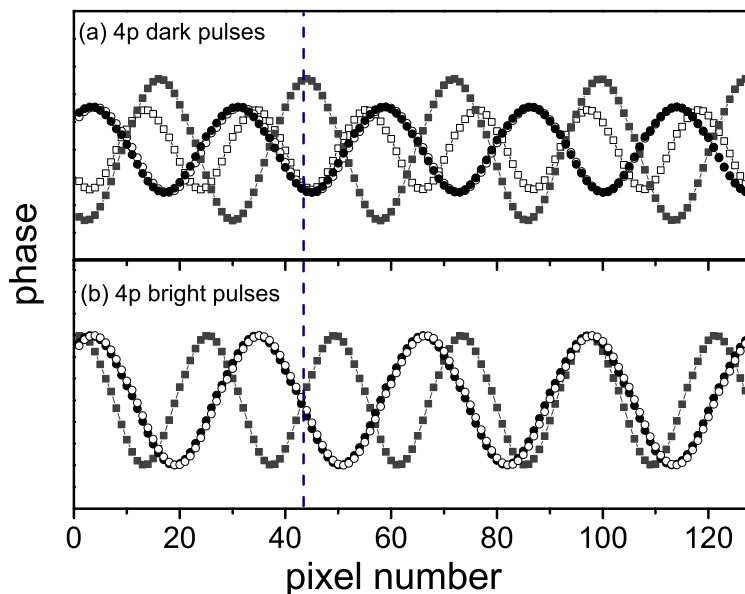


**Figure 2.13:** Periodic phase functions obtained from three consecutive optimization runs. In accordance with theory, traces show symmetry for dark (a) and antisymmetry for bright pulses (b). Dotted line marks pixel #43.

over the width of the mask. In the absence of this lower limit the algorithm would merely compensate the chirp of the incoming pulse to produce the Fourier limited shape, i.e. the pulse having the minimum time duration, which obviously maximizes  $S_2$ . To optimize the dark pulses  $b$  has been limited to yield a maximum of eight phase oscillations. Lifting this restriction would result in very long pulses which are dark due to insufficient intensity. In a further experiment we lifted the restriction on the dimensionality of the parameter space and tried a model of the phase filter which permitted an unbiased choice of parameters. Aiming at the generation of dark pulses we introduced a phase function defined by the minimum number of sampling points connected by a linear interpolation. Each of these points may assume 64 discrete values within a range from 0 to  $2\pi$ . Six parameters proved sufficient to achieve this goal. The dark pulse retrieved by the algorithm is shown in Fig. 2.14(a) whereas Fig. 2.14(b) represents the phase setting of the mask. The property of being “dark” is indeed phase-related, which is convincingly shown by comparison with the effect induced by a chirped pulse of equivalent energy and duration. The evolution of a dark pulse as mirrored by the decrease of the 4p fluorescence feedback signal is shown in the top row of Fig. 2.15. Compared to an unmodulated pulse the 5s population is reduced to  $<3\%$ . The left panel proves the insensitivity of the one-photon  $3s \rightarrow 3p$  transition to a phase-only modulation.

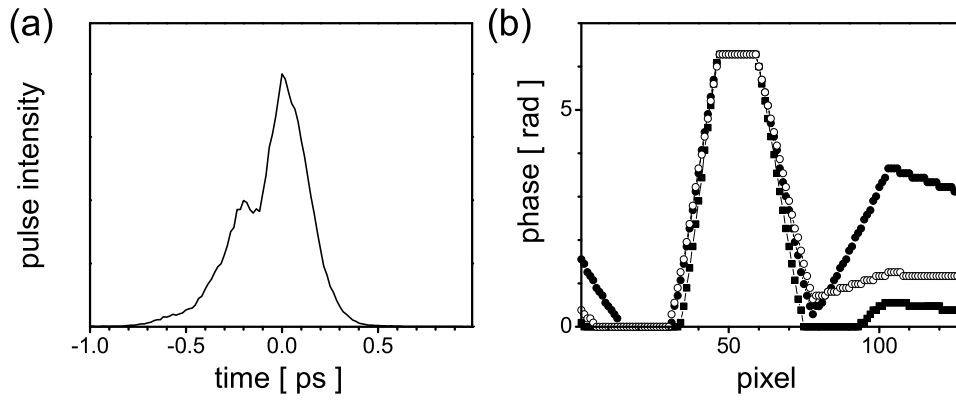


**Figure 2.14:** Free optimization using a six-parameter phase function with linear interpolation. (a) Cross-correlation of a typical dark pulse. (b) Phase values as achieved in three different runs.

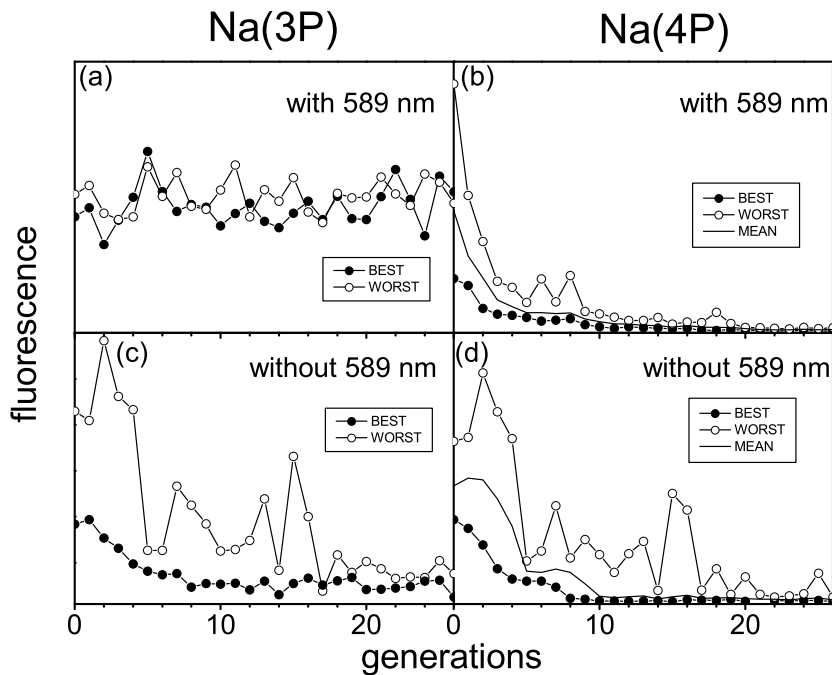


**Figure 2.15:** Convergence data of the six-parameter search for the dark pulse. Figure shows the best and worst mask patterns for each generation. (a),(b) If 589 nm light is present in the excitation spectrum 3p fluorescence is not a suitable feedback signal, since the direct excitation to 3p is phase insensitive. (c),(d) As long as 589 nm light is blocked, 3p and 4p fluorescence are equally suited as feedback signal.

Once the resonant pumping of 3p is suppressed by blocking the relevant wavelength the fluorescence from this level perfectly matches that of 4p [Fig. 2.15, bottom row]. 3p is now populated via radiative decay of 5s and is hence equally suited as feedback input.

Both, the three- as well as the six-parameter approach converge after less than 10 generations, i.e. within less than 5 minutes. A comparative inspection of the phase functions returned by either method raised the question of the existence of additional solutions which are of altogether different character. We thus expanded the previous parametrization to 128 sample points, each falling between 0 and  $2\pi$  as before. Fig. 2.16 documents the convergence towards the dark (left) and the bright pulse (right) which was attained after  $\approx 10$  generations. In accordance with theory an antisymmetric phase function causes population enhancement [Fig. 2.16 (b)]. No likewise apparent symmetry properties, however, characterize the suppression of two-photon pumping. Re-runs of the optimization procedure produced identical experimental results but differing phase functions. The solutions which the algorithm produced bore no resemblance with the prediction of theory. The shaped pulses show a complex phase- and amplitude-time structure of comparable duration ( $\approx 2$ ps). It is thus not their peak power but rather their phase distribution which produces qualities such as “bright” or “dark”.

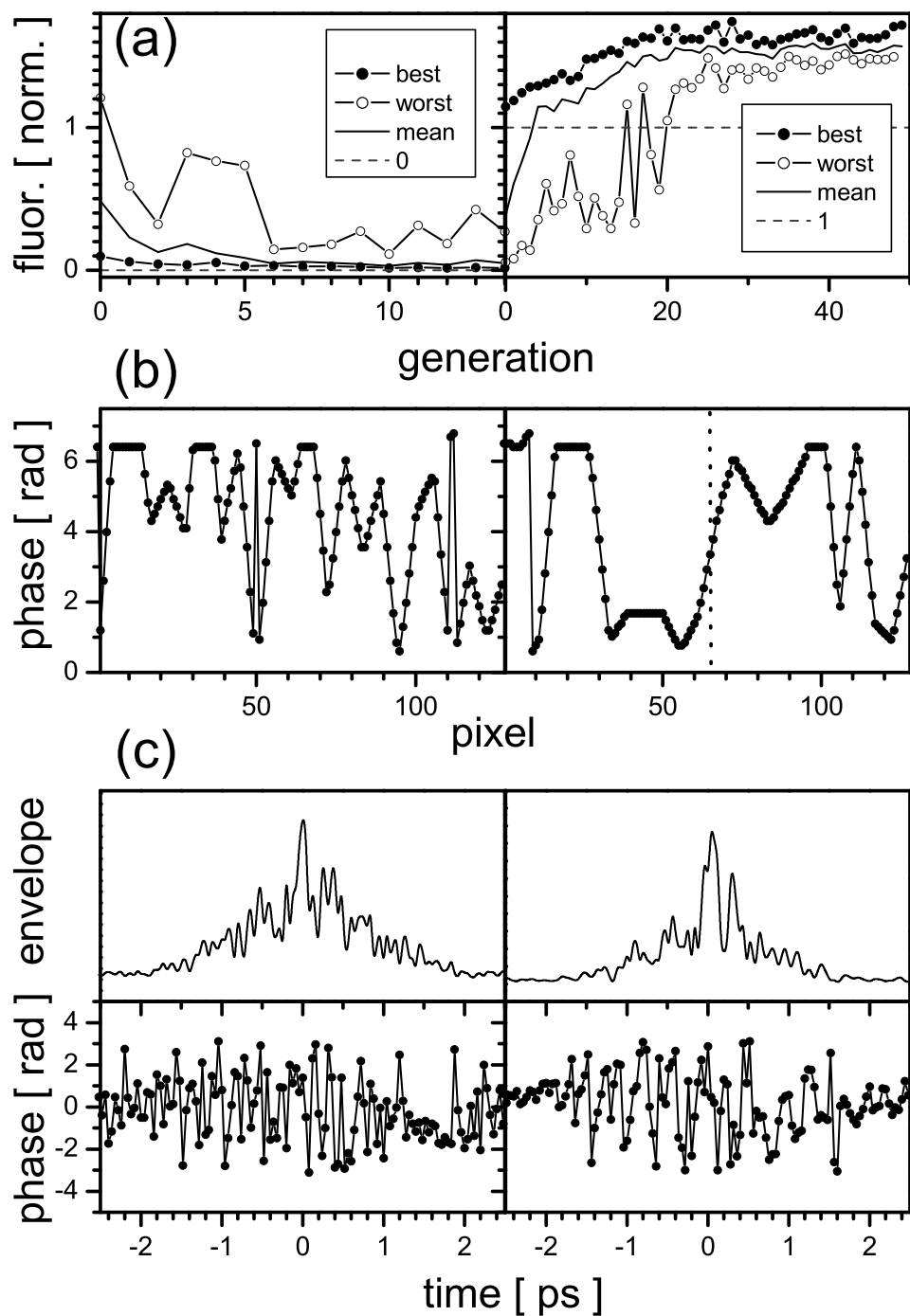


**Figure 2.16:** Convergence data of the 128-parameter search for the dark (left) and bright (right) pulse. (a) Normalized fluorescence intensity to document convergence. Dashed lines mark “no signal” (0) and “unshaped reference pulse” (1). (b) Right: phase structure of bright pulse showing antisymmetry. Reference position has shifted to pixel 64 ( $\equiv 602$  nm) due to re-alignment of optical setup. (c) Pulse shape and phase structure in the time domain. Bright and dark pulses show a complex structure, but note their similar durations.

## 2.4 Summary and Outlook

The influence of phase modulated femtosecond laser pulses on one- and two-photon transitions in an atomic prototype system was studied and the implementation of a feedback loop using evolutionary algorithms was tested under realistic experimental conditions. The one-photon-transition presents an excellent tool to test the quality of phase-related pulses, as the excitation of the 3p level in sodium depends critically on the relative phase of the double pulse. It has been shown that the experimental outcome could be explained by a combination of two limiting cases. The relative contribution depends on the nature of the phase coupling within the pulse sequence, which is influenced by the experimental conditions of the setup. The phase modulated excitation of the two-photon-transition shows that the feedback approach can be successfully used to find femtosecond laser pulses for different control objectives, even without an intelligent initial guess supplied by theory. The best solutions for both extremes were obtained within five generations. Allowing the feedback algorithm to search in an extended parameter space the algorithm found new phase structures in addition to known analytic solutions. These structures are not intuitively understandable and call for further theoretical studies.

Having a combined look at the results on the one- and two-photon transition the conclusion is, that it is in principle possible to control the linear versus the nonlinear process, since the pulse shapes for suppression and enhancement depend on the character of the transition. This can be done in an automated way using the learning-loop setup presented in Fig. 2.1(b).

## Chapter 3

# Control of dimers using shaped DFWM

In this chapter the powerful spectroscopic tool of nonlinear four-wave mixing (FWM) techniques is combined with pulse shaping. The FWM technique is an ideal method, since it can be used to monitor ground and excited state dynamics during pulse control. This peculiarity of the FWM process will be explained in the following where the time domain framework of nonlinear processes will be reviewed [86]. In section 3.2 a theoretical model describing a new type of control technique using shaped pulses within the degenerate FWM process will be derived and verified experimentally in section 3.3. In the final section the FWM response of the potassium dimer is spectrally resolved to provide a FROG-type measurement of the shaped excitation field used in these studies.

### 3.1 Theory of nonlinear spectroscopy

In nonlinear spectroscopy the radiation field interacts with the system creating a time-dependent material polarization  $P(\mathbf{r}, t)$  which generates an electric field according to Maxwell's equation. The intensity of this field is the experimental spectroscopic observable. The Hamiltonian  $H_{int}$  for the system's interaction with the external radiation fields is given by

$$H_{int} = -\mu(Q)E(\mathbf{r}, t), \quad (3.1)$$

where  $\mu(Q)$  and  $E(\mathbf{r}, t)$  denote the dipole operator depending on system degrees of freedom  $Q$  and the electric field of the external radiation, respectively. The definition of the material polarization  $P(\mathbf{r}, t)$  is given by [86]

$$P(\mathbf{r}, t) = \text{tr}\{\mu(Q)\rho(\mathbf{r}, t)\} \quad (3.2)$$

where  $\text{tr}$  means sum over all degrees of freedom in the total matter system, and  $\rho(\mathbf{r}, t)$  denotes the density operator obeying the Liouville equation,

$$\frac{\partial \rho(\mathbf{r}, t)}{\partial t} = \frac{1}{i\hbar} [H_M + H_{int}, \rho(\mathbf{r}, t)]. \quad (3.3)$$

$H_M$  is the Hamiltonian of the unperturbed matter system. Taking the interaction picture, one can obtain  $\rho(\mathbf{r}, t)$  in a perturbation series of  $H_{int}$  from Eq. (3.3). By substituting the resulting expression into Eq. (3.2), one gets the formal expression for  $P(\mathbf{r}, t)$  as follows [86]:

$$\begin{aligned} P(\mathbf{r}, t) &= \sum_{i=0}^{\infty} P^{(i)}(\mathbf{r}, t) \quad (3.4) \\ P^{(n)}(\mathbf{r}, t) &= \int_0^{\infty} dt_n \int_0^{\infty} dt_{n-1} \cdots \int_0^{\infty} dt_1 \bar{R}(t_n, t_{n-1}, \dots, t_1) \\ &\quad \vdots E(\mathbf{r}, t - t_n) E(\mathbf{r}, t - t_n - t_{n-1}) \cdots E(\mathbf{r}, t - t_n \\ &\quad - t_{n-1} \cdots - t_1), \quad (3.5) \end{aligned}$$

where  $\vdots$  denotes the tensor contraction, and  $\bar{R}(t_n, t_{n-1}, \dots, t_1)$  is the nonlinear response tensor of matter system defined by

$$\begin{aligned} \bar{R}(t_n, t_{n-1}, \dots, t_1) &= \left( \frac{i}{\hbar} \right)^n \langle \langle \langle \langle \langle \dots [\mu(t_n + \dots + t_1), \\ &\quad \mu(t_{n-1} + \dots + t_1), \dots], \mu(t)], \mu(0) \rangle \rangle, \quad (3.6) \end{aligned}$$

with  $\mu(t) = \exp(iH_M t/\hbar) \mu(Q) \exp(-iH_M t/\hbar)$  and the expectation value of an arbitrary operator  $\mathbf{A}$  being defined as  $\langle \mathbf{A} \rangle = \text{tr} \{ \mathbf{A} \rho(0) \}$ . Here  $\rho(0)$  denotes the initial density operator of the material system.

In four-wave mixing (FWM) spectroscopy, one selectively measures the third order polarization  $P^{(3)}(\mathbf{r}, t)$  among the perturbation series, and the nonlinear response tensor relevant to the FWM spectroscopy reads as

$$\begin{aligned} \bar{R}(t_3, t_2, t_1) &= \left( \frac{i}{\hbar} \right)^3 \langle \langle \langle \langle \langle [\mu(t_3 + t_2 + t_1), \mu(t_2 + t_1)], \\ &\quad \mu(t_1)], \mu(0) \rangle \rangle \rangle, \quad (3.7) \end{aligned}$$

An explicit expression for the nonlinear response tensor can be obtained if a specific Hamiltonian is assumed [87]. Once the response has been calculated, the polarization can be obtained for any shaped pulse  $E$  by a three-fold integration

$$\begin{aligned} P(\mathbf{r}, t, \tau, \tau_1) &= (-i)^3 \int_0^{\infty} dt_3 \int_0^{\infty} dt_2 \int_0^{\infty} dt_1 \bar{R}(t_3, t_2, t_1) \\ &\quad E(\mathbf{r}, t - t_3) E(\mathbf{r}, t - t_3 - t_2 + \tau_1) \\ &\quad E(\mathbf{r}, t - t_3 - t_2 - t_1 + \tau + \tau_1). \quad (3.8) \end{aligned}$$

Here a complete specification of the pulse ordering is used, where the pulse separation between the first and second is  $\tau$  and second and last laser pulse is  $\tau_1$ . Eq. (3.8) will be of central importance for the following sections. In general more than 64 double sided Feynman diagrams, representing different Liouville space pathways, contribute to the third order nonlinear response tensor. However, by controlling the center frequency, the polarization direction, and the propagation direction of the input external fields, and by measuring the signal field propagating along a specific direction, only a few of the components of the polarization vectors can be selectively measured. In the next section it is shown theoretically that it is possible to influence contributions to the degenerate FWM (DFWM) signal by shaping one (or more) of the excitation pulses. Then an experimental section follows showing that the theoretical predictions are accurate.

### 3.2 Control using shaped pulses in the DFWM process: Theory

In this section a theoretical description for a new control scheme is developed. Here the control is not achieved as in previous experiments (see Ref. [88] and the excursion in section 3.3), where an additional second time separation is introduced in the DFWM pulse sequence as control knob, but instead by correctly modulating one of the three pulses as depicted schematically in Fig. 3.1(a). The other two pulses are time coincident, that is  $\tau_1 = 0$  in Eq. (3.8). This sequence will be termed S-UU, where S denotes shaped

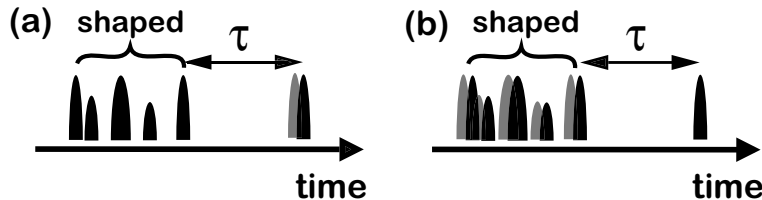


**Figure 3.1:** A new control mechanism based on the DFWM sequence of pulses depicted here is investigated. (a) S-UU pulse sequence. Here the pulse in one of the three DFWM beams is shaped (S) arbitrarily, while the unshaped (U) pulses in the other two beams are made time coincident. (b) SS-U sequence. Now the situation is reversed. The two time coincident pulse are tailored arbitrarily and arrive first in the interaction region, followed by one single unshaped pulse. Note that the time-coincident pulses are always identically shaped.

and U unshaped. A pulse sequence where the two time coincident pulses are identically shaped and the pulse in the third beam is unshaped will be termed SS-U in the following and is depicted in Fig. 3.1(b). At first a theory is developed that accounts for FWM control experiments using pulses tailored into a sequence of two or more subpulses with a constant phase in time.

This theory gives the same results for S-UU and SS-U and therefore it will exemplarily derived for the S-UU case. The theory is completely analytical and extraordinarily simple, however can not account for a time dependent phase within the pulse duration as happens for e.g. chirped pulses. Therefore, in the second part of the section a completely different theory based on a perturbative wave packet approach is used to lift this restriction of constant phase over the pulse envelope and predict the FWM signal for arbitrarily tailored pulses. Results are presented only for the experimentally measured case of linearly chirped pulses in the sequence SS-U. This second theory based on a numerical calculation is more general than the theoretical model restricted to pulse trains, which is still solvable analytically.

**Theory 1: Tailored pulse trains.**

If the pulse in one of the beams is shaped using an LC-SLM it can be expressed as a sum of Fourier limited pulses occurring at times  $\Delta_j$ , each with an envelope  $a_j$  and phase  $\phi_j$

$$E(t) = \sum_j a_j(t - \Delta_j) \exp(i\phi_j) \quad (3.9)$$

Replacing the first E-field of the three involved electric fields in Eq. (3.8) by the expression given in Eq. (3.9) transforms the polarization into summands of polarizations induced by three Fourier limited pulses (FL-DFWM)

$$\begin{aligned} E(t_1)E(t_2)E(t_3) &= \left[ \sum_j a_j(t - t_3 - \Delta_j + \tau) \exp(i\phi_j) \right] \\ &\quad E_2(t - t_3 - t_2)E_1(t - t_3 - t_2 - t_1) \\ &= \sum_j [a_j(t - t_3 - \Delta_j + \tau) \exp(i\phi_j) \\ &\quad E(t - t_3 - t_2)E(t - t_3 - t_2 - t_1)] \end{aligned} \quad (3.10)$$

If the phase of the subpulses is not a function of time, it can be taken out of the integral for each term, leading to the following expression for the nonlinear polarization P:

$$\begin{aligned} P^{(M)}(t, \Delta, \tau) &= \sum_j \exp(i\phi_j) \int_0^\infty dt_1 \int_0^\infty dt_2 \int_0^\infty dt_3 R^{(3)}(t_3, t_2, t_1) \\ &\quad a_j(t - t_3 - \Delta_j + \tau) E(t - t_3 - t_2) \\ &\quad E(t - t_3 - t_2 - t_1) \end{aligned} \quad (3.11)$$

It is therefore possible to express the multiple DFWM polarization as a summation of FL-DFWM terms  $P^{(M)} = \sum P^{(3)}(\tau, t - \Delta_j, \phi_j)$ . The resulting

DFWM signal, which is the integral over the polarization, is then also a sum over FL-DFWM signal contributions interfering with each other depending on their relative phase and delay

$$\begin{aligned} I^{(M)}(\tau) &= \int dt \left| P^{(M)}(t, \tau) \right|^2 \\ &= \int \left| \sum_j P^{(3)}(\tau, t - \Delta_j, \phi_j) \right|^2 = \sum_j I^{(3)}(\tau, \Delta_j, \phi_j). \end{aligned} \quad (3.12)$$

To obtain this result the incoherent sum over the polarizations was taken  $\left| \sum_j \dots \right|^2 = \sum_j |\dots|^2$ , which is necessary assumption in order to take into account the integration time of the acquisition electronics [89].

Clearly Eq. (3.12) shows that the expected DFWM signal when using tailored pulses can be simply expressed as a summation over retarded DFWM transients  $I^{(3)}$  as measured when using Fourier limited pulses (FL-DFWM). Once a model for the FL-DFWM transient [see Fig. 3.8] is derived the control theory is complete. The simplest model assumes a sum of two sine functions, one with the frequency of the electronic ground state vibration,  $\omega_g$ , of the potassium dimer and one with the frequency of the excited state vibration,  $\omega_e$ ,

$$I^{(3)}(\tau) = \sin(\omega_e \tau) + r \sin(\omega_g \tau). \quad (3.13)$$

The factor  $r$  is included for weighting. In the potassium dimer the vibrational round trip time in the ground state is 360 fs and in the first excited potential is 520 fs. Of course, a more sophisticated model for FL-DFWM could be used here instead but the model fits the data well enough. Damping effects are neglected because the dephasing time  $T_2$  ( $> 200$  ps) is much larger than the typical  $\tau$  values. Eq. (3.13) is the fundamental building block of the theoretical predictions for  $I^{(M)}$ . According to Eq. (3.12) it is only necessary to add several Eq. (3.13) to simulate the control experiments. In the following two examples of this theory are given.

- **Pulse train.** The case of excitation with an equidistant pulse train was modeled by adding terms given by Eq. (3.13) in number equal to the number of subpulses constituting the pulse train,

$$\begin{aligned} I(\tau) &= \sum_k I^{(3)}(t - k\Delta) = [\sin(\omega_e \tau) + r \sin(\omega_g \tau)] \\ &\quad + [\sin(\omega_e(\tau - \Delta)) + r \sin(\omega_g(\tau - \Delta))] \\ &\quad + [\sin(\omega_e(\tau - 2\Delta)) + r \sin(\omega_g(\tau - 2\Delta))] + \dots \end{aligned} \quad (3.14)$$

- **Phase related double pulse.** The shaped double pulse excitation can be then expressed according to Eq. (3.12) as a sum of a transient,

that is not delayed and a delayed transient, which has an inherent phase  $\phi$  transferred by the second subpulse,

$$\begin{aligned}
 I(\tau) = I^{(3)}(\tau) + I^{(3)}(\tau - \Delta) &= [\sin(\omega_e \tau) + r \sin(\omega_g \tau)] \\
 &+ [\sin(\omega_e(\tau - \Delta) + \phi) \\
 &+ r \sin(\omega_g(\tau - \Delta) + \phi)] \quad (3.15)
 \end{aligned}$$

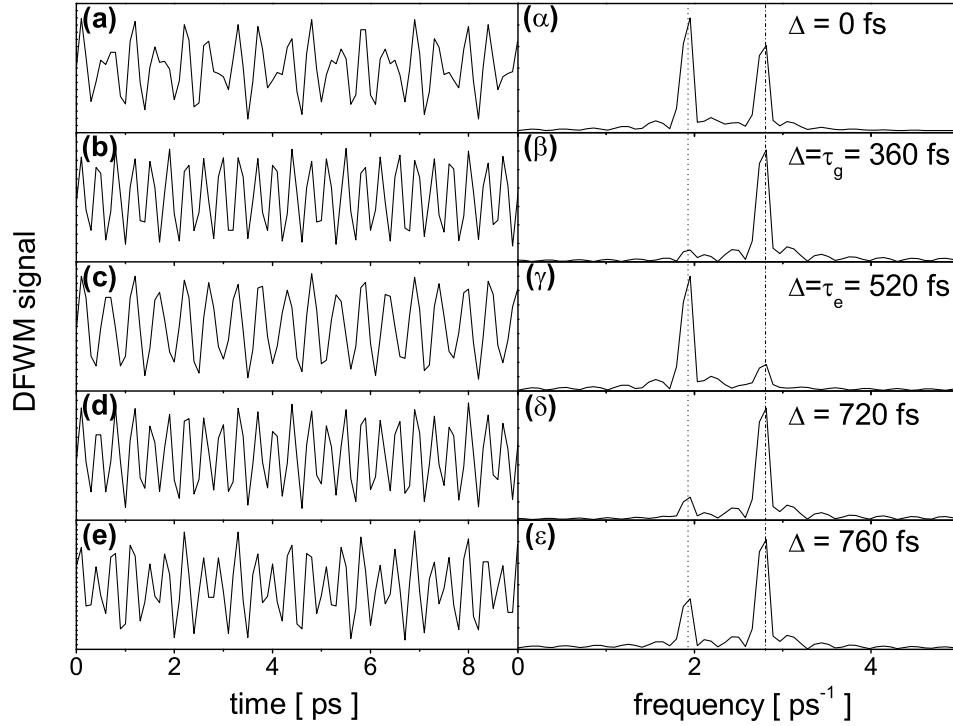


**Figure 3.2:** Theoretical model calculation for the DFWM signal using one pulse train with interpulse separation  $\Delta$  and two unshaped time coincident pulses. (a)-(e) Simulated transient for different  $\Delta$ . ( $\alpha$ )-( $\epsilon$ ) Fourier transform data of the transients. FL-DFWM transient for reference is (a) and ( $\alpha$ ), respectively.

The control of the DFWM signal using a pulse train excitation according to equation (3.14) is shown in Fig. 3.2 for different interpulse separations. In (a) to (e) the transient is shown and its Fourier transform data is shown in ( $\alpha$ ) to ( $\epsilon$ ). The data in (a) and ( $\alpha$ ) serves as reference and shows the transients obtained using Fourier limited pulses (empty mask). In Fig. 3.3 the control of DFWM signal X and A contributions using a double pulse with phase  $\alpha = 0$  and variable delay (a) to (e) and using a double pulse with variable phase  $\alpha$  and with an interpulse separation  $\Delta = \tau_g$  ( $\alpha$ ) to ( $\epsilon$ ) is shown as calculated according to Eq. (3.15). The FL-DFWM is shown in (a) and serves as reference. Both numerical simulations show that control

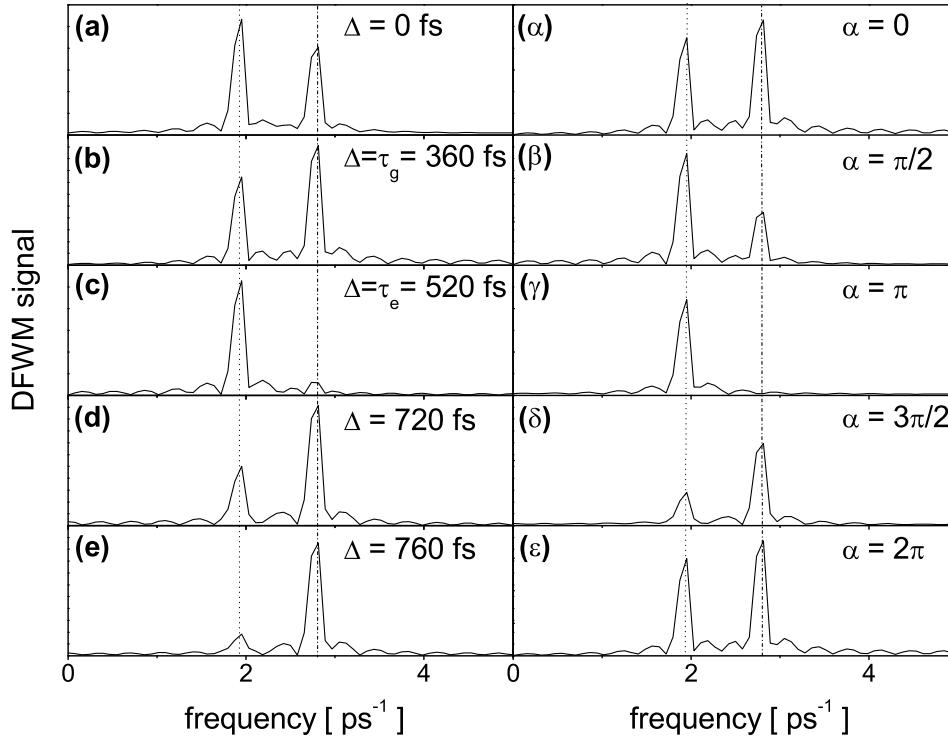


**Figure 3.3:** Theoretical model calculation for the DFWM signal using one shaped double pulse with variable time separation  $\Delta$  and relative phase  $\alpha$  and two unshaped time coincident pulses. (a)-(e) Fourier transform data of the DFWM transient for different  $\Delta$  and  $\alpha = 0$ . ( $\alpha$ )-( $\epsilon$ ) Fourier transform data of the transient for  $\Delta = \tau_g$  and different relative phases  $\alpha$ . Fourier transform data of the FL-DFWM in (a) serves as reference. Note that ( $\alpha$ ) and (b) are the same pulse configuration.

over the wave packet contributions in the DFWM signal is indeed possible, and that there is a quantitative difference between using a pulse train or a double pulse. In the pulse train case exact matching of the inter pulse separation to integer multiples of the vibrational round trip time of the state to be selected is optimal [Fig. 3.2 (b)-(d)]. Instead when using double pulses especially in order to select the ground state contribution in the signal an exact matching is not as optimal as some intermediate inter pulse separation [see Fig. 3.3(e)]. The control using the relative phase in the shaped double pulse shows a periodicity of  $2\pi$  and the X and A contributions can be completely influenced.

**Theory 2: Arbitrarily shaped pulses.**

The theoretical model derived previously is restricted to pulses with constant phase in time. Certainly it is also of interest to predict the outcome of a four-wave mixing (FWM) experiment using a chirped or even an arbitrary tailored pulse excitation. Therefore a different theoretical model is used here, based on a numerical third order perturbative calculation of the FWM polarization. This theory was developed by S. Meyer [89] for the case of unshaped excitation pulses in FWM and has been very successful in calculating the FWM response of I<sub>2</sub> in the gas phase [90]. The basics of this theory will be sketched here only shortly and the reader interested in more details is referred to Refs. [89, 91]. In the context of this thesis it will be extended to the case of arbitrarily tailored excitation pulses.

In the following the pulse sequence SS-U is assumed with  $\tau$  being the pulse separation between the two time coincident shaped pulses SS and the unshaped pulse U. These pulses will be identified by their wave vectors  $k_s$ ,  $k_{s'}$  and  $k_u$ , respectively. Starting point is again a formula for the polarization

$$P(t) = \langle \psi(t) | \mu | \psi(t) \rangle, \quad (3.16)$$

where  $\mu$  is the transition dipole moment. The wave function of the system  $\psi$  is decomposed according to perturbation theory into the following sum

$$|\psi(t)\rangle = \sum_{N=0}^{\infty} |\psi^{(N)}\rangle. \quad (3.17)$$

Here  $N$  indicates the order of the perturbation, that is the number of interactions of the system with the laser field. The FWM process occurs between the ground electronic potential  $g$  and a single excited electronic potential  $e$  being in resonance with the center wavelength of the interacting laser pulses. The unperturbed initial wave function  $|\psi^{(0)}\rangle$  is a thermally populated vibrational eigenstate of the ground state potential. The time-dependent wave function for an odd (even) number of interactions  $N$  will be in the electronic excited (ground) state potential. In general the  $N$ -th order wave packet in the electronic potential  $p$  at time  $t + \Delta t$  is generated from a wave packet of equal order in the same electronic state  $p$  ( $|\psi_p^{(N)}(t)\rangle$ ) and a wave packet in the other electronic state  $p'$  with order  $N-1$  ( $|\psi_{p'}^{(N-1)}(t)\rangle$ ) both at time  $t$  via the iterative scheme [92]

$$\begin{aligned} |\psi_p^{(N)}(t + \Delta t)\rangle &= U_p(\Delta t) |\psi_p^{(N)}(t)\rangle \\ &\quad + iE_j(t + \Delta t)\mu U_{p'}(\Delta t) |\psi_{p'}^{(N-1)}(t)\rangle. \end{aligned} \quad (3.18)$$

Here  $p \neq p'$  stand for the two different electronic potentials  $g$  and  $e$  involved in the FWM process.  $U_p$  is the field-free propagator in the electronic potential  $p$  and  $E_j(t)$  describes the time-dependence of the electric field  $j$ . The

way the electric fields are calculated here, is the major difference to the original formulation by S. Meyer. The two shaped pulses  $E_s$  and  $E_{s'}$  are given according to the pulse shaping equation  $E_j(\omega) = M_j(\omega)E^{FL}(\omega)$  from the complex Fourier limited field  $E^{FL}(t) = g(t)\exp(-i\omega t)$ . The pulse envelope of the unshaped pulse  $g(t)$  is chosen as a Gaussian. The time-propagation is performed using the split-operator technique (see Ref. [93] and section 5.2).

In order to evaluate the polarization within this perturbative regime Eq. (3.17) up to third order is inserted into the Eq. (3.16). The processes contributing to the resulting third order polarization are schematically represented using double-sided Feynman diagrams. For the pulse sequence SS-U considered here, three double-sided Feynman constitute the FWM polarization signal [91]<sup>1)</sup>

$$\begin{aligned}
 P^{(3)}(t, \tau; |\psi_g^{(0)}\rangle) &= 2\text{Re} \left\{ \left\langle \psi_g^{(2)}(k_{s'} - k_u) \middle| \mu \middle| \psi_e^{(1)}(k_s) \right\rangle \right. \\
 &\quad + \left\langle \psi_g^{(2)}(k_{s'} - k_s) \middle| \mu \middle| \psi_e^{(1)}(k_u) \right\rangle \\
 &\quad \left. + \left\langle \psi_g^{(0)} \middle| \mu \middle| \psi_e^{(3)}(k_s - k_{s'} + k_u) \right\rangle \right\}. \quad (3.19)
 \end{aligned}$$

The  $k$  vector interactions with negative sign are  $g \leftarrow e$  electronic state emissions and are calculated using the conjugate of the electric field, that is  $E_j^*$ , while the positive sign interactions use  $E_j$  and indicate  $g \rightarrow e$  absorption. Of course Eq. (3.19) calculates only the polarization contribution of one single vibrational state  $v$ , that served as initial condition  $|\psi_g^{(0)}\rangle = |v\rangle$ . In order to account for a thermal ensemble of molecules the incoherent sum of all polarization contributions of different vibrational states within the Boltzmann distribution must be evaluated. The total DFWM signal  $I(\tau)$  is then given by integrating the sum of all polarization contributions from the thermal ensemble over two times the *fwhm* (full width at half maximum) duration of the last interacting pulse U [89]

$$I(\tau) \approx \sum_v \int_{\tau-fwhm}^{\tau+fwhm} |P(t, \tau; |v\rangle)|^2 dt. \quad (3.20)$$

A model system is chosen based on the characteristic properties of the potassium dimer with some modifications to reduce the necessary computing time. The model system consists of an harmonic potential as ground state X, the real anharmonic excited state potential  $A^1\Sigma_u$  and the K-K separation dependent dipole moment between X and A potentials [see Fig. 3.4]. The

<sup>1)</sup>The errata to this publication

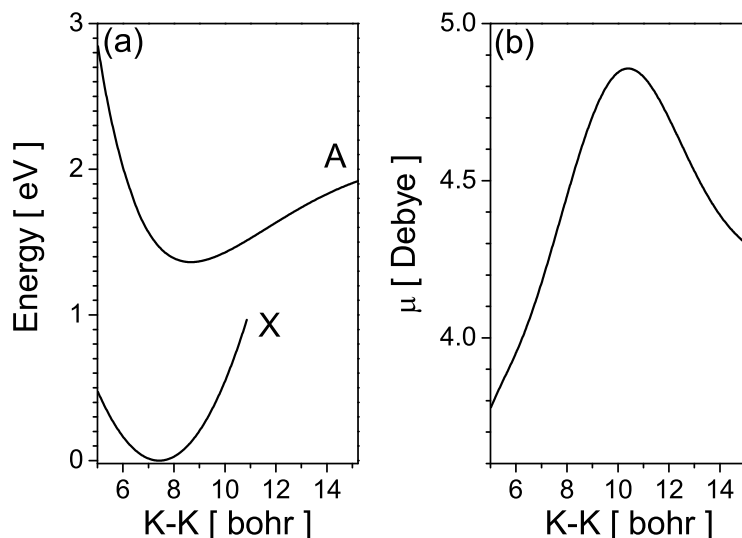


**Figure 3.4:** A simplified model for the  $K_2$  molecule. (a) The electronic potentials. The ground state potential is assumed to be an harmonic oscillator with the minimum displaced by the same amount relative to the minimum of the excited state as in the real system. The excited state potential is the real  $A^1\Sigma_u$   $K_2$  potential. (b) The real K-K distance dependent dipole transition moment  $\mu$  between the two potentials.

minima of X and A state are spaced by 1.36 eV which corresponds to a wavelength of 910 nm ( $11\,000\text{ cm}^{-1}$ ). Also the relative displacement of the two potentials in radial direction corresponds to the real system. The mass of the prototype system was chosen to be 3000 a.u. (which is about ten times lighter than the real  $K_2$  mass) to accelerate the dynamics and thereby reduce the necessary time for propagation. For the same reason the pulse duration of the interacting pulses was chosen to be only 7 fs with a center wavelength at 820 nm.

A thermal ensemble is assumed, where only the first three vibrational states of the ground state potential are considerably populated. The calculations of the DFWM signal  $I(\tau)$  are performed for different amount of linear frequency chirp of both positive and negative sign. In Fig. 3.5 the Fourier transform data of the transients obtained for the different amount of chirp are shown, where the data was normalized to have the same value of the X peak to directly see the effect of chirp on the A state peak. The maximum chirp of  $\pm 90\text{ fs}^2$ , broadens the initially 7 fs pulse to about 36 fs. The inset shows the difference in peak heights A-X for the different chirp values, summarizing the information of the Fourier transform data of the DFWM signal displayed in the main graph. Clearly for the largest negative chirp

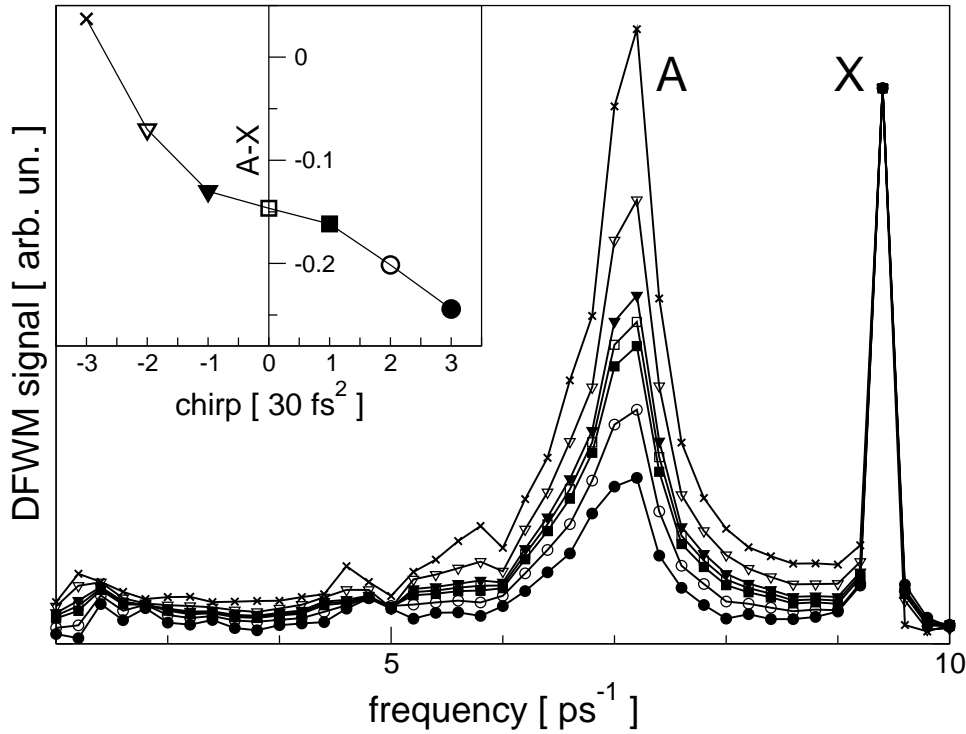


**Figure 3.5:** The Fourier transform of the DFWM signal obtained through excitation with a SS-U sequence, where the two time coincident pulses are shaped with a linear chirp. Each dotted line corresponds to a different linear chirp. Clearly visible the X and A peak corresponding to the vibrational recurrence time in the respective potential. The data is normalized to have the same X state peak magnitude. The peak height difference A-X is plotted as a function of chirp in the inset and summarizes the information of the main graph.

the A state is maximal, while for the largest positive chirp it is minimal <sup>2)</sup>. A further enhancement of the peak difference A-X can be expected if the anharmonicity of the ground state potential is taken into account. Finally these calculations indicate that the control of the peak heights in the Fourier data of the DFWM signal is not due to a considerable manipulation of population, since the norm of the wave packets evolving on the potentials is only slightly influenced by chirp within this perturbative regime. Thus the control of peak heights as displayed in Fig. 3.5 must be due to an interference of the three summands in Eq. (3.19).

<sup>2)</sup>The effect depends moreover on the center-wavelength and bandwidth of the interacting laser pulses.

### 3.3 Control using shaped pulses in the DFWM process: Experiment

#### Experimental setup.

In order to realize the theoretical control predictions of the previous section a femtosecond DFWM experiment according to Fig. 3.6 was built up and the molecule  $K_2$  was chosen. Laser pulses of 100 fs at 825 nm from a commercial femtosecond laser system with chirped pulse amplification (CPA) are split into three beams each having an energy of 50 nJ / pulse. The polarization of each beam was horizontal and the beams were arranged in a folded forward BOXCARS geometry typically used in DFWM-gas phase studies [94] [see Fig. 3.6(a)]. Here the three parallel incident beams are

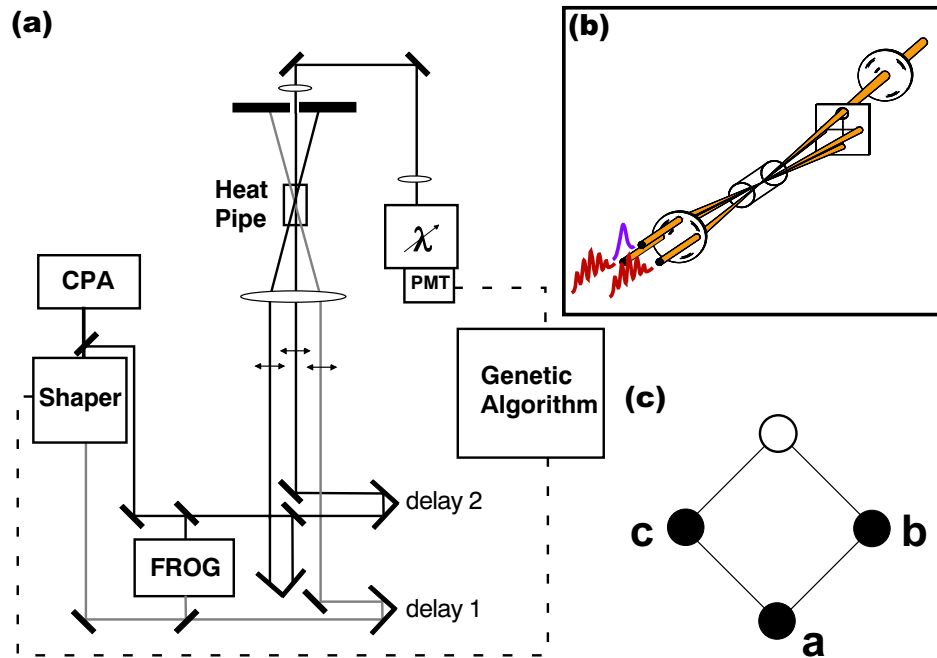


**Figure 3.6:** (a) Experimental setup showing the fs-DFWM learning loop. (b) Arrangement of the beams in space. (c) Nomenclature for the different directions in the BOXCARS square.

aligned to trespass the edges of a square in space [see Fig. 3.6(b) and (c)], a configuration that naturally conserves the momentum. The signal is then only captured in the direction marked with a hollow dot [see Fig. 3.6(c)] and is  $\mathbf{k}_s = -\mathbf{k}_a + \mathbf{k}_b + \mathbf{k}_c$  with a frequency given by  $\omega_s = -\omega_a + \omega_b + \omega_c$ . Since the FWM signal is measured in a new direction it is essentially background free and is moreover a highly localized probe, since it is generated by a polarization created in the small focal region in space where the three incident beams cross. The signal is detected either in a spectrometer fitted

with a linear array CCD detector (Ocean Optics S2000), or in a scanning monochromator (Acton Research SpectraPro 300i). The beams are focused into a heat pipe filled with potassium and argon as buffer gas heated to a temperature of 360°C. One of the beams is sent through an all-reflective pulse shaper with a phase and amplitude modulating LC-SLM at its Fourier plane (see section 1.1) opening thereby the possibility to shape one or even two of the incident pulses into an arbitrary pulse form. The pulse shape is optimized by letting an evolutionary algorithm steer the pulse shaper as already described in the introductory chapters.

### Review of earlier experiments.

The center frequency of 825 nm of all beams matches the high Franck-Condon overlap region between the X and A state potential of the potassium dimer [see Fig. 3.7]. This ensures resonant enhancement of the third order

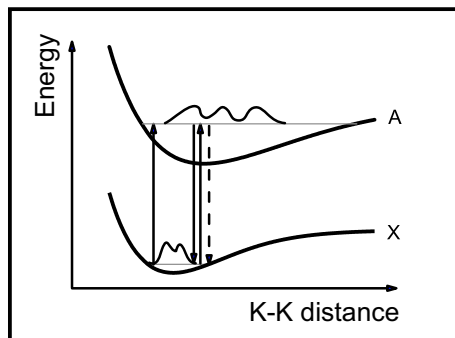


**Figure 3.7:** Sketch of the potentials of ground and first excited state of  $K_2$  and the DFWM process.

signal and excitation of wave packets on both ground and excited state. This kind of gas phase FWM measurement was explored by A. Materny et al. on  $I_2$  supported by theory from V. Engel and coworkers [90, 95, 96]. They used a temporal ordering of the pulses, where the first pulse arrived separated in time by a delay  $\tau$  from the time-coincident pulses inside the other two beams. The Feynman diagrams for this time-ordering of the pulses predict that the signal has contributions from ground and excited state potential surfaces. Fig. 3.8 shows such a measurement on  $K_2$  where the spectrally integrated DFWM signal is recorded as a function of delay  $\tau$ . In good agreement with earlier experiments the Fourier analysis of the data reveals two main peaks, corresponding to the vibrational round trip time in the ground X ( $\tau_g = 360 fs \sim 92.4 cm^{-1}$ ) and excited A potential energy surface ( $\tau_e = 520 fs \sim 70 cm^{-1}$ ). Due to the broad bandwidth up to six A-state and three ground state vibrations are coherently excited, leading to the higher harmonic lines of the next but one vibrational beating clearly visible in the Fourier spectrum (2X and 2A). This data can be further an-

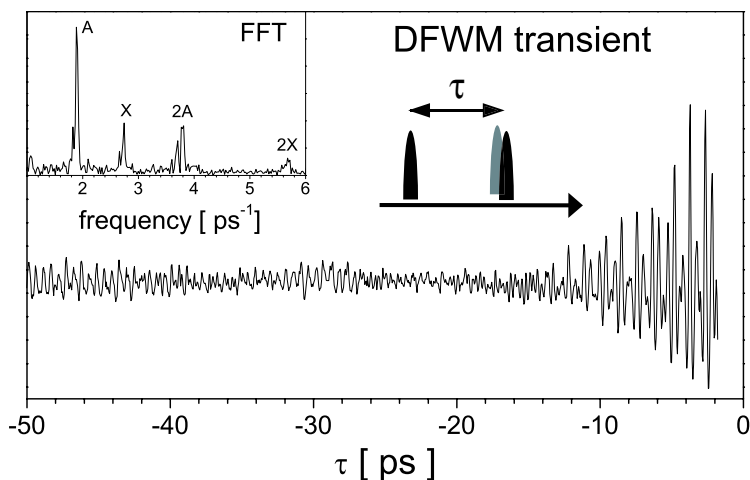


**Figure 3.8:** DFWM transient resulting from excitation with three unshaped femtosecond pulse showing the vibrational period of potassium A and X state. In the inset the corresponding spectrum (FFT) of the transient is plotted. The DFWM pulse excitation sequence, where one pulse is delayed by  $\tau$  with respect to the other time-coincident pulses is also shown.

alyzed by performing a short time Fourier transform. Here the convolution of the data with a Gaussian window function is calculated and then Fourier transformed. This procedure is repeated for different temporal position of the window function. Thereby a two-dimensional data set is obtained, that reveals the temporal evolution of the spectral components (not shown). The spectrogram of the 60 ps long DFWM transient revealed a weak, irregular beat structure with the main revivals being in good agreement with the measurements of E. Schreiber and coworkers on  $^{39,41}\text{K}_2$  [97]. No regular beat oscillation maxima with a period of 10 ps, typical of the  $^{39,39}\text{K}_2$  isotope, could be observed.

The control idea pursued in this chapter is to either enhance the A state contribution in the DFWM signal with respect to X or vice versa by suitably shaping the first pulse. Before proceeding however it should be noted that a change in the contributions to the DFWM signal does not necessarily mean that molecular population is controlled. Instead it can simply be the selection of Feynman diagrams that leads to a different DFWM signal, i.e. the dynamics are still there however can not be probed since the diagram is disallowed. That such a selection of diagrams is indeed possible was first shown by M. Dantus and coworkers [88,98,99]. Here a further time delay  $\tau_1$  was introduced separating in time the previous time coincident second and third pulse. The parameter  $\tau$  still served as the scanning delay. They showed that it is possible to manipulate the DFWM signal contributions by choosing different values for  $\tau_1$  [88]. Indeed the signal has only A state contribution if either  $\tau_1 = n\tau_g$  or  $\tau_1 = n + \frac{1}{2}\tau_e$  is fulfilled. Here n is an

integer multiple. Correspondingly both conditions  $\tau_1 = n\tau_e$  or  $\tau_1 = n + \frac{1}{2}\tau_g$  will lead to mere X state contribution in the DFWM signal. The measurements on the potassium dimer [see Fig. 3.9] agree with their experiments on  $I_2$ . Here the first two interacting pulses generate such a population coher-

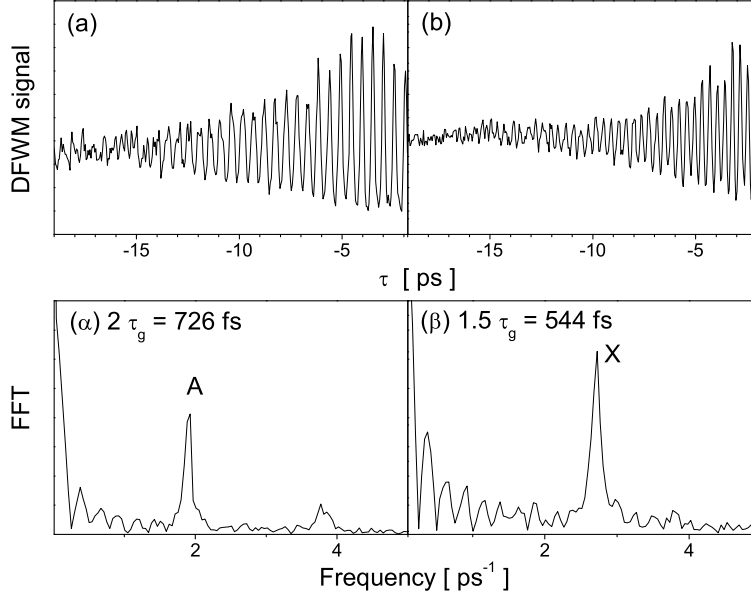


**Figure 3.9:** DFWM using a variable time separation  $\Delta$  between the first two pulses. For the case of  $\Delta = 2 \times$  the vibrational period in the ground state ( $\tau_g$ ). (a) shows the transient, that shows only A state dynamics ( $\alpha$ ). (b) and ( $\beta$ ) depict transient and its Fourier transform for  $\Delta = 1.5 \tau_g$ .

ence depending on their time separation, that the third pulse producing the macroscopic DFWM polarization projects out only a specific dynamics. It is however clear that completely suppressing, e.g. the ground state dynamics in the transient does not mean that no ground state wave packet is generated by the FWM pulse sequence. In fact the ground state wave packet is there, its dynamics is however not captured any more. This short excursion to previous experiments shows, that care must be taken in DFWM experiments to distinguish control over the dynamics projected into the signal with control over populations, that could also give rise to only a specific dynamics in the signal.

### Experiments with the new control scheme.

In the following the new control scheme as proposed in section 3.2 is experimentally verified. Here a pulse sequence is chosen, where  $\tau_1 = 0$  and the control is instead achieved by shaping one of the three excitation pulses. In order to also extend the theoretical control predictions of section 3.2 a learning-loop setup is used, automatically finding the optimal solutions. All

constituting components were already discussed before and only the feedback signal has to be explained in detail. In the experiments a transient of 5 ps (termed FFT window) was recorded with the monochromator fixed at one wavelength [Fig. 3.10]. The transient was sufficiently long to clearly

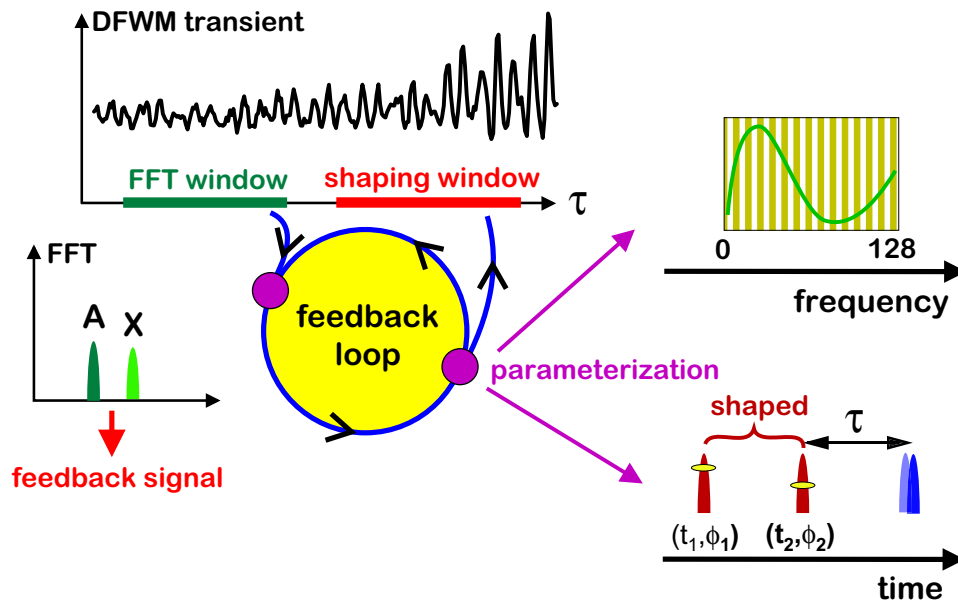


**Figure 3.10:** The feedback signal is derived from the transient by FFT and evaluating the difference in peak heights between A and X. This number serves as feedback to an evolutionary algorithm which uses genes either representing frequency or time domain.

resolve the two peaks of X and A state vibration in the Fourier transform data. The A peak at  $1.9 \text{ ps}^{-1}$  will be labelled by  $I(\nu_e)$  and the X peak at  $2.7 \text{ ps}^{-1}$  by  $I(\nu_g)$  in the following. The feedback signal was computed by subtracting from the difference of the vibrational peak heights  $[I(\nu_e) - I(\nu_g)]$  the noise level of the Fourier data:

$$\text{Feedback signal} = \pm(I(\nu_e) - I(\nu_g)) - b \cdot \text{noise} \quad (3.21)$$

The variable  $b$  is a weighting factor multiplying the noise subsoil which is calculated by summing over the intensities at the frequencies ranging from  $5 \text{ ps}^{-1}$  until  $19 \text{ ps}^{-1}$ . This assures that the contrast between peak heights and noise is high for any optimized pulse. The algorithm should maximize the difference in peak heights,  $\pm(I(\nu_e) - I(\nu_g))$ , taking the + sign for A optimization and the - sign for X.

Crucial requirement for this feedback to work is the acquisition of the transient for time separations  $\tau$  greater than the temporal shaping window of the modulator in order to avoid probing while the system is still being excited [Fig. 3.10]. The shaping window is computed as number of pixels times

temporal resolution of the SLM and can be interpreted as the maximum time span into which a shaped pulse may extend (see section 1.1) [45]. The necessary scanning of the delay unit over a range of 5 ps with a resolution of 50 fs in order to obtain the feedback-signal took about half a minute. Since the algorithm converged within five generations, each consisting of 20 individuals, it took about one hour to get the optimal pulses. Much longer times would have been needed if the algorithm would have had to adjust the 256 voltages, two for each pixel, of the mask. Instead parameterizations, as described in section 1.2, were used throughout reducing the number of control knobs and therefore the size of the search space drastically. Three different control mechanisms were studied: phase-related double pulses (pump-dump) [12, 13], pulse trains (impulse stimulated Raman scattering) [84] and finally chirped pulses [9, 42, 100]. The parameterization was either chosen directly in the time or in the frequency domain, depending which domain required less parameters to represent the desired field. Switching between the two different parameterizations did not afford adapting internal strategy parameters of the evolutionary algorithm. In all the optimizations the pulse sequence was SS-U.

#### **Parameterization in the time domain.**

A parameterization in the time-domain is used as an effective way of restricting the optimization to phase-related double pulses. This is good starting point to test the theoretical control results for the case of Eq. (3.15). For the representation of such a double pulse in the frequency domain at least 256 parameters are needed, using the applied voltages to the shaper as genes whereby each parameter comes with a discretization of 64 grey levels. In contrast using genes that represent each pulse in the time only four parameters are needed: amplitude and phase at a specific temporal position. The temporal position could attain 128 values corresponding to the discrete position spaced by half the incident pulse temporal width [4] within the shaping window (see section 1.1). Phase in the range of  $[0, 2\pi]$  and amplitude in the range  $[0, 1]$  were discretized in 20 steps. The algorithm converged for both optimizations of A and X within five generations. A double pulse of time separation 540 fs optimizes A and a time separation of 740 fs optimizes X, respectively [Fig. 3.11]. The theoretical predictions assuming the model of Eq. (3.15) accurately matches experimental results [solid line in Fig. 3.11]. Also additional double pulses matching a multiple of the vibrational periods were tried giving similar results in perfect agreement with theory (not shown). The importance of the phase-relationship between the two subpulses [101] was investigated by recording DFWM transients for various double pulses with different phases but fixed interpulse separation. The data was Fourier transformed, and the ratio of the vibrational contributions from the A and X states was calculated. In Fig. 3.12 this ratio is plotted against the applied phase differences. Each point represents one measure-

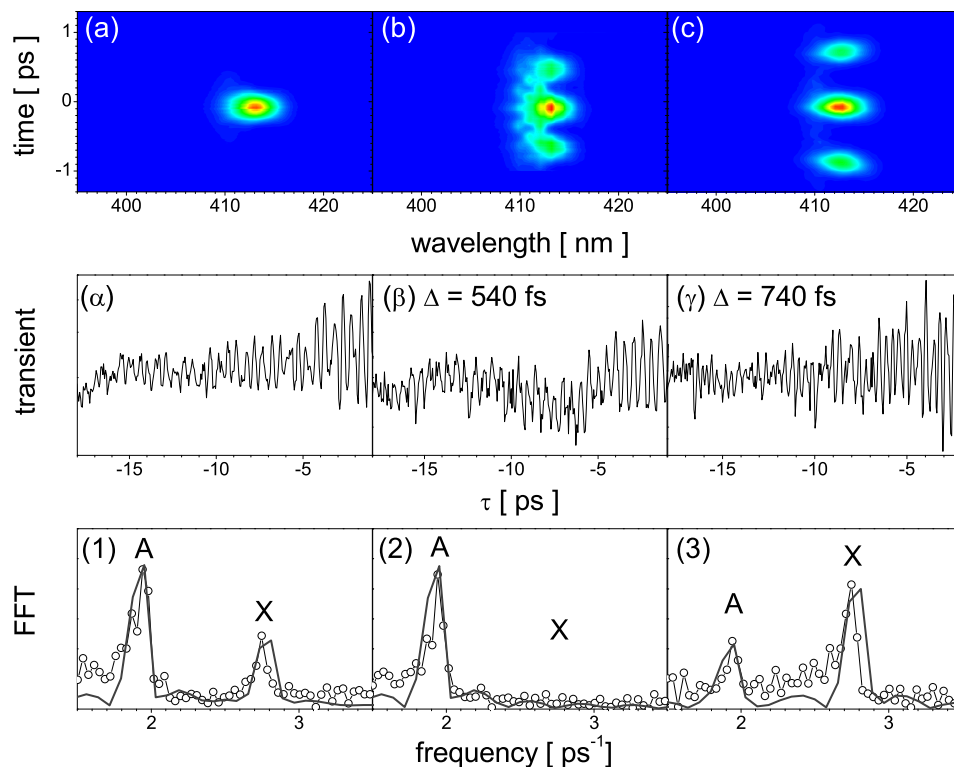


**Figure 3.11:** FROG measurements of (a) reference pulse and (b), (c) optimized pulses using a direct time parameterization. The corresponding transients are  $(\alpha)$  and  $(\beta), (\gamma)$ . The Fourier transform of this data (1)-(3) and theoretical model (solid line) shows that pulse (b) optimizes A contribution while (c) X contribution.

ment. The data show a  $2\pi$  period and this result is independent of whether the shaped double pulse in the DFWM sequence arrives first or last in the interaction volume. This implies that the ratio between A and X contributions can be controlled for any fixed pulse separation by varying the relative phase only. Using again the theoretical model [Eq. (3.15)] gives good agreement with the experimental phase data [see Fig. 3.12]. Theory can now be used to predict the outcome of the experiment for a whole range of interpulse separation and phase relationships. The results of this calculation is shown in Fig. 3.13: the signal landscape or merit function  $[I(\nu_e) - I(\nu_g)]$  as a function of phase difference and time delay of the shaped double pulse. The maxima (white) correspond to the set of solutions for maximal A state, while the minima (black) to maximal X state. Therefore an “egg carton” like merit function was experimentally realized, that was ideally suited to test the performance of the evolutionary algorithm in the experiment. There is a series of maxima and minima along the cut at 370 fs, 570 fs, 790 fs and 1030 fs alternating with mod  $2\pi$ . Indeed the maxima are most pronounced

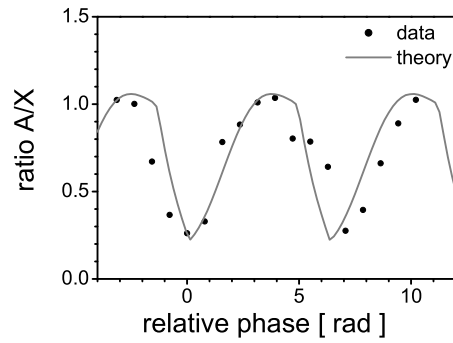


**Figure 3.12:** Ratio of the vibrational contribution of A and X state (A/X) to the transient plotted versus the phase difference in the double pulse sequence.

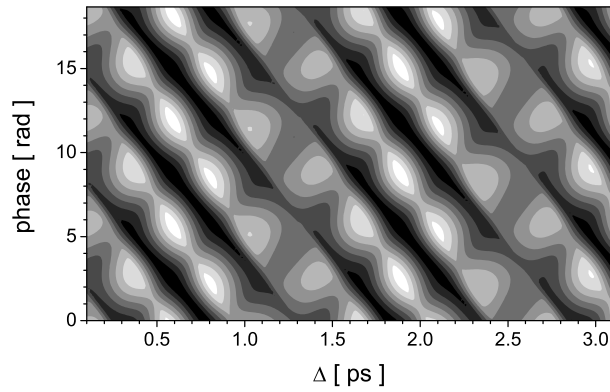


**Figure 3.13:** Merit function of the optimization problem restricted to phase-related double pulses. It was calculated by computing the feedback signal according to Eq. (3.21) for different time separations and delays of the shaped double pulse. Note that the delay  $\Delta$  starts at 0.1 ps, where the tailored double pulse consists of clearly separated subpulses in time.

at 570 fs and 790 fs and seem to be of nearly equal amplitude. At around 2 ps there is again a recurrence of maxima and minima but with slightly lower amplitude. It is interesting to note that the algorithm found the solutions at 540 fs and 740 fs for this double pulse excitation and avoided the shallow minima and maxima around.

### Parameterization in the frequency domain.

The frequency domain is ideally suited to parameterize pulse trains and chirped pulse. In order to find the optimum pulse train and thereby verifying Eq. (3.14) a phase function  $\phi(x) = a \sin(b \cdot x + c)$  with parameters  $a, b, c$  was set onto the mask. If the spectral phase of a femtosecond pulse is modulated by such a periodic pattern, it leads to replication of the incoming Fourier limited pulse at equidistant times forming a pulse train. The parameter  $b$  adjusts the interpulse separation. The algorithm restricted to these 3 parameters should aim for a pulse sequence ideally suited to excite only X state dynamics. It found a pulse shape with an interpulse separation of exactly twice the vibrational period in the ground state, that is 720 fs [see Fig. 3.14]. This however is not the only optimal pulse train solution to

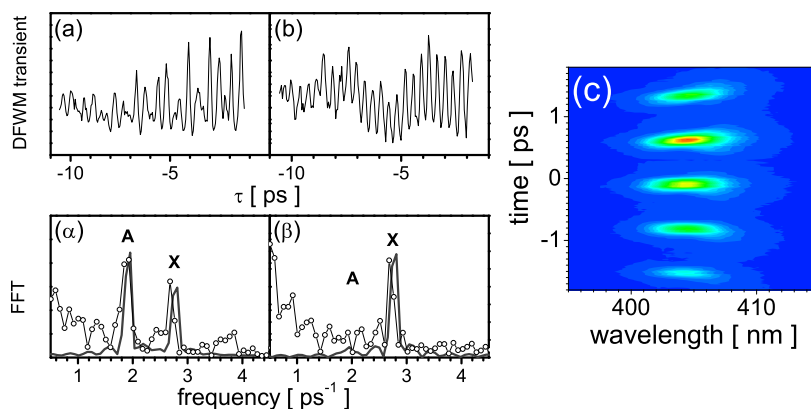


**Figure 3.14:** Transient and FFT before (a),( $\alpha$ ) and after (b),( $\beta$ ) optimization using the  $\phi(x) = a \sin(b \cdot x + c)$  parameterization in the frequency domain. Solid line in ( $\alpha$ ) and ( $\beta$ ) is theoretical model calculation. (c) The FROG trace of the optimal pulse.

the problem as could be verified by adjusting the parameter  $b$  and thereby the interpulse separation to an integer multiple of the upper state (530 fs) - leading to excitation of only A state dynamics [Fig. 3.15 bottom row] - or ground vibrational roundtrip time of 380 fs exciting specifically only X [Fig. 3.15 middle row]. The theoretical results are shown as solid line in this figure. The other interpulse separations predicted by the theoretical model [see Fig. 3.2] were also found to be correct (results not shown).

Finally by investigating the effect of chirp, solutions beyond the multiple pulse DFWM theory could be found. Instead of building the genes for the evolutionary algorithm from individual pixel values, the genes here represent Taylor coefficients ( $a, b, c, d$ ) of a third order polynomial expansion:  $\phi(x) = a(x - d)^3 + b(x - d)^2 + c(x - d)$ . This analytic function is the phase function applied to the SLM and is ideally suited to shape chirped pulses (see section 1.4 and Refs. [61, 76]). The algorithm should find the critical

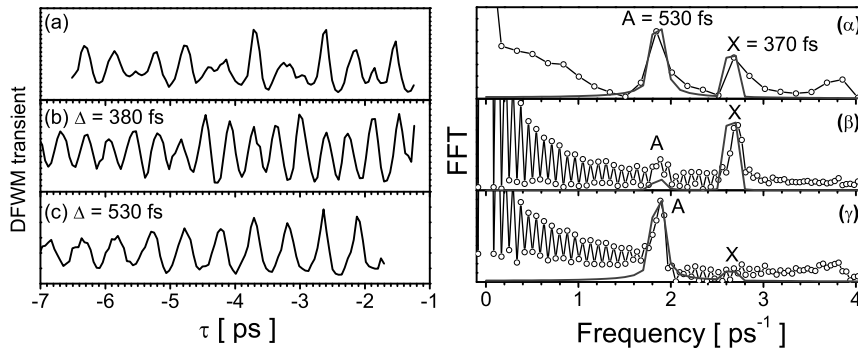


**Figure 3.15:** Pulse trains modulated by spectrally periodic phase functions,  $a \sin(bx + c)$ . The DFWM transient (a)-(c) and its FFT ( $\alpha$ )-( $\gamma$ ) for excitation with a FL pulse, pulse train with  $\Delta = 380$  fs and pulse train with  $\Delta = 530$  fs. Theoretical prediction (solid line, right figures) is accurate.

chirp needed to completely suppress the X state dynamics and it came up with the solution shown in Fig. 3.16. Analysis of the pulse reveals mainly negative quadratic but also some cubic phase. It was experimentally verified that for a positive linear chirp of the same amount leading to the same longer pulse duration no enhancement of A state dynamics could be observed. The tendency that negative chirp enhances the A state contribution in the signal is very well predicted by the theoretical model of the previous section [see Fig. 3.5]. These encouraging results call for a more detailed theoretical study, that will be done in the near future.

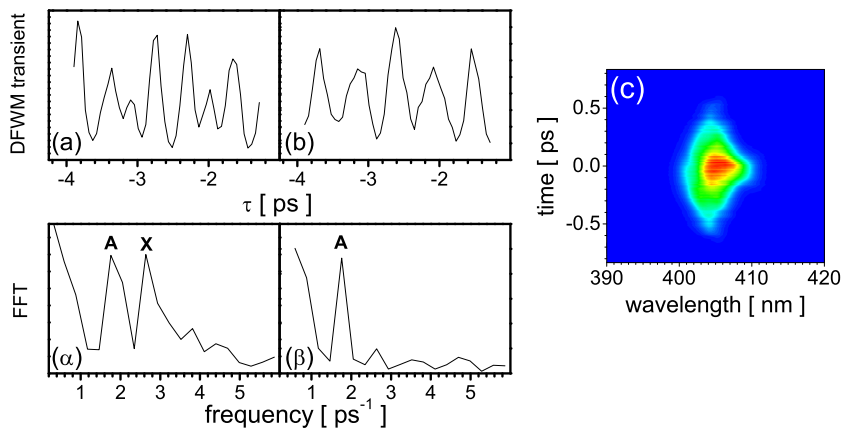


**Figure 3.16:** Transient and FFT before (a),( $\alpha$ ) and after (b),( $\beta$ ) optimization using polynomial parameterization in the frequency domain. (c) The FROG trace of the optimal pulse. The A optimizing pulse has negative linear and quadratic chirp and a pulse duration of about 560 fs.

### 3.4 Using DFWM as an in situ-FROG

Using a fiber optics spectrometer fitted with a linear multichannel CCD detector (Ocean Optics S2000) instead of a photomultiplier, it was possible to analyze the spectrum of the DFWM signal, and all frequency components inherent in the FWM signal were captured at once. Since the excitation pulse consists of a broad and coherent spectrum, a very wide coupling of ro-vibronic levels between ground and excited state is observed with each spectral component of the DFWM signal showing its own vibrational dynamics [90].

The spectrally resolved FWM data does not only consists of a molecular dynamics part, but also provides a cross-correlation measurement of the unshaped pulses with the tailored pulse. This part of the two dimensional dataset is equivalent to a  $\chi^{(3)}$  FROG [102], where the electronic part of the optical response,  $R^{(3)}$ , of the molecule provides  $\chi^{(3)}$ . This signal,  $D(\omega, t)$ , also known as wavelength resolved stimulated photon echo (WRSPE) [103] is described by the following equation:

$$D(\omega, \tau) = \left| \int dt R^{(3)} E^2(t) E(t - \tau) \exp(-i\omega t) \right|^2. \quad (3.22)$$

A FROG retrieval algorithm could be used to calculate from this WRSPE data the electric field of the tailored pulse. However the WRSPE data in itself already reveals some information about the shaped pulse used in DFWM. This is clearly visible in Fig. 3.17 where the spectrally resolved DFWM signal is shown for three differently modulated excitations. From left to right these are: empty mask, negative linear chirp, positive quadratic chirp and a phase related double pulse. For example it is possible to see the amount, the sign and the type of laser pulse chirp in the interaction volume [Fig. 3.17(b) and (c)]. It is interesting that the FWM response of the molecule directly resembles the phase of the exciting pulse. This is due to the fact that the frequencies are emitted in the same order as they are excited. Since the frequency is the first order differential of the phase, the frequency of a pulse with quadratic phase increases linearly, while parabolically for cubic phase. This means that the phase of the pulse is directly transferred to the molecule. Excitation with a tailored double pulse leads to the formation of the clearly separated time bands due to a deep modulation of the DFWM spectrum. The amplitude and phase modulation pattern of the shaped excitation pulse [see Fig. 2.7] coincides with the pattern of the DFWM spectrum [see Fig. 3.17(d)]. The frequency emission pattern of the molecule shifts along the wavelength direction under a variation of the phase accomplished by a shift of the mask pattern, but also the vibrational motion goes over from the excited to the ground state as displaced on the vertical and vice versa (not shown here, but discussed earlier).

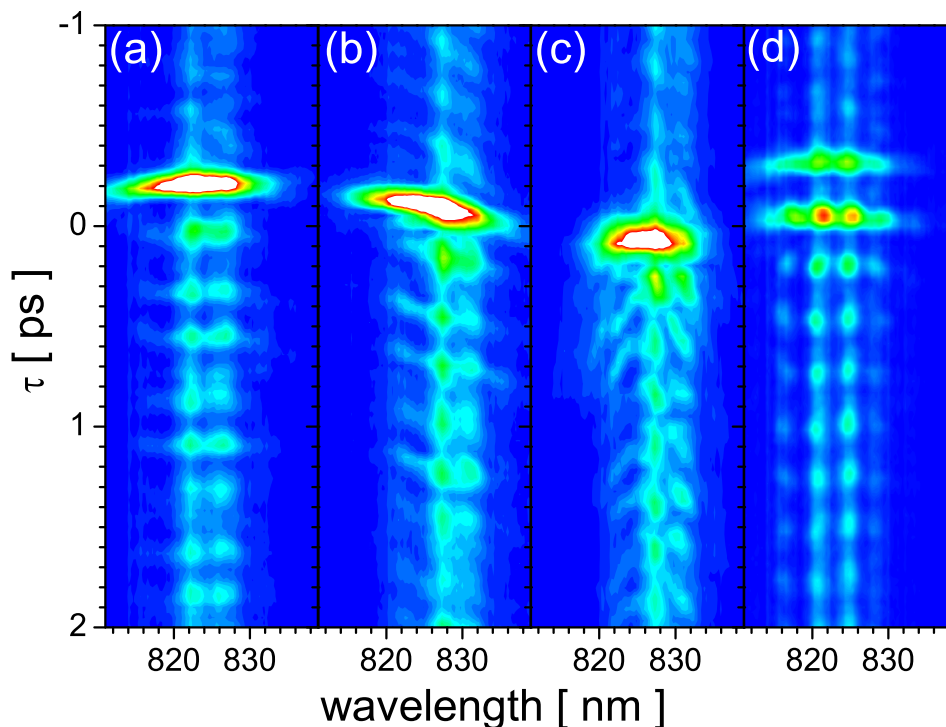


**Figure 3.17:** Spectrally resolved DFWM signal. (a) Unmodulated pulse. (b) negative linear chirp. (c) positive quadratic chirp. (d) phase-related double pulse  $\Delta = 480$  fs and  $\alpha = \pi$ .

### 3.5 Summary and Outlook

In the potassium dimer studies of this chapter, molecular dynamics in both involved electronic states could be studied simultaneously. Especially the ground state dynamics are difficult to access by other means. DFWM also has the advantage to be selective to a very localized region in space; the interaction region of the three involved beams. Therefore volume effects are naturally excluded. In addition, the control scheme of multiple pulse DFWM is not restricted to electronically resonant processes which increases the possibilities to obtain control where resonances are experimentally difficult to access.

The results presented here show, that it is possible to control the DFWM response of the potassium dimer. Especially a learning-loop approach is feasible despite the sophisticated feedback signal if parameterizations are used. The results are in perfect agreement with a theoretical model developed along these lines.

A theoretical analytical model was derived explaining the control of the FWM signal as interference effect outside the molecule. The theory clearly

assumes that each subpulse of the tailored sequence together with the time-coincident pulses generates the same DFWM signal, but time delayed and phase shifted. These identical ejected signals interfere with each other leading to an overall signal with only one dynamics. The molecule hence responds always in the same way to each subpulse and the control occurs outside the molecule, due to an interference of the emitted radiation. Still this analytical theory could not be applied to the case of chirped excitation, and a different model was used based on a numerical perturbative approach. Thereby an enhancement of the A state contribution in the signal with negative chirped could be explained. However a complete vanishing of the X state peak as observed in experiment is still not understood. Future calculations will help clarify this effect.

Moreover it was shown that a wavelength resolved DFWM signal serves as a molecular FROG. This shows that tailored pulses are faithfully delivered into the interaction region. Also different spectral regions of this two-dimensional data correspond to processes of coherent anti-Stokes Raman scattering (CARS), coherent Stokes Raman scattering (CSRS) and DFWM. The small wavelength side corresponds to CARS, the center wavelength portion to DFWM and finally the large wavelength spectral part to CSRS processes [95]. A heterodyne measurement would moreover give full information about the electric field of the DFWM signal [66].

Four-wave mixing experiments especially the recent developments of multidimensional spectroscopies [104–106] are ideal to study complex molecules. The broad featureless line shapes of 1-D spectroscopies are expanded with these higher dimensional methods into a second dimension leading to diagonal and cross peaks revealing the microscopic dynamics. In essence multidimensional spectroscopy is the analog of NMR in the femtosecond regime [107]. From this similarity one can understand, that application of carefully shaped and timed femtosecond pulses can provide a novel multidimensional view of molecular structure as well as vibrational and electronic motions, interactions, and relaxation processes. A combination of pulse shaping with nonlinear spectroscopies as was done in this thesis is therefore a very promising field. Indeed there exist already experiments showing, that this new control method is applicable to microscopy [108,109]. Another perspective of this method is to probe an altered ground state population distribution among the vibrational states, since the FWM signal is composed of the individual vibrational contributions weighted by their respective populations. An altered ground state population of a specific shape can be produced using tailored pulses as will be shown in section 8.1.

## Chapter 4

# Coherent control experiments: Concluding remarks

The control examples of this experimental part have shown, that a learning-loop is a powerful control setup. The prerequisite, that shaped pulses arrive in the interaction zone without important phase or amplitude distortions is fulfilled. This is proven, by the experimental one parameter scans agreeing perfectly with theoretical predictions and also by direct measurements in the interaction region by using DFWM. All control results, that could be compared with a theory have converged to the global optimum, despite the "egg carton" shaped merit functions with many local minima. Evolutionary algorithm seem to be therefore very appropriate. There convergence rate and fidelity depends on the number of control knobs. In all experiments parameterizations were used for this reason, but also to enable control experiments with time consuming feedback signals and to simplify the interpretation of the optimal pulse in the end. Parameterization is a constraint, that is used to incorporate knowledge about a possible control mechanism. In the next part of this thesis the effort will be to unite theoretical methods predicting optimal pulses with experimental constraints. Modifications to the optimal control algorithm are presented, such that finally the calculated pulses can be directly implemented in experiment, so that in principle optimal control pulses beyond parameterized results can be understood.



## Part II

# Coherent control theory



In the first part we have seen that the experimental method to obtain optimized pulses for some aim is to use a learning-loop approach. This approach could also be implemented by a direct mapping of all the elements: pulse shaper, experiment and learning algorithm into theory. However the learning-loop setup converges only after thousands of experiments, a fact that is not important in experiment since the system is able to solve its Hamiltonian in real time. However the theoretical implementation will have to solve the Hamiltonian by a time consuming numerical propagation of the underlying dynamical equations. Therefore it is necessary to develop a new optimization algorithm that needs less number of iterations. This was accomplished independently by D. J. Tannor [29] and H. Rabitz [27] by formulating the problem with variational calculus, being aware of the fact that the future information can be used to speed up performance considerably. Section 5 will explain this optimal control algorithm. The next sections concentrate on trying to link theoretically tailored laser fields for the control of the potassium dimer with experiment, on discovering new control mechanisms and solving two different control aims: state selective transfer and molecular population inversion. In trying to accomplish this task the optimal control algorithm has to be extended in order to provide experimentally realizable pulses. Moreover the needed mask patterns to shape these pulses are calculated.



## Chapter 5

# Essentials: Optimal Control Theory (OCT)

Whereas in experiment optimal pulses are designed by a learning-loop setup, the design in theory is performed with two major computation tools [110, 111]: local [32, 112] and global control [110, 113]. The algorithm used in the global approach is also known as optimal control theory (OCT). Both methods assume the complete knowledge of the system Hamiltonian and essentially use in time propagation to optimize the fields. The important differences to both approaches are:

In local control at every instant of time the control field is chosen to achieve monotonic increase in the desired objective. Two conditions are used at any time step, one to determine the phase of the field and one to determine the amplitude. In order to write down the condition to be fulfilled at all times it is necessary to already know of a mechanism that will effectively drive the initial state to the desired target. In contrast to OCT, which incorporates information on later time dynamics through forward - backward iteration, these methods use only information on the current state of the system. OCT is a much more versatile computational tool, since it needs only information on the initial and target state. The algorithm uses both of this information in future and past to find the optimal field, that connects both states. The field is not constraint to any condition and therefore the algorithm itself will discover the most suitable pathway. It therefore includes all the solutions of local control as a subset. In rare cases, since convergence to the global optimum is not proven for OCT, it may be outperformed by local control. A direct comparison of the two methods is presented in Ref. [111]. In the following section variants of global control will be explained.

## 5.1 Global control as a variational problem

The task of finding an optimal laser field for a given objective is solved by the mathematical framework of control theory [114]. Here it is assumed, that the system is characterized either classically by momentum and location or quantum-mechanically by its wave function or density matrix and obeys a dynamical equation. The evolution depends not only on the initial state, but also in a deterministic way on a time dependent external control variable, in our case the laser field. Moreover an additional constraining function is considered, that limits the control to certain boundaries or forbids system trajectories, that do not obey the equations of motion. The task is now to find the control field that will steer the system from its initial state as close as possible to its final state in a specified time  $T$ . Control theory states that in order to solve this problem a functional incorporating the objective and the constraining function must be defined with the help of a Lagrange multiplier. This functional is then to be maximized. That is done by setting its functional derivative equal to zero. The functional derivative is calculated by variation with respect to the parameters of the functional, being continuous functions over the optimization interval. The obtained optimal control equations typically have the structure of three coupled differential equations: one for the wave function, one for the Lagrange multiplier, each with certain boundary conditions and finally, an equation for the optimal field, which in turn is expressed in terms of the wave function and the Lagrange multiplier. These are the general remarks and now a detailed derivation follows.

Variational calculus can be used to find an extremum of any function  $f(x)$  constraint by an equation  $G(x) = 0$ . The extremum is then found by calculating  $J'_\lambda(x)$ , where  $J_\lambda(x) = f(x) - \lambda G(x)$  and  $\lambda$  is the real valued Lagrange multiplier. In the case of optimal control theory  $G(x)$  is complex function. Variational calculus can be easily extended to cope with this complication. The functional expressed using only real functions is then  $J_{\lambda_1, \lambda_2} = f(x) - \lambda_1 G_r(x) - \lambda_2 G_i(x)$ . Here  $G_r$  and  $G_i$  are the real and imaginary parts of  $G$ . Using the relationship

$$\begin{aligned} \lambda_1 G_r + \lambda_2 G_i &= \frac{\lambda_1}{2}(G + G^*) + \frac{\lambda_2}{2i}(G - G^*) \\ &= (\lambda_1 - i\lambda_2)G + (\lambda_1 + i\lambda_2)G^* \end{aligned} \quad (5.1)$$

$$\lambda_1 G_r + \lambda_2 G_i = \operatorname{Re}(\lambda G) \quad (5.2)$$

where  $\lambda = \lambda_1 - i\lambda_2$  is now a complex Lagrange multiplier. This allows to write the variational problem simply as

$$J_\lambda = f(x) - \operatorname{Re}(\lambda G) \quad (5.3)$$

$$J'_\lambda(x) = 0 \quad (5.4)$$

$$G(x) = 0 \quad (5.5)$$

Moreover it is important to match the variation at the boundaries to the boundary values supplied. Now this variational approach can be specialized for optimal control theory [27–29, 115] using explicit expressions for  $G$  and  $f$

$$f(\psi(t), \varepsilon(t)) = |A|^2 - \alpha \int_0^T dt \frac{|\varepsilon(t)|^2}{s(t)}. \quad (5.6)$$

Optimization is performed only within a time interval  $[0, T]$ . The functional  $f$  is composed of two summands. The first specifies the yield, that is the overlap with the target state  $\psi_f$  or the expectation value of an hermitian operator  $X$ , depending how the control aim is most favorably expressed. The target state description could for example be used to optimize for a specially shaped wave packet, while it is better to use an operator to e.g. aim for wave packet focusing without specifying the specific shape of the target wave function. In the following the OCT will be termed differently depending on the form of  $A$ : if  $A = \langle \psi_f | \psi(T) \rangle$  it will be called *wave function OCT* [27] and if  $A = \langle \lambda(T) | X | \psi(T) \rangle$  *operator OCT* [35, 116, 117].

The second term in  $J$  penalizes the electric field fluence. The weight factor  $\alpha$ , also known as penalty factor, allows for flexibility in choosing the relative importance of the physical objective and the fluence. The shape function  $s(t)$  was first introduced into OCT by Ref. [115] and is used to avoid abruptly changing fields and set a minimum for the pulse bandwidth. Especially  $s(t)$  is a function of smooth switch on and off behavior imprinting this property on the optimized field. The maximization of  $f$  is constrained by the dynamical equation for  $\psi$ , which in the case of wave functions is the Schrödinger equation.

$$G = i\partial_t \psi(t) - [H_0 - \mu\varepsilon(t)] \psi(t), \quad \psi(t=0) = \psi_i. \quad (5.7)$$

Other dynamical equations will be treated in chapter 11 of this thesis. The unconstrained objective functional  $J_\lambda$  can be formed according to Eq. (5.3) by employing a complex valued Lagrange multiplier function  $\lambda(t)$

$$J_\lambda = f - 2\text{Re} \left[ A \int_0^T dt \langle \lambda(t) | \left[ i(H_0 - \mu\varepsilon(t)) + \frac{\partial}{\partial t} \right] | \psi(t) \rangle \right]. \quad (5.8)$$

At an extremum of the objective functional  $J$  the condition  $\delta J_\lambda = 0$  is satisfied. The prefactor  $A$  is necessary to obtain separable differential equations after variation. The prefactor could be omitted when  $A$  is used as target in the functional instead of  $|A|^2$ .<sup>1)</sup> The Lagrange multiplier  $\lambda(t)$  is chosen

<sup>1)</sup>However the numerical iteration works perfectly without this prefactor.

such that the variation of  $J_\lambda$  with respect to  $\psi$  is zero, i.e.,  $\partial J_\lambda / \partial \psi = 0$  [see Eq. (5.4)]. This leads to the following differential equation

$$i\partial_t \lambda(t) = [H_0 - \mu \varepsilon(t)] \lambda(t), \quad \lambda(t = T) = \psi_f. \quad (5.9)$$

$\psi_f$  is the boundary condition for  $\psi$  at  $t=T$  for wave function OCT, while for operator OCT no such boundary exists, and  $\psi_f = X\psi(T)/|X\psi(T)|$ . Performing the variation with respect to the electric field  $\varepsilon(t)$ , the subsequent differential equation is obtained

$$\frac{\alpha}{s(t)} \varepsilon(t) + \text{Im} \{ \langle \psi(t) | \lambda(t) \rangle \langle \lambda(t) | \mu | \psi(t) \rangle \} = 0. \quad (5.10)$$

Eqs. (5.7), (5.9) and (5.10) are coupled through the electric field. Three different schemes were proposed to solve this coupled set of three equations with boundary conditions at final and initial time. Their difference lies merely in the way Eq. (5.10) is used.

**Gradient-type. Open form iteration scheme.** Here Eq. (5.10) is taken as the gradient of  $J_\lambda$  with respect to  $\varepsilon(t)$  [31, 34, 118, 119]

$$\frac{\delta J_\lambda}{\delta \varepsilon(t)} = \frac{\alpha}{s(t)} \varepsilon(t) + \text{Im} \{ \langle \psi(t) | \lambda(t) \rangle \langle \lambda(t) | \mu | \psi(t) \rangle \}, \quad (5.11)$$

and is used in a steepest-descent procedure to optimize  $\varepsilon(t)$ . The iterative scheme for calculating the optimal field is as follows:

1. Establish the initial state vector  $\psi(0) = \psi_i$ , and an initial guessed field  $\varepsilon^{k=0}(t)$ .
2. Propagate  $\psi(0)$  forward to final time  $T$ , simultaneously calculating the objective  $f$  [Eq. (5.6)].
3. Propagate backwards  $\lambda(T) = \psi_f$  (or  $\lambda(T) = X\psi(T)/|X\psi(T)|$  for operator OCT) to time  $t = 0$  using Eq. (5.9). Simultaneously propagate backwards  $\psi(T)$  as well [or if possible use the stored values from the forward propagation Eq. (5.7)]. During these reverse propagations use again the field  $\varepsilon^{k=0}(t)$  and calculate the gradient  $\delta J_\lambda / \delta \varepsilon(t)$  for all  $t$  using Eq. (5.11).
4. The new field is

$$\varepsilon^{k+1} = \varepsilon^k - \beta \frac{\delta J_\lambda}{\delta \varepsilon(t)}, \quad (5.12)$$

where  $\beta$  is a positive constant determined by a search procedure that minimizes  $f^{k+1} = f[\varepsilon_\beta^{k+1}(t)]$ .

5. Repeat step 2 - 4 until  $f^{k+1}$  converges to a maximum.

Into this gradient-type approach experimental constraints can be most easily implemented, just by modifying the gradient. A very common situation in coherent control is to parameterize the field  $\epsilon(c_i, t)$  (see section 1.2). The gradient can be easily adapted to this case by calculating the derivative with respect to the parameters

$$\frac{\delta J_\lambda}{\delta c_i} = \int_0^T dt' \left[ \frac{\alpha}{s(t')} + \text{Im} \{ \langle \psi(t') | \lambda(t') \rangle \langle \lambda(t') | \mu | \psi(t') \rangle \} \right] \frac{\delta \epsilon(t')}{\delta c_i}, \quad (5.13)$$

and use them in the gradient approach [118, 119]. However this approach has one central disadvantage linked to the use of a gradient. The method is prone to get stuck in the local minima of search space and the convergence rate is rather slow. This is the reason why a global iterative procedure was developed, termed Krotov method [114, 120, 121]. This scheme uses an immediate feedback and converges quadratically [27].

**Krotov or closed iteration schemes.** This method implements an iteration scheme differing from the one presented before in unifying step (3) and (4) into one single step. Instead of propagating  $\lambda(T)$  with  $\epsilon^k(t)$  backwards all time steps until  $t=0$ ;  $\lambda(T)$  is now propagated back with the improved field  $\epsilon^{k+1}(t)$ . In order to do so the new field is calculated at each time step using as immediate feedback the equation obtained by variation with respect to the field

$$\epsilon^{k+1} = \frac{s(t)}{\alpha} \text{Im} \{ \langle \psi(t) | \lambda(t) \rangle \langle \lambda(t) | \mu | \psi(t) \rangle \}. \quad (5.14)$$

The iteration scheme has to proceed then in a stepwise manner:  $\lambda(T)$  is propagated to  $\lambda(T - dt)$  by the field  $\epsilon^{k+1}$  using Eq. (5.14) evaluated at  $T$ , then back again one step with  $\epsilon^{k+1}$  computed using  $\psi$  and  $\lambda$  at  $T - dt$  and so on until initial time. The wave function  $\psi(t)$  however is propagated back as in the gradient iteration scheme using the old field  $\epsilon^k$ . This iterative procedure is pictured in Fig. 5.1.

It is also possible to use instead of Eq. (5.14) the following one

$$\epsilon^{k+1} = \epsilon^k + \frac{s(t)}{\alpha} \text{Im} \{ \langle \psi(t) | \lambda(t) \rangle \langle \lambda(t) | \mu | \psi(t) \rangle \}, \quad (5.15)$$

that is the overlap term is not directly equal to the new field, but is only used as correction to the field from the previous iteration. This method will be termed modified Krotov in the following. It is known to reach a higher maximum for the objective than Eq. (5.14). It is important to say that in this rapidly convergent scheme it is impossible to parameterize the field. Instead the electric field is changed freely at each point of time by the algorithm as it proceeds.

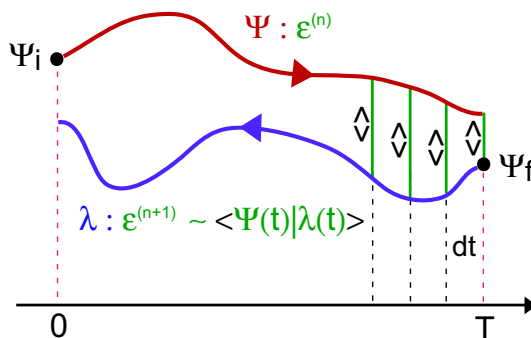


**Figure 5.1:** Schematic of the numerical iterative procedure used to solve the coupled system of equations obtained from the variation of the functional. The boundary conditions are the wave functions at initial time  $\psi_i$  and final time  $\psi_f$ . One iteration consists of a forward in time propagation of  $\psi$  with the field  $\epsilon^{(n)}$  of the previous iteration  $n$  until final time. Followed by the backward propagation of the Lagrange multiplier  $\lambda$  from final time using the new field  $\epsilon^{(n+1)}$ , that obtains a new value at each time step using essentially the overlap of  $\psi$  and  $\lambda$  [Eq. (5.14)].

## 5.2 Propagators for the dynamical equation

Central to all the presented optimal control algorithms is of course the solution of the time dependent dynamical equation. The time dependent Schrödinger equation is a first order differential equation. Therefore in principle all numerical tools solving these could be simply applied, such as adaptive Runge-Kutta or predictor-corrector schemes. Over the years however much more efficient and meanwhile widely used methods have been developed [122–124]. Some of the advantages are that they allow accurate control over the propagation error, make a balanced overall treatment possible by using the Fourier representation [125] and normally conserve some physical quantity. The following discussion is not an excessively detailed one, however profound enough to explain the merits and generality of the Chebychev expansion scheme especially with respect to its use in the OCT algorithm by comparing it with other two popular schemes: second-order-differencing (SOD) and split-operator (SPO).

**Second order scheme (SOD).** The explicit second order scheme is  $\psi(t + \Delta t) \approx \psi(t - \Delta t) - 2i\Delta t H \psi(t)$ . If the Hamiltonian is Hermitian, the SOD propagation scheme preserves norm calculated as  $\langle \psi(t - \Delta t) | \psi(t) \rangle = \langle \psi(t) | \psi(t - \Delta t) \rangle = \text{const}$  and energy  $\langle \psi(t - \Delta t) | H | \psi(t) \rangle = \text{const}$ . The exact form of energy and norm conservation (e.g.  $\langle \psi(t) | \psi(t) \rangle$ ), can be used to monitor the calculated error, since neither of these values is strictly conserved. The non-conservation of the real quantities leads to ambiguities in how to calculate the overlap between  $\lambda$  and  $\psi$  in Eq. (5.10). Various possibili-

ties exist, e.g.  $\langle \psi(t) | \lambda(t - \Delta t) \rangle$ ,  $\langle \psi(t - \Delta t) | \lambda(t) \rangle$  and all other combinations, but all of them lead to more than exponential explosion of the norm in the OCT scheme for values of the penalty factor below some threshold. That means while the mere SOD propagation scheme has still no problem with the intensity of the field, the SOD OCT will not be able to use that field as initial guess.

Therefore other propagation methods must be used in optimal control theory. The following two methods exploit the closed form expression of the Schrödinger equation propagator  $U = \exp[iH(t)dt]$  and are superior.

**Split Operator Method (SPO).** Since the Hamiltonian is the addition of the kinetic and potential part ( $H = T + V(\epsilon)$ ) the propagator can be written approximately as  $U \approx \exp(-\frac{i}{2}Tdt) \exp(iV(\epsilon)dt) \exp(-\frac{i}{2}Tdt) + O(\Delta t^3)$ . The potential part includes the interaction with the laser field. It is therefore non-diagonal. If the diagonal matrix of the  $V$  is called  $D$  and  $Z$  is the matrix of eigenvectors, then the split-operator scheme is simply  $U \approx \exp(-\frac{i}{2}Tdt) Z \exp(iDdt) Z^t \exp(-\frac{i}{2}Tdt) + O(\Delta t^3)$ . The algorithm can not handle operators that mix spatial coordinates and momenta. The scheme does not conserve energy. The error can only be controlled by choosing a smaller time step.

**Chebyshev Scheme (CH) [126].** CH is a global propagator, since in case the problem is time independent sometimes a *single* time step completes the calculation. This does not mean that it is not suited for time dependent problems, on contrary it is one of the most accurate propagation schemes to date. The main idea behind global propagators is to use a polynomial expansion of the exponential in the evolution operator  $U \approx \sum_{n=0}^N a_n P_n(-iHt)$ . The problem then becomes the choice of the optimal polynomial approximation. It is known that the complex Chebyshev polynomials optimally approximate the evolution operator [122, 126]. In practical implementation, the maximum order  $N$  can be chosen such that the accuracy is dominated by the accuracy of the computer. There is no need to use a smaller time step. The method is not unitary but due to its extreme accuracy the deviation from unitarity can be used as accuracy check. The time reverse propagation is done by simply changing the sign of the expansion coefficients. The method can work with any functional form of the Hamiltonian operator provided an estimate of the eigenvalue range can be made. If this range is underestimated it becomes unstable. There exist a generalization to this scheme, that is capable of propagating nonlinear Schrödinger equations [127].

Finally the performance of the propagation schemes depends critically on the basis set the time-dependent Hamiltonian is expanded in. This can be eigenstates of the field free Hamiltonian, statistical wave functions to

treat ensemble problems most efficiently [128] or the coordinate and momentum space [124,125]. Especially the last basis set is the most promising, since the key operation used, the Fourier transform can be implemented as parallel code on many processors [129]. Moreover a nonlinear mapping of the coordinate space can be used to efficiently support highly bound states reaching far out to interatomic distances above 50 a.u. [130]. Also repulsive potentials and conical intersection [131] can be treated.

The propagators for the Liouville equation with dissipation and the Gross-Pitaevskii equation will be discussed in the corresponding chapters 10 and 11, respectively.

## Chapter 6

# The system and the transfers under study

The aim of the following theoretical chapters is to modify optimal control theory in order to find experimentally realizable pulses. Realizability concerns the complexity of the pulse shape, the intensity and the spectral bandwidth which must be within the current state of the art capabilities. In order to perform realistic calculations the potassium dimer is chosen as a prototype system. This dimer is well characterized experimentally and the potentials and dipole transition moments are accurately known. Since the experimentally used laser pulses centered around 820 nm excite initial ground state population mainly into the first excited ( $A\ ^1\Sigma_u$ ) and through multiphoton-excitation into other resonant electronic potentials ( $2\ ^1\Pi_g$ ,  $4\ ^1\Sigma_g$  and the ion channel) these potentials were taken into account in the theoretical model [see Fig. 6.1]. Due to this provision multi-photon processes are naturally accounted for during optimization. For reasons of simplicity these surfaces will be termed X,A,2,4,ion. In the following the wave function  $|\psi\rangle$  is represented as a vector in the electronic components (X,A,2,4). The coupling of the ion is much too weak to play any role in the studied control processes. The Schrödinger equation can be either cast into space or eigenfunction representation. In the most simplistic description only the bond length  $r$  of the molecule is included in the dynamics. In this case the Schrödinger equation is

$$i\partial_t\langle\mathbf{x}|\psi\rangle = \frac{-\hbar^2}{2m_{red}} \{ \partial_r^2 + \langle\mathbf{x}|V|\mathbf{x}\rangle \} \langle\mathbf{x}|\psi\rangle + \langle\mathbf{x}|V_{int}(\epsilon)|\mathbf{x}\rangle\langle\mathbf{x}|\psi\rangle, \quad (6.1)$$

with the interaction potential

$$\begin{aligned} \langle\mathbf{x}|V_{int}(\epsilon)|\mathbf{x}\rangle &= \epsilon(t) \{ |X\rangle\langle A|\mu_{XA}(x) + |A\rangle\langle 2|\mu_{A2}(x) \\ &+ |A\rangle\langle 4|\mu_{A4}(x) + c.c. \}. \end{aligned} \quad (6.2)$$

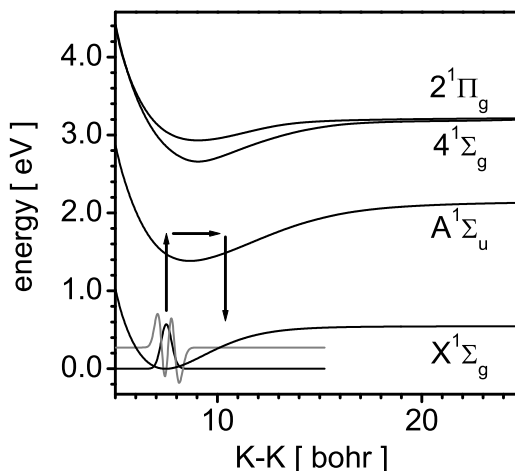


**Figure 6.1:** The potential surfaces of the potassium dimer taken into account in the calculations. The coupling to the ion is so weak, that it plays no role. All the potentials depicted here are resonant to the center frequency of the exciting laser.

Here the partial derivatives  $\frac{\partial}{\partial i}$  are written as  $\partial_i$  for convenience. The reduced mass for the system is  $m_{red} = 35804.977$  a.u. The dipole moments  $r$ -dependence must be taken into account [132] since transfers can occur at different interatomic separations, e.g. the inner or outer turning point. The potentials  $V$  represent the electronic surfaces X,A,2,4 considered and are discretized on a regular grid of  $dx = 0.02$  a.u. with 512 points. The interatomic distances ranging from 5.0 to 15.22 a.u. suffice to support the vibrational bound states populated during the interaction of the system with the laser field. The ionic state can be safely ignored since the intensities allowed in the optimization are not sufficient to ionize  $K_2$ . The time step was chosen to be 6.0 a.u.

More specifically two different transfers in the  $K_2$  molecule are optimized using ultrashort laser pulses: state selective transfer (in the following abbreviated by SST) [115] between two eigenstates of the ground electronic potential ( $X^1\Sigma_g$ ) and population inversion (in the following abbreviated by PI). Since the potassium dimer is a homonuclear molecule the direct light induced transfer between two eigenstates of the same electronic potential is forbidden. In order to connect these initial and final eigenstates the transfer has to take a detour that includes a potential surface with different electronic structure. The interest in SST lies in the fact that a broadband pulse normally creates a superposition of eigenstates. A suitably induced Raman-pumping between the wave packets evolving on the surfaces during the optimal pulse however must be capable of focusing the population again into a single target eigenstate at final time. Due to the ultrafast timescale of this transfer dissipation effects are negligible. Therefore and due to its near

unit transfer efficiency it is a real alternative to stimulated Raman scattering involving adiabatic passage (STIRAP).

In the PI calculations the aim is to transfer ground state population either concentrated in a single vibrational state, resembling the conditions in a cold-molecular beam, or in a thermal distribution of eigenstates, as occurs in a heat pipe oven, to A  $^1\Sigma_u$  [42]. It is then possible to characterize the difference between pulses producing real population transfer into the A state and those of chapter 3 controlling the A state contribution in the four-wave mixing signal. The calculations for SST and PI are presented in chapter 8.



## Chapter 7

# Experimentally realizable laser pulses

The aim of this chapter is to define an interface between optimal control theory and experiment that characterizes whether a calculated pulse is also applicable in experiment. Since the Hamiltonian is normally only an approximation to reality these theoretical pulses will not have the same degree of control in experiment as they have in theory. However the hope is, that they can provide a feedback-signal above the experimental noise level in order to start the learning-loop approach. This link between theory and experiment is especially important for problems, where the control is difficult to achieve without a good starting point, to check the theoretical model and to understand the mechanism.

Experimentally, pulses with nearly arbitrary time-frequency behavior can be tailored using pulse shaping techniques. In view of the direct implementation to experiment the pulse shaper constraint should be included in optimal control theory. In this case the calculated pulse will always be within the experimental possibilities. The standard functional has no provisions in this respect and therefore it is not surprising that it is left partly to chance whether an optimal pulse is realizable or not. The exact reason for pulse complexity will be explained in detail in section 7.2. In the following different possibilities to include pulse shaping into OCT using gradient methods are suggested. These proposition will not be further pursued in this thesis due to the local and therefore inferior search of gradient type methods. In addition these methods were already proposed in literature and are adapted here only to the pulse shaping situation.

- **Pulse shaping constraint in the time-domain.** A pulse modulated by a pixelated Spatial Light Modulator is expressible as a sum of incident Fourier limited pulses with variable phases  $\phi_n$  and amplitudes  $a_n$  (see section 7.2). It is then possible to use simply the gradient OCT

scheme (see section 5.1), that allows for fields of a certain functional form and use the set  $(a_n, \phi_n)$  as parameters.

- **Pulse shaping constraint in the frequency-domain.** The frequency domain picture of pulse shaping has the advantage to be the most general. Not only a pixelated SLM can be considered but any kind of 4f-setup pulse shaper. A functional building in this constraint has the form

$$J_{new} = J + \int d\omega \{ \epsilon(\omega) - M(\omega)\epsilon_{FL}(\omega) \}^2. \quad (7.1)$$

This again would lead to open form iterative equations known as the gradient-filtering procedure first introduced by Gross et al. [31]. The variation of the functional with respect to the electric field

$$\frac{\partial J}{\partial \epsilon(t)} = -2\text{Im} \left\{ \langle \lambda(t) | \frac{\partial H}{\partial \epsilon(t)} | \psi(t) \rangle \right\} \quad (7.2)$$

$$(7.3)$$

is filtered spectrally using the relation

$$\frac{\partial J}{\partial \epsilon(t)}_{filter} = \int d\omega \text{FFT} \left\{ \frac{\partial J}{\partial \epsilon(t)} \right\} M(\omega) e^{i\omega t} \quad (7.4)$$

and only then applied in the Krotov equation to calculate the improved electric field

$$\epsilon^{(k+1)} = \epsilon^{(k)} - \frac{\partial J}{\partial \epsilon(t)}_{filter}. \quad (7.5)$$

This restricts the optimal field to the frequencies impinging on the mask  $M(\omega)$ . However this approach cannot be used in the closed form iteration scheme since this would require to build the improved electric field at each time step and immediately use it to propagate  $\lambda$  a time step further (see section 5.1). This means that the gradient  $\frac{\partial J}{\partial \epsilon(t)}$  only exist at every point of time but never in the whole interval  $[0, T]$ . A necessary condition for its Fourier transform to exist and indispensable to evaluate Eq. (7.5).

The above approaches always lead to schemes applying gradient type methods of optimization. Since these are inferior to the global search capabilities of the closed form equations of OCT, in the following sections methods are presented, that constrain the pulse spectrum and reduce pulse complexity compatible with the closed and therefore global and rapidly convergent iteration scheme.

## 7.1 The definition of a realizable laser pulse

An experimentally realizable pulse is best defined by the mask pattern needed to shape it. If this pattern has no complex features and does not extend over a too broad spectral range it will be possible to load this pattern directly onto the shaping device. Therefore the mask pattern is the direct interface between coherent control theory and experiments. The algorithm to extract the mask pattern proceeds as follows.

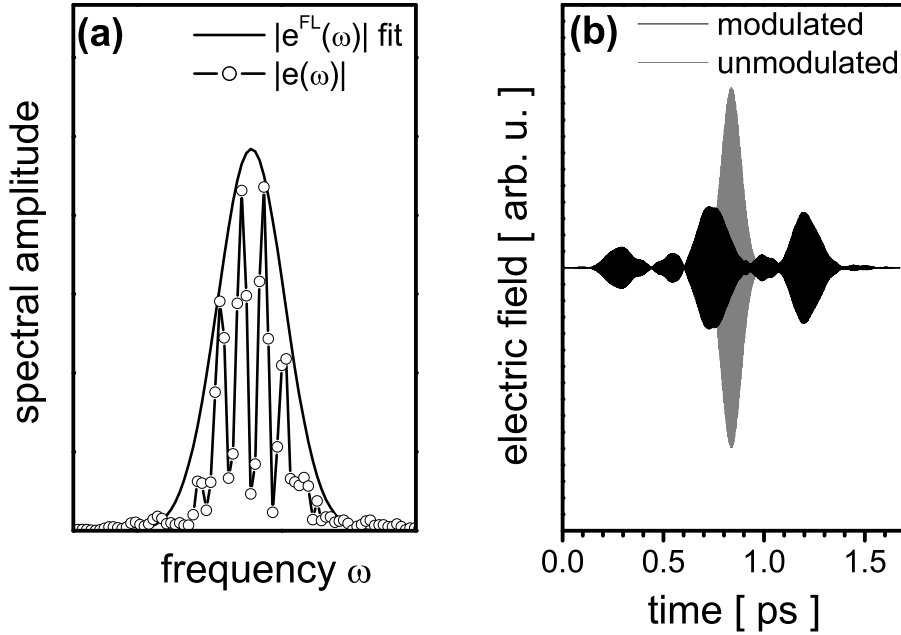


**Figure 7.1:** Schematic of the mask extraction algorithm. (a) The spectrum of the tailored pulse is tightly fitted by a Gaussian. The mask is calculated by dividing the tailored by the fitted spectrum. (b) As a result the unmodulated pulse (gray line) is obtained from the modulated one (black line).

1. The real optimized pulse defined on the interval  $[0, T]$  with time steps  $dt$  is Fourier transformed to obtain its spectrum.
2. The spectrum is complex and fulfills the condition  $\epsilon(\omega) = -\epsilon^*(-\omega)$  since  $\epsilon(t)$  is real and has two maxima centered around  $\pm\omega_0$  [termed  $\epsilon^\pm(\omega)$ ] the center frequency of the laser pulse. Time and frequency discretization are connected through the relation  $d\omega = 2\pi/(Ndt)$  where  $N$  is the number of discrete points.
3. The properties of pulse shaping are essential to this step. The spectral part  $\epsilon^+(\omega)$  centered around  $+\omega_0$  is taken and fitted with a Gaussian spectrum with no phase modulation  $\epsilon_{in}(\omega) = \text{gauss}(\omega - \omega_0)$ . This fit

shall represent the spectrum of a bandwidth limited pulse, which in normal operation is incident to the pulse shaping device. No extra frequencies are generated during pulse shaping since this device can only attenuate and retard spectral components. Therefore the fit must not be of smaller bandwidth than  $\epsilon^+(\omega)$ . It should also not be chosen much broader since the number of needed pixels would increase unnecessarily. This is due to the fact that the pixelated mask in order to work correctly has to extend over the range of significant amplitude  $[\omega_0 - \Delta\omega_{in}, \omega_0 + \Delta\omega_{in}]$  of the incident spectrum. Therefore a direct connection between incident spectral width ( $\Delta\omega_{in}$ ) and the number of pixels exists:  $\#pixel = 2\Delta\omega_{in}/d\omega$ . In conclusion the fit is chosen to closely encompass  $\epsilon^+(\omega)$  [see Fig. 7.1(a)]. The width of the Gaussian allows one to compute the time duration of the incident pulse using the time-bandwidth product and the Fourier limited field is obtained by a Fourier transformation of the Gaussian [see Fig. 7.1(b)].

4. The mask pattern consisting of a transmission and phase modulation is finally calculated according to

$$M(\omega) = \epsilon^+(\omega)/\epsilon_{in}(\omega). \quad (7.6)$$

$M(\omega)$  is then a complex function  $M_n = T_n \exp(i\phi_n)$ , where  $n$  is the pixel index. The transmission pattern is accordingly  $T_n$  coerced into the range  $[0,1]$  and the phase is  $\phi_n$ . The frequency bandwidth seen by each pixel is  $d\omega$ .

This algorithm can now be applied to optimal control pulses to calculate the needed shaping pattern and supplies a decision criterion for the realizability of the pulse. Normally due to the required amplitude modulation, the Fourier limited pulse will be shorter and of higher intensity, usually by a factor of five [see Fig. 7.1(b)]. As an example we take a typical control pulse obtained through optimization with the standard functional (section 5.1). In this case it is a pulse optimizing the  $v''=0$  to  $v''=3$  transfer in  $X^1\Sigma_g$  via the first excited state with a yield of 96%. Performing a 5 fs short-time Fourier transform (STFT) of the pulse Fig. 7.2(a) is obtained. The resulting optimal mask is shown in Fig. 7.2(b). It exhibits a very complicated structure, requires a high number of pixels and an incident FL pulse with a duration of about 6 fs. These modulated pulses are hardly realizable with state of the art technology and are therefore not suited for comparison between experiment and theory. Nevertheless, by calculating the mask pattern the connection between theory and experiment on optimal control is established and the gap between them is disclosed. The next chapters describe methods that simplify the pulse structure.

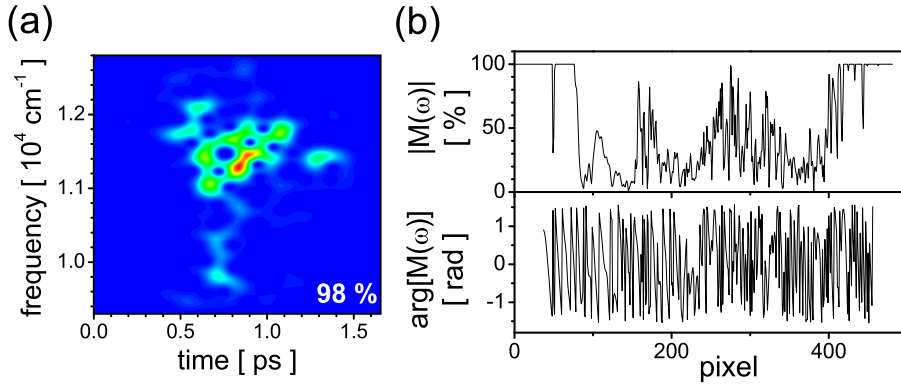


**Figure 7.2:** (a) STFT of the pulse optimizing the  $v''=0$  to  $v''=3$  transfer in  $X^1\Sigma_g$  via  $A^1\Sigma_u$ . (b) The required mask pattern to tailor the pulse in (a). Here  $|M(\omega)|$  denotes the transmission and  $\arg[M(\omega)]$  the phase of the mask pattern.

## 7.2 The role of the penalty factor

The idea of this chapter is to find a way of finding robust and simple optimal fields. As described in the introduction to chapter 7 and Ref. [133] this can be done by using local control and changing the functional, parameterizing the fields and using a e.g. gradient scheme or genetic algorithm to do the optimization task. Here it is shown that it can be accomplished directly within the rapidly convergent algorithm. The advantages of doing so are multiple: the convergence is fast and the optimization is unconstrained and global.

The penalty factor  $\alpha$  is introduced in the OCT functional to regulate the pulse intensity of the optimized field. It is also suited to reduce the pulse complexity as a rather abstract following discussion will explain.

The central points: dependence of the threshold value for  $\alpha$  on the initial guess and the important correlation between high thresholds and robust optimal pulses are illustrated by performing OCT calculations on the potassium dimer (described in chapter 6). In all optimizations presented, the shape function was set to  $s(t) = \sin(\pi t/T)$  with  $T = 1.6$  ps. Figure 7.3 shows the spectra of pulses optimizing the  $v''=0$  to  $v''=3$  transfer via the first excited state all with a yield above 90%, for different  $\alpha$  values. The dependence of the optimized pulse on this penalty factor will be discussed in the following.

First it is reasonable to assume, that multiple pathways exist connecting the initial with the target state of the system and moreover that these pathways are not all equivalent. The equivalence statement is central to this argumentation and means that each pathway has a different activation threshold, i.e. there exist pathways that can be excited with rather

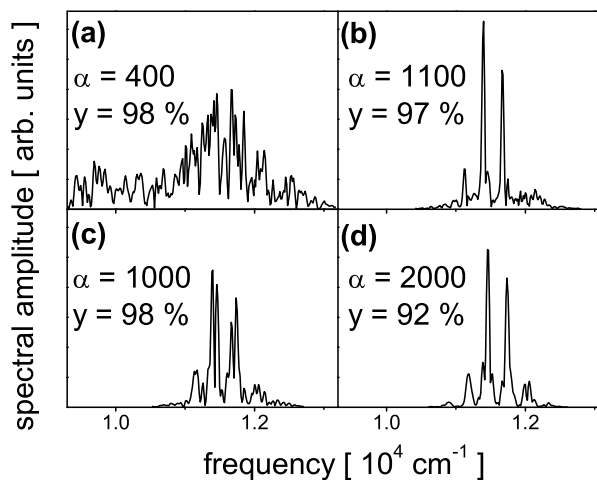


**Figure 7.3:** Optimization results with maximum penalty factor, starting from different initial guess pulses. 1.6 ps at  $10\,974\text{ cm}^{-1}$ . (b) 1.6 ps at  $11\,698\text{ cm}^{-1}$  (c) Broadband addition fo 3-fs pulses. (d) Second run with optimized field from (a) as initial guess.

low pulse intensities, such as resonant one-photon processes and other that deserve much higher pulse intensities due to perhaps their non-resonant or multiphoton character. Moreover the equivalence statement means that not all transitions contribute equally much to the yield, i.e. there may be some pathways that are so effective in connecting the initial with the target state that no other pathway has to be excited and perfect control is achieved. Of course each pathway consists of a number of transitions and therefore requires that the excitation pulse has frequencies matching these transitions. It logically follows that a low value for the penalty factor leads to complex optimal pulses since the allowed intensity is sufficient to excite many pathways each differing in its transition frequencies consequently leading to broad excitation spectra. On the contrary if the penalty factor is chosen very high the field intensity can be only very modest, and the optimal pulse can only spent a limited amount of energy in building up just the frequencies, that excite the very few yield promoting transitions with low activation energy. As a result the optimal field will be very simple and the yield as high as for the low  $\alpha$  case. From that one could easily conclude that it is very simple to obtain a realizable and simple pulse, the optimization only has to be performed with high  $\alpha$ . But in order to do so the initial guess has to be nearly perfect (i.e. has to have already a high yield) as the maximal value for  $\alpha$  depends strongly on the performance of the initial guess. The following argumentation should make this important point clear. In order to allow for high  $\alpha$  values the very few pathways have to be excited having a low activation threshold and high yield. This however deserves

already a tailored pulse with the correct time-frequency ordering, which is normally not known, since this pulse is the goal of the optimization. For this reason it is safe to assume in the following that the initial guess will excite non-optimal transitions, their number and character depending of course on the pulse intensity. In this set a transition with minimum ( $\mu_-$ ) and maximum ( $\mu_+$ ) dipole moment will exist. Their respective excitation thresholds will be called  $\hat{\epsilon}^-$  and  $\hat{\epsilon}^+$ , where  $\hat{\epsilon}^- > \hat{\epsilon}^+$ . The pulse in the following iteration is given by Eq. (5.10) and therefore its maximum amplitude is  $\propto \mu_+/\alpha$ . Now, if  $\alpha$  is substantially larger than one, such that

$$\mu_+/\alpha < \hat{\epsilon}^- \quad (7.7)$$

the new field will not be capable to excite over again the  $\mu_-$  transitions in all the forthcoming iterations. That is in the following iterations the  $\mu_-$  transition will be eliminated from the pulse's excitation capabilities until finally no transition is left over. Eq. (5.10) amounts to zero and the zero field results.

On the contrary if  $\alpha$  is small enough, such that

$$\mu_+/\alpha > \hat{\epsilon}^- \quad (7.8)$$

no frequencies are eliminated. The algorithm can improve the laser field in the next iterations and Eq. (7.8) will be always fulfilled since improvement of the field means excitation of regions with stronger and stronger transition dipole moments. Of course the transition frequencies of the region excited by the initial guess pulse will remain also in the optimal field ending up in a complex pulse [see Fig. 7.3(a)] of unnecessarily high intensity ( $10^{12}$  W/cm<sup>2</sup>).

The maximum choice of this value therefore depends on the initial guess optimality. In the case of imperfect initial guess the  $\alpha$  threshold can be much too low to obtain a simple pulse [see Fig.7.3(a)]. In Fig. 7.3(a) and 7.3(b) the initial guess

$$\varepsilon_0(t) = (0.001 \text{ a.u.})s(t) \cos(\omega t) \quad (7.9)$$

was tried with the center frequency at  $\omega = 10\,974 \text{ cm}^{-1}$  (a) [ $\omega = 11\,698 \text{ cm}^{-1}$  in Fig.7.3(b)] which allowed for  $\alpha = 400$  ( $\alpha = 1100$ ). A comparison of the complex broadband spectrum Fig. 7.3(a) with the two separated frequency bands in Fig. 7.3(b) impressively demonstrates the impact of  $\alpha$ . Enormous simplification was attained with a negligible loss of yield. As already pointed out such a good initial is normally unknown. One can accommodate for the lack of knowledge of the optimal frequencies by taking a broadband initial guess, e.g., a few femtosecond cycle pulse. However this provision does not account for the perhaps necessary time-ordering of these optimal frequencies. In the considered transfer here, however it already permits the setting

of  $\alpha = 1000$  [see Fig. 7.3(c)].

A more generally applicable procedure is to perform a first OCT optimization with a small  $\alpha$  value and the use this optimized field, however complex, as initial guess for a second OCT run. In the second run  $\alpha$  can be set to unprecedented high values and consequently after a few iteration cycles the intensity of the pulse is so much reduced ( $10^9$  W/cm<sup>2</sup>) that it can only excite the most robust and strongest transitions. As a result the pulse is very simple and experimentally realizable [see Fig. 7.3(d)]. By this means  $\alpha = 2000$  could be chosen and the yield was still 94%. When an even higher value for  $\alpha$  was chosen, no remarkable further simplification could be obtained (i.e.  $\alpha = 3000$  gives 90%). The main advantage of this second filtering OCT run is that the dependence of the OCT performance in retrieving robust pulses on the initial guess pulse is completely eliminated. Figures 7.3(c) and 7.3(d) again demonstrate, that simple spectral structure is unequivocally correlated with high  $\alpha$  values.

In summary I have shown, that whenever a pulse with a complex time-frequency behavior is optimal it might be necessary to rerun the optimization with this complex pulse as initial guess, allowing for a high penalty factor. This proposition is based on the fact that most of the time-frequency behavior only leads to an increase of pulse energy with the consequence of exciting secondary multiphoton or off-resonant pathways. There contribution to the yield being of minor importance. The second high  $\alpha$  optimization extracts from the complex pulse, the time-frequency behavior necessary to excite the most fundamental and important pathway. Looking back it is now clear, that only if the initial guess has the time-frequency distribution necessary to excite the optimal pathway, i.e. the important frequencies must be ordered correctly in time, a high  $\alpha$  optimization is possible. Comparing again Figs. 7.3(a), 7.3(b), 7.3(c) and 7.3(d) the following interpretation can be made: the pulses in Figs. 7.3(b) and 7.3(d) have similar spectra and therefore seem to excite the same pathway, meanwhile a second only slightly different pathway could be isolated Fig. 7.3(c) with merely a different choice of initial guess. Since the frequencies of the robust pathways in Figs. 7.3(b) and 7.3(c) are also inherent in the spectrum Fig. 7.3(a), its complexity can therefore be attributed to the simultaneous excitation of many different pathways. It would be very valuable if all these possible control mechanisms could be distilled in an isolated fashion, however Figs. 7.3(b) and 7.3(c) show that this is only limitedly possible by choosing different initial guesses. This will be the central topic of the next section.

### 7.3 The additional laser source

In order for the optimized laser field to be a probe for different control mechanisms it must be simple. In the last section it was proven that a simple pulse can only result for high  $\alpha$  values, which are in turn only allowed if the initial guess pulse excites the strongest transitions in the system. As a consequence this means that only the most prominent control mechanism is reflected in the optimal pulse. In this section a new functional will be devised that allows the optimal field to be also a probe for alternative control pathways besides the most prominent one. As a signature of a new pathway the optimized pulse spectrum will be used. If for the same objective pulses with clearly different frequency signature can be optimized, than each of these pulses stands for a different control mechanism. The achieved yield for each different process is only of secondary importance, since it can not be assumed that every control process is a 100% efficient.

How must the functional be changed in order for OCT to explore a different control mechanism or stated in different words, how can OCT be obliged to sustain frequencies besides the most prominent ones even for high  $\alpha$ ? A simple answer to this question is to search for all system transitions offering these frequencies and replace their dipole transition moments by strong artificial ones and also include the optimization of these transitions as an extra objective in the functional of Eq. (5.8). This provision will make them contribute essentially to the yield. The disadvantage of this simple answer is that changing the dipole transition moment of one transition will change the system as a whole.

Therefore based on this idea, but in a more flexible non-invasive implementation, the new functional is defined as

$$J = J_L + J_S + \alpha \int_0^T dt \frac{|\varepsilon(t)|^2}{s(t)}, \quad (7.10)$$

where

$$J_L = |\langle \Psi_f^L | \Psi^L(T) \rangle|^2 - 2\text{Re} \left[ \langle \Psi_f^L | \Psi^L(T) \rangle \int_0^T dt \langle \Lambda^L(t) | \left[ i(H_L - \mu_L \varepsilon(t)) + \frac{\partial}{\partial t} \right] | \Psi^L(t) \rangle \right]. \quad (7.11)$$

As before  $J_S$  describes the system with its free evolution Hamiltonian  $H_S$  and dipole transition moment  $\mu_S$  [Eq. (5.8)].  $J_L$  is a new additional functional. Instead of changing transitions in the system a two-level atom with an adjustable transition frequency  $\omega_{12}$  and a dipole transition moment fulfilling the requirement  $\mu_L \gg$  any  $\mu_S$  of the system is added as an independent

unit. An extra objective  $\left| \langle \Psi_f^L | \Psi^L(T) \rangle \right|^2$  in Eq. (7.11) realizes the influence of the  $\omega_{12}$  transition on the yield. Both provisions always allow the algorithm to find an optimal pulse for the two-level system, even for very high  $\alpha$  values where it is still impossible for a system transition to be excited due to their by definition lower dipole transition moments  $\mu_S$ . Only by gradually reducing  $\alpha$  the OCT will start optimizing the system as well by including the necessary frequencies in *addition* to  $\omega_{12}$ . If there exists a pathway for excitation of the molecule at the adjusted laser frequency a simple optimal pulse will emerge characterizing further this new control mechanism, by its frequency signature. The addition of the laser system as a second system to be optimized in the functional of Eq. (7.10) assures the constant existence of the frequency  $\omega_{12}$  of Eq. (7.15) inside any optimized field for the whole system consisting of molecule and two-level atom.

Identifying the two-level atom as an accurate representation of a laser, it is clear that this generalized functional describes a more realistic optimal control experimental setup, since it makes a vital extension in also including the laser and not only the quantum mechanical system. This is necessary, since it is not self-evident that a laser can be tuned to and shaped at any wavelength. Instead, a laser system, together with a pulse shaping device, exist for a wavelength range, and the question arises whether they can control the system by a suitable adjustment.

Variation of the whole functional leads to five coupled equations; two for the time evolution of the system, two for the evolution of the laser system and, one for the field. Only the last three are written down here explicitly, since the system equations are known already from the earlier sections

$$i \frac{\partial \Psi^L(t)}{\partial t} = [H_L - \mu_L \varepsilon(t)] \Psi^L(t), \quad \Psi^L(t=0) = \Phi_i \quad (7.12)$$

$$i \frac{\partial \Lambda^L(t)}{\partial t} = [H_L - \mu_L \varepsilon(t)] \Lambda^L(t), \quad \Lambda^L(t=T) = \Phi_f \quad (7.13)$$

$$\begin{aligned} \varepsilon(t) = & -s(t) \text{Im} \left\{ \langle \lambda(t) | \psi(t) \rangle \langle \psi(t) | \frac{\mu_S}{\alpha} | \lambda(t) \rangle \right. \\ & \left. + \langle \Lambda^L(t) | \Psi^L(t) \rangle \langle \Psi^L(t) | \frac{\mu_L}{\alpha} | \Lambda^L(t) \rangle \right\}. \end{aligned} \quad (7.14)$$

The solution of this set of nonlinear coupled differential equations is computed iteratively as before. The additional numerical effort to propagate the laser system is negligible. The algorithm has to optimize two objectives: a transfer in the system from  $\psi(t=0)$  to  $\psi(t=T)$  and the laser transition from  $\Psi^L(t=0) = \begin{pmatrix} 1 \\ 0 \end{pmatrix}$  to  $\Psi^L(t=T) = \begin{pmatrix} 0 \\ 1 \end{pmatrix}$ . The initial guess is no longer an input to the algorithm, but is instead always computed according to

$$\varepsilon_0(t) = (0.001 \text{ a.u.}) s(t) \cos(\omega_{12} t). \quad (7.15)$$

Eq. (7.15) describes a field that maximizes the laser yield, since it is in resonance.

By performing optimizations with this new functional for different  $\omega_{12}$  it is for the first time possible to show up in an isolated fashion one pathway after another for a single objective in the system under consideration. The optimal pulse has a clear structure and a mixture of all pathways shadowing each other is avoided. This new feature is illustrated in Figs. 7.4(a) and 7.4(b). In Fig. 7.4(b) the optimum electric field spectrum is depicted, where the initial guess center frequency  $\omega_{12}$  was tuned to  $11\,698\text{ cm}^{-1}$  corresponding to the location of one of the most prominent peaks in the spectrum of Fig. 7.3(b). This optimal laser tuning allows for the highest  $\alpha$  values and the least supplementary frequencies. A system yield of 94% was reached with  $\alpha = 2000$  [see Fig. 7.4(b)]. The initial guess pulse for these two data sets was the same, but the new functional allowed for higher  $\alpha$  values. Note the similarity of the optimized pulse spectra Fig. 7.3(b) and Fig. 7.4(b). In Fig. 7.4(a) the spectrum of the optimized field is shown for a laser frequency  $\omega_{12} = 10\,974\text{ cm}^{-1}$ , which is detuned from optimum. The initial guess is automatically calculated through Eq. (7.15). At  $\alpha = 1300$  a system yield of 96% is reached. It has to be noted that although the initial guess pulses are the same for the data in Fig. 7.3(a) and Fig. 7.4(a), the new formulation of the functional allows an  $\alpha$  value three times higher than in the standard functional ( $\alpha = 400$ ). Again due to the high value of the penalty factor the intensity of the pulse is considerably reduced to maximum amplitude of  $0.0002\text{ a.u.}$  (or intensity of  $10^9\text{ W/cm}^2$ ). The four extra remote frequency bands are essential and cannot be suppressed. This was tested by gradually decreasing the penalty factor from the value where only the laser transition frequency can exist. The algorithm for calculating the necessary mask pattern explained in section 7.1 was applied and resulted in the transmission and retardance mask functions of Figs. 7.4( $\alpha$ ) and 7.4( $\beta$ ). The colors mark the regions where the phase behavior is important due to significant spectral intensity.

The new functional in combination with the Krotov method of building the new field without memory behaves similarly to the modified Krotov method with the difference that Eq. (7.14) is a correction equation to the *initial* guess field which is  $\epsilon_{ini}$

$$\varepsilon(t) = \epsilon_{ini}(t) - s(t)\text{Im} \left\{ \langle \lambda(t) | \psi(t) \rangle \langle \psi(t) | \frac{\mu S}{\alpha} | \lambda(t) \rangle \right\}, \quad (7.16)$$

with

$$\epsilon_{ini}(t) = -s(t)\text{Im} \left\{ \langle \Lambda^L(t) | \Psi^L(t) \rangle \langle \Psi^L(t) | \frac{\mu L}{\alpha} | \Lambda^L(t) \rangle \right\}. \quad (7.17)$$

Clearly this is different from the modified Krotov (see section 5.1), where the correction is applied to the field of the *previous* iteration. In other words one could say that in modified Krotov the memory lasts only one iteration, while in the new functional the memory of the beginning is kept. As a result in

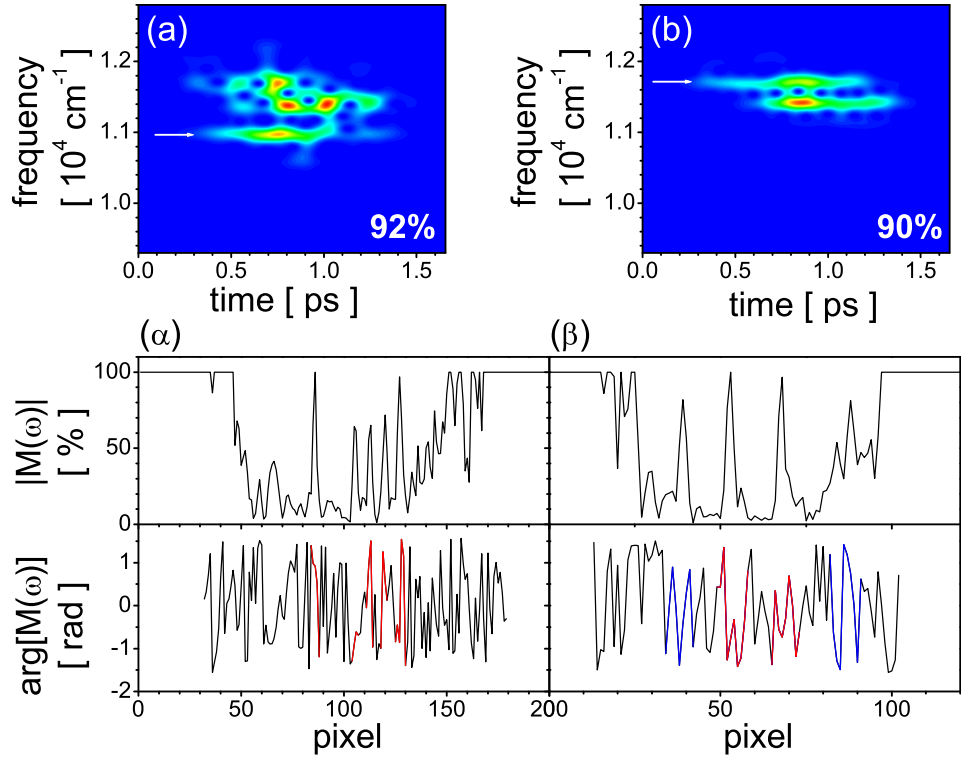


**Figure 7.4:** Optimal fields calculated with the generalized functional for two different laser source center frequency tunings indicated as white arrows. (a)  $\omega_{12} = 10\,974\text{ cm}^{-1}$ . (b)  $\omega_{12} = 11\,698\text{ cm}^{-1}$ . ( $\alpha$ ) Mask pattern of (a). ( $\beta$ ) Mask pattern of (b). Here  $|M(\omega)|$  denotes the transmission and  $\arg[M(\omega)]$  the phase of the mask pattern. Only the colored regions of the phase mask are important, since only there considerable spectral amplitude is transmitted through. Within the colored phase regions red sections are most important, while blue are less important.

modified Krotov the laser transition frequency can vanish, while it can not, when using Eq. (7.14) since an additional yield term for the laser system that needs the initial guess is included in the functional [see Eq. (7.10)]. The functional presented here is even able to control the amount of spectral frequency at the laser transition within the optimal pulse, by controlling  $\mu^L$  and thus is more general.

Besides of the previously discussed features, the functional of Eq. (7.10) is the first step towards controlling simultaneously multiple objectives with a single laser pulse. It was already mentioned that Eq. (7.10) leads to an OCT variant, that optimizes the light field of the laser source and the system simultaneously for low enough  $\alpha$ . This idea can be generalized and it is possible to assume even more objectives in the same system [134] or

more generally in different systems

$$J = \sum_{k,s} \left\{ \left| \langle \psi_f^{k,s} | \psi^{k,s}(T) \rangle \right|^2 - 2\text{Re} \left[ \langle \psi_f^{k,s} | \psi^{k,s}(T) \rangle \int_0^T dt \langle \lambda^{k,s}(t) | \left[ i(H^s - \mu^s \varepsilon(t)) + \frac{\partial}{\partial t} \right] | \psi^{k,s}(t) \rangle \right] \right\}. \quad (7.18)$$

This equations will deliver an optimal pulse for the transfer into  $k$  target states starting from  $m$  ( $\leq k$ ) initial states in  $s$  different systems, incoherently from one another. Incoherent because the absolute value of each individual target is taken as objective and not the absolute value of their sum. Variation of this functional gives equations similar to Eqs. (7.12)-(7.14)

$$i\partial_t \lambda^k(t) = [H^s - \mu^s \varepsilon(t)] \lambda^k(t), \quad \lambda^s(t=0) = \phi_i^m \quad (7.19)$$

$$i\partial_t \psi^k(t) = [H^s - \mu^s \varepsilon(t)] \psi^k(t), \quad \psi^k(t=T) = \phi_f^k \quad (7.20)$$

$$\varepsilon(t) = -\frac{s(t)}{\alpha} \sum_k \text{Im} \left\{ \langle \lambda^k(t) | \psi^k(t) \rangle \langle \psi^k(t) | \mu^s | \lambda^k(t) \rangle \right\}. \quad (7.21)$$

A possible application of this very general functional is to solve the problem of molecular  $\pi$ -pulses, that invert an initial Boltzmann distribution. Another recent application of this functional is the design of laser pulses suitable for molecular quantum computing [135], where operation of a single pulse on several qubits is required.

In conclusion new strategies to reduce the complexity of pulses obtained by the OCT algorithm and to discover new control mechanisms were developed. The parameter  $\alpha$  is of critical importance if robust pulses are to be retrieved. A new formulation of the functional including the laser system, allows high  $\alpha$  values and therefore produces immediately spectrally purified pulses. These robust pulses are amenable to a detailed study and their experimental realization is an easy task with state of the art pulse shaping technology. The new, more general functional can be used to distill all optimal control pathways for an objective by tuning the laser frequency. The pathways are thereby made accessible to a more detailed study. This powerful tool can be used to clear off complex excitation patterns and discover new optimal control processes in quantum mechanical systems, since the solutions will always include the laser frequency and be as simple as possible.

## 7.4 Projector method

The aim of this section is to derive a new OCT functional that provides optimal pulses with a pre-specified spectral width and leading to coupled

equations still solvable with the closed loop iteration scheme.

In the early formulation of the OCT algorithm a filtering technique [31] was proposed to restrict the optimal fields to a specified frequency bandwidth (see introductory remarks to chapter 7). This technique cannot be applied within the framework of closed equations [Eqs. 5.7, 5.9 and 5.10]. The electric field in the closed form iteration is calculated at each step and not in a one-cycle-to-next-cycle (one cycle of iteration includes a number of steps) style as in gradient type methods (see discussion in section 5.1). Therefore a spectral constraint using filtering in the Fourier domain can only be applied at the end of the iteration cycle, where the complete spectral information of the pulse is present. Consequently the algorithm has felt no spectral constraint during the whole cycle and application of the filter would only disturb the convergence. In the following a new functional is presented which allows for spectral pressure also within this closed form, rapidly convergent OCT.

In order to derive the new functional, that allows to include spectral pressure, the following idea is central. The electric field is essentially build from the overlap of populated eigenstates of the field free Hamiltonian [see Eq. (5.10)]. Even if the wave function is represented on a grid its eigenstate composition can be obtained through projection. The spectral width of the optimal pulse is controlled *indirectly* by allowing the wave functions  $\psi$  and  $\lambda$  to consist only of a pre-specified set of eigenfunctions. The idea behind this reduction of the number of eigenstates contributing to a wave packet is, that a spectrally broad pulse will excite coherently many eigenfunctions, while a spectrally narrow pulse will excite only a few eigenfunctions at any time. The projection of the wave function on the constituting vibrational eigenstates at three different times and for three excitation pulses with a *fwhm* of 10 fs, 50 fs and 100 fs is shown in Fig. 7.5. Clearly the width of the decomposition greatly reduces as the pulse becomes of smaller bandwidth. Therefore an intelligent reduction of contributing eigenstates in Eq. (5.10) will reduce the number of transitions with different frequencies and hence these frequencies will be the only ones appearing in the pulse spectrum. To be more specific let us consider an optimal transfer in the potassium dimer involving only the X and A state and their vibrational levels. Taking the case that the initial state is a single vibrational eigenstate the spectral width can be simply controlled by allowing only vibrational levels around this initial state (set X) and a set of vibrational levels in the A state (set A). The choice of these two eigenstate sets will specify the center wavelength and spectral width of the pulse. The maximum frequency will be given by the transition between the lowest eigenstate in set X and the highest in set A, while the minimum allowed frequency is simply the difference of energies between the highest energetic eigenstate in set X and the lowest in set A. Since the sets X and A can be chosen arbitrarily, for instance they do not have to be connected, the spectrum of the pulse can be arbitrarily tailored. Indeed only a not-connected set X will allow pump-dump pulses with very

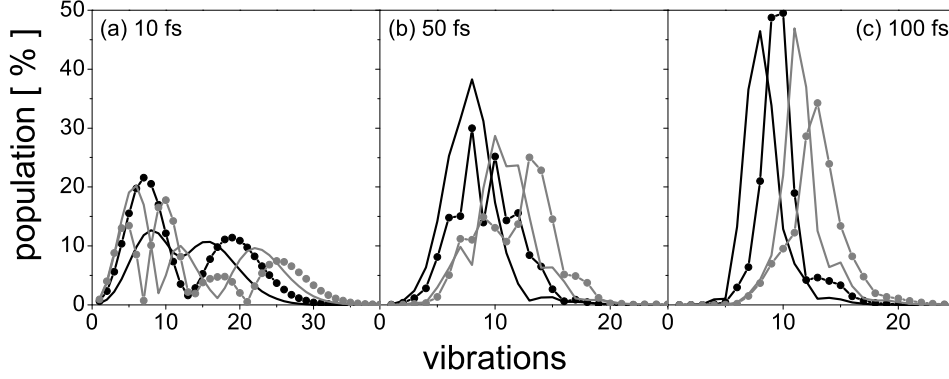


**Figure 7.5:** A state wave packet decomposition in eigenstates at initial, intermediate and final time for excitation with three different pulse durations. (a) 10 fs (b) 50 fs and (c) 100 fs. Each line depicts a snapshots of the wave function at one specific time.

different frequencies of the pump and dump step. Similarly to the shape function  $s(t)$  that influences the appearance of the optimal pulse envelope a shape function on the eigenstates will mold the pulse spectrum.

If  $P$  is the projector onto the subsets of eigenstates and  $\bar{P}$  the projector on all other eigenfunctions, the relation  $1 = P + \bar{P}$  holds true. This relation is used to split Eq. (5.10) into two summands  $\varepsilon(t) = \varepsilon(t)^y + \varepsilon(t)^n$ , where the first summand is the spectrally small part, while the other with superindex  $n$  contains further spectral components to be eliminated.

$$\frac{\alpha}{s(t)}\varepsilon(t) = \underbrace{-\text{Im} \left\{ \left( \sum_{k,l=1}^N W(l)^2 a_l^{\dagger i} a_k^f \delta_{kl} \right) \left( \sum_{k,l=1}^N W(l)W(k) \langle v_l | a_l^{\dagger f} \mu a_k^i | v_k \rangle \right) \right\}}_{\varepsilon(t)^y} - \underbrace{\text{Im} \left\{ \left( \sum_{k,l=N+1}^{\infty} \dots \right) \left( \sum_{k,l=N+1}^{\infty} \dots \right) \right\}}_{\varepsilon(t)^n}. \quad (7.22)$$

Here the complex numbers  $a_l^i(t) = \langle v_l | \psi_i(t) \rangle$  have been used. Considering only the term  $\varepsilon(t)^y$  leads to the new OCT algorithm with spectral restriction. The closed equations for  $\lambda$  and  $\psi$  itself are the same as before with the exception of the equation for  $\varepsilon(t)$  which has changed into Eq. (7.22). Numerically this formula is implemented by applying the projector on both wave functions  $\psi_i(t)$  and  $\psi_f(t)$  each time a new point of the electric field is calculated through Eq. (5.10), i.e. at each time step of the iteration. These projected wave functions are only used to construct the electric field. The propagation is continued with the original unprojected wave functions for

the next time step followed again by the projection step. This process is repeated until the end of the cycle. Propagation on a grid as is performed here needs the original wave functions to be propagated and not the projected ones, since this would lead to the destruction of convergence. Therefore the projector can not be included directly in the Schrödinger equation constraint of Eq. (5.8). Alternatively, when all eigenfunctions are known and not only the ones needed for the projector in Eq. (7.23), the propagation can be performed directly in the basis of eigenfunctions and not on a grid. In the case of the potassium dimer about 30 vibrational eigenstates of each electronic state are needed to achieve the same numerical results as with a grid of 256 points. A reduced set of eigenfunctions can be used only in the projector to evaluate the electric field according to Eq. (7.22), but not for the propagation of the molecular system.

The iterative scheme is started by taking as a favorable initial guess the optimized pulse from an unconstrained OCT run. After convergence the mask function can be extracted from the spectrum of the optimal pulse by using Eq. (7.6). Since the spectral width of the optimal pulse is controlled with the parameter  $\Delta v$  in the shape function  $W$ , the number of pixels can be reduced drastically. It is now possible to design experimentally realizable pulses with this OCT variant that controls the spectral width of the optimal laser pulse. Moreover it is a fast and efficient code for providing optimally shaped pulses which can directly serve as input to the experiment. Spectral pressure also tends to simplify the laser pulse features, enabling the extraction of the control mechanism.

Just to show that this works, the population transfer from  $v'' = 0$  ( $|v''_0\rangle$ ) to  $v'' = 2$  ( $|v''_2\rangle$ ) in the ground state using the first electronic excited state  $A^1\Sigma_u$  as an intermediate pathway will serve as prototype control. It is not necessary to define a projector in the ground state, since initial and target vibrational state are within the bandwidth of a 50 fs pulse. Only a projector onto a specified subset of  $N$  excited state vibrational eigenfunctions  $|v_n\rangle$  of the field free Hamiltonian  $H_0$  is defined and weighted with a shape function  $W(n)$

$$P = \sum_{n=1}^N W(n) |v_n\rangle \langle v_n|. \quad (7.23)$$

The shape function was chosen to be a Gaussian distribution

$$W(n) = \exp \left\{ - \left( \frac{v - v_0}{\Delta v} \right)^2 \right\}. \quad (7.24)$$

Here  $v_0$  is the maximum and  $\Delta v$  is the width of the desired eigenfunction distribution. In the extreme case  $v_0 = 6$  and  $\Delta v = 3$  was selected, which

corresponds to a pulse at  $\approx 820$  nm with spectral bandwidth corresponding to 50 fs.

The results are shown in Fig. 7.6. The yield  $y$  is defined as the overlap with the target eigenfunction

$$y = |\langle \psi_i(t=T) | \phi_f \rangle| \text{ or alternatively as } y = |\langle \psi_f(t=T) | \phi_i \rangle|, \quad (7.25)$$

where  $|\phi_i\rangle = |v''_0\rangle$  and  $|\phi_f\rangle = |v''_2\rangle$ . The first column shows a pulse calcu-

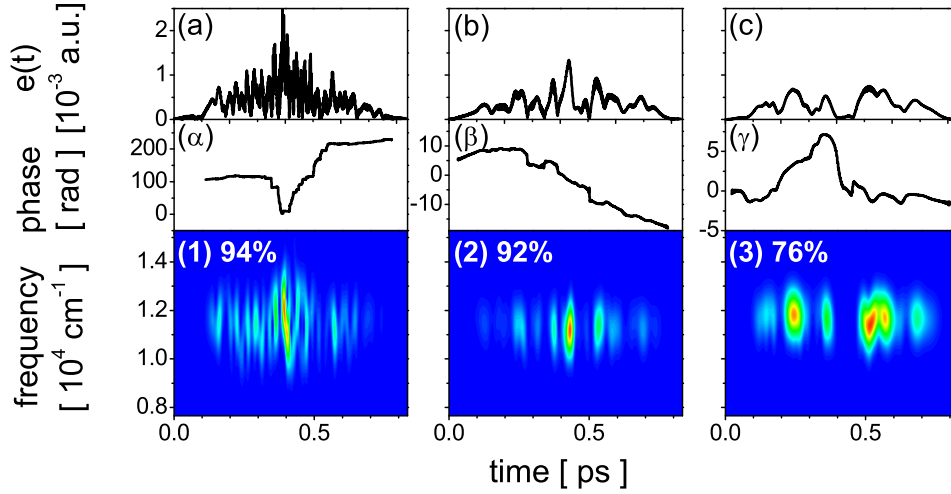


**Figure 7.6:** Optimal control pulses transferring population from  $v'' = 0$  to  $v'' = 2$  in the ground state using the first electronic excited state  $A^1\Sigma_u$  as an intermediate pathway. Each column depicts one optimal pulse, retrieved by gradually increasing spectral pressure. (a)-(c) pulse envelope. ( $\alpha$ )-( $\gamma$ ) pulse phase. (1)-(3) STFT of the pulse.

lated with OCT using no spectral restriction. The optimized pulse produces a yield of 0.94. The FL pulse from which the shaped pulse originates has a duration of 10 fs and a complex mask pattern with a number of pixels exceeding the usual experimental number of 128 [see Fig. 7.7(a)]. When spectral pressure is applied by reducing the parameter  $\Delta v$  the optimal field becomes more robust, but efficiency is gradually reduced. These results are shown in Fig. 7.6(a) and 7.6(b), respectively. Interestingly some spectral pressure can be applied without losing much efficiency (b). This pulse still has a yield of 0.92 with the advantage of having a spectrum corresponding to a longer pulse of 20 fs and a realizable mask pattern [see Fig. 7.7(a) and 7.7(b)]. Figure 7.6(c) shows a pulse that has a yield of 0.76, and is even easier to shape due to its 40 fs FL duration and simplex mask pattern [Fig. 7.7(c)]. The pulse consists of a clearly structured pulse sequence, where the third pulse is linearly negatively chirped.

The difference of the projector and the new functional method is best explained in view of its application. The projector method should be used,

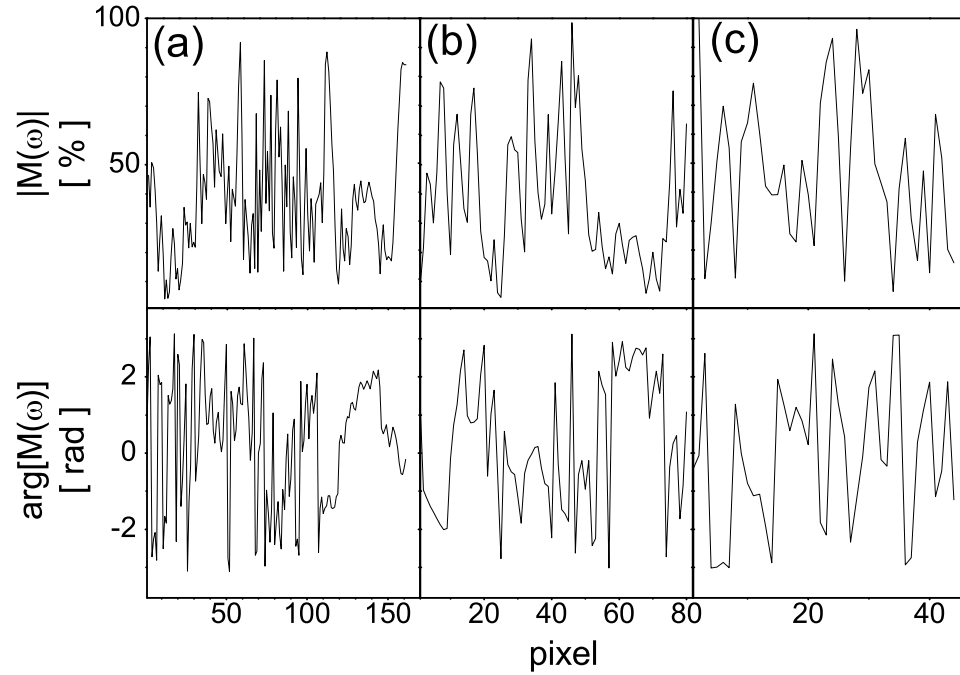


**Figure 7.7:** Transmission  $|M(\omega)|$  and phase  $\arg[M(\omega)]$  of the mask patterns needed to tailor the pulses of Fig. 7.6. (a) Is the mask pattern for the pulse in Fig. 7.6(a), (b) for the pulse in Fig. 7.6(b) and (c) for the pulse in Fig. 7.6(c).

when the spectral shape, especially bandwidth, shall be constraint. The pulse simplicity can be adjusted by the spectral width of the projectors and it is best to use very low values for  $\alpha$ . Since the algorithm is not able to search freely for the most robust pathways and is instead constraint to the allowed frequencies, the optimal pulse must have sufficient energy to excite the allowed, but perhaps non-optimal pathways.

The new functional answers the question what extra frequencies besides the laser center frequency are needed to optimize the target, that is which is the most efficient transfer mechanism for a given laser source. The new functional provides more potential applications, it can also be applied whenever a electric field is sought that optimizes several targets at once. The main difference to the method of this section is the impossibility to constrain the new emerging frequencies to a specified spectral window. Using the algorithm of the past section appropriately means to start with high  $\alpha$  values and reduce the  $\alpha$  parameter to enable a growth of the frequencies in the optimized pulse until the desired yield is achieved. The optimized pulse obtained by the method of section 7.3 has always the lowest possible pulse energy, just enough to excite the most robust pathways out of the excitation region selected by the center frequency of the laser source.

## Chapter 8

# Application

In the following two sections simple femtosecond laser pulses are obtained using the method of section 7.2 for the SST and PI transfer introduced in chapter 6.

### 8.1 State selective population transfer (SST)

In this section the efficient femtosecond-laser induced transfer of population between two eigenstates of the ground electronic state is investigated. Both states must be connected via the first electronically excited state since a direct IR transition is forbidden due to the homonuclear character of the potassium dimer. Earlier work [136] has shown that this system can be effectively treated as a lambda system if nanosecond or continuous wave lasers are used. In this realm STIRAP can be efficiently used. Here a completely different regime is investigated, where the applied pulses have a broad frequency spectrum coherently exciting a superposition of many eigenstates, but as will be shown are still selective to a single eigenstate due to their proper pulse shape. Moreover the simultaneous excitation of many eigenstates makes the problem not reducible to a simple lambda system. This conceptual formulation is appropriately solved with the rapidly convergent OCT (see section 5.1), which naturally excludes the counterintuitive STIRAP solutions since only frequencies of *populated* levels constitute the pulse during the iterations. The results extend previous work of our group [115].

**Single well defined initial state.** The powerful method of high penalty factor optimization allows to deduce the control mechanism behind these optimal pulses by merely looking at their short-time Fourier transform. A comparison of the STFT of the pulse transferring above 90% of the population from  $v'' = 0$  to  $v'' = 2$  [Fig. 8.1(a)] with the pulse doing this for  $v'' =$

0 to  $v'' = 5$  [Fig. 8.1(b)] reveals a Tannor-Rice-Kosloff pump-dump mechanism. The pump and dump frequencies differ by the energy spacing between initial and target vibrational state and the overlap in time of the subpulses is bigger in the case of  $v'' = 0$  to  $v'' = 5$ . The correct time separation, phase and center frequencies of the subpulses lead to a pump-dump mechanism that is vibrationally state selective at final time. Figure 8.2 shows snap-

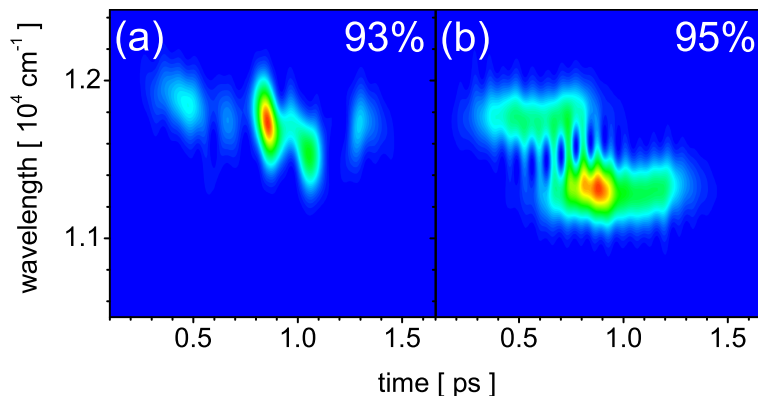


**Figure 8.1:** Pulses optimizing transfer between two eigenstates of  $X \ ^1\Sigma_g$  via  $A \ ^1\Sigma_u$ . (a)  $v'' = 0$  to  $v'' = 2$ . (b)  $v'' = 0$  to  $v'' = 5$ .

shots of the wave packet during the optimal  $v'' = 0$  to  $v'' = 2$  transfer on the grid 8.2(a)-(d) and its projection onto eigenstates 8.2( $\alpha$ )-( $\delta$ ). At intermediate times [Figs. 8.2(b) and (c)] the ground state wave packet consists of a coherent superposition of eigenstates, while at initial and final time it is a single eigenstate of the field free Hamiltonian. The pulse is hence tailored to be selective to states within its excitation bandwidth. The Raman pumping realized between moving wave packets on the potential surfaces, is such that population ends again in the ground state and is concomitantly shaped into an eigenstate. Once the target wave packet has the shape of an eigenstate it will also have its energy. There remains some population in high energy ground eigenstates, since the transfer is not complete, that is 100%. The population in the higher excited potentials is negligible and essentially the pulse couples only the two lowest electronic states, X and A. This is general to all eigenstate transfers with moderate  $\Delta v$ , since the optimal pulses all have low peak amplitude on the order of  $2 \cdot 10^{-4}$  a.u. (= an intensity of  $10^9$  W/cm<sup>2</sup>) [see Figs. 8.3(a) and 8.4(a)-(d)]. The effect of phase in this transfer was also investigated. The subpulses of the tailored  $v'' = 0$  to  $v'' = 5$  laser field [Fig. 8.3(a) and its spectrum Fig. 8.3( $\alpha$ )] are calculated, by extracting from all Fourier components the ones belonging to the pump and to the dump frequency [115,137]. The resulting subpulses are shown in Figs. 8.3(b) and (c). Clearly the earlier pulse has the higher frequency and serves as pump, while the later pulse dumps the population [see

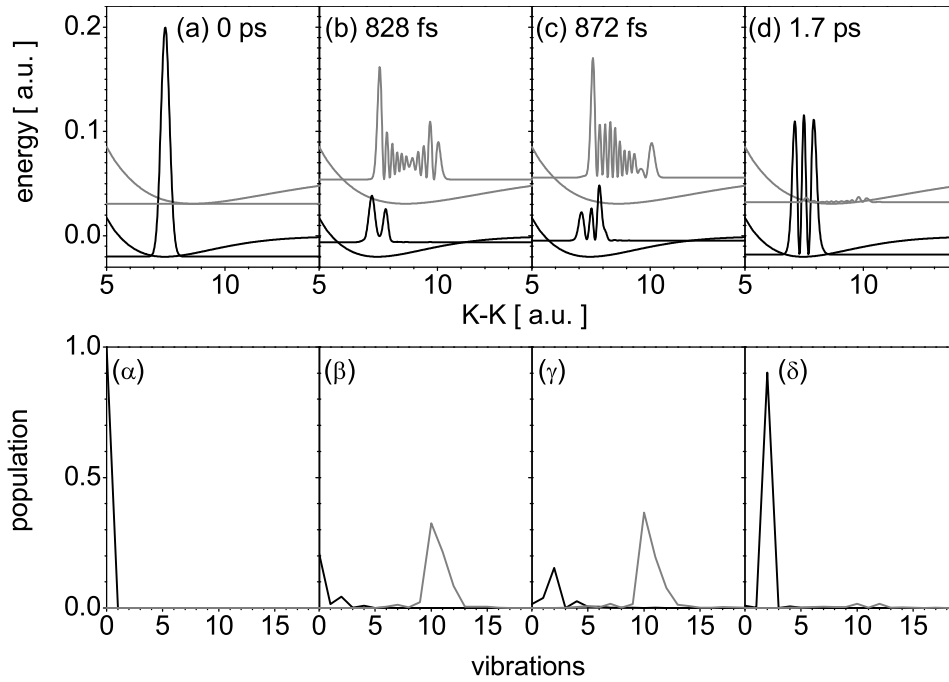


**Figure 8.2:** One dimensional wave packet propagation, showing snapshots of the optimal  $v'' = 0$  to  $v'' = 2$  transfer. (a)-(d) grid representation of the wave function. (α)-(δ) eigenfunction representation of the wave function.

Fig. 8.3(βγ)]. Having calculated the subpulses it is possible to combine them again to a single pulse using a method described in Ref. [115,137]. Thereby their relative phase can be changed, by adjusting the absolute phase of one of the pulses relative to the other. A change in phase just shifts the carrier with respect to the envelope and when combining with the other subpulse will lead to a phase dependent interference in the temporal overlap region of the two pulse constituents. The combined pulse is then propagated and a plot of phase versus yield can be generated [Fig. 8.3(1)] and shows a periodic modulation with a maximum yield at 1 rad. The maximum yield is below 95% since the spectrum of the combined pulses coincides only in the main two frequencies and thus is only an approximation to the original pulse of Fig. 8.3(a).

Another peculiarity of the eigenstate transfer with femtosecond pulses is that whenever  $v'' = 0$  is involved the optimal pulse is more complex and loses its time symmetry. This can be inferred from Fig. 8.4, where the optimal laser fields 8.4(a)-(d) and their spectra 8.4(α)-(δ) are plotted. Here the transfers with  $\Delta v = 2$  between  $v''=0$  to  $v''=2$  [Figs. 8.4(a) and α] and  $v''=2$  to  $v''=4$  [Figs. 8.4(b) and β] and  $\Delta v = 4$  from  $v''=0$  to  $v''=4$  [Figs. 8.4(c) and (γ)] and  $v''=4$  to  $v''=8$  [Figs. 8.4(d) and (δ)] clearly show that whenever  $v'' = 0$  is involved the laser field is asymmetric in time and the

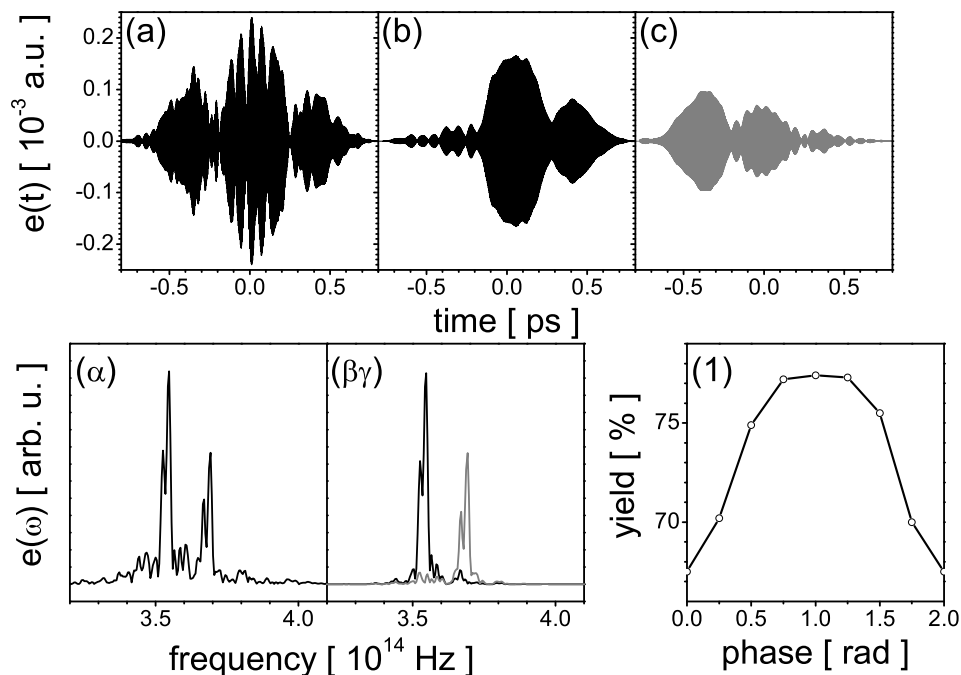


**Figure 8.3:** (a) Laser pulse optimized for  $v''=0$  to  $v''=5$ . (b) and (c) are its subpulses. (α) Spectrum of pulse (a) and (βγ) spectra of the subpulse (b) in black and subpulse (c) in gray. (1) Change of the yield as a function of the phase-relationship of the subpulses.

pump and dump frequencies show both a doublet. Inspection of Figs. 8.4(β) and 8.4(δ) reveals that the dump frequency in Fig. 8.4(β) and the pump frequency in Fig. 8.4(δ) coincide. The control process uses the same intermediate excited vibrational states for the transfer.

Another aspect to be considered in the following is the maximum value achievable for  $\Delta v$  in this kind of transfer. The larger  $\Delta v$  is chosen the smaller is the Franck-Condon factor connecting both states. However it is still possible to transfer population from vibrational states near the dissociation continuum to  $v'' = 0$  of the ground singlet potential. This kind of transfer is one of the key steps for conversion of a Bose-Einstein-condensate(BEC) of atoms to a molecular BEC (or MBEC) [138,139] with ultrashort coherent pulses as proposed in section 11.2.3. Methods so far proposed use STIRAP as a very effective and selective process to complete this task [140–143]( see also section 11.2). The total number of bound states in a potential depends critically on its depth and for the available ab initio X and A potentials the number of bound states in X was calculated to be 85 while it is 195 for the A state. As an initial eigenstate near dissociation  $v'' = 80$  was chosen, while the final state is  $v'' = 0$ . This calculation was performed in the eigenstate basis taking into account all bound vibrational eigenstates of the X and A

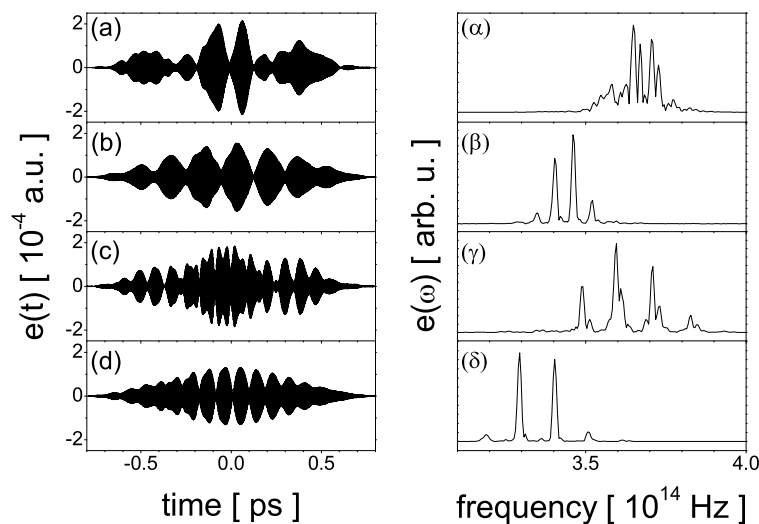


**Figure 8.4:** Laser pulses optimizing different eigenstate transfers. (a)  $v'' = 0$  to  $v'' = 2$ . (b)  $v'' = 2$  to  $v'' = 4$ . (c)  $v'' = 0$  to  $v'' = 4$ . (d)  $v'' = 4$  to  $v'' = 8$ . Their corresponding spectra are in  $(\alpha)$ - $(\delta)$ .

potential<sup>1)</sup>. Assuming a direct transfer to a vibrational state in the excited potential and back down to the final state, the effective transition dipole moment for this transfer is highest for  $v' = 41$ , but is three orders of magnitude smaller than the strongest transition in  $K_2$ . Nevertheless it is still possible to accomplish this transfer by a two-step process. The STFT of the pulse is depicted in Fig. 8.5(a) for low  $\alpha$  and 8.5(b) for high  $\alpha$ . Again it

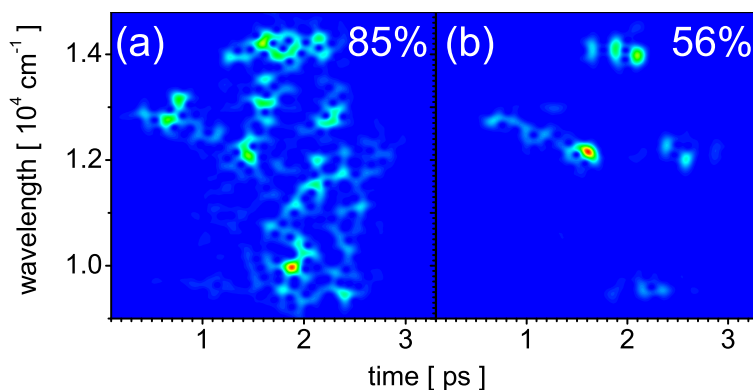


**Figure 8.5:** Laser pulse optimized for  $v''=80$  to  $v''=0$ . (a) Optimization with low and (b) with high penalty factor.

<sup>1)</sup>A grid based method would have been only effective with a nonlinear grid mapping to reduce the number of necessary points to accurately support the wave packet dynamics near dissociation.

is most simple to derive the central mechanism by inspecting the laser field Fig. 8.5(b). It consists of two main frequency bands at  $12\,000\text{ cm}^{-1}$  and  $14\,000\text{ cm}^{-1}$  and a less pronounced around  $9\,500\text{ cm}^{-1}$ . A time resolved analysis reveals, that the optimal transfer proceeds via a two-step process. First the population is transferred to an intermediate level (around  $v'' = 40$ ) and from there down to  $v'' = 0$ . This optimal process does not proceed over  $v' = 41$ , but over  $v' = 140$  [see Fig. 8.6( $\beta$ )] enhancing thereby the transition dipole moment of the overall process. In order to verify the tailored pulses

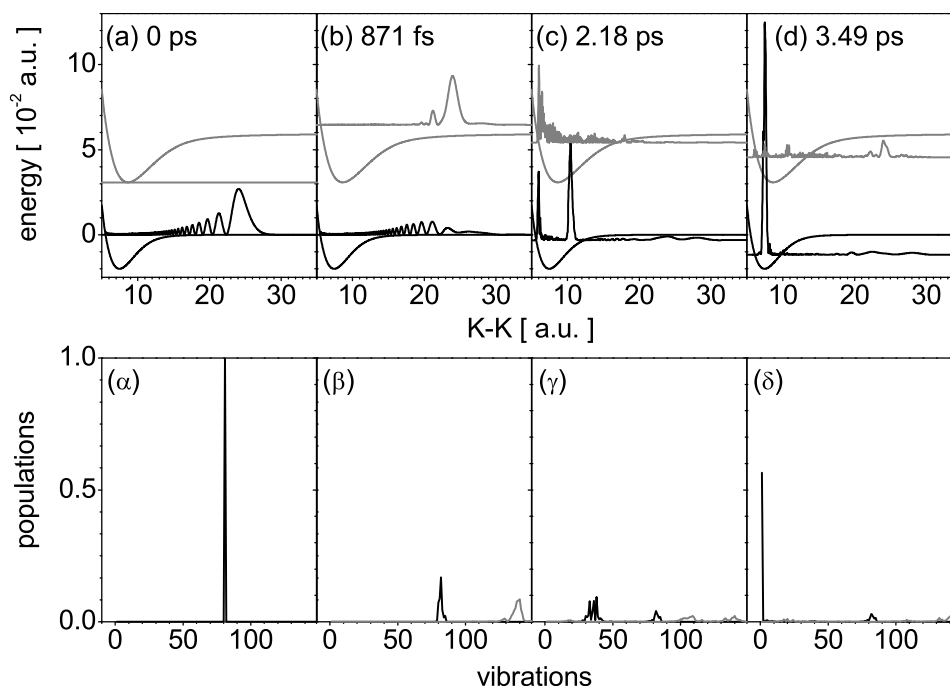


**Figure 8.6:** One dimensional wave packet propagation, showing snapshots of the optimal  $v'' = 80$  to  $v'' = 0$  transfer. (a)-(d) grid representation of the wave function. ( $\alpha$ )-( $\delta$ ) eigenfunction representation of the wave function.

for the SST transfer in experiment a beam of molecules or the preparation of a single vibrational state in an excited potential [144] would be the method of choice. Here the initial state would be well defined and coinciding with the assumptions made in theory.

Nevertheless an experimental setup using a heat pipe oven, where the alkalis are simply evaporated, is less involved. Here the dimers in the gas phase constitute a thermal ensemble. This case will be studied next.

**Thermal ensemble initial state.** The following calculations however show that it is still possible to have an experimental signature for an optimal eigenstate transfer even in a thermal ensemble. The main reason for this is that the anharmonicity of the vibrational ladder is high enough that an

optimized pulse will be efficient only between the specified initial and target eigenstate and not generally between vibrational eigenstates spaced by the same number of quanta. That is a pulse optimized for  $v'' = 0$  to  $v'' = 2$  is not optimal for  $v'' = 2$  to  $v'' = 4$ . The clear difference in the optimal pulses was already shown in Figs. 8.4(a), 8.4( $\alpha$ ), 8.4(b) and 8.4( $\beta$ ). The calculations assume an initial Boltzmann distribution over 16 vibrational states in the ground state. In Fig. 8.7(c) the final ground state population is plotted, for a tailored pulse optimized for  $v'' = 0$  to  $v'' = 1$  [Fig. 8.7(a)] and the corresponding bandwidth limited pulse [Fig. 8.7(b)]. A distinguished peak

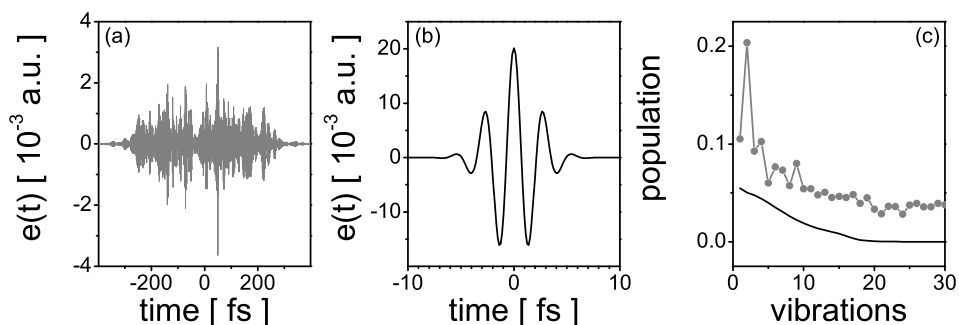


**Figure 8.7:** Thermal ensemble of  $K_2$  is excited with laser pulse optimized with low  $\alpha$  for the transfer from  $v''=0$  to  $v''=1$ . (a) The optimized electric field. (b) The corresponding Fourier limited laser pulses. (c) Final ground state distribution induced by laser pulse (a) in gray and (b) in black.

at  $v'' = 1$  rises above an else nearly flat unstructured ground state population. Clearly the two vibrational distributions would be distinguishable in experiment and the tailored pulse could be identified as optimizing  $v'' = 0$  to  $v'' = 1$ . As long as the Fourier limited pulse used to shape the optimal pulse is of broad bandwidth a clear signature is visible for a whole range of eigenstate transfers. This beautiful signature vanishes however if the bandwidth of the tailored laser pulse is in the regime of bandwidth limited 100 fs pulses [see Fig. 8.8(c)]. This can be shown by propagating the  $v'' = 0$  to  $v'' = 1$  obtained in a high  $\alpha$  OCT run [Fig. 8.8(a)]. This simple pulse can be shaped from a 100 fs Fourier limited pulse [Fig. 8.8(b)].

In a further example the possibility is considered of optimizing a pulse that transfers all the population from  $v'' = 0$  to a specified vibrational superposition state in the first excited potential. The population of the excited state will then reveal the eigenstate composition of the wave packet, despite the initial Boltzmann distribution of states [see Fig. 8.9(c)]. The two distinct peaks show evidence that the specified target state here is a superposition state with  $v' = 2$  and  $v' = 4$  contributions. The signature again nearly vanishes if a simple pulse optimized for the same target is to be used (not shown). Therefore the control will be very hard to detect in experiment using molecular gas cells with pulses above *fwhm* of 10 fs.

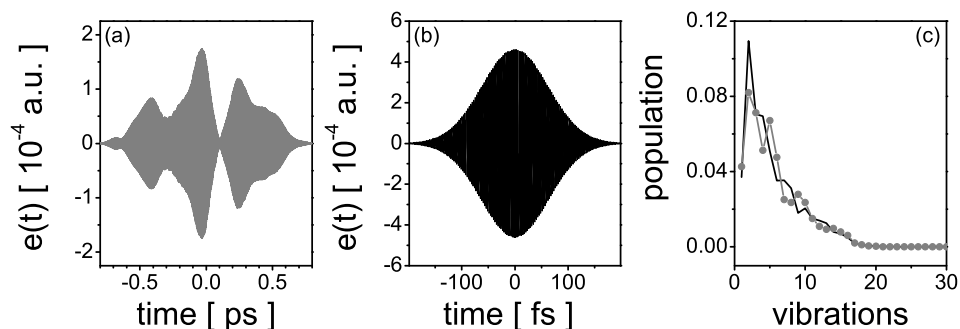


**Figure 8.8:** Thermal ensemble of  $K_2$  is excited with laser pulse optimized with high  $\alpha$  for the transfer from  $v''=0$  to  $v''=1$ . Else same as in Fig. 8.7.

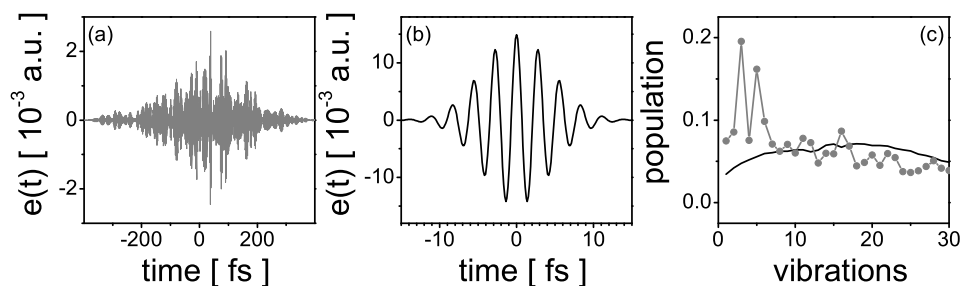


**Figure 8.9:** Thermal ensemble of  $K_2$  is excited with laser pulse optimized with low  $\alpha$  for the transfer from  $v''=0$  to a coherent superposition of  $v'=2$  and  $v'=4$ . Else same as in Fig. 8.7.

## 8.2 Molecular $\pi$ -pulse (PI)

Molecular  $\pi$ -pulses are light fields that transfer a thermal ensemble of states (a Boltzmann distribution) completely into another electronic state. They are analogous to atomic  $\pi$ -pulses where population of the ground state level is transferred completely to the excited state of the two-level system. The name  $\pi$ -pulse originates from these experiments, since a possible solution is to wait half a Rabi-cycle and then switch off the pulse. More sophisticated and robust mechanisms use chirped pulses, that transfer population in an adiabatic fashion [145, 146]. The concept of chirped pulses could be transferred to the molecular regime as demonstrated by Wilson and coworkers [42]. A chirp adapting to the form of the difference potential will make an effective pump-dump while a chirp adiabatically crossing this difference potential will transfer the whole population into the excited state surface. In the following the optimal  $\pi$  pulse for the potassium dimer is designed and analyzed.

**Single initial state.** At first the simpler problem is considered, where population is initially concentrated only in a single vibrational state and is

transferred by a suitably tailored pulse into the  $A^1\Sigma_u$  state. A summary of the resulting pulses starting from different initial states is shown in Fig. 8.10. Obviously the optimal pulses depend on the initial state. Figures 8.10(a) and 8.10(d) and also Fig. 8.10(c) and Fig. 8.10(f) bear near resemblance and are extremely ordinary consisting of a double or a single pulse, surrounded by two small amplitude pulses, at the same center frequency. Figures 8.10(b) and 8.10(e) are an intermediate case, where two main frequencies seem to be more favorable for an efficient transfer.

**Thermal initial state.** Using the new functional introduced in section 7.3 it is now possible to obtain a real molecular  $\pi$ -pulse. The initial population is exemplarily taken to be a thermal distribution involving five vibrational states in the ground state of  $K_2$ . In this case  $s=1$ ,  $k=m=5$  in equation 7.19. As target of the optimization the projector onto the first

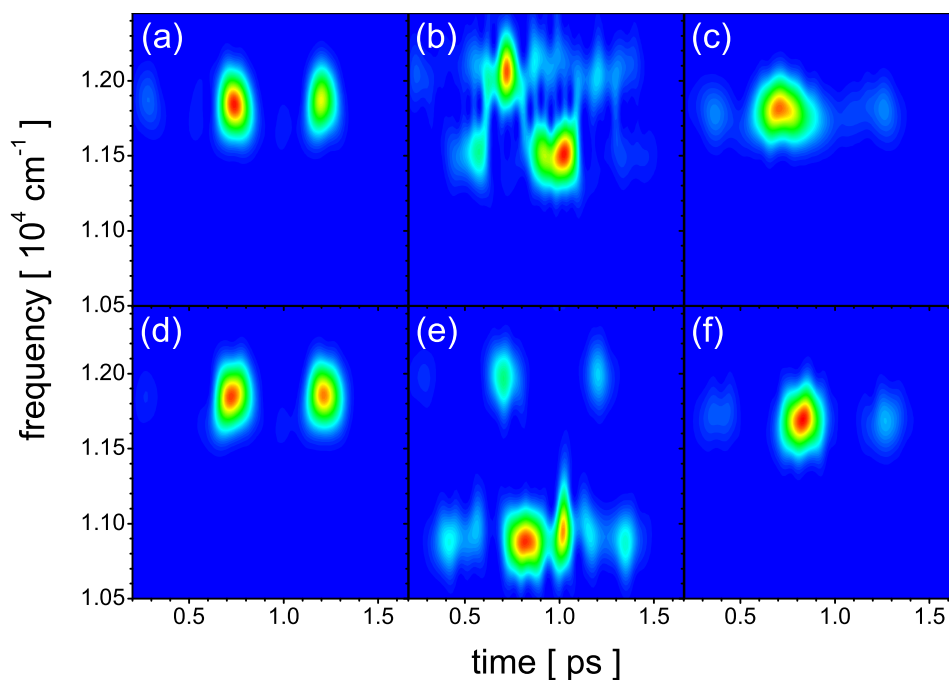


**Figure 8.10:** STFT of pulses that transfer population concentrated initially within a vibrational ground eigenstate  $v''$  into  $A^1\Sigma_u$ . Population is initially in (a)  $v''=0$ . (b)  $v''=1$ . (c)  $v''=2$ . (d)  $v''=3$ . (e)  $v''=4$ . (f)  $v''=5$ .

excited electronic state (A) is considered. The resulting optimal pulse is shown in Fig. 8.11. It has a nonlinear positive chirp and differs considerably from each of the optimal pulses that invert only the population of one single vibrational state [see Figs. 8.10(a)-(f)]. Therefore it can not be obtained by simply averaging over all these pulses.

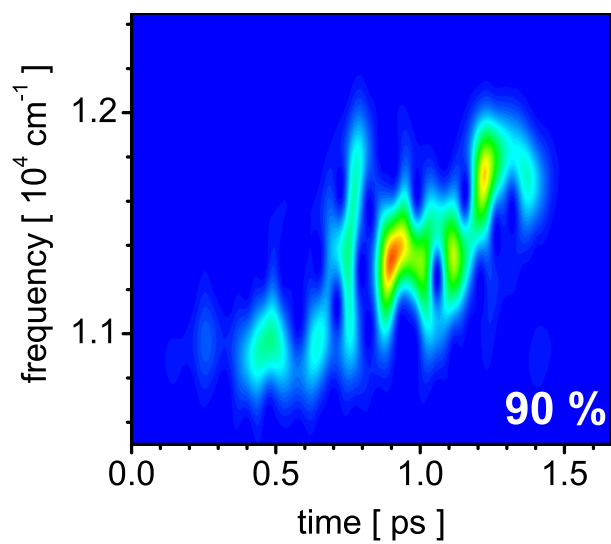


**Figure 8.11:** Molecular  $\pi$ -pulse transferring a initial Boltzmann distribution of five vibrational ground states  $v'' = 0 \dots 5$  into A  $^1\Sigma_u$ .

## Chapter 9

# Comparison experiment and theory

### 9.1 Rotation and orientation effects

The motivation for studying the ro-vibronic motion of potassium dimers is twofold. It is known from earlier work [147] that rotation can harm control and it is important to quantify this effect for the SST control of  $K_2$  studied in section 8.1. Moreover a direct comparison with experimental results is only possible if the rotational degree of freedom is considered besides the already treated initial thermal distribution (see section 8.2). In this section the effect of the molecular rotation on the selective population transfer between vibrational levels is studied with shaped femtosecond pulses. The population distribution within the rotational levels of one vibrational level can not be controlled, i.e. selective control over ro-vibronic levels with these broadband pulses is impossible, since the rotational spacing is ten times smaller than the vibrational energy spacing. This can be understood by rethinking about the control mechanism found to be responsible for state selective control over vibrations. There control was achieved by consecutive pumping and dumping of population between moving vibrational wave packets on both electronic states. A considerable nuclear motion during the pulse action is essential. Rotational wave packets move about ten times slower, their motion lying in the picosecond regime. This however means that a tailored femtosecond pulse would have to extend over several picoseconds in order to control by the same mechanism as found for the mere vibrational motion. This is experimentally difficult to realize.

Following this argument of time scale separation one would expect only a minor effect of the rotations on vibrational control. However for  $K_2$  a further complication arises, that is harmful for control. The transition-dipole moment lies along the internuclear axis. Consequently if the dimer is oriented orthogonal to the field the laser control over the molecule vanishes,

since the dipole moment for this orientation is zero. While the dynamics of rotations are slow their effect can still be important since the rotating dipole vanishes for orthogonal orientation to the external laser field. The theoretical calculations in this section are therefore an extension to earlier studies where only the static orientation of the molecule with respect to the field was considered [35]. Alignment by the laser pulse is however not considered and its influence is studied in future work.

In the following the wave function  $|\psi\rangle$  is represented as a vector in the electronic components (X,A,2,4). The Schrödinger equation can be solved either in coordinate space or in the eigenfunction representation. For completeness, the full spherical Hamiltonian for the ro-vibronic description is explicitly written down in both representations. On the grid the Hamiltonian is:

$$i\partial_t \langle \mathbf{x} | \chi \rangle = \frac{-\hbar^2}{2m} \left[ \partial_r^2 + \frac{1}{r^2} \left( \frac{\partial_\phi^2}{\sin^2(\theta)} + \cot(\theta) \partial_\theta + \partial_\theta^2 \right) \right] \langle \mathbf{x} | \chi \rangle + \langle \mathbf{x} | V_{int}(\epsilon) | \mathbf{x} \rangle \langle \mathbf{x} | \chi \rangle . \quad (9.1)$$

where the usual definition  $\langle \mathbf{x} | \chi \rangle = r \langle \mathbf{x} | \psi \rangle$  was used. This Hamiltonian is three dimensional since the bond length  $r$  and the angles  $\theta, \phi$  specifying the orientation in space of the molecule with respect to the laser field is considered. The interaction with the laser corresponds to the following matrix

$$\langle \mathbf{x} | V_{int}(\epsilon) | \mathbf{x} \rangle = \epsilon(t) \sin(\theta) \{ |X\rangle \mu_{XA}(r) \langle A| + |A\rangle \mu_{A2}(r) \langle 2| + |A\rangle \mu_{A4}(r) \langle 4| + c.c. \} . \quad (9.2)$$

Here the dipole moments between the electronic states  $i, j$  must be evaluated in the coordinate representation:  $\langle \mathbf{x} | i \rangle \mu_{ij} \epsilon(t) \langle j | \mathbf{x} \rangle = \epsilon(t) \sin(\theta) |i\rangle \mu_{ij}(r) \langle j|$  as the dipole moments are only  $r$  dependent. In the eigenfunction representation the Schrödinger equation is [148]

$$i\partial_t \langle nvlm | \psi \rangle = E_{nls} \langle nvlm | \psi \rangle + \sum_{n'l'm'} \langle nvlm | V_{int} | n'l'v'm' \rangle \langle n'l'v'm' | \psi \rangle . \quad (9.3)$$

$$\langle n'l'v'm' | V_{int}(\epsilon) | nvlm \rangle = \epsilon(t) \left\{ |X\rangle \langle A | \mu_{XA}^{n_X l_X, n_A l_A} + |A\rangle \langle C | \mu_{AC}^{n_A l_A, n_C l_C} + |A\rangle \langle D | \mu_{AD}^{n_A l_A, n_D l_D} + c.c. \right\} \quad (9.4)$$

The quantum numbers stand for:  $n$  - electronic state,  $v$  - vibration,  $l$  - orbital angular momentum and  $m$  - eigenvalue of the  $l_z$  component. The dipole transitions moments are calculated by a product of dipole matrix element

and the coefficients  $a_{l,m} = \sqrt{\frac{(l+m+1)(l-m+1)}{(2l+1)(2l+3)}}$  describing the orientation of the molecule relative to the laser [149]. The ro-vibronic eigenstates were calculated by a Numerov scheme on the centrifugally distorted potentials of the mere vibrating potassium molecule. They are in good agreement with spectroscopic data. The number of ro-vibronic eigenstates in each potential used in the expansion of the wave function was increased until the propagation data faithfully converged into agreement with the results on the grid. Since the rotational quantum number is a also measure for the laser field interactions, it is interesting to note that 15 rotations per vibration were needed for accurate results.

As a linearly polarized control laser is assumed, the selection rules  $\Delta m = 0$  ( $l_z$  is conserved) and  $\Delta l = \pm 1$  hold. Throughout this work a  $l'' = 0$  (which implies  $m'' = 0$ ) ro-vibronic eigenstate served as initial state. Therefore the quantum number remains always  $m = 0$ , which is equivalent to ignoring the  $\partial_\phi$  term on the grid.

The grid calculations reduce to an effective two dimensional problem with only the bond length  $r$  of the diatom and  $\theta$  the orientation angle of the molecule with respect to the laser. In the two-dimensional calculations the dipole transition moment was taken and extended to two dimensions by multiplying with  $\sin(\theta)$ . Here the angle  $\theta$  is chosen to be in the interval  $0 \dots 2\pi$ , which is two times the physical range, but necessary to fulfill periodic boundary conditions. The number of grid points in  $r$  were 128 and 80 in  $\theta$  direction.

The eigenfunction calculations also simplify since no sum over  $m$  has to be considered. The geometric coefficients  $a_{l,l',m}$  are then evaluated to  $a_{l,l+1,m=0} = \langle l | \cos(\theta) | l+1 \rangle_{m=0}$  between  $l$  and  $l+1$  and to  $a_{l,l-1,m=0} = \langle l | \cos(\theta) | l-1 \rangle_{m=0}$  between  $l$  and  $l-1$ . Here I recall the pure vibrational case treated in chapter 8, where Eq. (9.1) simplifies to  $H = \left[ \frac{-\hbar^2}{2m} \partial_r^2 + \langle \mathbf{x} | V_{int}(\epsilon) | \mathbf{x} \rangle \right] \langle \mathbf{x} | \chi \rangle$  and in Eq. (9.3) the quantum number of rotations  $l$  has not to be considered.

Calculations in both representations, were performed. The Chebychev scheme [126] was used to numerically solve the two-dimensional non Cartesian Hamiltonian in both space and eigenfunction representation. A second order differencing (SOD) approach is faster, but has dramatic instabilities when applied to the iterative equations of OCT (see section 5.2). Instability of the SOD occurred during the forward propagation of the iterative procedure when the final time  $T$  reached the few ps and also for  $\alpha < 100$ . Instead the Chebychev expansion allows for a bigger time step (6.0 a.u.) and a precise accuracy control. Twelve expansion coefficients were used.

In the following the vibrational only model will be termed 1-D and the ro-vibronic model introduced in this section as 2-D.

**1-D optimized pulses applied to 2-D problem.** The first step was to investigate whether the pulses of chapter 8 are also optimal for a rovi-

brating molecule. As mentioned in the introduction the degree of control is expected to depend on the initial orientation of the molecule with respect to the applied field. Three different orientation are considered [see Fig. 9.1(a)]: no angular orientation,  $\sin^2(\theta)$  and the tightest orientation described by a  $\sin^5(\theta)$ . At first the SST pulse optimizing the transfer from  $v'' = 0$  to  $v'' = 2$

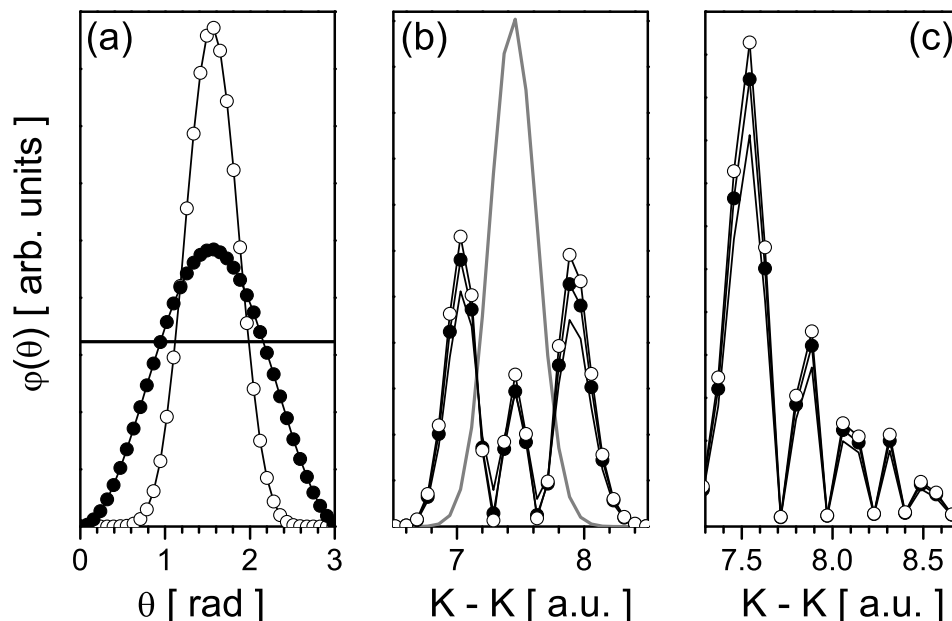


**Figure 9.1:** No angular orientation (line),  $\sin^2(\theta)$  (filled dots) and the tightest orientation described by a  $\sin^5(\theta)$  (hollow dots). (a) Orientation before pulse action. (b) Starting from the  $v'' = 0$  initial state (gray line), the final  $v'' = 2$  state is reached the better the pre-orientation. (c) The better the pre-orientation the better the transfer into the first excited electronic state.

(see section 8.1) is propagated using the ro-vibronic Hamiltonian [Eq. (9.1)]. The yield is calculated as the overlap of a  $v'' = 2$  vibrational eigenstate with the  $r$ -shape of the two dimensional ro-vibronic wave packet at final time  $T$ . The  $r$ -shape is evaluated by integrating over the  $\theta$  direction. The yield achieved by these pulses is only about 50%, if the molecule is not oriented (the angular probability distribution being uniform) with respect to the laser. This yield-loss can be attributed to the fact, that the molecule has finite probability to be oriented parallel to the laser  $\theta = 0$  and  $\theta = \pi$ , where no laser control is possible due to the vanishing dipole moment. Outside these non-accessible angles the laser control still behaves as before, reshaping the i.e. initial  $v'' = 0$   $r$ -shape [see Fig. 9.1(b)] into  $v'' = 2$ . The timescale of the ro-vibronic movement, that reshapes the  $\theta$  distribution is given by the rotational energy level separation in the potassium dimer. It is therefore very slow and a large amount of population stays at  $\theta = 0$  and  $\theta = \pi$  within

the optimization time of  $T = 1.74$  ps. Orientation of the molecule before laser control significantly enhances the yield. The data of Fig. 9.1(b) clearly shows that the better the molecule is oriented in a certain direction (here at right angles to the incident laser) the more pronounced the control. The same dependence of the yield on prior orientation of the molecule can be observed for the  $\pi$  pulses of section 8.2 under the additional influence of rotation. Fig. 9.1(c) shows the r-shape of the A state wave packet at final time. Note the increase of the norm as a function of initial orientation. The yield for an pre-orientation even in  $\theta$  is 73%, for  $\sin(\theta)$  is 83% and for  $\sin^5(\theta)$  is 90%. The line styles in Fig. 9.1(b) and 9.1(c) correspond to the three orientations of Fig. 9.1(a).

**2-D optimization of SST.** To improve the yield of the laser fields of section 8.1 for the two-dimensional problem, optimization with the grid based Hamiltonian of Eq. (9.1) was performed. The initial state considered is shown in Fig. 9.2(a). It is a  $v''=0$  state with a flat angular distribution

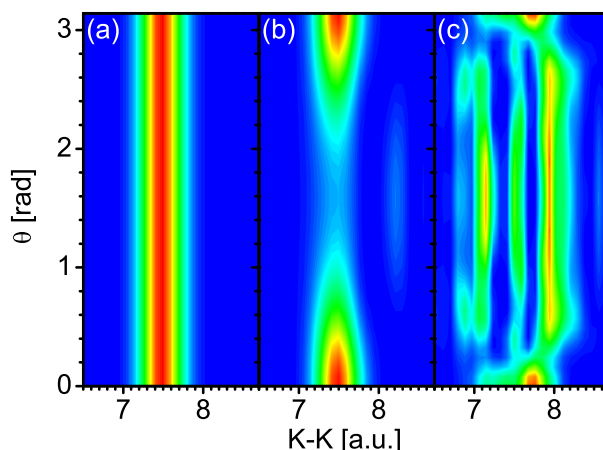


**Figure 9.2:** Snapshots of the two dimensional wave packet evolution on the grid at times (a) 0 ps, (b) 0.44 ps and (c) 1.74 ps.

( $l_z=0$  state). The target state was defined as  $\psi(r, \theta) = v_2''(r)$ , constant in  $\theta$ . Figure 9.3 shows the STFT of the pulse connecting initial to final state with a yield of 80%. The improvement of the yield compared to 56% is therefore significant. The change in shape is only minor as compared to the initial guess pulse taken from the pure vibrational model [see Fig 8.1(a)], but exhibits less pronounced subpulses in between. The propagation data of Fig. 9.2 shows a snapshot of the wave packet for the times (0, 0.44 ps, 1.74 ps) under the action of the pulse of Fig. 9.3. The wave packet at final time  $T = 1.74$  ps has a  $v''=2$  eigenfunction shape in r-direction, disturbed by less amount of finite uncontrollable population at  $\theta = 0$  and  $\theta = \pi$ .

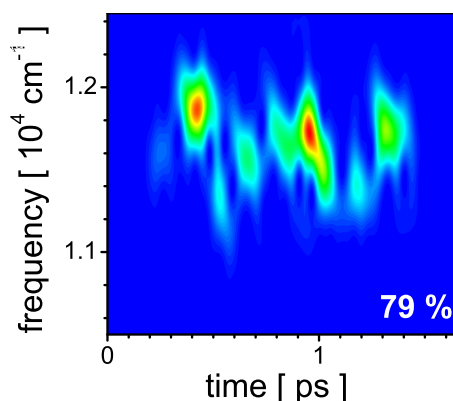


**Figure 9.3:** STFT of the laser pulse optimized within the two dimensional model to maximize the selective transfer from  $v'' = 0$  to  $v'' = 2$ .

**2-D optimization of PI transfer.** Taking the  $\pi$  pulses of section 8.2 as initial guess the complete inversion of population initially in the electronic ground state under the influence of rotations is considered. In order to calculate such an optimal pulse the yield term of the functional is replaced by  $|\langle \psi | P | \lambda \rangle|^2$  with the projection operator  $P = |A\rangle\langle A|$  onto the first excited electronic state  $A$ . It is assumed that all the ground state population is in  $v''=0$   $l''=0$ . The optimal pulse is shown in Fig. 9.4. It resembles a

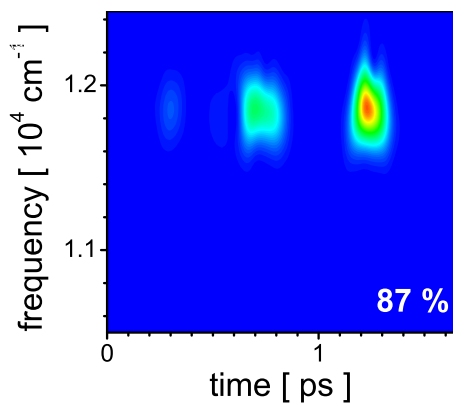


**Figure 9.4:** STFT of the laser pulse optimized within the two dimensional model to maximize the transfer from  $v'' = 0$  to  $A \ ^1\Sigma_u$ .

phase correlated double pulse with an interpulse separation of 510 fs, the vibrational period in the  $A$  state. The pulse of Fig. 9.4 is again similar to the corresponding  $\pi$  pulse [see Fig. 8.10(a)], but has a more pronounced intensity contrast. This optimization improved the transfer efficiency in the case of complete random orientation of the diatom from 73% achieved by the pulse of Fig. 8.10(a) to about 87% [see Fig. 9.4].

## Part III

# New directions of coherent control theory



This part is dedicated to cooling molecules, by two different methods. The first concerns cooling the internal degrees of freedom of an initially hot molecular ensemble by suitably shaped femtosecond pulses. It is a joint project with Prof. David Tannor (Weizmann Institute, Israel). The second approach is concerned with the partial conversion of an atomic to a diatomic molecular condensate via Raman transition, enhanced by a time-dependent magnetic field sweep over a Feshbach resonance. This research was done in collaboration with Prof. Boudewijn Verhaar (TU Eindhoven, The Netherlands).

The optimization of the laser fields in both approaches was performed with OCT based on density matrices. The usual wave packet approach fails, since dissipation plays a central role in both approaches.



## Chapter 10

# Cold molecules, a first approach

In the following the optimal control framework for density matrices [113,150] will be derived. Density matrix calculation provides the natural mathematical framework to describe coherences and dissipation. The density matrix has diagonal elements, that represent the populations and outer-diagonal elements, that are the coherences of the system. It fulfills the requirement  $\rho = \rho^\dagger$ . The Liouville equation  $i\partial_t\rho = -i[H, \rho]$  describes the time evolution of the density matrix. This equation can be extended to include dissipation. There exist many possible approaches, but the one that gives to the dynamics of the system the correct physical and mathematical properties is the Lindblad approach [151]. By correct is meant, that it allows for the probabilistic interpretation of the diagonal elements of the density matrix at any instant of time and is derived in a straightforward way from the quantum model of spontaneous emission [151,152]. For infinite Hilbert spaces it has the form [150,151]

$$\mathcal{L}_d\rho = \sum_{i=0}^{N_2} \left\{ C_i\rho C_i^\dagger - \frac{1}{2} [C_i^\dagger C_i, \rho]_+ \right\}. \quad (10.1)$$

Here the anti commutator is denoted as  $[, ]_+$ .  $C_i^\dagger = |b\rangle\langle a|$  and  $C_i = |a\rangle\langle b|$  are the lowering and raising operators of the  $i$ -th two-level system  $|a\rangle, |b\rangle$ . A total number of  $N_2$  two-level systems constitute altogether the whole system under study. That is in order to write down Eq. (10.1) explicitly each spontaneous emission decay channel of the system has to be treated separately as a two-level system decay and then summed over all these contributions. In order to illustrate this, let us assume a system composed of three levels, one excited level  $|e\rangle$  decaying into two ground state levels  $|g1\rangle$  and  $|g2\rangle$ . The

density matrix of the system is then a 3 x 3 matrix

$$\rho = \begin{pmatrix} \rho_{11} & \rho_{12} & \rho_{13} \\ \rho_{12}^\dagger & \rho_{22} & \rho_{23} \\ \rho_{13}^\dagger & \rho_{23}^\dagger & \rho_{33} \end{pmatrix} \quad (10.2)$$

and the raising operators for the two spontaneous emission channels are

$$C_1 = \begin{pmatrix} 0 & 0 & c_1 \\ 0 & 0 & 0 \\ 0 & 0 & 0 \end{pmatrix}, \quad C_2 = \begin{pmatrix} 0 & 0 & 0 \\ 0 & 0 & c_2 \\ 0 & 0 & 0 \end{pmatrix} \quad (10.3)$$

Having defined the matrices it is simple to evaluate Eq. (10.1)

$$\begin{aligned} \mathcal{L}_d \rho &= \begin{pmatrix} \gamma_1 \rho_{33} & 0 & -\frac{\gamma_1}{2} \rho_{13} \\ 0 & 0 & -\frac{\gamma_1}{2} \rho_{23} \\ c.c. & c.c. & -\gamma_1 \rho_{33} \end{pmatrix} + \begin{pmatrix} 0 & 0 & -\frac{\gamma_2}{2} \rho_{13} \\ 0 & \gamma_2 \rho_{33} & -\frac{\gamma_2}{2} \rho_{23} \\ c.c. & c.c. & -\gamma_2 \rho_{33} \end{pmatrix} \\ &= \begin{pmatrix} \gamma_1 \rho_{33} & 0 & -\frac{\gamma}{2} \rho_{13} \\ 0 & \gamma_2 \rho_{33} & -\frac{\gamma}{2} \rho_{23} \\ c.c. & c.c. & -\gamma \rho_{33} \end{pmatrix}. \end{aligned} \quad (10.4)$$

Here  $\gamma_i = c_i c_i^\dagger$  and  $\gamma = \gamma_1 + \gamma_2$ . Equation (10.4) is in words: the population of the excited state decays into both ground state levels with a time constant  $\gamma$  that is the sum of both these channels. The coherences between ground and excited state decay with half of the excited state lifetime. This is also known as  $T_1/T_2$  time decay mechanism, where the population decays with a time constant  $T_1$  that is always longer than the time constant of coherence decay  $T_2$ . The decaying population fills the ground state levels, each with its own rate  $\gamma_1$  or  $\gamma_2$ . So far the example, now let us turn to the derivation of the OCT equations.

The natural extension of the coherent control functional to the case of density matrices is to replace the wave functions and use as the dynamical constraint instead of the Schrödinger, the Liouville equation of motion [113,150]

$$\begin{aligned} J &= \text{tr}\{\rho_f \rho(T)\} - \alpha \int_0^T \epsilon^2 dt \\ &\quad - 2\text{Re} \left\{ \int_0^T \text{tr} \left\{ \left( \frac{\partial \rho}{\partial t} - \mathcal{L}(\rho) \right) \lambda \right\} dt \right\} \end{aligned} \quad (10.5)$$

Variation of this equation leads into

$$\frac{\partial \rho}{\partial t} = \mathcal{L} \rho, \quad \rho(0) = \rho_i \quad (10.6)$$

$$\frac{\partial \lambda}{\partial t} = -\mathcal{L}^\dagger \lambda, \quad \lambda(T) = \rho_f \quad (10.7)$$

$$\epsilon(t) = -\frac{s(t)}{\alpha} \text{Re tr} \{ \lambda \mu \rho \} \quad (10.8)$$

Note that the generalization of the overlap for matrices is the trace operation  $\text{tr}\{\}$ . The target state at final time  $T$  is  $\rho_f$ . The dipole matrix is  $\mu$  and  $\lambda$  is the conjugate density matrix (Lagrange multiplier) introduced to fulfill the dynamical constraint at all times. While the density matrix was defined to fulfill the Liouville equation with a Liouvillian  $\mathcal{L} = -i[H, \rho] + \mathcal{L}_d$  including dissipation,  $\lambda$  fulfills a different equation that corresponds to a backward in time propagation. Inserting the explicit expression for the conjugate of  $\mathcal{L}$  into Eq. (10.7) one obtains

$$\partial_t \lambda = +i[H, \rho] - \left( \sum_i C_i^\dagger \lambda C_i - \frac{1}{2} [C_i^\dagger C_i, \lambda]_+ \right). \quad (10.9)$$

The signs are reversed and the role of  $C_i$  and  $C_i^\dagger$  in the first summand interchanges due to conjugation. Evaluating the dissipative part for the previously introduced three level system illustrates this difference

$$\mathcal{L}_d \lambda = \begin{pmatrix} 0 & 0 & -\frac{\gamma}{2} \lambda_{13} \\ 0 & 0 & -\frac{\gamma}{2} \lambda_{23} \\ c.c. & c.c. & -\gamma \lambda_{33} + \gamma_1 \lambda_{11} + \gamma_2 \lambda_{22} \end{pmatrix}. \quad (10.10)$$

This set of equations is again solved iteratively using the Krotov or modified Krotov method [150] as described already in section 5.1. In contrast to the wave function analog of Eq. (10.8) here the coherences play a central role in shaping the optimal field as will be discussed in detail in the following section, where the optimal control equations based on density matrices will be applied to optimize STIRAP sequences.

In this chapter the Arnoldi method [153], which is a generalization of the short-iterative-Lanczos algorithm to complex asymmetric Liouville operators, was used to propagate in time the Liouville equation with dissipation. However there exist further schemes like split-operator with a symmetrized dissipative part to conserve the norm [154], and two further polynomial methods the Newton and Faber [155, 156] approximation. An efficient propagation scheme that uses a wave packet approach to the Liouville-von Neumann equation for dissipative systems [157] could not be used since the initial state considered is thermal and therefore an incoherent superposition.

## 10.1 Simple example: STIRAP an optimal control solution

STIRAP [136] is the optimal solution for coherent transfer between two states via a decaying excited state. No population is lost during the transfer affected by dissipation on the same timescale, since the population is transferred adiabatically via a dressed state that is a superposition of initial and

target state with no decaying state component. The superposition state is generated by a counterintuitive ordering of frequencies, the dump preceding the pump pulse. It is expected, as will be proven in a moment, that these optimal solutions do not come out of the closed form, rapidly convergent optimal control theory (OCT) formulation based on mere population evolution [27, 29]. Therefore there have been several attempts to devise other optimal control schemes also based on a wave packet description, like local control [112, 158] or gradient-type [32, 159] optimizations to naturally include these counterintuitive solutions. These methods however lack the global search capability of the closed form expressions and are therefore inferior. This section shall illustrate that it is not necessary to resort to these less optimal schemes, since OCT based on density matrices as written down in Eqs. (10.6-10.8) naturally includes the STIRAP solutions. This is due to the fact, that the electric field is build from the coherences as well as populations in the system [see Eq. (10.8)]. In contrast, the wave function OCT is not able to optimize STIRAP due to Eq. 5.10. This can be proven by contradiction. Without loss of generality let us assume the typical  $\Lambda$  system with ground state levels  $|g1\rangle$  and  $|g2\rangle$  and decaying excited state level  $|e\rangle$ . Let us assume further that wave packet OCT has converged into the counterintuitive STIRAP sequence. Convergence means that  $\psi$  and the Lagrange multiplier  $\lambda$  proceed along the same path in phase space. Since the field is a STIRAP sequence the population in the excited state  $\lambda_e$  and  $\psi_e$  is zero. Hence using Eq. (5.10) one obtains for the  $\Lambda$  system

$$\epsilon(t) = -\frac{s(t)}{\alpha} \text{Im}\{\langle \lambda_{g1} | \mu | \psi_e \rangle + \langle \lambda_{g2} | \mu | \psi_e \rangle + c.c\} = 0! \quad (10.11)$$

and the field is for all times zero, which is in contradiction to the assumption, that it is a STIRAP field.

If instead of the Krotov way of updating the field as assumed in Eq. (10.11), the modified Krotov is used the statement of the above proof is less strict. In this case it states that the *correction* to the field vanishes ones the STIRAP field is found. This proof was also checked numerically. The wave packet OCT in combination with Krotov is incapable of finding a STIRAP solution, even if the initial guess was already counterintuitive. Instead after some iterations the zero field solution emerged. However using the modified Krotov it was possible to optimize STIRAP, but it took several thousand iterations, since the corrections are proportional to the square of the populations and the populations of the decaying states being already small for counterintuitive pulse sequences close to STIRAP. A consequence of slow convergence is that the initial guess has to be already close to the optimal STIRAP solution.

The above mentioned proof breaks down for density matrix OCT, since clearly in the equation that predicts the electric field for the next iteration both populations and coherences enter. In STIRAP the populations for

the decaying states vanish, however *not* their coherences to the other levels. This is the key reason, why density matrix OCT includes counterintuitive solutions efficiently in its solutions space. To illustrate this, optimizations on the  $\Lambda$  system will be performed in the following.

In the density matrix formalism the current state of the  $\Lambda$  system is described by  $3 \times 3$  matrix. A decay using wave functions can only be described by an imaginary term  $i\gamma$ , which physically is a decay into nowhere. In the Lindblad formulation decays into nowhere do not exist and each decay channel must have a source and a sink. Hence the  $\Lambda$  system must be extended by a fourth, dark state  $|d\rangle$ . It merely serves as sink of the population decaying from the excited state  $|e\rangle$  and has no dipole coupling to any other state. This darkness of the state just defines that the population that decayed is lost to the laser transfer. A spontaneous decay back into the ground state levels would also have been a possibility, but it is not the exact analog of the  $i\gamma$  decay. The respective energies in wave numbers are  $\{E_{g1} = 0, E_e = 10973 \text{ cm}^{-1}, E_{g2} = 2195 \text{ cm}^{-1}\}$ . Due to the further dark state the density matrix is  $4 \times 4$

$$\rho = \begin{pmatrix} |g1\rangle\langle g1| & |g1\rangle\langle g2| & |g1\rangle\langle d| & |g1\rangle\langle e| \\ c.c. & |g2\rangle\langle g2| & |g2\rangle\langle d| & |g2\rangle\langle e| \\ c.c. & c.c. & |d\rangle\langle d| & |d\rangle\langle e| \\ c.c. & c.c. & c.c. & |e\rangle\langle e| \end{pmatrix}, \quad (10.12)$$

and the lowering operator describing spontaneous emission is

$$C = \begin{pmatrix} 0 & 0 & 0 & 0 \\ 0 & 0 & 0 & 0 \\ 0 & 0 & 0 & \Gamma \\ 0 & 0 & 0 & 0 \end{pmatrix}. \quad (10.13)$$

The consideration of coherences together with the  $\Lambda$  system extended by a dark state are the essentials to obtain STIRAP-type solutions. Fig. 10.1(a) displays the short-time Fourier transform (STFT) of the initial guess pulse. It was designed to have already the counterintuitive ordering of frequencies. However as the evolution of the populations in the system shows the upper state is populated to a considerable amount [see Fig. 10.2(a)]. This means, in the case spontaneous emission is turned on ( $\Gamma^{-2} \approx 150 \text{ fs}$ ), the target state is only poorly reached at final time [Fig. 10.2(c)]. The optimal control pulse found in the case of this decay strength ( $\Gamma^{-2} \approx 150 \text{ fs}$ ) is shown in Fig. 10.1(b). This pulse improves considerable on the amount of population transferred to the target state [see Fig. 10.2(d)]. That this pulse is indeed nearly perfectly a STIRAP pulse can be seen in the propagation without dissipation ( $\Gamma = 0$ ), where at final time a population of less than 2% accumulates in the excited state [Fig. 10.2(b)]. Due to the decay of coherences ( $T_2 = 2T_1$ ) in addition to population decay the transfer can not be complete.

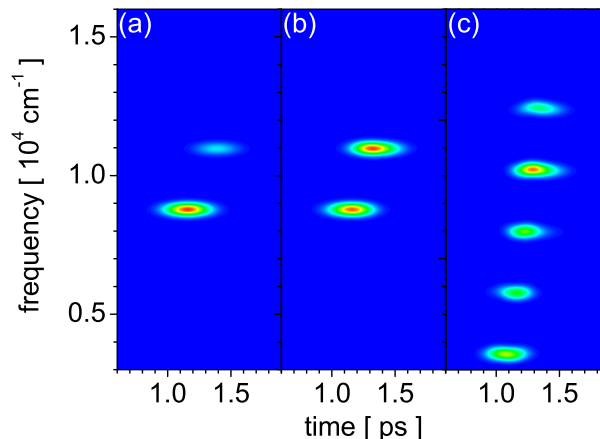


**Figure 10.1:** (a) Initial guess pulse. (b) Optimal pulse for  $\Gamma^{-2} \approx 150$  fs. (c) Optimal pulse for  $\Gamma^{-2} \approx 50$  fs.

In the case of even stronger decay ( $\Gamma^{-2} \approx 50$  fs) leading to even shorter  $T_1$  and  $T_2$  times, the optimal pulse of Fig. 10.1(c) generalizes STIRAP. Instead of only two center frequencies a comb of frequencies emerges to cope with the stronger coherence (or polarization) decay. The extra frequencies serve to build up further coherent bridges between the initial and final state, increasing thereby the overall coherence, in order to compensate for the stronger  $T_2$  decay.

After this simple illustrative example density matrix OCT is applied in the next section to the problem of molecular cooling as pioneered by Tannor and coworkers [150, 160].

## 10.2 Molecular cooling with shaped laser fields

Before presenting the results on molecular cooling a definition of cooling must be given. This introduction is based on a paper by D. Tannor [161]. The coolness of a sample is best defined by its purity, that is  $\text{tr} \{\rho^2\}$ , which is the expectation value of  $\rho$  itself. The adequacy of this measure is due to the fact that  $\text{tr} \{\rho^2\} = \int \int dq dp \rho^2(q, p)$ , the phase space density [160]. That means every pure ensemble  $\rho = |\psi\rangle\langle\psi|$  is absolutely cool, i.e. a coherent superposition or wave packet is absolutely cool. In essence it is important how the initial statistical mixture is transformed into a pure state. If this is done by just stripping away population, then  $\text{tr} \{\rho^2\}$  is constant<sup>1)</sup>, that means phase-space density is not increased and the sample is not cooler than it was initially in the sense of having approached Bose condensation. Now it is well known that the coldest gas in the universe, the Bose-Einstein-Condensate,

<sup>1)</sup>However in this process the von Neumann entropy decreases.

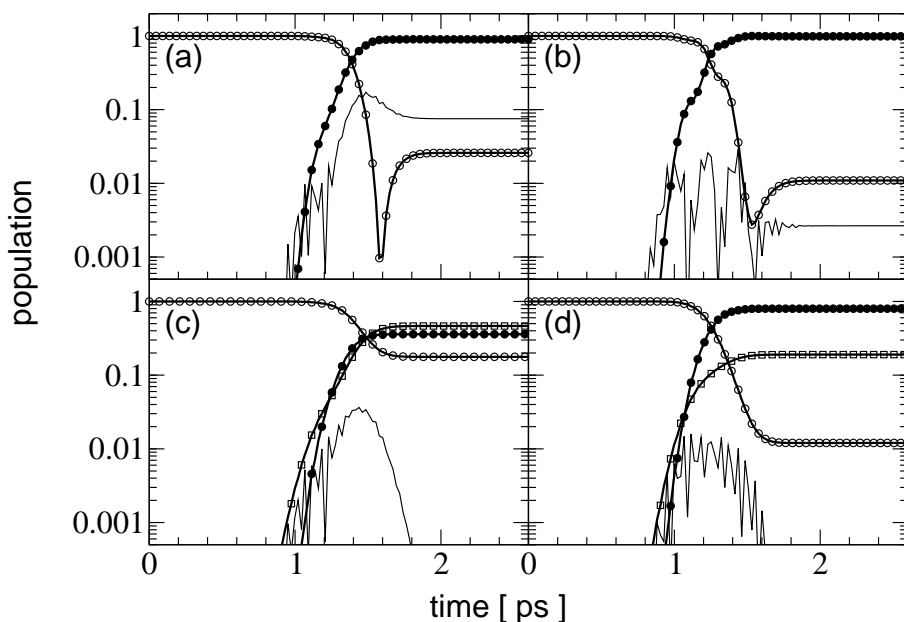


**Figure 10.2:** State populations of the extended  $\Lambda$  system: initial (filled dots), target (hollow dots), excited decaying (straight line) and dark/sink (hollow squares). (a) Evolution of population under influence of initial guess pulse.  $\Gamma = 0$ . (b) Evolution of population under influence of optimal pulse.  $\Gamma = 0$ . (c) Same as (a) but  $\Gamma^{-2} \approx 150$  fs. (d) Same as (b) but  $\Gamma^{-2} \approx 150$  fs.

can only be reached by increasing phase-space density. The central question of cooling is then: How can a statistical ensemble be transformed into a pure one, increasing at the same time the phase-space density? Atom physics tells us, that lasers can be used to accomplish that task. At first, cooling using electric fields seems to be a contradiction, since it is impossible to increase phase space density with time-dependent terms in the Hamiltonian as was shown in a paper from Ketterle and Pritchard [162]. One essential part of this paper can be summarized in a single equation, that calculates the change in purity achieved through an electric field [161]

$$\frac{d}{dt} \text{tr} \{ \rho^2 \} = 2 \text{tr} \{ \rho \dot{\rho} \} = 2 \text{tr} \{ \rho (-i) [H, \rho] \} = 0 ! \quad (10.14)$$

This equation states, that no cooling can be achieved, due to the permutation invariance of the trace  $\text{tr} \{ \rho H \rho - \rho \rho H \} = \text{tr} \{ \rho \rho H - \rho \rho H \} = 0$ . The essential key ingredient missing is dissipation, i.e. in the form of spontaneous emission. Interestingly however dissipation does not lead automatically to cooling, but can also lead to heating of the ensemble, depending on the initial population distribution [161]. As an example take a pure ensemble of two-level atoms, where the population of all atoms is initially in the decaying excited state. That means initially the ensemble is absolutely cool

since it is in a pure state. As time progresses decay heats the ensemble since the atoms will then be in an incoherent superposition: some atoms being already in the ground and other still in the excited state.

Interactions with the externally controllable laser field do not change the

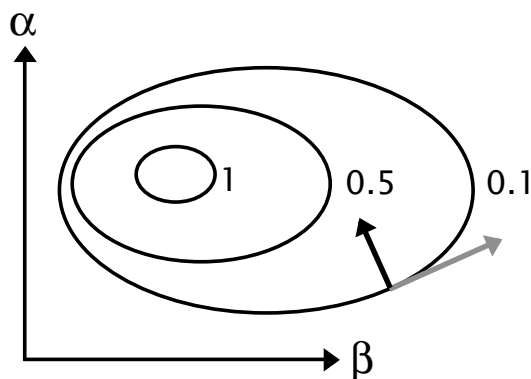


**Figure 10.3:** Schematic showing isopurity surfaces and the control possible with Hamiltonian (gray arrow) and dissipative operations (black arrow). The multidimensional space is spanned by sets of quantum numbers  $\alpha$  and  $\beta$  the purity depends upon.

purity and therefore move the ensemble around on an isopurity surface in phase space<sup>2)</sup>, while dissipation essentially uncontrollable is the only mechanism connecting the isopurity surfaces. A schematic showing these relations is shown in Fig. 10.3, where the black arrow shows a dissipative and the gray arrow an Hamiltonian action. Cooling is therefore an interplay of a controllable part: the laser field and an uncontrollable part: dissipation. Alternately cooling can be viewed as a two-step process, since  $d/dt(\text{tr}\{\rho^2\})$  does not depend on the electric field, however the second derivative of  $\rho$  does. Molecular cooling is then in a first time step an uncontrollable slow dissipative action and in a second step a purely Hamiltonian fast action. In atoms it is not important that dissipation is uncontrollable since closed transitions exist, that means dissipation takes the system on the same way back as it was excited. Even in Raman cooling the dissipation is not closed but strongly controlled, since the spontaneous emission is most favorable in the case of no velocity change. In molecules however dissipation takes the excited population back not only to the levels that where initially populated, but also to many others, leading essentially with each excitation to an ever increasing population spread over the molecule.

Bartana, Tannor and Kosloff proposed to solve this intricate problem of molecular cooling by using density matrix OCT [150]. They decomposed the problem into cooling of the vibrational and afterwards of the rotational

<sup>2)</sup>a surface where the purity is constant

manifold. The model for vibrational cooling was a molecule consisting of two electronic potentials. They found the following cooling mechanism: the optimal laser field does not interact with the target level in the ground potential (“dark state”), while it pumps the population in *all other* ground state levels to the excited state where it decays back into *all* ground state levels, including the dark state. After several vibrational periods of the molecule the induced cycling of population (excitation and decay) finally fills the dark state and the molecule ends in a pure state. Rotational cooling was studied in a truncated rotational manifold. The optimal cooling mechanism found in this case makes use of an alternation between right and left circularly polarized light [163].

In both cases the optimal pulses emerged automatically from the density matrix OCT [see Eq. (10.5)]. Note that the goal is to make the purity of the molecule equal to 1, however no optimal control scheme can be derived if  $\text{tr}\{\rho^2\}$  is defined to be the target in the functional  $J$ . Therefore one has to use the functional of Eq. (10.5) and define as target state some arbitrary pure state. As a consequence the optimal pulse shape and possibly the final purity can depend on the chosen target state. However from controllability arguments [164, 165] such a dependence on the target state is not expected to occur, since two different density matrices with the same purity can be transformed into one another by an Hamiltonian operation. This mere population transfer takes place fast compared to the dissipation. Therefore having reached some final value for the purity, transformation between the class of ensembles with the same purity but different population distribution among the levels in the system is possible.

The following numerical results however contradict this mathematical argumentation. Pure vibrational cooling is studied in a simplified molecular system consisting of an excited set of five vibrational levels that decay into five other vibrational ground state levels. The energy spacings are  $\Delta\lambda_g \approx 92 \text{ cm}^{-1}$  (360 fs),  $\Delta\lambda_e \approx 67 \text{ cm}^{-1}$  (520 fs) and correspond to the values in the potassium dimer. A rotating-wave approximation is performed and the dipole moments between excited and ground state levels were calculated by taking into account the  $r$ -dependent  $K_2$  dipole moments. Spontaneous emission occurs between all excited and all ground state levels and is not subject to any selection rule. It was taken in the Lindblad form, where the  $i$ -th lowering operator is  $\Gamma_i C_i$ . The decay constant  $\Gamma_i^{-2} \approx 2.5 \text{ ps}$ , the final time  $T = 28 \text{ ps}$  and a time step 2.3 fs were chosen. The initial state was taken to be the  $10 \times 10$  matrix with all zeroes except to the first five diagonal elements, that were set to 0.2. This is, the initial population is distributed equally over the five ground state levels. The STFT of the optimal pulses are shown in Fig. 10.4 for two different target states:  $v'' = 0$  [10.4(a)] and  $v'' = 2$  [10.4(b)]. The purity as a function of time for these two cases is shown in Fig. 10.5. Clearly not only do the pulse shapes differ considerably, but also the purity at the end depends strongly on the final pure state. As discussed

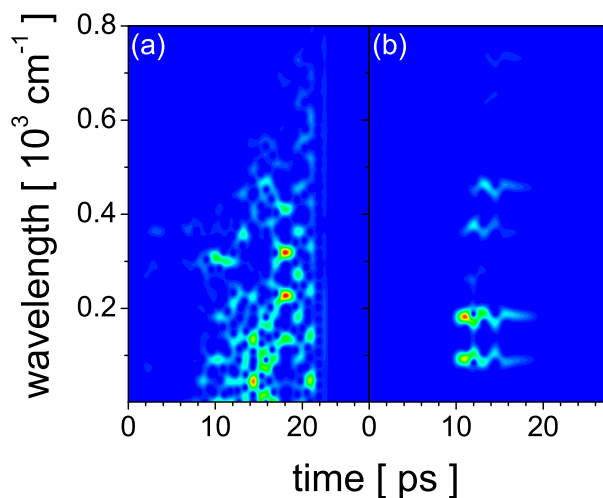


**Figure 10.4:** STFT of optimal pulses that cool an initial population distributed evenly over ground state levels. The pure target state was chosen to be  $v'' = 0$  (a) and  $v'' = 2$  (b).

earlier this result is mathematically not expected, since if it is possible to reach an ensemble purity of 0.7 with the population mostly in  $v'' = 0$  [see Fig.10.5 line], why should it not be possible to concentrate the population in  $v'' = 2$  without losing purity, just by a Hamiltonian operation?! The only explanation to this discrepancy is to assume that the OCT scheme does not find the most optimal solution or that the solution is not allowed due to the constraint on the pulse energy or shape  $s(t)$ . The optimal laser fields from chapter 8 connecting two pure states are in this mathematical sense also imperfect, since their yield is less than 100%. From the mathematical point of view both states are pure and therefore there must exist a Hamiltonian operation that fulfills the task with unit efficiency independent of the initial/final state pair.

Even more surprising is that the purity at earlier times reaches a maximum and falls off again on timescales much faster than dissipation before final time [see Fig. 10.5]. A purity change with a timescale faster than dissipation (2.5 ps) should be impossible, since the fast acting Hamiltonian operations are purity conserving.

The optimal pulses of Fig. 10.4 have to increase the purity and steer the population into some final density matrix. Instead by defining the final state to have the same diagonal elements, but the necessary coherences on the off-diagonal to be pure it is possible to eliminate the second, population transfer step from the pulses. The target state with  $\text{tr}\{\rho^2\}$  having the same

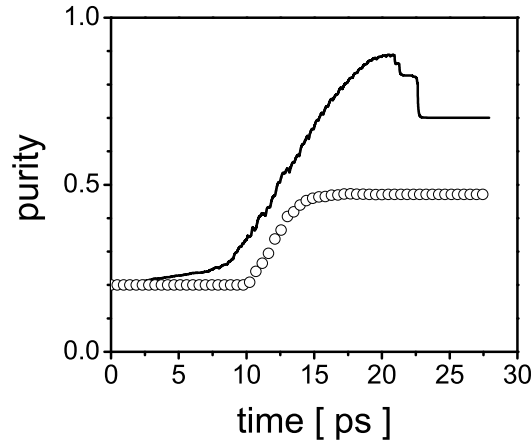


**Figure 10.5:** The evolution of purity in time for the two pulses of Fig. 10.4. Line corresponds to 10.4(a) and hollow dots to 10.4(b).

diagonal elements as the initial matrix is the density matrix

$$\rho_f = \begin{cases} 0.2 & \text{if } i, j = 1 \dots 5 \\ 0.0 & \text{else} \end{cases} \quad (10.15)$$

For this calculation the time step was reduced to  $dt = 1.16$  fs. The optimal pulse now resulting is shown in Fig. 10.6(c) and the purity at final time  $T = 7$  ps is 80% [see Fig. 10.7 line], that is a higher purity than was achieved for the two previous optimizations, that used a specific eigenstate as final state. In order to study the effect of the decay rate on the final purity a decay rate five times slower, that is  $\Gamma_i^{-2} \approx 12.5$  ps, is studied. Clearly for this system the lower spontaneous emission rate will lead to slower cooling rate and a smaller final purity. What happens however if not all, but only one dissipative channel is increased by a factor of five? Calculations, where only the  $v' = 0 \rightsquigarrow v'' = 0$  spontaneous emission channel is increased by a factor of five lead to the optimal field of Fig. 10.6(a) and to a purity versus time as shown in Fig. 10.7. Increasing more dissipative channels (all five connecting to  $v'' = 0$ ) by a factor of five results in the pulse of Fig. 10.6(b) and the purity in Fig. 10.7. A comparison of all the tailored fields in Fig. 10.6 clearly shows that the optimal pulse adapts to the spontaneous emission characteristics. Moreover Fig. 10.7 shows that an increase of only part of the channels can lead to an increased purity at final time. This increase of dissipation can be easily done numerically, however it is not clear what physical mechanism could be used to achieve such an increase. One possibility is to place the molecule inside a lossy cavity. It is known that the cavity changes the vacuum field density of modes increasing or decreasing thereby spontaneous emission [166–169]. The field modes of the cavity can be controlled by the curvature of the cavity mirrors [170]. The effect of the cavity can be

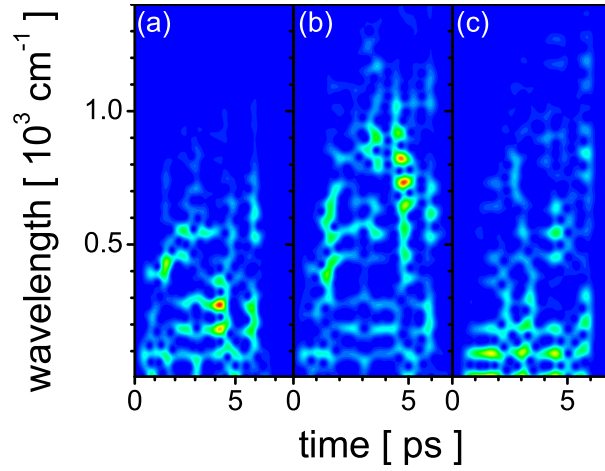


**Figure 10.6:** STFT of cooling pulse for different dissipation. (a)  $\Gamma_i^{-2} \approx 12.5$  ps but dissipative channel  $v' = 0 \rightsquigarrow v'' = 0$  increased by factor of five. (b)  $\Gamma_i^{-2} \approx 12.5$  ps but all dissipative channels ending in  $v' = 0$  enhanced by factor of five. (c) All dissipative channels with  $\Gamma_i^{-2} \approx 2.5$  ps.

expressed by a simple formula [166]

$$\eta = \frac{3Q\lambda^3}{4\pi^2V} \quad (10.16)$$

where  $\eta$  is the ratio of spontaneous emission to free-space emission rate,  $Q$  is the cavity quality factor,  $\lambda$  the transition wavelength and  $V$  the mode volume. In experiments  $\eta \approx 3 \dots 5$  can be realized. In a cavity a comb of transversal modes can be created, that depend on the curvature of the mirrors. Molecular cooling in a cavity was proposed by Vuletic et. al. [166], where the cavity mode is blue shifted with respect to all molecular transition, so that in a Raman scattering event the loss of energy is enhanced. Once the molecule is translationally cold the internal degrees of freedom could perhaps be cooled by matching the cavity modes with the band heads of ro-vibronic transitions. This possibility is the topic of further research as well as obtaining simpler cooling pulses, since electric fields like the one shown in Fig. 10.8 are not yet realizable.

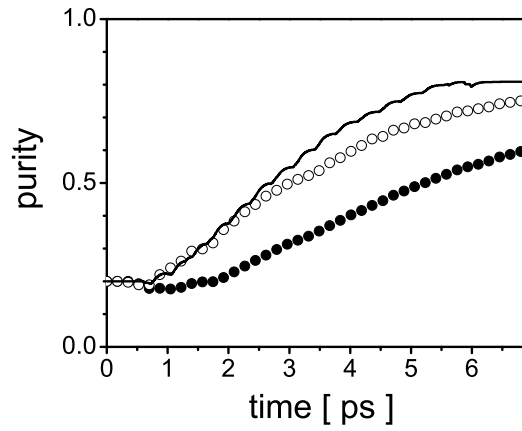


**Figure 10.7:** Purity evolution for the three pulses of Fig. 10.6. 10.6(a) corresponds to filled, 10.6(b) to the hollow dots and 10.6(c) to the line.

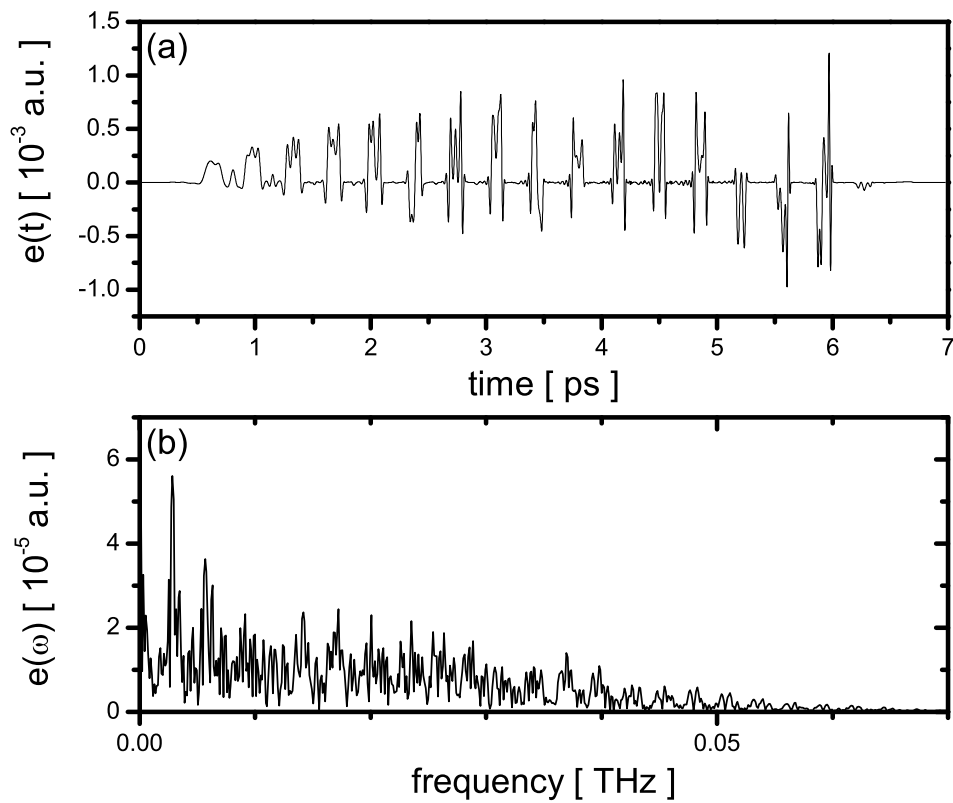


**Figure 10.8:** (a) Electric field in rotating wave approximation of the pulse in Fig. 10.6(c). (b) The spectrum of this pulse.



# Chapter 11

## Cold molecules, a second approach

### 11.1 Bose-Einstein-Condensates and Feshbach resonances

**The Bose-Einstein-Condensate (BEC).** The many-body Hamiltonian describing  $N$  interacting bosons confined by a trapping potential  $V_{trap}$  is given, in second quantization, by

$$H = \int d^3r \left[ -\frac{\hbar^2}{2m} \nabla^2 + V_{trap}(\mathbf{r}) \right] \hat{\psi}^\dagger(\mathbf{r}) + \frac{1}{2} \int \int d^3r d^3r' \hat{\psi}^\dagger(\mathbf{r}) \hat{\psi}^\dagger(\mathbf{r}') V(\mathbf{r} - \mathbf{r}') \hat{\psi}(\mathbf{r}') \hat{\psi}(\mathbf{r}) \quad (11.1)$$

where  $\hat{\psi}(\mathbf{r})$  and  $\hat{\psi}^\dagger(\mathbf{r})$  are the boson field operators that annihilate and create a particle at the position  $\mathbf{r}$ , respectively, and  $V(\mathbf{r} - \mathbf{r}')$  is the two-body interatomic potential. The dynamics of the condensate are predicted by the Heisenberg equation with the many-body Hamiltonian Eq. (11.1):

$$i\hbar \partial_t \hat{\psi}(\mathbf{r}, t) = [\hat{\psi}, H] \quad (11.2)$$

This equation is solved to first order with the Ansatz  $\hat{\psi}(\mathbf{r}, t) = \phi(\mathbf{r}, t) + \hat{\psi}'(\mathbf{r}, t)$ , where essentially the condensate contribution  $\phi$  is separated out from the bosonic field operator. Here  $\phi(\mathbf{r}, t)$  is a complex function defined as the expectation value of the field operator:  $\phi(\mathbf{r}, t) = \langle \hat{\psi}(\mathbf{r}, t) \rangle$ . Its modulus specifies the condensate density through  $n(\mathbf{r}, t) = |\phi(\mathbf{r}, t)|^2$ . The function  $\phi(\mathbf{r}, t)$  is a classical field having the meaning of an order parameter and is often called the “wave function of the condensate”. In a dilute and ultracold gas only binary collisions in s-wave ( $l=0$ ) geometry can occur, where a single parameter, the s-wave scattering length  $a$  suffices to describe these

interactions. All the details of the two-body potential are subsumed in the scattering length and therefore two potentials resulting in the same scattering length are not distinguishable. This allows one to replace  $V(\mathbf{r} - \mathbf{r}')$  with an effective interaction

$$V(\mathbf{r} - \mathbf{r}') = \frac{4\pi\hbar^2 a}{m} \delta(\mathbf{r} - \mathbf{r}'). \quad (11.3)$$

Inserting this potential into Eq. (11.2) together with the replacement  $\hat{\psi}$  with  $\phi$  yields the Gross-Pitaevskii (GP) equation for the order parameter:

$$i\hbar\partial_t\phi(\mathbf{r}, t) = \left( -\frac{\hbar^2\nabla^2}{2m} + V_{trap} + U_0|\phi(\mathbf{r}, t)|^2 \right) \phi(\mathbf{r}, t) \quad (11.4)$$

with

$$U_0 = \frac{4\pi\hbar^2 a}{m}. \quad (11.5)$$

The validity of the GP equation is based on the condition that the s-wave scattering length be much smaller than the average distance between atoms and that the number of atoms in the condensate be much larger than 1. The mean-field or self-energy term  $U_0|\phi|^2$  results from the above delta-function pseudopotential and shows that the interaction energy in a cloud of atoms is proportional to the density and the scattering length. The sign of the scattering length indicates whether the atomic interaction is effectively repulsive ( $a > 0$ ) or attractive ( $a < 0$ ). For negative  $a$  with  $V_{trap} = 0$  the GP equation does not have a stationary solution. In practice that means the condensate collapses. With a harmonic trap potential and  $a < 0$  the GP equation has a stable solution, but only if the mean-field energy is less than the spacing of the trap levels. When  $a = 0$  the atoms do not interact and the stationary solution equals the single-atom ground-state wave function in the trap potential (except for normalization).

**Feshbach resonances.** Feshbach resonances are scattering resonances that arise when the total energy (internal+translational) of a pair of colliding atoms matches the energy of the quasibound two-atom state, leading to resonant formation of this state during collision. Magnetic tuning is possible if the magnetic moments of the free and quasibound states are different. In a time-dependent picture, the two atoms are transferred to a quasibound state stick together and then return to an unbound state. Such a resonance strongly affects the scattering length (elastic channel). Near a Feshbach resonance the scattering length  $a$  varies dispersively as a function of the magnetic field  $B$ :

$$a = \tilde{a} \left( 1 - \frac{\Delta}{B - B_0} \right), \quad (11.6)$$

where  $\Delta$  is the width of the resonance at  $B = B_0$ , and  $\hat{a}$  is the scattering length outside the resonance. Clearly, the scattering length  $a$  covers the full continuum of positive and negative values, above and below the resonance. A microscopic understanding of a Feshbach resonance can be obtained in a quantum mechanical description of interaction processes between alkali atoms. The effective Hamiltonian describing the collisions of two ground-state alkali atoms is

$$H = \frac{\mathbf{p}^2}{2\mu} + \sum_{j=1}^2 \left( V_j^{hf} + V_j^Z \right) + V^c \quad (11.7)$$

comprising the relative kinetic energy operator with reduced mass  $\mu$ , a single-atom hyperfine  $V_j^{hf}$  and Zeeman term  $V_j^Z$  for each atom  $j$ , and a central two-atom interaction term  $V^c$ . The central interaction  $V^c$  represents all Coulomb interactions between the electrons and the nuclei of both atoms. It depends only on the quantum number  $S$  associated with the magnitude of the total electron spin  $\vec{S} = \vec{s}_1 + \vec{s}_2$ , which can be 0 or 1 for alkali atoms, and the internuclear distance  $r$ :

$$V^c = V_S(r)P_S + V_T(r)P_T \quad (11.8)$$

with  $P_S$  and  $P_T$  the projection on the singlet ( $S = 0$ ) and triplet ( $S = 1$ ) subspaces. The potentials  $V_S$  and  $V_T$  are the Born-Oppenheimer molecular potential curves connected to the  $3^2S_{1/2} + 3^2S_{1/2}$  separated-atom limit; in spectroscopic notation the corresponding molecular electronic states are  $X^1\Sigma_g^+$  and  $a^3\Sigma_u^+$ . At large separations ( $r > 16 a_0$  to  $19 a_0$ , depending on the atomic species), the central potentials may be written as

$$V_{S,T}(r) = -\frac{C_6}{r^6} - \frac{C_8}{r^8} - \frac{C_{10}}{r^{10}} \pm V_E(r). \quad (11.9)$$

The first term represents the van der Waals interaction. It is followed by the next two terms in an electric multipole expansion of the Coulomb interactions between the charge distributions of the two colliding atoms: the dipole-quadrupole and quadrupole-quadrupole interactions. The different permutation symmetries of the molecular electronic wave functions  $\psi_S$  and  $\psi_T$  are responsible for the exchange interaction energy  $V_E(r)$ .

The hyperfine terms are given by

$$V_j^{hf} = \frac{a_j^{hf}}{\hbar^2} \vec{s}_j \cdot \vec{i}_j, \quad (11.10)$$

where  $\vec{s}_j$  and  $\vec{i}_j$  are the electron and nuclear spin operators of atom  $j$  and  $a_j^{hf}$  a constant related to the hyperfine splitting. Alkali atoms have only one valence electron, therefore  $s_1 = s_2 = \frac{1}{2}$ . Under the influence of the hyperfine interaction the electronic ground state ( $3S$  for Na) splits into two new levels, with the total spin vector  $\vec{f} = \vec{i} + \vec{s} = i \pm \frac{1}{2}$  (see Fig. 11.1 at  $B = 0$ ).

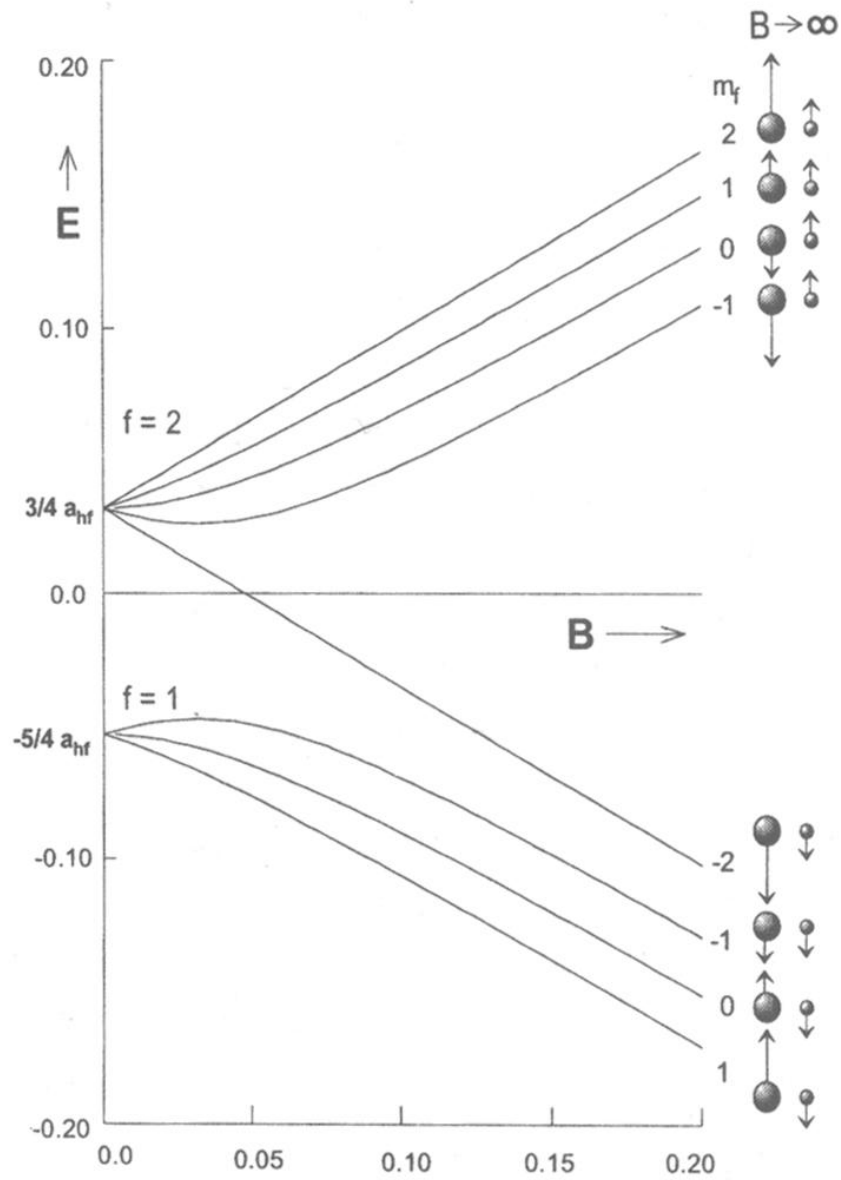


**Figure 11.1:** Hyperfine states of sodium  $|f, m_f\rangle$ . Shown is the energy dependence of these states in an external magnetic field  $B$  (Zeeman dependence). The relative orientation of the nuclear and electron spin is depicted by the large and small balls at the right.  $\vec{f} = \vec{i} + \vec{s}$  is the orientation dependent total spin vector of nuclear  $i$  plus valence electron spin  $s$ . The projection of  $\vec{f}$  on the quantization axis is given by  $m_f$ .

The Zeeman interaction accounts for the external magnetic field. Choosing the z-axis of the laboratory frame along the magnetic field  $\vec{B} = B\vec{e}_z$ , they have the form

$$V_j^Z = (\gamma_e s_{zj} - \gamma_N i_{zj})B. \quad (11.11)$$

Asymptotically, where the two-atom interaction  $V^c$  can be neglected, the system is described by separate atoms, each in an eigenstate of its own hyperfine and Zeeman operators. These are the magnetic-field dependent hyperfine states  $|f, m_f\rangle$  shown in Fig. 11.1. The kind of states with increasing (decreasing) energy with increasing magnetic field are called low-field (high-field) seeking states, respectively. While low-field seeking states can be trapped in a magnetic-field minimum, a BEC in a high-field seeking state can only be trapped by all optical means. The differences in field dependence between the hyperfine states are responsible for Feshbach resonances [171,172]. The details of a cold collision enhanced by a Feshbach resonance is shown schematically in Fig. 11.2. The colliding atoms are assumed to be in the

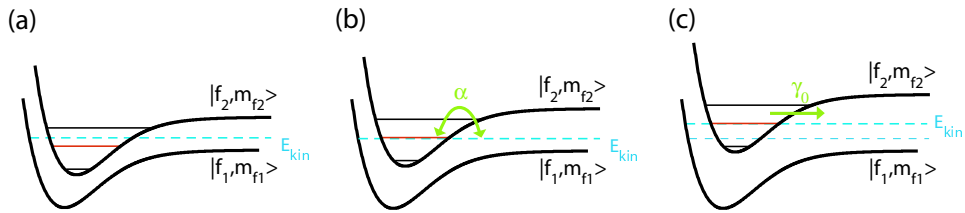


**Figure 11.2:** Shown are the collisional potential energy surfaces of two hyperfine states  $|f_1, m_{f1}\rangle$  and  $|f_2, m_{f2}\rangle$ . The atoms in the BEC are assumed to be in the hyperfine state  $|f_1, m_{f1}\rangle$  possessing a kinetic energy  $E_{kin}$ . (a) Off resonance situation. The colliding atoms can not penetrate the quantum reflection region. (b) The external magnetic field is tuned in resonance with the Feshbach resonance. Spin flip tunneling is now enhanced due to the bound state resonance condition. The tunneling rate is  $\alpha$ . (c) The quasibound state has a local lifetime. If during this time the external field changed, the dissociating atoms acquire additional kinetic energy leading to a trap loss  $\gamma_0$ .

lower energetic hyperfine state  $|f_1, m_{f1}\rangle$ . As they approach each other they enter a small range near the beginning of the long-range region ( $r \approx 20 a_0$ ), where the exchange interaction  $V_E$  is of the same order of magnitude as the hyperfine-Zeeman energies. This is a crucial region because in an external field the hyperfine induced spin flip of the one atom in presence of the other can bind the interacting atoms by bringing them to a hyperfine state  $|f_2, m_{f2}\rangle$  with a higher threshold energy. Normally no bound state of the  $|f_2, m_{f2}\rangle$  scattering potential coincides in energy with the total energy of the colliding atoms and the atoms get reflected back [see Fig. 11.2(a)]. If the Zeeman dependence of the two hyperfine states is different it is possible to tune a bound state of the  $|f_2, m_{f2}\rangle$  scattering potential exactly in

resonance with the collision threshold. Now the atoms can tunnel into the quasibound molecular state, where they are at small interatomic separations and form a molecular condensate [Fig. 11.2(b)]. After some local lifetime of the resonance the two atoms dissociate again. If during this lifetime the magnetic field is decreased and the  $|f_2, m_{f_2}\rangle$  hyperfine state is high-field seeking the quasibound state will have risen in energy. As a consequence the dissociating atoms will have acquired an additional kinetic energy and will be lost from the trap [173]. This decay is characterized by the constant  $\gamma_0$  [ Fig. 11.2(c)]. Note that this decay does not occur if the magnetic field was instead increased.

In the many body Hamiltonian, the spin flips to quasibound states are described by [174]

$$H_{FR} = \alpha \int d^3r \hat{\psi}_m^\dagger(\mathbf{r}) \hat{\psi}_a(\mathbf{r}) \hat{\psi}_a(\mathbf{r}) + c.c., \quad (11.12)$$

where  $\hat{\psi}_m, \hat{\psi}_m^\dagger$  ( $\hat{\psi}_a, \hat{\psi}_a^\dagger$ ) are the annihilation and creation field operators of the molecules (atoms). The  $\alpha$  parameter in Eq. (11.12) is the transition matrix element proportional to the overlap of the molecular continuum and bound state wave functions. The expectation value of the Heisenberg equations for atoms and molecules gives the equation of motion for the condensate fields  $\phi_m = \langle \hat{\psi}_m \rangle$  and  $\phi_a = \langle \hat{\psi}_a \rangle$ :

$$\begin{aligned} i\hbar\dot{\phi}_m &= \left[ -\frac{\hbar^2\nabla^2}{4M} + E_m + \lambda_m n_m + \lambda n_a \right] \phi_m + \alpha\phi_a^2 \\ i\hbar\dot{\phi}_a &= \left[ -\frac{\hbar^2\nabla^2}{2M} + U_0 n_a + \lambda n_m \right] \phi_a + 2\alpha\phi_a^* \phi_m, \end{aligned} \quad (11.13)$$

where  $M$  denotes the mass of a single atom,  $n_m$  and  $n_a$  represent the condensate densities,  $n_m = |\phi_m|^2$  and  $n_a = |\phi_a|^2$ , and  $\lambda_m, U_0$  and  $\lambda$  represent the strength of the molecule-molecule, atom-atom and molecule-atom interactions. The  $\alpha$ -terms that couple the equations describe the tunnelling of pairs of atoms between  $\phi_m$  and  $\phi_a$ -fields. Eq. (11.13) replaces the usual single condensate Gross-Pitaevskii equation (11.4).

The following sections study the stabilization of the naturally forming molecular condensate during a Feshbach resonance via optimally shaped Raman fields in the nanosecond and femtosecond regime.

## 11.2 Optimal conversion of an atomic to a molecular BEC

Cold molecules have been produced and detected through photoassociation [175–177] of laser-cooled atoms, where the molecules are formed incoherently in many different ro-vibrational levels and have a relatively large

energy spread of  $100 \mu\text{K}$ . However it is also possible to form molecules by a stimulated Raman transition from a freely moving pair of condensate atoms [138, 140, 142, 178, 179]. Note that the energy and impulse is conserved, since the Raman light fields can be applied counter propagating and the energy released during molecule formation is carried away by the light fields. The free to bound photoassociation process is not very efficient due to poor Franck-Condon overlap of the relatively short distances of atoms in the molecule and the diffuse interatomic distances of a pair of interacting trapped atoms. The free atoms can not penetrate small distances due to the quantum reflection region [180], which is opaque for atoms moving at 1 nK kinetic energies. A further complication is that the Franck Condon factors are best for bound states near the dissociation limit of the excited electronic states, and thus the pump laser tuned to this wavelength will unavoidably excite the nearby atomic transition.

A more promising scheme is the partial conversion of an atomic to a diatomic molecular condensate via a stimulated Raman transition, enhanced by a time-dependent magnetic field that sweeps over a Feshbach resonance [143]. Here a dramatic increase of the free-bound transition probability by seven orders of magnitude can be achieved, since the colliding atoms can penetrate to the short distance range. The conversion rate depends critically on the Raman fields used, which were hand-optimized guided by physical intuition [143]. In this thesis the required fields are calculated by optimal control theory [27, 29], which is very successful in finding solutions close to global optimum. In order to do so, the well known optimal control equations had to be extended to the case of nonlinearities in the dynamical equation. The BEC to M-BEC conversion is moreover a challenge, because it is part of the important class of problems in which the coherent transfer is affected by dissipation on the same timescale.

### 11.2.1 Nonlinearity

In order to make theoretical predictions useful for experiment, the theory will be specialized to a recent experiment on Feshbach resonances carried out at MIT [181, 182]. Here a BEC in the high-field seeking state  $|f = 1, m_f = +1\rangle$ , for which two Feshbach resonances at realizable magnetic field strengths of 853 G and 907 G were theoretically predicted [183], is trapped by all optical means. Then by sweeping the external magnetic field with a rate of  $0.31 \cdot 10^{-2} \text{G}/\mu\text{s}$  over the 853 G resonance 60% quasibound molecules could be created. The parameters of the Feshbach resonance and the Na BEC are summarized in Table 11.1. The atomic condensate (of Na atoms as an example) is described by the field  $\phi_a(\vec{x}, t)$ , the atom pairs in their intermediate Feshbach  $3^2S_{1/2} + 3^2S_{1/2}$  quasibound state as a molecular Bose-Einstein condensate with order parameter  $\phi_1(\vec{x}, t)$ . Two further condensate components are considered: the molecules in the intermediate electronically

**Table 11.1:** The parameters of the calculation.

$\tilde{a}$	3.3 nm	$\gamma_0$	5.3 $\mu\text{K}$
$\Delta$	0.0091 G	$\gamma_{sp}$	$6 \cdot 10^7 \cdot \hbar \text{ s}^{-1}$
n	$5.2 \cdot 10^{14} \text{ cm}^{-3}$	m	$0.38175 \cdot 10^{-25}$
$\dot{B}$	$\pm 0.31 \cdot 10^{-2} \text{ G}/\mu\text{s}$	$\alpha$	$\sqrt{2 \cdot 10^{-16} \hbar \gamma_0 / 8}$
$U_0$	$4\pi \hbar^2 \tilde{a} / m$	$\Delta\mu$	$2\alpha^2 / (U_0 \Delta)$
$\dot{e}_1$	$\dot{B} \cdot \Delta\mu$		

excited  $3^2S_{1/2} + 3^2P_{1/2}$  bound state with a bound state energy of  $-1346 \text{ cm}^{-1}$  ( $0_g^-$  symmetry  $(J, I, M_I) = (2, 3, +1)$ ) of the coherent Raman transition and the molecules in the final state, described by  $\phi_2(\vec{x}, t)$  and  $\phi_3(\vec{x}, t)$  respectively. The final internal state associated with  $\phi_3(\vec{x}, t)$  is chosen to be the ro-vibronic ground state of the molecule in the  $a^3\Sigma_u^+$  triplet potential with spin structure  $(S, M_S, I, M_I) = (1, +1, 3, +1)$ . The amplitudes of the coherent fields are assumed uniform  $\phi_j = \sqrt{n_j} \exp(i\Theta_j)$  and the interaction with the light fields with center frequencies  $\omega_1$  and  $\omega_2$  is taken in a rotating-wave approximation. The coupled Gross-Pitaevskii equations of Eq. (11.13) describing the evolution of a mixed atomic/molecular BEC at a Feshbach resonance had to be extended to further include the influence of the Raman pulse pair [143]:

$$\begin{aligned}
i\dot{\phi}_a &= U_0 |\phi_a|^2 \phi_a + 2\alpha \phi_a^* \phi_1 \\
i\dot{\phi}_1 &= \left( E_1 - \frac{i}{2} \gamma_0 \right) \phi_1 + \alpha \phi_a^2 + \frac{1}{2} \mu_1 \epsilon_{L1} \phi_2 \\
i\dot{\phi}_2 &= \left( E_2 - \frac{i}{2} \gamma_{sp} - \omega_{L1} \right) \phi_2 + \frac{1}{2} \mu_1 \epsilon_{L1} \phi_1 \\
&\quad + \frac{1}{2} \mu_2 \epsilon_{L2} \phi_3 \\
i\dot{\phi}_3 &= (E_3 - \omega_{L1} + \omega_{L2}) \phi_3 + \frac{1}{2} \mu_2 \epsilon_{L2} \phi_2
\end{aligned} \tag{11.14}$$

The system described by these equations is essentially a  $\Lambda$ -type molecular system, coupled to a source of atoms via tunnelling.  $U_0$  is the off-resonant strength of the condensate self-energy,  $\alpha$  the rate constant of atom to quasi-bound molecule conversion. The energy of the quasibound state  $E_1 - \frac{i}{2} \gamma_0$  is assumed complex, since it can dissociate into atoms leaving the trap whenever the energy  $E_1$  is positive (see section 11.1). That means that the decay is only nonzero after (before) crossing the resonance for a positive (negative) magnetic field sweep, respectively. The real part  $E_1$  undergoes a Zeeman shift varying linearly in time  $E_1 = \dot{B}t$  and is defined to cross the resonance value shifted to 0 at time 0, at which instant the  $\phi_1$  to  $\phi_2$  conversion is most efficient.  $E_2 - \frac{i}{2} \gamma_{sp}$  is the complex excited state energy with  $\gamma_{sp}$  the

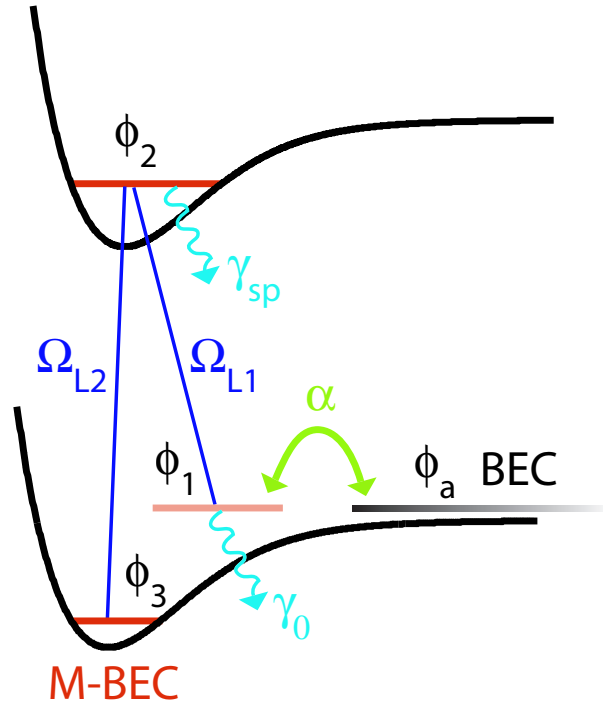


**Figure 11.3:** Schematic of the BEC to M-BEC conversion scheme using nanosecond Raman pulses with Rabi frequencies  $\Omega_{L1}$  and  $\Omega_{L2}$ . Indicated are the triplet potential  $a^3\Sigma_u^+$  and the excited potential of  $O_g^-$  symmetry. The colliding atoms of the BEC are described by the field  $\phi_a$ , the formed quasibound state by  $\phi_1$ , the bound level in the excited potential by  $\phi_2$  and finally the target level in the ground state potential by  $\phi_3$ . The decay due to spontaneous emission is  $\gamma_{sp}$  and the decay of the quasibound state due to dissociation and trap loss is  $\gamma_0$ .

spontaneous decay width and  $E_3$  the energy of the final bound molecular state. For a more detailed description see Ref. [143]. Included in this model is the boson stimulation of the free to bound transition [142] and also the change of self-energy of the condensate due to reduction of the atomic BEC component during the conversion process. Not included is the effect of atom-molecule and molecule-molecule self-energy terms [see Eq. (11.13)], since no accurate experimental or theoretical information on the relevant ultracold collisions is presently available.

The aim is to find pulses  $\epsilon_{L1}$  and  $\epsilon_{L2}$  that take the initial population in  $\phi_a$  (atomic BEC) completely over to  $\phi_3$  (stable molecular BEC). Starting point is the formulation of a functional, that is to be varied in order to obtain the

coupled equations solved iteratively on the electric fields:

$$\begin{aligned}
J = & \langle \phi_3 | \phi(T) \rangle - \alpha_1 \int_0^T \frac{\epsilon_1^2(t)}{s(t)} dt - \alpha_2 \int_0^T \frac{\epsilon_2^2(t)}{s(t)} dt \\
& - 2\text{Re} \left\{ \int_0^T \langle \lambda(t) | \partial_t + iW(\phi(t), t) | \phi(t) \rangle dt \right\} \quad (11.15)
\end{aligned}$$

Here  $\phi(t)$  is a vector with the four components  $\phi_i(t)$  describing the current state of the mixed condensate system governed by Eq. (11.14). Again, the first term describes the aim, that is to maximize the overlap with the bound molecular state at final time  $t_f$ . The next two terms are used to regulate the maximal pulse energy by choosing adequately the dimensionless parameters  $\alpha_1, \alpha_2$ . The dynamics predicted by Eq. (11.14) occur on an interval of  $t_i = -400 \mu\text{s}$  to  $t_f = 100 \mu\text{s}$ , while the laser interaction interval was constrained using a shape function to  $[-50 \mu\text{s}, 50 \mu\text{s}]$ . This selection of the optimization window will allow laser fields with a *fwhm* of several  $\mu\text{s}$  and not shorter than the dynamics induced by the initial guess pulse, which consists of a sequence of nanosecond pulses. In a later section the optimization window will be reduced to picosecond, leading then to a shaped femtosecond Raman pulse pair.

The functional becomes unconstrained due to the last term that takes into account that the evolution of  $\phi$  is governed by Eq. (11.14), written in the form  $i\partial_t\phi(t) = W(\phi(t), t)$ . Here  $W(\phi(t), t)$  is the right hand side of Eq. (11.14) and includes all nonlinear terms. In order to express this constraint to be fulfilled at every time step a Lagrange multiplier  $\lambda(t)$  is necessary. Variations with respect to  $\phi, \lambda, \epsilon_1$  and  $\epsilon_2$  have to be calculated to find the fields that maximize the functional. Beginning with the electric fields the following two equations are obtained:

$$\epsilon_1(t) = -\frac{s(t)}{\alpha_1} \mu_1 \text{Im} \{ \langle \lambda_1 | \phi_2 \rangle + \langle \lambda_2 | \phi_1 \rangle \} \quad (11.16)$$

$$\epsilon_2(t) = -\frac{s(t)}{\alpha_2} \mu_2 \text{Im} \{ \langle \lambda_2 | \phi_3 \rangle + \langle \lambda_3 | \phi_2 \rangle \} \quad (11.17)$$

Variation with respect to  $\lambda$  leads to Eq. (11.14) with the boundary condition at initial time  $\phi(t_i) = \phi_1$ . The  $\phi$  variation leads to the following equation

of motion for  $\lambda$

$$\begin{aligned}
i\dot{\lambda}_a &= U_0 \left( 2|\phi_a|^2 \lambda_a + \phi_a^2 \lambda_a^* \right) + 2\alpha (\phi_a^* \lambda_1 + \phi_1 \lambda_a^*) \\
i\dot{\lambda}_1 &= \left( E_1 + \frac{i}{2} \gamma_0 \right) \lambda_1 + 2\alpha \phi_a \lambda_a + \frac{1}{2} \mu_1 \epsilon_{L1} \lambda_2 \\
i\dot{\lambda}_2 &= \left( E_2 + \frac{i}{2} \gamma_{sp} - \omega_{L1} \right) \lambda_2 + \frac{1}{2} \mu_1 \epsilon_{L1} \lambda_1 \\
&\quad + \frac{1}{2} \mu_2 \epsilon_{L2} \lambda_3 \\
i\dot{\lambda}_3 &= (E_3 - \omega_{L1} + \omega_{L2}) \lambda_3 + \frac{1}{2} \mu_2 \epsilon_{L2} \lambda_2.
\end{aligned} \tag{11.18}$$

Due to the nonlinear nature of Eq. (11.14) the evolution of the Lagrange multiplier  $\lambda$  depends on  $\phi$  itself and is not independent as for the linear Schrödinger equation. The Lagrange multiplier has to fulfill the boundary condition  $\lambda_i(t_f) = \delta_{i4} \phi_4$  at *final* time.

The obtained system of four equations, where Eq. (11.14) and Eq. (11.18) depend on the fields  $\epsilon_1(t), \epsilon_2(t)$  given by Eq. (11.16) and Eq. (11.17), respectively, is solved as usual by iteration on the electric fields [27]. One iteration is composed of the following steps. Starting with an initial guess pulse,  $\phi(t)$  is propagated from its initial value until final time is reached. These values of  $\phi(t)$  at each point of time are stored. Then  $\phi(t_f)$  is projected onto the final state  $\phi_4$  and normalized to one. This vector is then used as the boundary condition for  $\lambda$  at final time  $t_f$ . Both electric fields at  $t = t_f$  are calculated using Eq. (11.16) and Eq. (11.17). These field values are used in conjunction with the stored value of  $\phi$  to calculate  $\lambda$  a further step backward. This is repeated until initial time is reached. The obtained improved field is used as initial guess in the next iteration.

The proposed iteration scheme, one out of three possible in the case of the linear Schrödinger equation, is the only one that will work, since  $\lambda$  can only be propagated if  $\phi$  is already known and moreover the propagation will only be well-behaved if Eq. (11.18) is propagated *backward* in time, due to the + sign of the  $\gamma_0$  and  $\gamma_{sp}$  decay terms. Numerically the propagation is performed using a variable-order, variable-step Adams method [184]. An alternative propagator could have been the polynomial in time proposed by R. Baer [127].

The optimization is not expected to work efficiently in the case of spontaneous emission from the excited state, since the OCT is based on wave functions and not density matrices (see the proof in section 10.1). Therefore the following results were obtained with  $\gamma_{sp} = 0$  and only in the next section a density matrix based OCT for this problem will be derived.

Using the Krotov method and starting with a sequence of counterintuitive pulses in analogy to Ref. [143] [Fig. 11.4(a)], which are known to be a good initial guess, the results of Fig. 11.4(b) are obtained for  $\alpha_1 = 5 \cdot 10^4$  and

$\alpha_2 = 1 \cdot 10^{10}$ . The population induced by the initial guess evolves according to Fig. 11.5(a) reaching a population in the molecular BEC at final time of 12%. The optimal pulse population dynamics are shown in Fig. 11.5(b) with a clearly improved conversion rate to the M-BEC of 42%. The optimal pulse is a  $\mu\text{s}$  changing field with the subpulse coupling the quasibound to excited state preceding the subpulse coupling the bound to bound transition. Therefore population is slowly transferred into the excited state and thereafter dumped completely again [Fig. 11.5(b)]. With  $\gamma_{sp}$  turned on this pulse is no more optimal, since the laser transfer occurs on the same timescale as the decay and population will be lost.

In the following two sections the optimal control equations will be modified in order to provide solutions even in the presence of dissipation. Dissipation is circumvented by not populating the decaying levels (section 11.2.2) or being faster than the decay mechanism by applying tailored femtosecond pulses (section 11.2.3).

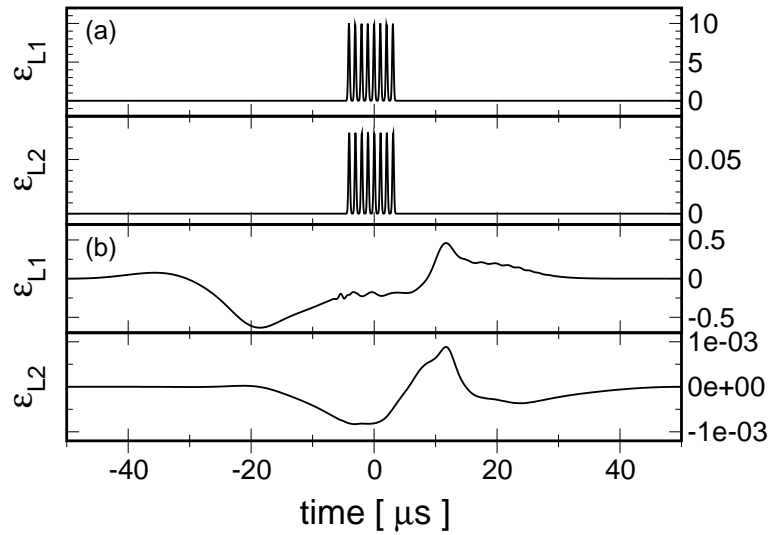


**Figure 11.4:** (a) Initial guess consisting of a STIRAP sequence of nanosecond pulses. (b) Optimal pulse.

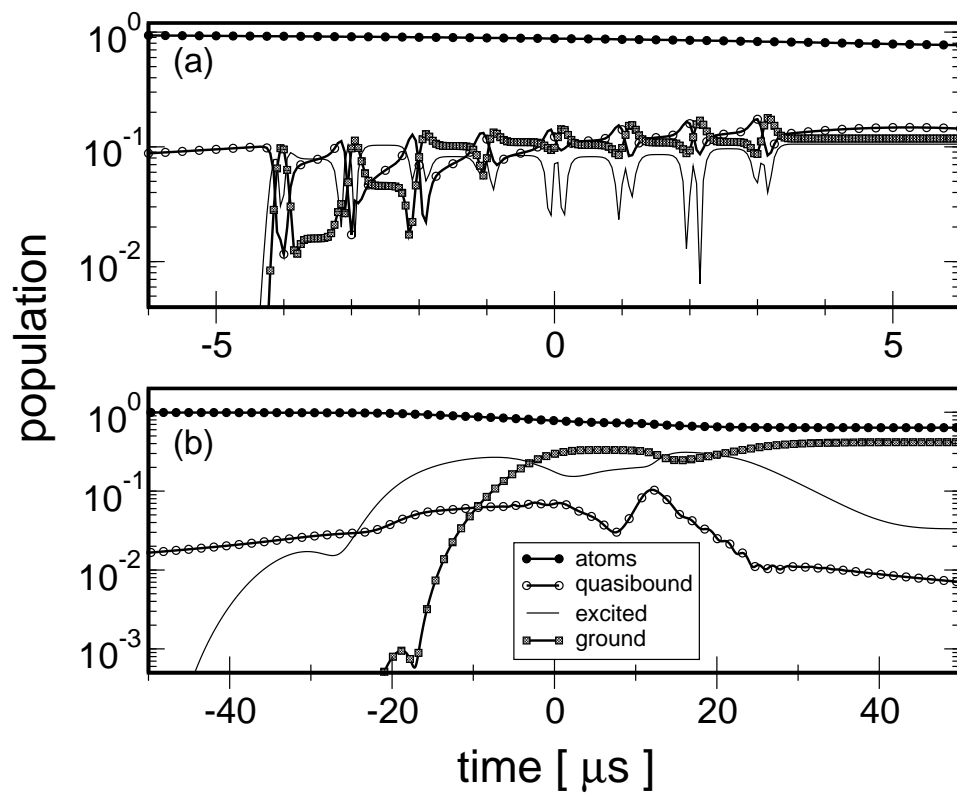


**Figure 11.5:** Atomic BEC (filled dots) and molecular BEC: quasibound (hollow dots), excited (line), ground (squares) with  $\gamma_{sp} = 0$ . (a) Population transfer induced by initial guess. (b) Population transfer induced by optimal pulse.

### 11.2.2 Use of optimal nanosecond pulses

In this section the density matrix analog of the GP equations of Ref. [143] is derived to include also the evolution of the coherences in the system. This is necessary in order to obtain optimal pulses for the real problem of BEC to M-BEC conversion in the  $\mu s$  regime, where dissipation of the excited state is a central problem. This was shown already in section 10.1, where an optimal control functional based on dissipation was capable of optimizing STIRAP pulse sequences. In this section the density matrix formulation of optimal control theory is combined with the nonlinear dynamical equation of the previous subsection to provide experimentalists with highly efficient  $\mu s$  pulse sequences converting an atomic to a molecular BEC. The density matrix elements are  $\rho_a = \langle \phi_a | \rho | \phi_a \rangle$ ,  $\rho_{ai} = \langle \phi_a | \langle \phi_a | \rho | \phi_i \rangle$  and  $\rho_{ij} = \langle \phi_i | \rho | \phi_j \rangle$  with  $i, j = 1 \dots 3$  indexing the molecular levels. Here  $\rho_{ai}$  describes the formation of the molecular quasibound state from the two colliding atoms as in Eq. (11.12). Now the density matrix analog of the coupled Gross-Pitaevskii equations [ Eq. (11.14)] predict the population dynamics

$$\begin{aligned}
 i\dot{\rho}_a &= 2\alpha\rho_{a1} - c.c. \\
 i\dot{\rho}_{11} &= E_1\rho_{11} - \alpha\rho_{a1} + \Omega_{L1}\rho_{12} - c.c. \\
 i\dot{\rho}_{22} &= E_2\rho_{22} - \Omega_{L1}\rho_{12} + \Omega_{L2}\rho_{23} - c.c. \\
 i\dot{\rho}_{33} &= E_3\rho_{33} - \Omega_{L2}\rho_{23} - c.c.
 \end{aligned} \tag{11.19}$$

and the coherence dynamics

$$\begin{aligned}
 i\dot{\rho}_{a1} &= (E_1 - 2U_0\rho_a)\rho_{a1} - 4\alpha\rho_a(\rho_{11} - \frac{1}{4}\rho_a) + \Omega_{L1}\rho_{a2} \\
 i\dot{\rho}_{a2} &= (E_2 - 2U_0\rho_a)\rho_{a2} - 4\alpha\rho_a\rho_{12} + \Omega_{L1}\rho_{a1} + \Omega_{L2}\rho_{a3} \\
 i\dot{\rho}_{a3} &= (E_3 - 2U_0\rho_a)\rho_{a3} - 4\alpha\rho_a\rho_{13} + \Omega_{L2}\rho_{a2} \\
 i\dot{\rho}_{12} &= (E_2 - E_1^*)\rho_{12} - \alpha\rho_{a2} + \Omega_{L1}(\rho_{11} - \rho_{22}) + \Omega_{L2}\rho_{13} \\
 i\dot{\rho}_{13} &= (E_3 - E_1^*)\rho_{13} - \alpha\rho_{a3} - \Omega_{L1}\rho_{23} + \Omega_{L2}\rho_{12} \\
 i\dot{\rho}_{23} &= (E_3 - E_2^*)\rho_{23} - \Omega_{L1}\rho_{13} + \Omega_{L2}(\rho_{22} - \rho_{33}).
 \end{aligned} \tag{11.20}$$

Here I used the same nomenclature as in the previous section. Again the aim is to find pulses  $\epsilon_{L1}$  and  $\epsilon_{L2}$  that take the initial population in  $\rho_a$  (atomic BEC) completely over to  $\rho_{33}$  (stable molecular BEC) without populating the intermediate decaying excited state. Starting point is the formulation of a functional, that is to be varied in order to obtain the coupled equations

solved iteratively on the electric fields:

$$\begin{aligned}
J = & \langle 3|\rho(t_f)|3 \rangle - \alpha_1 \int_{t_i}^{t_f} \epsilon_{L1}^2(t) dt - \alpha_2 \int_{t_i}^{t_f} \epsilon_{L2}^2(t) dt \\
& - 2\text{Re} \left\{ \int_{t_i}^{t_f} \text{tr} \{ [\dot{\rho}(t) + W(\rho(t), t)] \lambda(t) \} dt \right\} \quad (11.21)
\end{aligned}$$

Here  $\rho(t)$  is the  $4 \times 4$  matrix

$$\rho = \begin{pmatrix} \rho_a & \rho_{a1} & \rho_{a2} & \rho_{a3} \\ c.c. & \rho_{11} & \rho_{12} & \rho_{13} \\ c.c. & c.c. & \rho_{22} & \rho_{23} \\ c.c. & c.c. & c.c. & \rho_{33} \end{pmatrix} \quad (11.22)$$

describing the current state, including coherences, of the mixed condensate system governed by Eq. (11.19). The first term describes the aim, that is to maximize the overlap with the bound molecular state at final time  $t_f$ . The next two terms are used to regulate the maximal pulse energy by choosing adequately the parameters  $\alpha_1, \alpha_2$ . The optimization interval is  $[t_i, t_f]$  and in the calculations  $t_i = -400 \mu\text{s}$  and  $t_f = 100 \mu\text{s}$  were chosen. Beginning with the electric fields the following two equations are obtained:

$$\begin{aligned}
\Delta\epsilon_{L1}(t) = & -\frac{\mu_1}{\alpha_1} \text{Im} \{ \rho_{12}(\lambda_{22} - \lambda_{11}) + \lambda_{12}(\rho_{11} - \rho_{22}) - \\
& \lambda_{13}\rho_{23}^* - \lambda_{23}\rho_{13}^* + \lambda_{a1}\rho_{a2}^* + \lambda_{a2}\rho_{a1}^* \} \quad (11.23)
\end{aligned}$$

$$\begin{aligned}
\Delta\epsilon_{L2}(t) = & -\frac{\mu_2}{\alpha_2} \text{Im} \{ \rho_{23}(\lambda_{33} - \lambda_{22}) + \lambda_{23}(\rho_{22} - \rho_{33}) + \\
& \lambda_{12}\rho_{13}^* + \lambda_{13}\rho_{12}^* + \lambda_{a2}\rho_{a3}^* + \lambda_{a3}\rho_{a2}^* \}. \quad (11.24)
\end{aligned}$$

Clearly these equations, that are used to predict the optimal fields in each iteration, depend on the populations and coherences of the system. In comparison the equations (11.16) and (11.17), obviously lack the coherence terms. The iteration behavior using Eqs. (11.23) and (11.24) with Eqs. (11.16) and (11.17) was compared. The density matrix formulation of the GP equations is not only a physically more complete picture, but the coherence terms lead to a much faster optimization of STIRAP light fields compared to wave function OCT (see the proof in section 10.1).

Variation with respect to  $\lambda$  leads to Eq. (11.19) with the boundary condition at initial time  $\rho(t_i) = \rho_a$ . The  $\rho$  variation leads to the following equation of

motion for  $\lambda$

$$\begin{aligned}
i\dot{\lambda}_a &= -2U_0(\rho_{a1}^*\lambda_{a1} + \rho_{a2}^*\lambda_{a2} + \rho_{a3}^*\lambda_{a3}) + \\
&\quad 2\alpha[(\rho_a - 2\rho_{11})\lambda_{a1} - 2\rho_{12}^*\lambda_{a2} - 2\rho_{13}^*\lambda_{a3}] - c.c. \\
i\dot{\lambda}_{11} &= E_1^*\lambda_{11} - 4\alpha\rho_a^*\lambda_{a1} + \Omega_{L1}\lambda_{12} - c.c. \\
i\dot{\lambda}_{22} &= E_2^*\lambda_{22} - \Omega_{L1}\lambda_{12} + \Omega_{L2}\lambda_{23} - c.c. \\
i\dot{\lambda}_{33} &= E_3^*\lambda_{33} - \Omega_{L2}\lambda_{23} - c.c. \\
i\dot{\lambda}_{a1} &= (E_1^* - 2U_0\rho_a)\lambda_{a1} - \alpha(\lambda_{11} - 2\lambda_a) + \Omega_{L1}\lambda_{a2} \\
i\dot{\lambda}_{a2} &= (E_2^* - 2U_0\rho_a)\lambda_{a2} - \alpha\lambda_{12} + \Omega_{L1}\lambda_{a1} + \Omega_{L2}\lambda_{a3} \\
i\dot{\lambda}_{a3} &= (E_3^* - 2U_0\rho_a)\lambda_{a3} - \alpha\lambda_{13} + \Omega_{L2}\lambda_{a2} \\
i\dot{\lambda}_{12} &= (E_2^* - E_1)\lambda_{12} - 4\alpha\rho_a\lambda_{a2} + \Omega_{L1}(\lambda_{11} - \lambda_{22}) + \Omega_{L2}\rho_{13} \\
i\dot{\lambda}_{13} &= (E_3^* - E_1)\lambda_{13} - 4\alpha\rho_a\lambda_{a3} - \Omega_{L1}\lambda_{23} + \Omega_{L2}\lambda_{12} \\
i\dot{\lambda}_{23} &= (E_3^* - E_2)\lambda_{23} - \Omega_{L1}\lambda_{13} + \Omega_{L2}(\lambda_{22} - \lambda_{33})
\end{aligned} \tag{11.25}$$

Due to the nonlinear nature of Eq. (11.19) the evolution of the Lagrange multiplier  $\lambda$  depends on  $\rho$  itself and is not independent as for the linear Schrödinger equation. The Lagrange multiplier has to fulfill the boundary condition  $\lambda_{i,j}(t_f) = \delta_{i4,j4}$  at *final* time. The obtained system of four equations (Eq. (11.19), (11.23), (11.24), and (11.25)), where Eqs. (11.19) and (11.25) depend on the fields  $\epsilon_1(t), \epsilon_2(t)$  given by Eqs. (11.23) and (11.24), respectively, is solved by iteration on the electric field using the modified Krotov method, since the Krotov method always results in a zero light field when  $\gamma_{sp}$  is turned on. This was already proven in section 10.1. Iteration was stopped when the yield did not increase monotonically anymore. Critical to the iteration performance are the values of  $\alpha_1$  and  $\alpha_2$ , which were chosen as close as possible to their thresholds, below which convergence breaks down and strong oscillatory behavior sets in. Too high values will slow down convergence drastically. For the problem at hand  $\alpha_1 = \alpha_2 = 2 \cdot 10^3$  proved to be the best and closest to threshold.

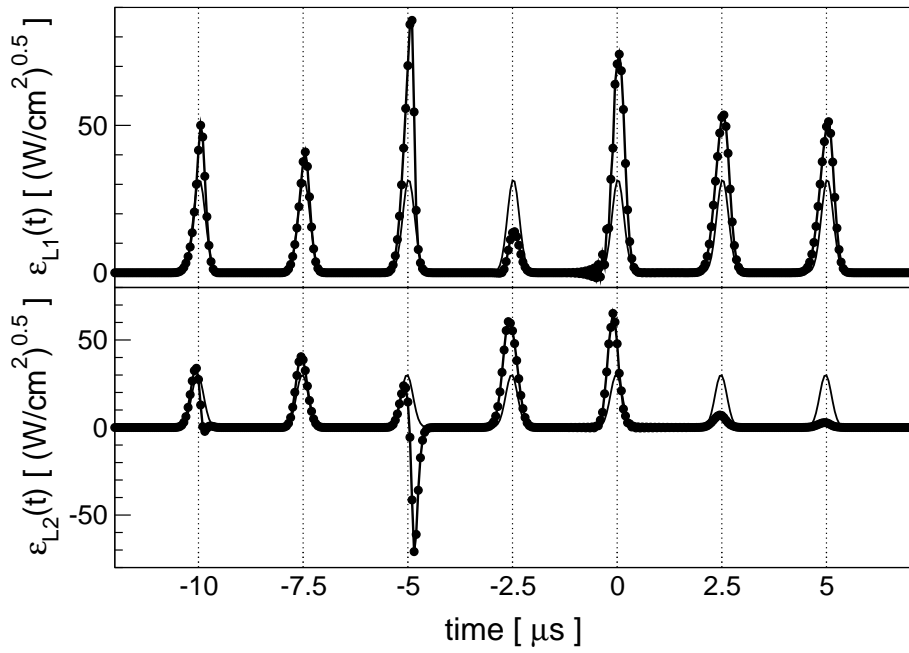


**Figure 11.6:** Optimal Raman pulse pair for positive magnetic field sweep. Light field ( $\epsilon_{L1}$ ) coupling quasibound state with excited state and light field ( $\epsilon_{L2}$ ) inducing transition between excited and target molecular state. As reference the initial guess Raman sequence of Ref. [143] is shown as line.

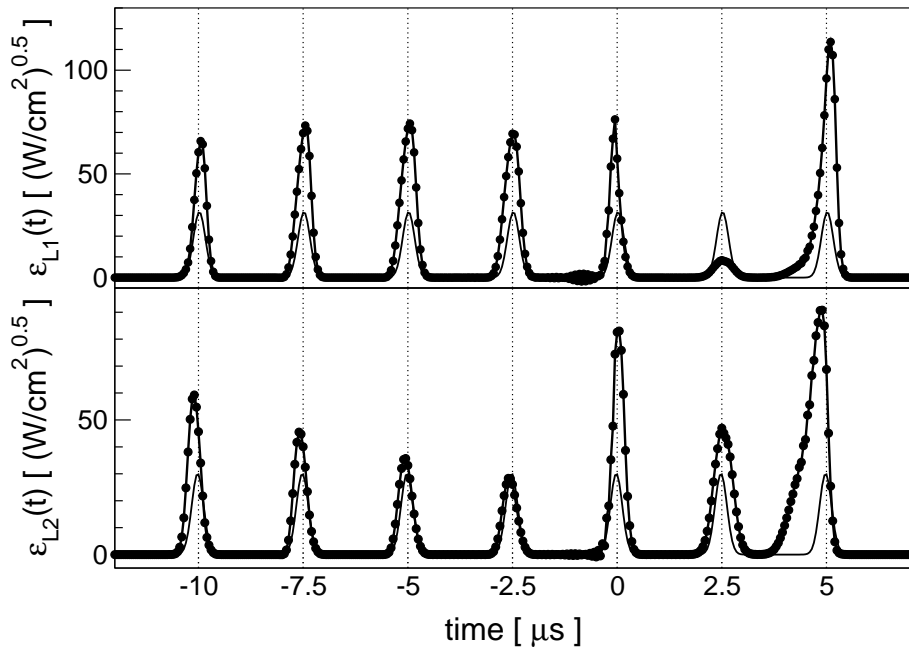


**Figure 11.7:** As Fig. 11.6 for negative magnetic field sweep.

The STIRAP sequence of seven consecutive equidistant pulses of Ref. [143] [Figs. 11.6 and 11.7] transfers 16% of the population into the molecular BEC if a positive magnetic field sweep is applied [see Fig. 11.8(a)] and 25% in conjunction with a negative sweep [see Fig. 11.8(b)].

Taking this STIRAP sequence as initial guess Raman pulse into the op-

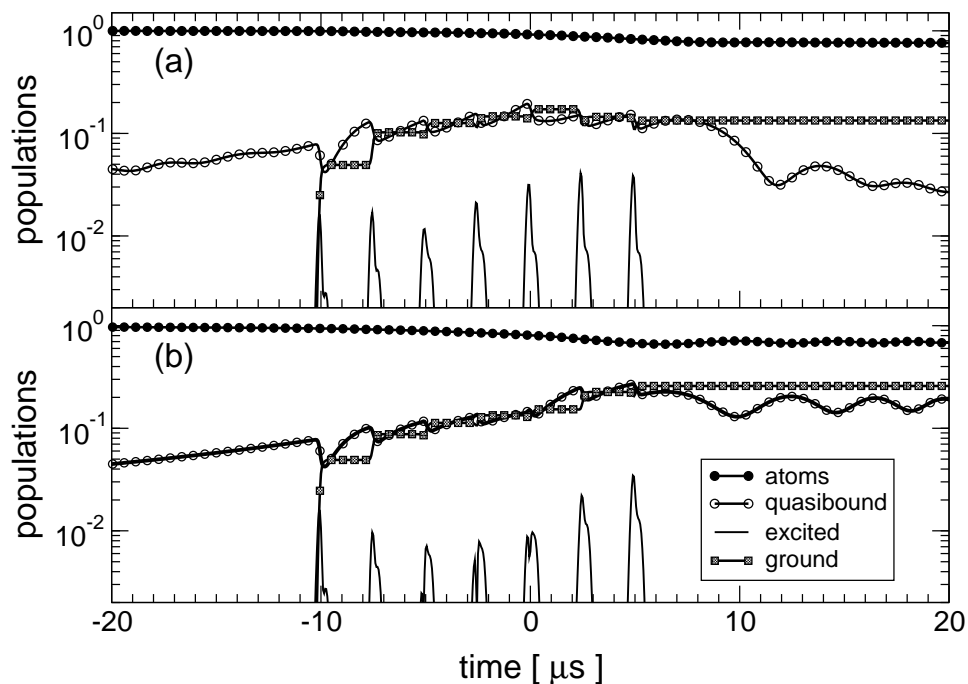


**Figure 11.8:** Population dynamics as induced by the STIRAP sequence of seven pulses. (a) for positive linear magnetic field sweep. (b) for negative linear magnetic field sweep.

timal control formulation, the yield could be improved upon considerably. The resulting optimal light fields are shown in Figs. 11.6 and 11.7, for the case of positive and negative magnetic field sweep, respectively. Under the influence of the pulse in Fig. 11.6 [Fig. 11.7] the population evolves according to Fig. 11.9 [Fig. 11.10]. In the upper panel the population dynamics are depicted and in lower panel the coherences. While the population in the excited state  $\rho_{22}$  is less than 1% during the transfer the coherence terms, especially the important one,  $\rho_{13}$ , coupling the quasibound state with the target state, are ten times larger. These terms give important corrections to the electric fields in each iteration via Eqs. (11.23) and (11.24), while they are completely missing in the electric field correction equations in the wave function OCT.

The optimal Raman pulses of Figs. 11.6 and 11.7 achieve 42% molecular BEC depending only slightly on the magnetic field sweep direction. The optimal pulses for these two cases differ considerably, since decay and tran-

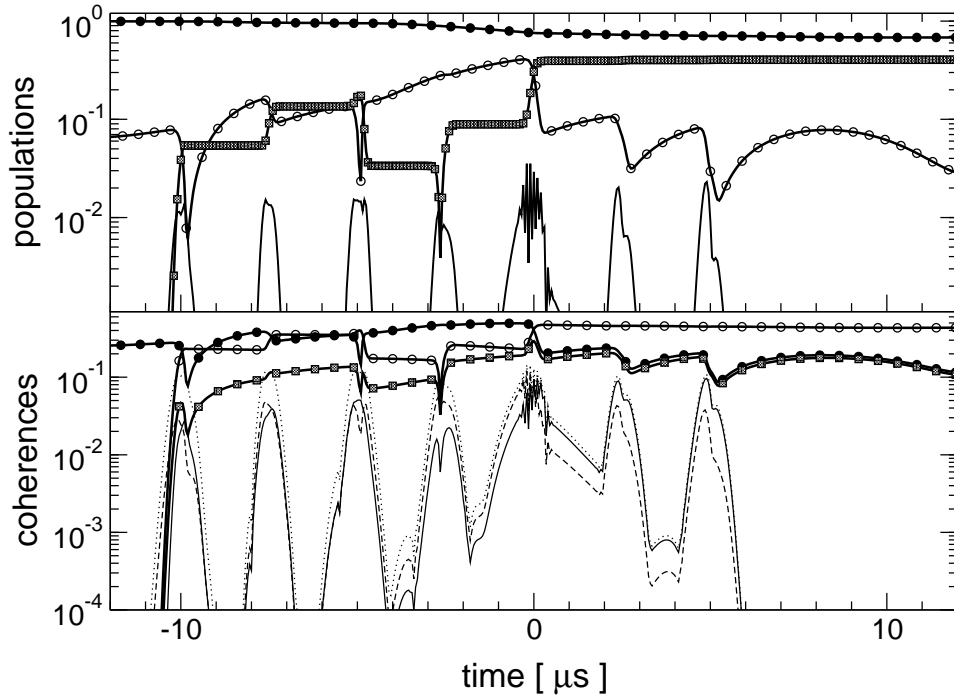


**Figure 11.9:** Dynamics of population (a) and coherences (b) induced by optimal pulse for positive magnetic field sweep. Populations: atomic BEC  $\rho_a$  (filled dots), quasibound  $\rho_{11}$  (hollow dots), excited  $\rho_{22}$  (line) and ground  $\rho_{33}$  (filled squares). Coherences:  $\rho_{a1}$  (filled dots),  $\rho_{a2}$  (line),  $\rho_{a3}$  (hollow dots),  $\rho_{12}$  (dotted line),  $\rho_{13}$  (filled squares) and  $\rho_{23}$  (dashed line).

sition frequency have a time behavior, that depends on the magnetic field sweep. Remember, that the decay is only active at  $t < 0$  ( $t > 0$ ) and the free to bound transition frequency increases (decreases) for a negative (positive) magnetic field sweep. Besides of some subpulses with a different pulse shape, amplitude and slight time shifts within the sequence the optimal pulses still show a clear resemblance with the initial guess pulse. Note that nearly all the  $\epsilon_{L2}$  subpulses precede the  $\epsilon_{L1}$  pulses in the optimized results as was also the case for the initial guess STIRAP sequence. Only the fifth pulse pair of the field in Fig. 11.7 acting during the maximum Feshbach resonance has intuitive ordering. This shifting between intuitive and counterintuitive ordering is perhaps necessary to avoid back dissociation via the reverse bound-bound-free transition, which is only partly suppressed by the Zeeman shift over time of the quasibound state. Note also that the excited state molecular population is much reduced for the optimal field [see Fig. 11.10] in comparison to the initial guess [see Fig. 11.8]. This leads to the conclusion, that the optimal mechanism for the negative magnetic field sweep is to improve the STIRAP sequence.

A further reason for the improvement in the transfer efficiency could be that

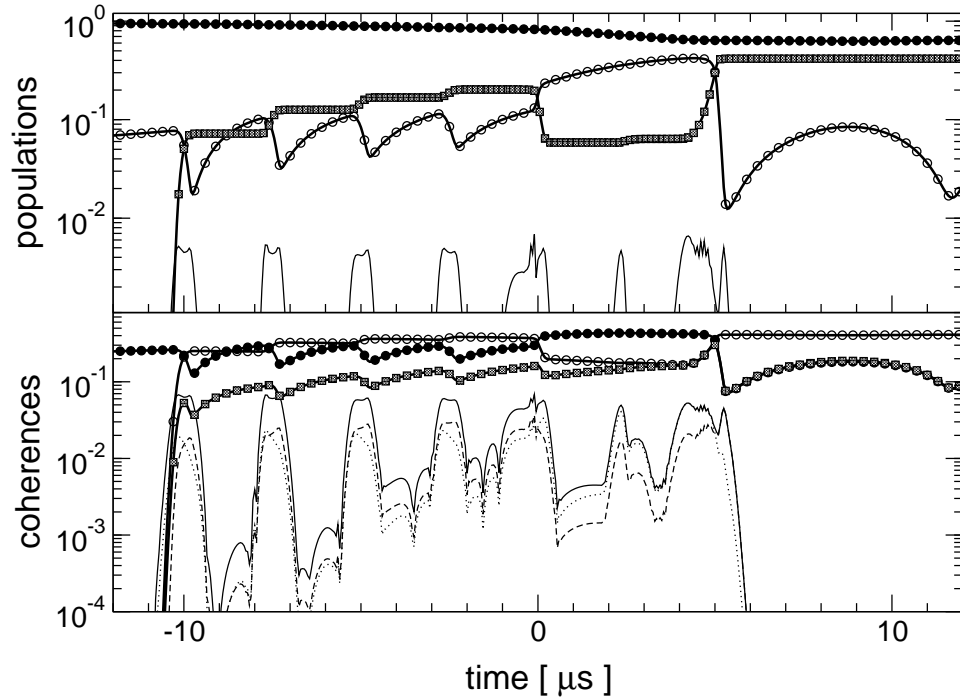


**Figure 11.10:** As Fig. 11.9 for negative magnetic field sweep.

the optimal pulses are suitably modulated to adapt to the nonlinearities and the refilling by the atomic BEC in this process. At least a different pulse sequence is calculated starting from the same initial guess if only the  $\Lambda$  system, consisting of quasibound state with external magnetic field dependent energy, the excited bound and final state, is considered.

In conclusion, the Gross-Pitaevskii equation modeling the BEC to M-BEC conversion via Raman light fields and a magnetic field sweep, was modeled using a density matrix formalism. This is an ideal Ansatz for the formulation of the optimal control framework in the case of dissipation. With it two Raman pulse sequences, each for a different sign of the magnetic field sweep, that both achieve 42% molecular BEC were obtained. In this thesis it could be shown for the first time, that optimal control theory can be derived and applied successfully in the regime of nonlinear Schrödinger equations. STIRAP-like sequences are natural solutions of this density matrix based optimal control formulation and it is not necessary to resort to other proposed, less efficient optimal control schemes.

### 11.2.3 Use of optimal femtosecond pulses

The decay of the excited state during the transfer from an atomic to a molecular BEC occurs on a nanosecond time scale. One also notices that the depletion of the quasibound state by each STIRAP pulse pair is only partial, indicating that higher pulse intensities are necessary. A natural way to avoid excited state decay and increase pulse intensity is to shorten the pulse duration of the Raman pulse pairs. In this chapter the feasibility of tailored femtosecond pulses for the atomic to molecular BEC transfer is studied. An appealing feature of femtosecond pulses is their coherent bandwidth allowing the preparation of a macroscopic BEC wave packet, whose time evolution can then be watched directly.

In order to optimize a femtosecond pulse the optimization window was reduced to  $T = 1$  ps and the duration of the shape function accordingly. Note that it is no more necessary to use the density matrix formulation of the Gross-Pitaevskii equations, since populating the excited state for only one picosecond will not lead to any decay. Due to the broad bandwidth of the femtosecond pulses the number of excited and ground target states was increased from one to three and their dynamics were accounted for by expanding the Gross-Pitaevskii equations [Eq. (11.14)].

$$\begin{aligned}
i\dot{\phi}_a &= U_0|\phi_a|^2\phi_a + 2\alpha\phi_a^*\phi_1 \\
i\dot{\phi}_1 &= \left(E_1 - \frac{i}{2}\gamma_0\right)\phi_1 + \alpha\phi_a^2 + \frac{1}{2}\mu_1\epsilon_{L1}\sum_{k=1}^3\phi_{2k} \\
i\dot{\phi}_{2i} &= \left(E_{2i} - \frac{i}{2}\gamma_{sp} - \omega_{L1}\right)\phi_{2i} + \frac{1}{2}\mu_1\epsilon_{L1}\phi_1 \\
&\quad + \frac{1}{2}\mu_2\epsilon_{L2}\sum_{k=1}^3\phi_{3k} \\
i\dot{\phi}_{3i} &= (E_{3i} - \omega_{L1} + \omega_{L2})\phi_{3i} + \frac{1}{2}\mu_2\epsilon_{L2}\sum_{k=1}^3\phi_{2k}
\end{aligned} \tag{11.26}$$

Here the index  $i$  and  $k$  extend from 1 to 3. Note that the dipole moments from the quasibound state to all target states are assumed equal to  $\mu_1$ , as also the dipole moment  $\mu_2$  from each excited state to each final ground state in the triplet potential. The objective was chosen to be the overlap with the third eigenstate of the triplet potential, i.e.  $\langle\phi|\phi_{33}\rangle$ , where  $\phi = (\phi_a, \phi_1, \phi_{2i}, \phi_{3i})$  is the wave function of the coupled BEC/M-BEC system. Two regimes for the energy spacings  $E_{2i}$  and  $E_{3i}$  were studied: near degeneracy as is the case for hyperfine energy spacings and vibrational spacings giving rise to 500 fs dynamics. The initial state of the optimization was calculated by starting a propagation without Raman fields at  $-400 \mu\text{s}$ . Only a magnetic field is applied with a negative slope of  $-0.31 \cdot 10^{-2} \text{ G}/\mu\text{s}$  until it

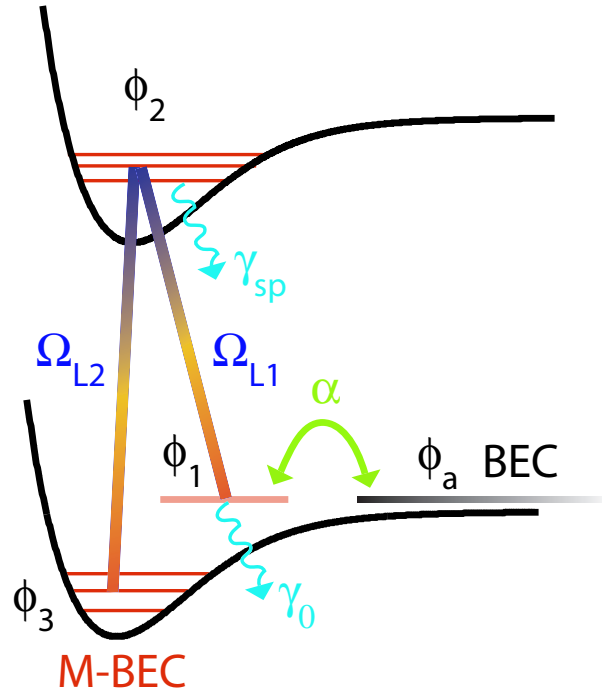


**Figure 11.11:** Schematic of the BEC to M-BEC conversion scheme using femtosecond Raman pulses with Rabi frequencies  $\Omega_{L1}$  and  $\Omega_{L2}$ . Indicated are the triplet potential  $a^3\Sigma_u^+$  and the excited potential of  $O_g^-$  symmetry. The colliding atoms of the BEC are described by the field  $\phi_a$ , the formed quasibound state by  $\phi_1$ , the populated bound levels in the excited potential by  $\phi_{2i}$  and finally the levels in the ground state potential by  $\phi_{3i}$ . The decay due to spontaneous emission is  $\gamma_{sp}$  and the decay of the quasibound state due to dissociation and trap loss is  $\gamma_0$ .

reaches the Feshbach resonance value at time 0 (same as in the calculations of the previous chapters). Then the magnetic field is kept at this value until the quasibound state population reaches a maximum. That occurs about 20  $\mu s$  later as shown in Figure 11.12(a). The atomic component at this point is about 28% [Fig. 11.12(b)] since it has tunneled into the quasibound level populating it to 60%, while the missing population (12%) has decayed at times  $< 0$  due to the  $\gamma_0$  decay. Since no laser fields were active the population in the other molecular states is still zero.

**Vibrationally spaced levels.** The state of the system at 20  $\mu s$  is taken as initial condition to the optimization, which is performed in the time interval  $[20 \mu s, 20 \mu s + 1 \text{ ps}]$  obtaining the pulses in Fig. 11.12(b). The dynamics induced by this optimal femtosecond Raman pulse pair is shown in Fig. 11.12(a). Note that the nonlinear coupling term  $\alpha$  in the GP equations is negligible over this timescale and therefore the atomic BEC component stays absolutely constant at its initial value of 28%. The three excited state

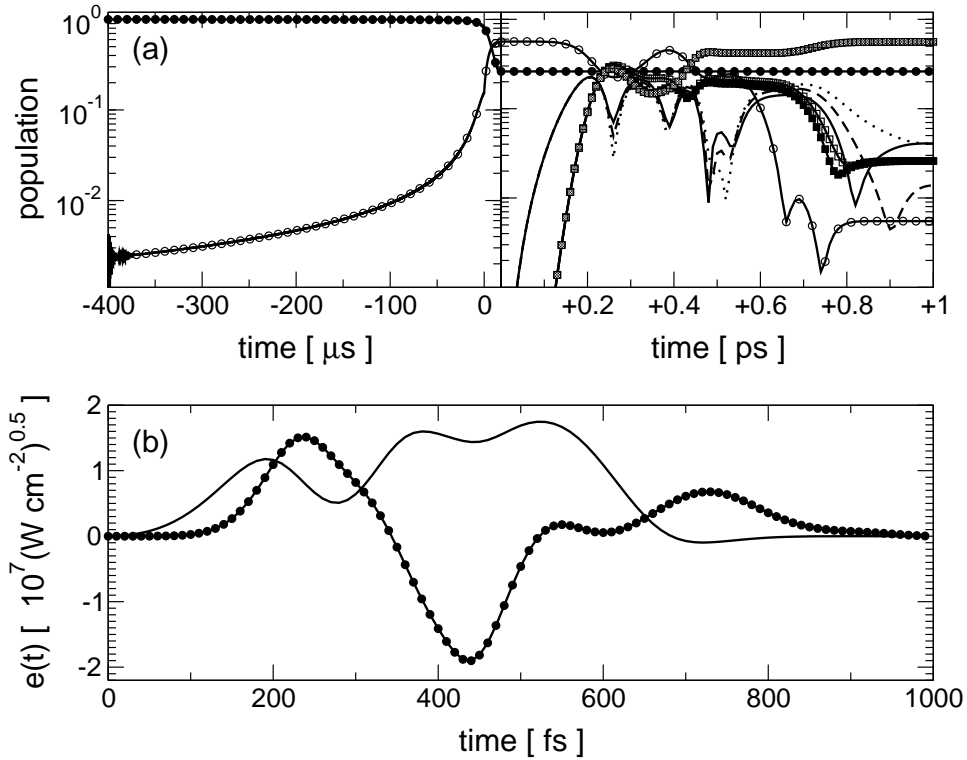


**Figure 11.12:** Molecular levels at vibrational spacing. Filled dots atomic BEC, quasibound hollow dots, excited vibrational states lines without symbol and ground vibrations lines with square symbols. (a) Evolution of the BEC during a magnetic field sweep without external light fields until the time  $20 \mu\text{s}$ . The evolution after the time  $20 \mu\text{s}$  is an expanded view of the  $1$  ps pulse pair action on the condensate. (b) The femtosecond tailored pulse pair.  $\epsilon_{L1}$  is black line and  $\epsilon_{L2}$  is filled dots.

levels are populated at intermediate times, but completely dumped at final time  $T$  [Fig. 11.12(a)]. With a 100% efficiency the quasibound state population is transferred to one single target bound state in the triplet potential. This transfer is moreover highly selectively as the population in the other two bound triplet levels is negligible at final time  $T$ . Therefore a single femtosecond pulse pair produces 60% molecular BEC, completely depleting the quasibound state population at the instant of its action. Therefore this scheme is much more efficient than the nanosecond STIRAP sequence. Even a higher percentage of molecular BEC could be produced if after the quasibound state is replenished from the atomic BEC source a second optimized pulse pair is applied. However this pulse must have a different shape to avoid back pumping of the already achieved triplet potential population to the quasibound state. It would be also possible to apply the same pulse pair of Fig. 11.12(b) successfully a second time if after each pulse pair action the molecular component is separated from the atomic BEC. Anyway it will be

only possible to pump the remaining part of the BEC component expecting then a 28% increase in molecular BEC if no three body decay is assumed.

**Near degenerate levels.** Further results are presented in Figure 11.13 for near degenerate molecular levels  $\phi_{2i}$  and  $\phi_{3i}$ . Since the levels have a small energy spacing it is not possible to selectively populate one triplet potential level and the populations in all the levels are equal [Fig. 11.13(a)]. In order to be able to calculate the total population in the molecular state the square of the populations is plotted. Again at about 20  $\mu\text{s}$  the complete emptying of the quasibound state component by the femtosecond pulse pair is observed. The pulse pair is shown in Fig. 11.13(b) and is a simple double pulse sequence for this case of near degenerate levels. In Fig. 11.13(a) the propagation was continued to about 220  $\mu\text{s}$  after the pulse action to see the recurrence of the quasibound state component referred to in the previous paragraph. Here no three body decay loss is assumed. Again, applying a second pulse pair at the time 80  $\mu\text{s}$  could then transfer even more population into the molecular BEC component. Future work will consider the dependence of the dipole couplings between the levels and the exact energies of the levels and describe more accurately the three body decay mechanisms. It is then also possible to optimize the external magnetic field besides the Raman field.

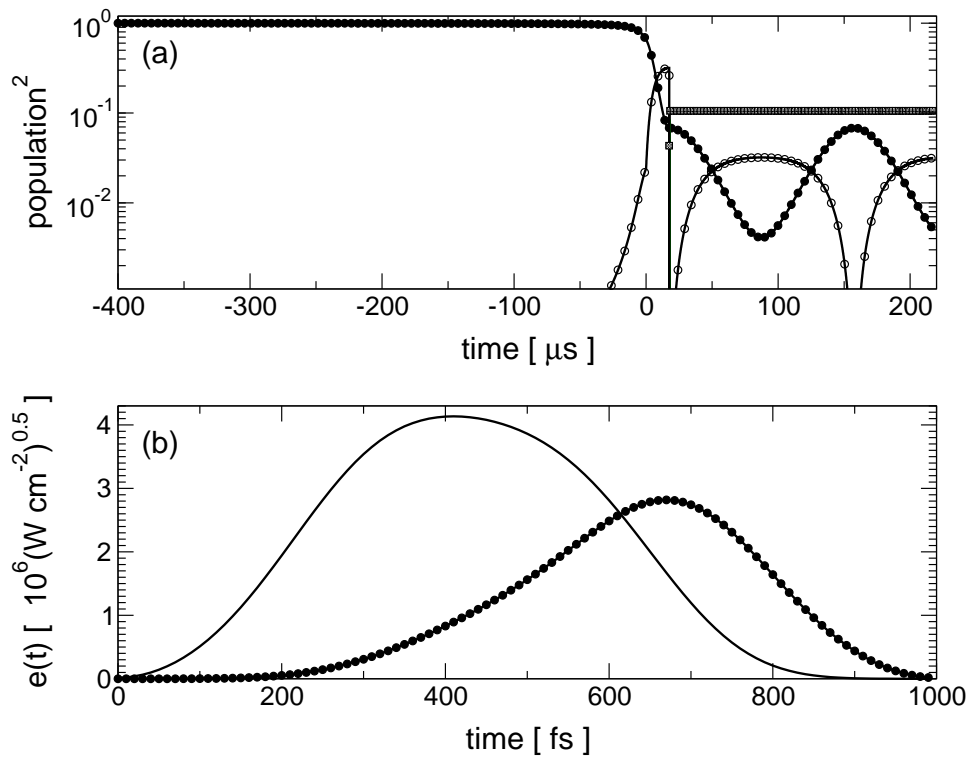


**Figure 11.13:** Molecular levels at near degeneracy. Line style same as in Fig. 11.12. (a) Evolution of the BEC during a negative magnetic field sweep, but without external light field until time  $20 \mu\text{s}$ . Optimal pulse pair action during 1 ps at  $t=20\mu\text{s}$  and then evolution of the condensate under a magnetic field staying at the Feshbach resonance value. (b) Optimal femtosecond Raman pulse pair.  $\epsilon_{L1}$  is black line and  $\epsilon_{L2}$  is the filled dots.



## Chapter 12

# Coherent control theory: Concluding remarks

In the theoretical part of this thesis the framework of optimal control theory was introduced and further developed. Among these developments three are of central importance.

At first a strategy was derived on how to obtain simple, robust and therefore experimentally realizable pulses. With this strategy the optimal result is only slightly dependent on the initial guess, that is there exist no more multiple solutions for one aim, but only the most robust survives. Experiment can directly implement the calculated pulses by applying the optimal mask pattern onto the shaping device.

Second a new generalized functional was presented, with which it is possible to obtain multiple, different optimal control solutions by scanning the laser center frequency provided by the laser source. Thereby again multiple solutions for a single aim can be obtained with the advantage that each of the results is simple, robust and therefore amenable to detailed study. Among the results obtained with the above insight into optimal control theory the following can be emphasized. Experimentally realizable pulses inducing a state selective transfer among vibrational levels spaced by less than the spectral bandwidth could be shown. Molecular  $\pi$ -pulses were presented starting from an initial Boltzmann distribution of states. Optimal control using density matrices was applied to obtain for the first time STIRAP pulses and was also employed to molecular cooling.

Finally the optimal control framework could be extended to include the Gross-Pitaevskii equation, that is a non linear dynamical equation. Here the Raman-photoassociation process of a BEC to a M-BEC assisted by a Feshbach resonance could be improved by letting optimal control theory find tailored nanosecond STIRAP or femtosecond shaped fields. The hope is now to have encouraged experiments to try out the optimal nanosecond and femtosecond Raman pulses proposed here. These pulses could perhaps

be further improved or adapted to the experimental peculiarities using a learning-loop approach. A possible experimental learning-loop setup could be to outcouple small bunches of matter from the BEC and let it fall through the photoassociation tailored laser crossed by a probe laser detecting the number of molecules produced. Thereby a feedback signal would be obtained from each falling BEC droplet.

# Bibliography

- [1] P. Brumer and M. Shapiro, *Laser Control of Chemical Reactions*, Scientific American **3**, 34 (1995).
- [2] D. J. Tannor, R. Kosloff and S. A. Rice, *Coherent pulse sequence induced control of selectivity of reactions: exact quantum mechanical calculations*, J. Chem. Phys. **85**, 5805 (1986).
- [3] A. M. Weiner, *Femtosecond optical pulse shaping and processing*, Prog. Quant. Electr. **19**, 161 (1995).
- [4] M. M. Wefers and K. A. Nelson, *Generation of high-fidelity programmable ultrafast optical waveforms*, Opt. Lett. **20**, 1047 (1995).
- [5] J. X. Tull, M. A. Dugan and W. S. Warren, *High Resolution, Ultrafast Laser Pulse Shaping and its Applications*, Advances in Magnetic and Optical Resonance **20**, 1 (1997).
- [6] E. Zeek, K. Maginnis, S. Backus, U. Russek, M. M. Murnane, G. Mourou, H. C. Kapteyn and G. Vdovin, *Pulse compression by use of deformable mirrors*, Opt. Lett. **24**, 493 (1999).
- [7] D. G. Lee, J. H. Kim, K. H. Hong and C. H. Nam, *Coherent control of high-order harmonics with chirped femtosecond laser pulses*, Phys. Rev. Lett. **87** (2001).
- [8] W. S. Warren, H. Rabitz and M. Dahleh, *Coherent Control of Quantum Dynamics: The Dream Is Alive*, Science **259**, 1581 (1993).
- [9] C. J. Bardeen, Q. Wang and C. V. Shank, *Selective excitation of vibrational wave packet motion using chirped pulses*, Phys. Rev. Lett. **75**, 3410 (1995).
- [10] C. J. Bardeen, J. Che, K. R. Wilson, V. V. Yakovlev, C. C. M. V. A. Apkarian, R. Zadoyan, B. Kohler and M. Messina, *Quantum control of I<sub>2</sub> in the gas phase and in condensed phase solid Kr matrix*, J. Chem. Phys. **106**, 8486 (1997).

- [11] D. Meshulach and Y. Silberberg, *Coherent quantum control of two-photon transitions by a femtosecond laser pulse*, Nature **396**, 239 (1998).
- [12] V. Blanchet, M. A. Bouchene and B. Girard, *Temporal coherent control in the photoionization of Cs<sub>2</sub> - Theory and Experiment*, J. Chem. Phys. **108**, 4862 (1998).
- [13] N. F. Scherer, A. Matro, L. D. Ziegler, M. Du, R. J. Carlson, J. A. Cina and G. R. Fleming, *Fluorescence-detected wave packet interferometry. II. Role of rotations and determination of the susceptibility*, J. Chem. Phys. **96**, 4180 (1992).
- [14] R. S. Judson and H. Rabitz, *Teaching Lasers to Control Molecules*, Phys. Rev. Lett. **68**, 1500 (1992).
- [15] R. A. Bartels, S. Backus, E. Zeek, L. Misoguti, G. Vdovin, I. P. Christov, M. M. Murnane and H. C. Kapteyn, *Shaped-pulse optimization of coherent emission of high-harmonic soft X-rays*, Nature **406**, 164 (2000).
- [16] M. F. DeCamp, D. A. Reis, P. H. Bucksbaum, B. Adams, J. M. Caraher, R. Clarke, C. W. S. Conover, E. M. Dufresne, R. Merlin, V. Stoica and J. K. Wahlstrand, *Coherent control of pulsed X-ray beams*, Nature **413**, 825 (2001).
- [17] T. C. Weinacht, R. A. Bartels, S. Backus, P. H. Bucksbaum, B. Pearson, J. M. Geremia, H. Rabitz, H. C. Kapteyn and M. M. Murnane, *Coherent learning control of vibrational motion in room temperature molecular gases*, Chem. Phys. Lett. **344**, 333 (2001).
- [18] R. J. Levis, G. M. Menkir and H. Rabitz, *Selective bond dissociation and rearrangement with optimally tailored, strong-field laser pulses*, Science **292**, 709 (2001).
- [19] T. Brixner, N. H. Damrauer, P. Niklaus and G. Gerber, *Photosensitive adaptive femtosecond quantum control in the liquid phase*, Nature **414**, 57 (2001).
- [20] A. Assion, T. Baumert, M. Bergt, T. Brixner, B. Kiefer, V. Seyfried, M. Strehle and G. Gerber, *Control of Chemical Reactions by Feedback-Optimized Phase-Shaped Femtosecond Laser Pulses*, Science **282**, 919 (1998).
- [21] R. A. Bartels, T. C. Weinacht, S. R. Leone, H. C. Kapteyn and M. M. Murnane, *Nonresonant control of multimode molecular wave packets at room temperature*, Phys. Rev. Lett. **88**, 33001 (2002).

- [22] J. B. Ballard, H. U. Stauffer, Z. Amitay and S. R. Leone, *Optimization of wave packet coefficient in  $Li_2$  using an evolutionary algorithm: The role of resonant and nonresonant wavelengths*, J. Chem. Phys. **226** (2002).
- [23] T. Feurer, *Feedback-controlled optimization of soft-X-ray radiation from femtosecond laser-produced plasmas*, Appl. Phys. B **68**, 55 (1999).
- [24] T. Feurer, A. Glass, T. Rozgonyi, R. Sauerbrey and G. Szabo, *Control of the photodissociation process of  $CsCl$  using a feedback-controlled self-learning fs-laser system*, Chem. Phys. **267**, 223 (2001).
- [25] W. Wohlleben, J. L. Herek, D. Zeidler and M. Marcus, *Quantum control of energy flow in photosynthesis*, in: *Verhandlungen der deutschen physikalischen Gesellschaft*, p. 83 (2002).
- [26] A. P. Peirce, M. A. Dahleh and H. Rabitz, *Optimal Control of quantum-mechanical systems: Existence, numerical approximation, and applications*, Phys. Rev. A. **37**, 4950 (1988).
- [27] W. Zhu, J. Botina and H. Rabitz, *Rapidly convergent iteration methods for quantum optimal control of population*, J. Chem. Phys. **108**, 1953 (1998).
- [28] D. J. Tannor and S. A. Rice, *Control of selectivity of chemical reaction via control of wave packet evolution*, J. Chem. Phys. **83**, 5013 (1985).
- [29] R. Kosloff, S. A. Rice, P. Gaspard, S. Tersigni and D. J. Tannor, *Wavepacket dancing: achieving chemical selectivity by shaping light pulses*, Chem. Phys. **139**, 201 (1989).
- [30] A. Bartana, R. Kosloff and D. J. Tannor, *Laser cooling of molecular internal degrees of freedom by a series of shaped pulses*, J. Chem. Phys. **99**, 196 (1993).
- [31] P. Gross, D. Neuhauser and H. Rabitz, *Optimal control of curve crossing systems*, J. Chem. Phys. **96**, 2834 (1992).
- [32] I. R. Solá, V. S. Malinovsky and D. J. Tannor, *Optimal pulse sequences for population transfer in multilevel systems*, Phys. Rev. A **60**, 3081 (1999).
- [33] C. Rangan and P. H. Bucksbaum, *Optimally shaped terahertz pulses for phase retrieval in a Rydberg-atom data register*, Phys. Rev. A **64**, 033417 (2001).
- [34] T. Rössler and J. B. Page, *Optical creation of vibrational intrinsic localized modes in anharmonic lattices with realistic interatomic potentials*, Phys. Rev. B **62**, 11460 (2000).

- [35] R. de Vivie-Riedle and K. Sundermann, *Design and interpretation of laser pulses for the control of quantum systems*, Appl. Phys. B **71**, 285 (2000).
- [36] T. Brixner, N. H. Damrauer and G. Gerber, *Femtosecond quantum control*, Advances in atomic, molecular, and optical physics **46**, 1 (2001).
- [37] P. Gaspard and I. Burghardt (Eds.), *Chemical Reactions and Their Control on the Femtosecond Timescale*, Vol. 101 Series *Adv. Chem. Phys.*, Wiley, Brussels (1997).
- [38] H. Rabitz, R. de Vivie-Riedle, M. Motzkus and K.-L. Kompa, *Whither the Future of Controlling Quantum Phenomena?*, Science **288**, 824 (2000).
- [39] S. A. Rice, *Optical control of reactions*, Nature **403**, 496 (2000).
- [40] M. Shapiro and P. Brumer, *Coherent control of atomic, molecular, and electronic processes*, Advances in atomic, molecular, and optical physics **42**, 287 (2000).
- [41] D. Meshulach and Y. Silberberg, *Coherent quantum control of multiphoton transitions by shaped ultrashort optical pulses*, Phys. Rev. A **60**, 1287 (1999).
- [42] J. Cao, C. J. Bardeen and K. R. Wilson, *Molecular  $\pi$  pulse for total inversion of electronic state population*, Phys. Rev. Lett. **80**, 1406 (1998).
- [43] P. Kral and M. Shapiro, *Cyclic population transfer in quantum systems with broken symmetry*, Phys. Rev. Lett. **87**, 183002 (2001).
- [44] A. M. Weiner, D. E. Leaird, J. S. Patel and J. R. W. II, *Programmable shaping of femtosecond optical pulses by use of 128-element liquid crystal phase modulator*, IEEE Journal of Quantum Electronics **28**, 908 (1992).
- [45] M. M. Wefers and K. A. Nelson, *Analysis of programmable ultrashort waveform generation using liquid crystal spatial light modulators*, J. Opt. Soc. Am. B **12**, 1343 (1995).
- [46] M. A. Dugan, J. X. Tull and W. S. Warren, *High-resolution acousto-optic shaping of unamplified and amplified femtosecond laser pulses*, J. Opt. Soc. Am. B **14**, 2348 (1997).
- [47] M. M. Wefers and K. A. Nelson, *Space-Time profiles of shaped ultrafast optical waveforms*, IEEE Journal of Quantum Electronics **32**, 161 (1996).

- [48] T. Hornung, *Amplituden- und Phasenmodulation von ultrakurzen Lichtimpulsen mit einer Flüssigkristallmaske und ihre Anwendung zur Kontrolle von Photonübergängen in Na*, Diplomarbeit, Max-Planck-Institut für Quantenoptik (1999).
- [49] M. Hacker, G. Stobrawa and T. Feurer, *Iterative Fourier transform algorithm for phase-only pulse shaping*, Optics Express **9**, 191 (2001).
- [50] G. Stobrawa, M. Hacker, T. Feurer, D. Zeidler, M. Motzkus and F. Reichel, *A new high-resolution femtosecond pulse shaper*, Appl. Phys. B **72**, 627 (2001).
- [51] T. Brixner and G. Gerber, *Femtosecond polarization pulse shaping*, Opt. Lett. **26**, 557 (2001).
- [52] T. Feurer, J. C. Vaughan, R. M. Koehl and K. A. Nelson, *Multidimensional control of femtosecond pulses using a programmable liquid crystal matrix*, Opt. Lett. (in press).
- [53] M. Hacker, R. Netz, M. Roth, G. Stobrawa and T. Feurer, *Frequency doubling of phase-modulated, ultrashort laser pulses*, Appl. Phys. B **73**, 273 (2001).
- [54] T. Witte, D. Zeidler, D. Proch, K.-L. Kompa and M. Motzkus, *Programmable amplitude and phase modulated fs laser pulses in the mid-infrared*, Opt. Lett. **27**, 131 (2002).
- [55] H.-P. Schwefel, *Evolution and Optimum Seeking*, Wiley, New York (1995).
- [56] D. E. Goldberg, *Genetic Algorithms in Search, Optimization, and Machine Learning*, Addison-Wesley, Reading, MA (1993).
- [57] S. Kirkpatrick, C. D. Gelatt and M. P. Vecchi., *Optimization by simulated annealing*, Science **220**, 671 (1983).
- [58] D. Zeidler, S. Frey, K.-L. Kompa and M. Motzkus, *Evolutionary algorithms and their application to optimal control studies*, Phys. Rev. A **64**, 023420 (2001).
- [59] T. Hornung, R. Meier and M. Motzkus, *Optimal control of molecular states in a learning loop with a parameterization in frequency and time domain*, Chem. Phys. Lett. **326**, 445 (2000).
- [60] T. Hornung, M. Motzkus and R. de Vivie-Riedle, *Adapting optimal control theory and using learning loops to provide experimentally feasible shaping mask patterns*, J. Chem. Phys. **115**, 3105 (2001).

- [61] J.-C. Diels and W. Rudolph, *Ultrashort Laser Pulse Phenomena*, Chap. 1, Optics and Photonics, Academic Press, Inc., San Diego (1995).
- [62] R. Trebino, K. W. DeLong, D. N. Fittinghoff, J. N. Sweetser, M. A. Krumbügel and B. A. Richman, *Measuring ultrashort laser pulses in the time-frequency domain using frequency-resolved optical gating*, Rev. Sci. Instrum. **68**, 3277 (1997).
- [63] C. Iaconis and I. A. Walmsley, *Self-referencing spectral interferometry for measuring ultrashort optical pulses*, IEEE Journal of Quantum Electronics **35**, 501 (1999).
- [64] T. Shuman, I. A. Walmsley, L. Waxer, M. Anderson, C. Iaconis and J. Bromage, *Real-time SPIDER: ultrashort pulse characterization at 20 Hz*, Opt. Express **5**, 134 (1999), and references therein.
- [65] D. N. Fittinghoff, J. L. Bowie, J. N. Sweetser, R. T. Jennings, M. A. Krumbügel, K. W. DeLong, R. Trebino and I. A. Walmsley, *Measurement of the intensity and phase of ultraweak, ultrashort laser pulses*, Opt. Lett. **21**, 884 (1996).
- [66] I. A. Walmsley, *Measuring ultrafast optical pulses*, Optics & Photonics News pp. 29–33 (1999).
- [67] T. Brixner, B. Kiefer and G. Gerber, *Problem complexity in femtosecond quantum control*, Chem. Phys. **267**, 241 (2001).
- [68] T. Hornung, M. Motzkus and R. de Vivie-Riedle, *Teaching optimal control theory to distill robust pulses even under experimental constraints*, Phys. Rev. A **65**, 021403R (2001).
- [69] T. Wilhelm, J. Piel and E. Riedle, *Sub-20-fs pulses tunable across the visible from a blue-pumped single-pass noncollinear parametric converter*, Opt. Lett. **22**, 1494 (1997).
- [70] A. Shirakawa, I. Sakane, M. Takasaka and T. Kobayashi, *Sub-5-fs visible pulse generation by pulse-front-matched noncollinear optical parametric amplification.*, Applied Physics Letters **74**, 2268 (1999).
- [71] G. Cerullo, M. Nisoli, S. Stagira and S. Desilvestri, *Sub-8-fs pulses from an ultrabroadband optical parametric amplifier in the visible*, Opt. Lett. **23**, 1283 (1998).
- [72] G. M. Gale, M. Cavallari, T. J. Driscoll and F. Hache, *Sub-20-fs tunable pulses in the visible from an 82-MHz optical parametric oscillator*, Opt. Lett. **20**, 1562 (1995).

- [73] L. A. W. Gloster, Z. X. Jiang and T. A. King, *Characterization of an Nd-YaG-pumped  $\beta$ -BaB<sub>2</sub>O<sub>4</sub> optical parametric oscillator in collinear and noncollinear phase-matched configurations*, IEEE Journal of Quantum Electronics **30**, 2961 (1994).
- [74] T. Baumert, T. Brixner, V. Seyfried, M. Strehle and G. Gerber, *Femtosecond pulse shaping by an evolutionary algorithm with feedback*, Appl. Phys. B **65**, 779 (1997).
- [75] D. Meshulach, D. Yelin and Y. Silberberg, *Adaptive ultrashort pulse compression and shaping*, Optics Communications **138**, 345 (1997).
- [76] D. Zeidler, T. Hornung, D. Proch and M. Motzkus, *Adaptive compression of tunable pulses from a non-collinear-type OPA to below 16 fs by feedback-controlled pulse shaping*, Appl. Phys. B **70**, S125 (2000).
- [77] A. Efimov, C. Schaffer and D. H. Reitze, *Programmable shaping of ultrabroad-bandwidth pulses from a Ti:sapphire laser*, J. Opt. Soc. Am. B **12**, 1968 (1995).
- [78] T. Feurer, A. Glass and R. Sauerbrey, *Two-photon photoconductivity in SiC photodiodes and its application to autocorrelation measurements of femtosecond optical pulses*, Appl. Phys. B **65**, 295 (1997).
- [79] C. R. Vidal, *Vapor cells and heat pipes*, in: F. B. Dunning and R. G. Hulet (Eds.), *Atomic, Molecular and Optical Physics: Atoms and Molecules*, Vol. 29B Series *Experimental Methods in the Physical Sciences*, pp. 67–83, Academic Press, New York (1996).
- [80] M. D. Crisp, *Propagation of small-area pulses of coherent light through a resonant medium*, Phys. Rev. A **1**, 1604 (1970).
- [81] J. K. Ranka, R. W. Schirmer and A. L. Gaeta, *Coherent spectroscopic effects in the propagation of ultrashort pulses through a two-level system*, Phys. Rev. A **57**, R 36 (1998).
- [82] A. W. Albrecht, J. D. Hybl, S. M. G. Faeder and D. M. Jonas, *Experimental distinction between phase shifts and time delays: Implications for femtosecond spectroscopy and coherent control reactions*, J. Chem. Phys. **111**, 10934 (1999), errata in: J. Chem. Phys. **115**, 5691 (01).
- [83] M. M. Wefers, H. Kawashima and K. A. Nelson, *Automated multi-dimensional coherent optical spectroscopy with multiple phase-related femtosecond pulses*, J. Chem. Phys. **102**, 9133 (1995).
- [84] H. Kawashima, M. M. Wefers and K. A. Nelson, *Femtosecond pulse shaping, multiple-pulse spectroscopy, and optical control*, Ann. Rev. Phys. Chem. **46**, 627 (1995).

- [85] S. Speiser and J. Jortner, *The 3/2 power law for high order multiphoton processes*, Chem. Phys. Lett. **44**, 399 (1976).
- [86] S. Mukamel, *Principles of Nonlinear Optical Spectroscopy*, Oxford University Press, New York (1995).
- [87] J. Sung and R. J. Silbey, *Four wave mixing spectroscopy for a multi-level system*, J. Chem. Phys. **115**, 9266 (2001).
- [88] B. I. Grimberg, V. V. Lozovoy, M. Dantus and S. Mukamel, *Ultrafast nonlinear spectroscopic techniques in the gas phase and their density matrix representation*, J. Phys. Chem. **106**, 697 (2002).
- [89] S. Meyer, *Nichtlineare Kurzzeitspektroskopie an kleinen Molekülen: Korrelation zwischen induzierter Wellenpaketdynamik und zeitaufgelösten Observablen*, PhD. Thesis, Universität Würzburg (1999), see especially chapter 3.
- [90] T. Chen, V. Engel, M. Heid, W. Kiefer, G. Knopp, A. Materny, S. Meyer, R. Pausch, M. Schmitt, H. Schwörer and T. Siebert, *Determination of wave packet dynamics by femtosecond time-resolved pump-dump-probe and four-wave mixing techniques*, J. Mol. Struct. **480-481**, 33 (1999).
- [91] S. Meyer, M. Schmitt, A. Materny, W. Kiefer and V. Engel, *A theoretical analysis of the time-resolved femtosecond CARS spectrum of I<sub>2</sub>*, Chem. Phys. Lett. **281**, 332 (1997), errata in: Chem. Phys. Lett. 287 (1998) 753-754.
- [92] V. Engel, *Excitation processes with ultrashort laser pulses: exact time-dependent quantum calculations*, Comp. Phys. Commun. **63**, 228 (1991).
- [93] M. D. Feit, J. A. F. Jr. and A. Steiger, *Solution of the Schrödinger Equation by a Spectral Method*, J. Comp. Phys. **47**, 412 (1982).
- [94] M. Motzkus, S. Pedersen and A. H. Zewail, *Femtosecond Real-time Probing of Reactions. 19. Nonlinear (DFWM) Techniques for Probing Transition States of Uni- and Bimolecular Reactions*, J. Phys. Chem. **100**, 5620 (1996).
- [95] M. Schmitt, G. Knopp, A. Materny and W. Kiefer, *Femtosecond time-resolved four-wave mixing spectroscopy in iodine vapour*, Chem. Phys. Lett. **280**, 339 (1997).
- [96] M. Schmitt, *Femtosekunden-zeitaufgelöste kohärente vierwellenmisch-Spektroskopie zur zustandsselektiven Untersuchung molekularer Dynamik einfacher Systeme*, PhD. Thesis, Universität Würzburg (1998).

- [97] E. Schreiber, *Femtosecond real-time spectroscopy of small molecules and clusters*, Vol. 143 Series *Springer Tracts in Modern physics*, Chap. 3, p. 69, Springer, Berlin (1998).
- [98] I. Pastirk, E. J. Brown, Q. Zhang and M. Dantus, *Quantum control of the yield of a chemical reaction*, *J. Chem. Phys.* **108**, 4375 (1998).
- [99] I. Pastirk, E. J. Brown, B. I. Grimberg, V. V. Lozovoy and M. Dantus, *Sequences for controlling laser excitation with femtosecond three-pulse four-wave mixing*, *Faraday Discuss.* **113**, 401 (1999).
- [100] C. J. Bardeen, V. V. Yakovlev, K. R. Wilson, S. D. Carpenter, P. M. Weber and W. S. Warren, *Feedback quantum control of molecular electronic population transfer*, *Chem. Phys. Lett.* **280**, 151 (1997).
- [101] M. S. Pshenichnikov, W. P. Deboeij and D. A. Wiersma, *Coherent control over Liouville-space pathways interference in transient four-wave mixing spectroscopy*, *Phys. Rev. Lett.* **76**, 4701 (1996).
- [102] M. S. Pshenichnikov, A. Baltuska, F. de Haan and D. A. Wiersma, *Ultrashort Pulse Characterization by Frequency-Resolved pump-probe*, in: T. Elsaesser, S. Mukamel, M. M. Murnane and N. F. Scherer (Eds.), *Ultrafast Phenomena XII*, pp. 147–149, Springer (2000).
- [103] L. D. Book and N. F. Scherer, *Wavelength-resolved stimulated photon echoes: Direct observation of ultrafast intramolecular vibrational contributions to electronic dephasing.*, *J. Chem. Phys.* **111**, 792 (1999).
- [104] W. P. de Boeij, M. S. Pshenichnikov and D. A. Wiersma, *Ultrafast solvation dynamics explored by femtosecond photon echo spectroscopies*, *Ann. Rev. Phys. Chem.* **49**, 99 (1998).
- [105] G. R. Fleming, D. A. Blank, M. H. Cho and A. Tokmakoff, *Fifth-order two-dimensional Raman spectroscopy of the intermolecular and vibrational dynamics in liquids*, *Ultrafast infrared and Raman Spectroscopy* **26**, 437 (2001).
- [106] S. Mukamel, *Multidimensional femtosecond correlation spectroscopies of electronic and vibrational excitations*, *Annu. Rev. Phys. Chem.* **51**, 691 (2000).
- [107] C. Scheurer and S. Mukamel, *Design strategies for pulse sequences in multidimensional optical spectroscopies*, *J. Chem. Phys.* **115**, 4989 (2001).
- [108] D. Oron, N. Dudovich, D. Yelin and Y. Silberberg, *Narrow-Band coherent anti-stokes Raman signals from broad-band pulses*, *Phys. Rev. Lett.* **88**, 063004 (2002).

- [109] Y. Silberberg, *Coherent Control of CARS spectroscopy*, in: *2nd International Workshop on Optimal Control of Quantum Dynamics: Theory and Experiment* (2001).
- [110] D. J. Tannor, R. Kosloff and A. Bartana, *Laser cooling of internal degrees of freedom of molecules by dynamically trapped states*, *Faraday Discuss.* **113**, 365 (1999).
- [111] I. R. Solá, J. Santamaria and D. J. Tannor, *Optimal control of multiphoton excitation - a black box or a flexible toolkit*, *J. Phys. Chem.* **102**, 4301 (1998).
- [112] V. S. Malinovsky, C. Meier and D. J. Tannor, *Optical paralysis in electronically congested systems: Application to large-amplitude vibrational motion of ground state Na<sub>2</sub>*, *Chem. Phys.* **221**, 67 (1997).
- [113] Y. Ohtsuki, W. Zhu and H. Rabitz, *Monotonically convergent algorithm for quantum optimal control with dissipation*, *J. Chem. Phys.* **110**, 9825 (1999).
- [114] V. F. Krotov, *Global methods in optimal control theory*, in: *Monographs and Textbooks in Pure and Applied Mathematics*, Vol. 195, Marcel Dekker Inc., New York (1996).
- [115] K. Sundermann and R. de Vivie-Riedle, *Extensions to quantum control algorithms and applications to special problems in state selective molecular dynamics*, *J. Chem. Phys.* **110**, 1896 (1999).
- [116] W. Zhu and H. Rabitz, *Uniform, rapidly convergent algorithm for quantum optimal control of objectives with a positive semidefinite Hessian matrix*, *Phys. Rev. A* **58**, 4741 (1998).
- [117] W. Zhu and H. Rabitz, *A rapid monotonically convergent iteration algorithm for quantum optimal control over the expectation value of a positive definite operator*, *J. Chem. Phys.* **109**, 385 (1998).
- [118] S. Shi, A. Woody and H. Rabitz, *Optimal control of selective vibrational excitation in harmonic linear chain molecules*, *J. Chem. Phys.* **88**, 6870 (1988).
- [119] S. Shi and H. Rabitz, *Optimal control of selective vibrational excitation of harmonic molecules: Analytic solution and restricted forms for the optimal fields*, *J. Chem. Phys.* **92**, 2927 (1990).
- [120] J. Somloi, V. A. Kazakov and D. J. Tannor, *Controlled dissociation of I<sub>2</sub> via optical transitions between X and B electronic states*, *Chem. Phys.* **172**, 85 (1993).

- [121] D. J. Tannor, V. A. Kazakov and V. Orlov, *Time dependent quantum molecular dynamics*, Nato ASI Series B **299**, 347 (1992).
- [122] C. Leforestier, R. H. Bisseling, C. Cerjan, M. D. Feit, R. Friesner, A. Guldborg, A. Hammerich, G. Jolicard, W. Karrlein, H.-D. Meyer, N. Lipkin, O. Roncero and R. Kosloff, *A Comparison of Different Propagation Schemes for the Time Dependent Schrödinger Equation*, J. Comp. Phys. **94**, 59 (1991).
- [123] R. Kosloff, *Propagation methods for quantum molecular dynamics*, Annu. Rev. Phys. Chem. **45**, 145 (1994).
- [124] R. Kosloff and E. Fattal, *Grid Methods in Quantum Molecular Dynamics*, Recent research developments in physical chemistry **2**, 501 (1998).
- [125] D. Kosloff and R. Kosloff, *A Fourier Method Solution for the Time Dependent Schrödinger Equation as a Tool in Molecular Dynamics*, Journal of Computational Physics **52**, 35 (1983).
- [126] G. Katz, R. Baer and R. Kosloff, *A new method for numerical flux calculations in quantum molecular dynamics*, Chem. Phys. Lett. **239**, 230 (1995).
- [127] R. Baer, *Accurate and efficient evolution of the nonlinear Schrödinger equation*, Phys. Rev. A **62**, 0638101 (2000).
- [128] U. Manthe and F. Matzkies, *Rotational effects in the  $H_2 + OH \rightarrow H + H_2O$  reaction rate: Full-dimensional close coupling results*, JCP **113**, 5725 (2000).
- [129] M. Frigo and S. G. Johnson, *The Fastest Fourier Transform in the West*, Tech. Rep., Massachusetts Institute of Technology (1997).
- [130] V. Kokoouline, O. Dulieu, R. Kosloff and F. Masnou-Seeuws, *Theoretical treatment of channel mixing in excited  $Rb_2$  and  $Cs_2$  ultracold molecules: Determination of predissociation lifetimes with coordinate mapping*, Phys. Rev. A **6203**, 2716 (2000).
- [131] A. Hofmann, *Ultraschnelle molekulare Quantendynamik durch konische Durchschneidungen*, PhD. Thesis, Ludwig-Maximilians-Universität München (2001).
- [132] S. Rutz, R. de Vivie-Riedle and E. Schreiber, *Femtosecond wave-packet propagation in spin-orbit-coupled electronic states of  $^{39,39}K_2$  and  $^{39,41}K_2$* , Phys. Rev. A **54**, 306 (1996).

- [133] J. M. Geremia, W. Zhu and H. Rabitz, *Incorporating physical implementation concerns into closed loop quantum control experiments*, J. Chem. Phys. **113**, 10841 (2000).
- [134] Y. Ohtsuki, K. Nakagami, Y. Fujimura, W. Zhu and H. Rabitz, *Quantum optimal control of multiple targets: Development of a monotonically convergent algorithm and application to intramolecular vibrational energy redistribution control*, J. Chem. Phys. **114**, 8867 (2001).
- [135] C. M. Tesch, L. Kurtz and R. de Vivie-Riedle, *Applying optimal control theory for elements of quantum computation in molecular systems*, Chem. Phys. Lett. **343**, 633 (2001).
- [136] K. Bergmann, H. Theuer and B. W. Shore, *Coherent population transfer among quantum states of atoms and molecules*, Reviews of Modern Physics **70**, 1003 (1998).
- [137] K. Sundermann, *Parallele Algorithmen zur Quantendynamik und optimalen Laserpulskontrolle chemischer Reaktionen*, PhD. Thesis, FU Berlin (1998).
- [138] R. Wynar, R. S. Freeland, D. J. Han, C. Ryu and D. J. Heinzen, *Molecules in a Bose-Einstein condensate*, Science **287**, 1016 (2000).
- [139] D. J. Heinzen, R. Wynar, P. D. Drummond and K. V. Kheruntsyan, *Superchemistry: Dynamics of Coupled Atomic and Molecular Bose-Einstein condensates*, Phys. Rev. Lett. **84**, 5029 (2000).
- [140] A. Vardi, M. Shapiro and K. Bergmann, *Complete population transfer to and from a continuum and the radiative association of cold Na atoms to produce translationally cold Na<sub>2</sub> molecules in specific vibrational states*, Optics Express **4**, 91 (1999), and references therein.
- [141] P. S. Julienne, K. Burnett, Y. B. Band and W. C. Stwalley, *Stimulated Raman molecule production in Bose-Einstein condensates*, Phys. Rev. A **58**, R797 (1998).
- [142] M. Mackie, R. Kowalski and J. Javanainen, *Bose-stimulated Raman adiabatic passage in photoassociation*, Phys. Rev. Lett. **84**, 3803 (2000).
- [143] S. J. J. M. F. Kokkelmans, H. M. J. Vissers and B. J. Verhaar, *Formation of a Bose condensate of stable molecules via a Feshbach resonance*, Phys. Rev. A **63**, 0316011 (2001).
- [144] R. Ueberna, Z. Amitay, R. A. Loomis and S. R. Leone, *Phase control of wavepacket dynamics using shaped femtosecond pulses*, Faraday Discuss. **113**, 385 (1999).

- [145] J. S. Melinger, S. R. Gandhi, A. Hariharan, J. X. Tull and W. S. Warren, *Generation of Narrowband Inversion with Broadband Laser Pulses*, Phys. Rev. Lett. **68**, 2000 (1992).
- [146] J. S. Melinger, S. R. Gandhi, A. Hariharan, D. Goswami and W. S. Warren, *Adiabatic population transfer with frequency-swept laser pulses*, J. Chem. Phys. **101**, 6439 (1994).
- [147] D. J. Maas, M. J. J. Vrakking and L. D. Noordam, *Rotational interference in vibrational ladder climbing in NO by chirped infrared laser pulses*, Phys. Rev. A **60**, 1351 (1999).
- [148] L. Pesce, Z. Amitay, R. Uberna, S. R. Leone, M. Ratner and R. Kosloff, *Quantum dynamics simulation of the ultrafast photoionization of Li<sub>2</sub>*, J. Chem. Phys. **114**, 1259 (2001).
- [149] P. Backhaus and B. Schmidt, *Femtosecond quantum dynamics of photoassociation reactions: the exciplex formation of mercury*, Chem. Phys. **217**, 131 (1997).
- [150] A. Bartana, R. Kosloff and D. J. Tannor, *Laser cooling of molecules by dynamically trapped states*, Chem. Phys. **267**, 195 (2001), and references therein.
- [151] G. Lindblad, *Entropy, information and quantum measurements*, Communications in Mathematical Physics **33**, 305 (1973).
- [152] A. Vardi and M. Shapiro, *Matter-field entropy transfer in stimulated photoassociation*, Phys. Rev. A **62**, 5401/1 (2000).
- [153] W. T. Pollard and R. A. Friesner, *Solution of the Redfield equation for the dissipative quantum dynamics of multilevel systems*, J. Chem. Phys. **100**, 5054 (1994), specially section C.
- [154] Y. Ohtsuki, *Optimal Control of Laser-Induced Surface Processes: Development of Solution Algorithms and Applications*, in: *2nd International Workshop on Optimal Control of Quantum Dynamics: Theory and Experiment* (2001).
- [155] W. Huisinga, L. Pesce, R. Kosloff and P. Saalfrank, *Faber and Newton polynomial integrators for open-system density matrix propagation*, J. Chem. Phys. **110**, 5538 (1999).
- [156] L. Pesce, *Dissipative Quantum Dynamics of Elementary Chemical Processes at Metal Surfaces*, PhD. Thesis, Freie Universität Berlin (1998).

- [157] T. Gerdtts and U. Manthe, *A wave packet approach to the Liouville-von Neumann equation for dissipative systems*, J. Chem. Phys. **106**, 3017 (1997).
- [158] V. S. Malinovsky and D. J. Tannor, *Simple and robust extension of the stimulated Raman adiabatic passage technique to N-level systems*, Phys. Rev. A **56**, 4929 (1997).
- [159] N. Wang and H. Rabitz, *Optimal control of population transfer in an optically dense medium*, J. Chem. Phys. **104**, 1173 (1996).
- [160] A. Bartana, R. Kosloff and D. J. Tannor, *Laser cooling of internal degrees of freedom II*, J. Chem. Phys. **106**, 1435 (1997).
- [161] D. J. Tannor and A. Bartana, *On the interplay of control fields and spontaneous emission in laser cooling*, J. Phys. Chem. A **103**, 10359 (1999).
- [162] W. Ketterle and D. E. Pritchard, *Atom cooling by time-dependent potentials*, Phys. Rev. A **46**, 4051 (1992).
- [163] D. J. Tannor, *Laser Cooling of Molecules: A Theory of Purity Increasing Transformations*, in: *2nd International Workshop on Optimal Control of Quantum Dynamics: Theory and Experiment* (2001).
- [164] V. Ramakrishna, M. V. Salapaka, M. Dahleh, H. Rabitz and A. Peirce, *Controllability of molecular systems*, Phys. Rev. A **51**, 960 (1995).
- [165] G. Turinici and H. Rabitz, *Quantum wavefunction controllability*, Chem. Phys. pp. 1–9 (2001).
- [166] V. Vuletic and S. Chu, *Laser cooling of atoms, ions, or molecules by coherent scattering*, Phys. Rev. Lett. **84**, 3787 (2000).
- [167] S. E. Morin, C. C. Yu and T. W. Mossberg, *Strong Atom-Cavity coupling over large volumes and the observation of subnatural intracavity atomic linewidths*, Phys. Rev. Lett. **73**, 1489 (1994).
- [168] G. Björk, S. Machida, Y. Yamamoto and K. Igeta, *Modification of spontaneous emission rate in planar dielectric microcavity structures*, Phys. Rev. A (1991).
- [169] D. J. Heinzen, J. J. Childs, J. E. Thomas and M. S. Feld, *Enhanced and Inhibited Visible spontaneous emission by atoms in a confocal resonator*, Phys. Rev. Lett. **58**, 1320 (1987).
- [170] A. E. Siegmann, *Lasers*, Chap. 19, University Science Books, California (1986).

- [171] A. J. Moerdijk, B. J. Verhaar and A. Axelsson, *Resonances in ultracold collisions of  $^6\text{Li}$ ,  $^7\text{Li}$  and  $^{23}\text{Na}$* , Phys. Rev. A **51**, 4852 (1995).
- [172] H. Feshbach, *Theoretical nuclear physics*, Wiley, New York (1992).
- [173] F. A. van Abeelen and B. J. Verhaar, *Time-Dependent Feshbach Resonance Scattering and Anomalous decay of a Na Bose-Einstein Condensate*, Phys. Rev. Lett. **83**, 1550 (1999).
- [174] E. Timmermans, P. Tommasini, M. Hussein and A. Kerman, *Feshbach resonances in atomic Bose-Einstein condensates*, Physics Reports-Review Section of Physics Letters **315**, 199 (1999).
- [175] J. T. Bahns, P. L. Gould and W. C. Stwalley, *Formation of cold ( $T \leq 1\text{ K}$ ) molecules*, Advances in atomic, molecular and optical physics **42**, 171 (2000).
- [176] A. Fioretti, D. Comparat, A. Crubellier, O. Dulieu, F. Masnou-Seeuws and P. Pillet, *Formation of cold  $\text{Cs}_2$  molecules through photoassociation*, Phys. Rev. Lett. **80**, 4402 (1998).
- [177] M. Vatasescu, O. Dulieu, R. Kosloff and F. Masnou-Seeuws, *Optimal control of photoassociation of cold atoms and photodissociation of long-range molecules: characteristic times for wave-packet propagation*, Phys. Rev. A **63**, 03340701 (2001).
- [178] P. D. Drummond, K. V. Kheruntsyan and H. He, *Coherent molecular solitons in Bose-Einstein Condensates*, Phys. Rev. Lett. **81**, 3055 (1998).
- [179] Y. B. Band and P. S. Julienne, *Ultracold-molecule production by laser-cooled atom photoassociation*, Phys. Rev. A **51**, R4317 (1995).
- [180] A. Mody, M. Haggerty, J. M. Doyle and E. J. Heller, *No-sticking effect and quantum reflection in ultracold collisions*, Phys. Rev. B **64**, 085418 (2001), and references therein.
- [181] S. Inouye, M. R. Andrews, J. Stenger, H.-J. Miesner, D. M. Stamper-Kurn and W. Ketterle, *Observation of Feshbach resonances in a Bose-Einstein condensate*, Nature **392**, 151 (1998), and references therein.
- [182] J. Stenger, S. Inouye, M. R. Andrews, H.-J. Miesner, D. M. Stamper-Kurn and W. Ketterle, *Strongly enhanced inelastic collisions in a Bose-Einstein condensate near Feshbach resonances*, Phys. Rev. Lett. **82**, 2422 (1999).
- [183] F. A. van Abeelen and B. J. Verhaar, *Time-dependent Feshbach resonance scattering and anomalous decay of a Na Bose-Einstein condensate*, Phys. Rev. Lett. **83**, 1550 (1999).

[184] NAG Co., *d02pcf Routine*.

## Danksagung

An erster Stelle gilt mein Dank Regina de Vivie-Riedle und Marcus Motzkus für die tatkräftige Unterstützung in allen Phasen der Promotion, die vielen anregenden Diskussionen und die nahezu freundschaftliche Betreuung. Beiden bin ich sehr dankbar, dass sie sich für diese theoretisch/experimentelle Doktorarbeit eingesetzt haben. Dass meine Zukunftspläne bald Realität werden, dazu haben beide auch wesentlich mitgewirkt. Vielen Dank!

Ich danke, Prof. K.-L. Kompa, der es mir ermöglichte meine experimentellen Ergebnisse auf nationalen und internationalen Konferenzen zu vertreten und eine sowohl experimentell als auch theoretische Arbeit genehmigte.

Der ganzen experimentellen Gruppe danke ich für die gute Zusammenarbeit. Tobias Lang, Susanne Frey, Wendel Wohlleben, Dirk Zeidler und besonders Richard Meier, mit dem die Zeiten im Labor und ausserhalb richtig Spass gemacht haben. Angelika Hofmann und Lukas Kurtz haben mir beide sehr geholfen in der Kontrolltheorie Fuss zu fassen. Für ein erfrischendes Arbeitsklima danke ich noch Carmen Tesch, Dorothee Geppert und Ulrike Troppmann.

Ein herzlicher Dank gilt auch Sergei Gordienko für seine Hilfsbereitschaft und Giovanna Morigi, Pepijn Pinkse und Amalia Apalategui Rebollo für die lebhaften Diskussionen.

Auch geht mein Dank an Hans Bauer, unserem Techniker, der bei technischen Konstruktionsarbeiten Hervorragendes leistete. Ebenso danke ich der Werkstatt, dem Einkauf, der Verwaltung und allen Mitarbeitern des Institutes, die auf ihre Weise zum Gelingen dieser Arbeit beigetragen haben.

Prof. Verhaar danke ich für die sehr freundliche Aufnahme während meines Aufenthaltes an der TU Eindhoven, die hervorragende Erklärung seiner theoretischen Methoden und die tolle Zusammenarbeit. In diesem Sinne sei auch Prof. Tannor und Shlomo Sklarz gedankt - für eine lebhaft deutsch-israelische Kooperation.

Meinen Eltern gilt grosser Dank für die Ermöglichung meines Studiums, ihre Sorge um mein Wohlergehen und für jene Sicherheit in schweren Situationen.

Meiner Frau danke ich ganz besonders für ihren Beistand, für ihre Geduld und Liebe.

